“On the Impact of Micro- and Nanostructural Characteristics on the Deformation Behavior and Mechanical Properties of High- and Medium-Manganese Steels”

Von der Fakultät für Georessourcen und Materialtechnik
der Rheinisch-Westfälischen Technischen Hochschule Aachen

zur Erlangung des akademischen Grades eines

Doktors der Ingenieurwissenschaften

genehmigte Dissertation

vorgelegt von **M.Sc.**

Simon Sevsek

aus Kamp-Lintfort

Berichter: Univ.-Prof. Dr.-Ing. Wolfgang Bleck

Prof. Dr.rer.nat. Dmitri Molodov

Tag der mündlichen Prüfung: 13. Juni 2019

Diese Dissertation ist auf den Internetseiten der Universitätsbibliothek online verfügbar

This thesis includes the following articles that have been published in international peer-reviewed journals:

Chapter II – **S. Sevsek**, W. Bleck: Ab Initio-Based Modelling of the Yield Strength in High-Manganese Steels. Metals 8 (1) (2018) 34. https://doi.org/10.3390/met8010034.

Chapter III – **S. Sevsek**, F. Brasche, C. Haase, W. Bleck: Combined deformation twinning and short-range ordering causes serrated flow in high-manganese steels. Materials Science & Engineering A 746 (2019) 434-442. https://doi.org/10.1016/j.msea.2019.01.042.

Chapter IV – **S. Sevsek**, F. Brasche, D. Molodov, W. Bleck: On the Influence of Grain Size on the TWIP/TRIP-Effect and Texture Development in High-Manganese Steels. Materials Science & Engineering A 754 (2019) 152-160. https://doi.org/10.1016/j.msea.2019.03.072.

Chapter V – **S. Sevsek**, C. Haase, W. Bleck: Strain-Rate-Dependent Deformation Behavior and Mechanical Properties of a Multi-Phase Medium-Manganese Steel. Metals 9 (3) (2019) 344. https://doi.org/10.3390/met9030344.

Additionally, the following extended abstracts have been published in the conference proceedings of 4th International Conference on Medium and High Manganese Steels (4th HMnS):

Appendix I – **S. Sevsek**, S. Wesselmecking, M. Haupt, W. Bleck: The Impact of Microstructural Characteristics and Testing Parameters on the Formability of High-Manganese Steels. Conference Proceedings of the 4th International Conference on Medium and High Manganese Steels, Aachen, Germany, April 1-3 (2019) 310-313.

Appendix II – T. Allam, **S. Sevsek**, X. Guo, A. Hamada, W. Bleck: On the mechanical and corrosion properties of a precipitation-strengthened medium manganese austenitic stainless steel. Conference Proceedings of the 4th International Conference on Medium and High Manganese Steels, Aachen, Germany, April 1-3 (2019) 365-368.

Appendix III – M. Haupt, M. Müller, C. Haase, **S. Sevsek**, A. Schwedt, G. Hirt: Impact of warm rolling on microstructure and mechanical properties of high manganese steels. Conference Proceedings of the 4th International Conference on Medium and High Manganese Steels, Aachen, Germany, April 1-3 (2019) 97-100.

Acknowledgements

An erster Stelle gilt mein Dank Prof. Dr.-Ing. Wolfang Bleck für die Betreuung bei der Erstellung dieser Dissertation, für die gewährten Freiheiten im Teilprojekt C2 des SFB 761 und die Möglichkeit die Arbeit am Institut für Eisenhüttenkunde anzufertigen. Zusätzlich möchte ich mich für das Vertrauen bedanken, sowohl im Rahmen des SFB 761 als auch insbesondere bei der Koordination und Organisation der Arbeiten im Exzellenzcluster „Internet of Production".

Prof. Dr. rer. nat. Dmitri A. Molodov möchte ich neben der Übernahme des Zweitgutachtens auch für die gemeinsame Arbeit im SFB 761 danken.

Mein besonderer Dank gilt Dr. Christian Haase und Frederike Brasche. Die Zusammenarbeit und Gespräche, ob fachlich oder persönlich, empfand ich stets als sehr angenehm und konstruktiv.

Die schnelle Vollendung dieser Arbeit war nur möglich durch die gegebenen Rahmenbedingungen der Arbeit am Institut für Eisenhüttenkunde. Meinen Gruppenleitern Adrian Rüskamp und Sebastian Wesselmecking bin ich zu tiefstem Dank verpflichtet in dem Bewusstsein, dass mir zeitliche Freiheiten zur wissenschaftlichen Arbeit eingeräumt wurden, die ich nicht als selbstverständlich erachte. Hannah, Adrian, Sascha und Andreas möchte ich zudem für die gute Stimmung im Büro danken und dafür, dass wir die zahlreichen fachlichen und auch persönlichen Hochs und Tiefs immer vertraulich miteinander teilen konnten.

Zusätzlich möchte ich mich bei Frau Christiane Beumers und Frau Martina Sparrer für die organisatorische Koordination zahlreicher Termine bedanken. Ebenso gilt mein Dank Kirsten, Nicole und Ulrike, für ihren Durchblick und die Unterstützung bei der Einhaltung zahlreicher administrativer Formalia. Stellvertretend für alle Techniker danke ich Jürgen, Dietmar und Robert für die erstklassige Betreuung bei der Durchführung der experimentellen Arbeiten.

Meinen Kollegen im SFB 761 danke ich für die fachlichen Diskussionen und die konstruktive Zusammenarbeit im Rahmen der zahlreichen gemeinsamen Veranstaltungen. Besonders möchte ich Marco Haupt danken, der einen großen Teil des Materials bereitgestellt hat, welches in dieser Arbeit experimentell untersucht wurde.

Zum Abschluss gilt mein Dank meiner Familie.

Abstract

Owing to substantial efforts of the scientific community, the remarkable mechanical properties of high-manganese steels (HMnS) and medium-manganese steels (MMnS) have led to their emergence as candidates for lightweight, structural components in the automotive industry. By adjusting the stacking fault energy (SFE) and the microstructure, the strain hardening behavior can be tailored to achieve a broad range of strength-ductility combinations. Despite the advantages and opportunities these alloys offer, a limited fundamental understanding of various metallurgical parameters has prevented the establishment of HMnS and MMnS as a replacement for conventional high-strength steels.

In the interest of furthering the understanding of the mechanical properties of HMnS and MMnS, this thesis analyzes the impact and scale-bridging interplay of different micro- and nanostructural features on the yield strength and the deformation behavior. To this end, the experimental determination of the mechanical properties of several alloys via tensile testing was combined with the microstructural characterization by means of optical microscopy, scanning electron microscopy, electron backscatter diffraction (EBSD) and X-ray diffraction (XRD) experiments, energy-dispersive X-ray spectroscopy and in-situ digital image correlation (DIC) techniques. Additionally, a simulation approach based on the density functional theory was developed to quantify the influence of nanoscale short-range ordered clusters on the macroscopic mechanical properties.

Integrating data from density-functional-theory-based simulations into a modelling approach for HMnS revealed the impact of short-range ordered clusters on the yield strength. This allowed for the quantification of the individual impact of C, Mn and Al on the yield strength both in terms of short-range ordering and solid solution strengthening. While the impact of alloying additions of C and Al to the contribution of short-range ordered clusters to the yield strength within the usual range of chemical compositions of HMnS was very effective, the high alloying contents of Mn in HMnS limited the effectiveness of further Mn additions.

The analysis of deformation-induced twinning (TWIP) during plastic deformation in two HMnS showed that short-range ordered clusters affect the strain hardening behavior by means of short-range-ordering-assisted deformation twinning. Further analysis of the deformation behavior in fully-recrystallized, partially-recrystallized and recovery-annealed material states at different

testing temperatures disclosed that the orientation-dependent localized activation of the TWIP effect on the microscale was responsible for the occurrence of serrated flow curves. Accordingly, it was shown that short-range ordering on the nanoscale significantly affects the deformation behavior on the microscale, which in turn determines the mechanical properties on the macroscale. Subsequent XRD, macrotexture and EBSD experiments regarding the impact of grain size showed that while the fine-grained materials had significantly higher yield strengths, the activation of the TWIP effect and the deformation-induced phase transformation (TRIP) to martensite was partially suppressed.

The findings on the importance of the initial microstructure for both yield strength and strain hardening behavior in HMnS were put into context of a multi-phase MMnS. Using interrupted and in-situ DIC tensile tests at different strain rates coupled with EBSD experiments, it was shown that the strain-rate sensitivity of the MMnS on the macroscale was driven by the strain-rate-dependent strain-partitioning and phase-transformation behavior on the microscale.

Finally, the influences of the microstructure of HMnS and MMnS on the yield strength and strain hardening behavior were analyzed, compared and put into the context of the impact of microstructural homogeneity on the mechanical properties. To conclude, the possibility of adjusting the yield strength and the strain hardening behavior independently by tailoring the microstructure was discussed.

Zusammenfassung

Aufgrund ihrer herausragenden mechanischen Eigenschaften haben sich Hochmanganstähle (HMnS) und Mittelmanganstähle, unterstützt durch weltweite Forschungsaktivitäten, für die Anwendung als Leichtbaukomponenten in der Automobilindustrie empfohlen. Durch die Kontrolle der Stapelfehlerenergie (SFE) und der Mikrostruktur kann das Verfestigungsverhalten dieser Stähle gezielt eingestellt werden, sodass eine große Breite an Festigkeit-Duktilität Kombinationen realisierbar ist. Trotz der Vorteile und vielversprechenden Perspektiven konnten die HMnS und MMnS sich bislang gegen konventionelle hochfeste Stähle nicht etablieren, was primär durch ein mangelndes Verständnis der relevanten metallphysikalischen Einflussfaktoren auf die mechanischen Eigenschaften zu erklären ist.

Im Rahmen der vorliegenden Arbeit soll daher das Verständnis der skalenübergreifenden und kombinierten Auswirkungen mikro- und nanostruktureller Einflussfaktoren bezüglich der mechanischen Eigenschaften von HMnS und MMnS vertieft werden. Dazu wurde die experimentelle Prüfung der mechanischen Eigenschaften im Zugversuch mit den mikrostrukturellen Untersuchungsmethoden der Rasterelektronenmikroskopie, Messungen der Elektronenrückstreubeugung (EBSD), Röntgenbeugung (XRD), energiedispersiven Röntgenspektroskopien und Methoden der in-situ digitalen Bildkorrelation (DIC) kombiniert. Zusätzlich wurde der Einfluss der Formation von Nahordnungsphänomenen simulativ auf Basis vorliegender Berechnungen der Ordnungsenergien basierend auf der Dichtefunktionaltheorie untersucht.

Durch die Verwendung von dichtefunktionaltheoretischen Simulationsergebnissen in der Modellierung der Fließgrenze von HMnS wurde der Beitrag von Nahordnungsphänomenen abgebildet. Dabei wurde der Einfluss von C, Mn und Al auf die Festigkeitssteigerung durch Nahordnungsphänomene von dem Einfluss auf die Mischkristallhärtung unterschieden. Die Effektivität der Festigkeitssteigerung bezüglich der nahgeordneten Cluster durch die Legierungselemente C und Al war dabei im Rahmen der üblichen Legierungsgehalte von HMnS sehr hoch. Die Effektivität von Legierungszugaben von Mn war durch die ohnehin hohen Legierungsgehalte in HMnS limitiert.

Mithilfe der Untersuchung der verformungsinduzierten Zwillingsbildung (HMnS) in zwei HMnS konnte gezeigt werden, dass Nahordnungsphänomene die Verfestigungsrate während

der plastischen Verformung durch die Unterstützung der Zwillingsbildung erhöhen. Der Vergleich des Verfestigungsverhaltens in Abhängigkeit der Verformungstemperatur in einem vollständig rekristallisierten, teilweise rekristallisierten und erholungsgeglühten Zustand zeigte, dass die Orientierungsabhängigkeit der verformungsinduzierten Zwillingsbildung den sägezahnartigen Verlauf der Fließkurve bewirkte. Durch die skalenübergreifende Beschreibung konnte dementsprechend der Einfluss von Nahordnungsphänomenen auf der Nanoskala auf das Verfestigungsverhalten auf der Mikroskala nachgewiesen werden, aus welchem die mechanischen Eigenschaften auf der Makroskala resultieren. Anschließende XRD und Makrotexturuntersuchungen sowie EBSD Experimente bezüglich des Einflusses der Korngröße wiesen nach, dass in HMnS mit feinkörniger Mikrostruktur die Fließgrenze deutlich erhöht ist, jedoch der TWIP-Effekt und die verformungsinduzierte Phasenumwandlung von Austenit zu Martensit (TRIP) teilweise unterdrückt werden.

Die gewonnenen Erkenntnisse bezüglich des Einflusses der Mikrostruktur auf die Fließgrenze und das Verfestigungsverhalten in HMnS wurden auf den Anwendungsfall mehrphasiger MMnS übertragen. Mithilfe des Einsatzes von EBSD Experimenten und in-situ DIC Methoden während unterbrochener Zugversuche bei verschiedenen Dehnraten wurde nachgewiesen, dass die Dehnratenabhängigkeit der MMnS auf der Makroskala durch die Dehnratenabhängigkeit des TRIP-Effekts und der Aufteilung der plastischen Verformung auf die Mikrostrukturkomponenten verursacht wird.

Abschließend wurde der Einfluss der Mikrostruktur auf die Fließgrenze und das Verfestigungsverhalten in HMnS und MMnS verglichen und die Bedeutung mikrostruktureller Homogenität für die mechanischen Eigenschaften herausgestellt. In diesem Zusammenhang wurde die Möglichkeit diskutiert, die Fließgrenze und das Verfestigungsverhalten unabhängig voneinander durch die Anpassung der Mikrostruktur einzustellen.

Declaration on Publications

This thesis includes the following articles that have been published in international peer-reviewed journals:

Chapter II – **S. Sevsek**, W. Bleck: Ab Initio-Based Modelling of the Yield Strength in High-Manganese Steels. Metals 8 (1) (2018) 34. https://doi.org/10.3390/met8010034.

Chapter III – **S. Sevsek**, F. Brasche, C. Haase, W. Bleck: Combined deformation twinning and short-range ordering causes serrated flow in high-manganese steels. Materials Science & Engineering A 746 (2019) 434-442. https://doi.org/10.1016/j.msea.2019.01.042.

Chapter IV – **S. Sevsek**, F. Brasche, D. Molodov, W. Bleck: On the Influence of Grain Size on the TWIP/TRIP-Effect and Texture Development in High-Manganese Steels. Materials Science & Engineering A 754 (2019) 152-160. https://doi.org/10.1016/j.msea.2019.03.072.

Chapter V – **S. Sevsek**, C. Haase, W. Bleck: Strain-Rate-Dependent Deformation Behavior and Mechanical Properties of a Multi-Phase Medium-Manganese Steel. Metals 9 (3) (2019) 344. https://doi.org/10.3390/met9030344.

Additionally, the following extended abstracts have been published in the conference proceedings of 4th International Conference on Medium and High Manganese Steels (4th HMnS):

Appendix I – **S. Sevsek**, S. Wesselmecking, M. Haupt, W. Bleck: The Impact of Microstructural Characteristics and Testing Parameters on the Formability of High-Manganese Steels. Conference Proceedings of the 4th International Conference on Medium and High Manganese Steels, Aachen, Germany, April 1-3 (2019) 310-313.

Appendix II – T. Allam, **S. Sevsek**, X. Guo, A. Hamada, W. Bleck: On the mechanical and corrosion properties of a precipitation-strengthened medium manganese austenitic stainless steel. Conference Proceedings of the 4th International Conference on Medium and High Manganese Steels, Aachen, Germany, April 1-3 (2019) 365-368.

Appendix III – M. Haupt, M. Müller, C. Haase, **S. Sevsek**, A. Schwedt, G. Hirt: Impact of warm rolling on microstructure and mechanical properties of high manganese steels.

Conference Proceedings of the 4th International Conference on Medium and High Manganese Steels, Aachen, Germany, April 1-3 (2019) 97-100.

For the publications in international peer-reviewed journals in Chapter II – Chapter V, the experimental setup and conceptual design of the publication was conceived by the candidate, who also wrote the first draft of those publications, incorporated editorial suggestions as well as additional results and was the corresponding author. Additionally, the mechanical testing and electron backscatter diffraction experiments including metallographic preparation and subsequent data analysis performed in those works was conducted by the candidate.

Additionally, the modelling approach in Chapter II and subsequent regression analysis was performed by the candidate.

In Chapter III, the forescatter detector images in the scanning electron microscope and the calculation of the twin volume fraction based on image quality maps and electron backscatter diffraction maps with colorcoding according to the inverse pole figure was also conducted by the candidate.

In addition to the aforementioned procedures, the interpretation of the texture analysis in Chapter IV was performed by the candidate. To this end, the calculation of the position of first-order deformation twins in the orientation distribution function sections was carried out by the candidate.

In Chapter V, the tensile tests at different strain rates using in-situ digital image correlation and the subsequent data and image analysis was also conducted by the candidate, as was the energy-dispersive X-ray spectroscopy.

For the extended abstract in Appendix I, in addition to the electron backscatter diffraction experiments, the candidate conducted the Nakajima tests, analyzed the experimental results and wrote the first draft. Subsequent editorial comments and suggestions for adaptations were included by the candidate, who was also scheduled as the speaker for the 4th HMnS.

In Appendix II, the microstructural characterization based on electron backscatter diffraction measurements was performed by the candidate, who also gave editorial suggestions for the final version.

In Appendix III, the tensile tests were conducted by the candidate.

Table of Contents

Acknowledgements i

Abstract ii

Zusammenfassung iv

Declaration on Publications vi

Table of Contents viii

List of Abbreviations x

List of Symbols xiii

List of Figures xv

List of Tables xx

Chapter I – Introduction 1

1.1 Fundamentals 4

1.1.1 Accommodation of Plastic Deformation in Austenite 4

1.1.1.1 Impact of the Chemical Composition on the Stacking Fault Energy 5

1.1.1.2 TWinning-Induced Plasticity (TWIP) 6

1.1.1.3 TRansformation-Induced Plasticity (TRIP) 9

1.1.1.4 Slip Band Refinement-Induced Plasticity (SRIP) 10

1.1.2 Textures in High-Manganese Steels 10

1.1.3 Short-Range Ordering and κ'-phase 12

1.1.4 Strain Localization Phenomena in High- and Medium Manganese Steels 13

1.1.5 Heat Treatment of High- and Medium-Manganese Steels 14

1.2 Objectives and Scope of the Thesis 16

1.3 Results and Contribution to Original Knowledge 18

References 24

Chapter II – Ab Initio-Based Modelling of the Yield Strength in High-Manganese Steels 33

Chapter III – Combined deformation twinning and short-range ordering causes serrated flow in High-Manganese steels 49

Chapter IV – On the Influence of Grain Size on the TWIP/TRIP-Effect and Texture Development in High-Manganese Steels 59

Chapter V – Strain-Rate-Dependent Deformation Behavior and Mechanical Properties of a Multi-Phase Medium-Manganese Steel 69

Appendix I - The Impact of Microstructural Characteristics and Testing Parameters on the Formability of High-Manganese Steels 90

Appendix II - On the mechanical and corrosion properties of a precipitation-strengthened medium manganese austenitic stainless steel 95

Appendix III - Impact of warm rolling on microstructure and mechanical properties of high manganese steels 100

Curriculum Vitae 105

List of Abbreviations

1NN	First-Nearest Neighbors
2NN	Second-Nearest Neighbors
3NN	Third-Nearest Neighbors
AHSS	Advanced High Strength Steel
APT	Atom-Probe Tomography
B	{110}<112>Brass texture component
B-B	Bogers-Burgers orientation relationship
bcc	body centered cubic
C	Carbon / {001}<100>Cube texture component
CG	Coarse-Grained (microstructure)
CP	Crystal Plasticity
CR	Cold Rolling
CSL	Coincidence Site Lattice
Cu	{112}<111>Copper texture component
CuT	{552}<115>CopperTwin texture component
DFT	Density Functional Theory
DIC	Digital Image Correlation
EBSD	Electron BackScatter Diffraction
EDS	Energy-Dispersive X-ray Spectroscopy
fcc	face centered cubic
FG	Fine-Grained (microstructure)
FLC	Forming Limit Curve
FLD	Forming Limit Diagram
FSD	Fore Scatter Detector (image)
G	{110}<100>Goss texture component
GB	Grain Boundary
GOS	Grain Orientation Spread
hcp	hexagonal close packed
HMnS	High-Manganese Steel
HR	High-Resolution

HSLA	High-Strength Low-Alloy (steel)
IA	Intercritical Annealing
IF	Interstitial-Free (steel)
IPF	Inverse Pole Figure
IQ	Image Quality (EBSD maps)
KAM	Kernel Average Misorientation
K-S	Kurdjumov-Sachs
LF	Linear-best-Fit method
LRO	Long-range Ordered / Long-Range Ordering
MBIP	MicroBand-Induced Plasticity
MFP	Mean Free Path of dislocation movement
MMnS	Medium-Manganese Steel
ND	Normal Direction
NN	Nearest Neighbor
NNN	Next-Nearest Neighbor
ODF	Orientation Distribution Function
OR	Orientation Relationship
PLC	Portevin-Le Châtelier
pRX	partially-Recrystallized (microstructure)
PS	Pre-Straining / Pre-Strained
RD	Rolling Direction
REC	RECovery-annealed (microstructure)
RT	Room Temperature
RtCu	{112}<110>Rotated Copper texture component
RtG	{110}<110>Rotated Goss texture component
RX	(fully) Recrystallized (microstructure)
S	{123}<634>S texture component
SANS	Small Angle Neutron Scattering
SE	Secondary Electron (image)
SEM	Scanning Electron Microscope
SFE	Stacking Fault Energy
SM	Section Method
S-N	Shoji-Nishiyama orientation relationship
SR	Short-Range

SRIP	Slip Band Refinement-Induced Plasticity
SRO	Short-Range Ordered / Short-Range Ordering
TA	Tensile Axis
TD	Transversal Direction
TE	Total Elongation
TEM	Transmission Electron Microscopy/Microscope
TRIP	TRansformation-Induced Plasticity
TVF	Twin Volume Fraction
TWIP	TWinning-Induced Plasticity
UFG	UltraFine-Grained
UTS	Ultimate Tensile Strength
VASP	Vienna Ab initio Simulation Package
VPSC	Visco-Plastic Self-Consistent
WHR	Work-Hardening Rate
WR	Warm-Rolled / Warm Rolling
XRD	X-ray diffraction
YS	Yield Strength

List of Symbols

γ	austenite
b	Burgers vector
a_γ	lattice parameter of austenite
ε	ε-martensite
γ_{SF}	stacking fault energy
$\sigma^{\gamma/\varepsilon}$	interfacial energy between γ and ε
ρ_{sur}	molar surface energy along {111} slip plane
$\Delta G_{chem}^{\gamma\rightarrow\varepsilon}$	contribution of chemical interaction to the stacking fault energy
$\Delta G_{mag}^{\gamma\rightarrow\varepsilon}$	contribution of magnetic transformation to the stacking fault energy
T_N^γ	Néel temperature
E	Young's modulus
G	shear modulus
m	Schmid factor
α'	α'-martensite
w_{SF}	stacking fault separation width
α	ferrite
σ_Y	yield strength
σ_0	base strength of the austenite matrix
σ_{SS}	contribution of solid solution strengthening
σ_{SRO}	strengthening contribution of short-range ordered zones
n_H	instantaneous strain hardening exponent from Holloman's equation
σ_{GS}	strengthening contribution to the yield strength by grain refinement
E_{Order}	energy difference between configurations of randomly distributed C atoms and an ordered distribution of C atoms
E_{random}	ordering energy of the system assuming randomly distributed C atoms
E_{SRO}	ordering energy of the system assuming an ordered distribution of C atoms
χ_i	molar fraction of element i in the chemical composition of an alloy

k_y	Hall-Petch parameter
M	Taylor factor
n_{kl}	unit cell configuration with k Mn atoms and l Al atoms
θ_i	molar fraction of element i, regarding only substitutional alloying elements in austenite
ΔE_{Ckl}	ordering energy difference of a unit cell with k Mn atoms, l Al atoms and an C atom in the central interstitial octahedral position compared to a unit cell without Mn or Al atoms
ΔE_{Sol}	energy difference required to bring C into solution in a unit cell with k Mn atoms and l Al atoms compared to a unit cell without Mn or Al atoms
ΔE_{Lat}	change in ordering energy resulting from lattice distortion due to the presence of k Mn and l Al atoms
n_{Ckl}	unit cell configuration with k Mn atoms, l Al atoms and an C atom in the central interstitial octahedral position
$\sigma_{Y,calc}$	calculated yield strength
$\sigma_{Y,exp}$	experimentally determined yield strength
d_m	average grain size
$\sigma_{SS,exp}$	solid-solution strengthening based on experimental results
$\frac{r_{OL}}{r_{Fe}}$	radius of octahedral position compared to the radius of a Fe atom
$\sigma_{Y,model}$	calculated yield strength using models from literature
d_{avg}	average grain size
D_C^{γ}	diffusion rate of C in austenite
ε_f	total elongation to fracture
T	Texture index
f	volume fraction of texture component
$\dot{\varepsilon}$	strain rate
ε_{eng}	engineering strain
σ_γ	intragranular stress in austenite
$\Delta\sigma$	relative strength of α and α’ compared to γ

List of Figures

Chapter I - Introduction

Figure 1	Current and projected world-wide CO2-regulations and use of AHSS for passenger vehicles in North America; based on [5,6].	1
Figure 2	Strength-Ductility Diagram of steel grades commonly used for automotive applications; based on [6].	2
Figure 3	Price development of Mn, Al, Ni, FeCr, FeV and MoO, which are commonly used in HMnS and austenitic stainless steels; derived from [16].	3
Figure 4	(a) slip systems in fcc and (b) stacking sequence of {111} planes with dislocation dissociation reaction.	5
Figure 5	(a) perfect dislocations on subsequent slip planes dissociate into Shockley partials, which changes the stacking sequence of crystal lattice planes and subsequently results in a three-layer twin nucleus [30]; (b) crystallographic twin-matrix relationship.	7
Figure 6	(a) definition of m; (b) orientation dependence of m for slip and twinning in fcc, based on [37].	8
Figure 7	(a) perfect dislocations on every other slip plane dissociate into Shockley partials, which changes the stacking sequence of crystal lattice planes and subsequently results in a five-layer hcp nucleus (based on [30]); (b) OR between γ, ε and α'.	9
Figure 8	(a) selection of texture components relevant to the deformation behavior of HMnS and their position in (b) the $\varphi_2 = 45°$ ODF section and (c) the $\varphi_2 = 65°$ ODF section.	11
Figure 9	Position of C in central octahedral interstitial site of an fcc elementary cell for (a) energetically preferential SRO configuration with 6 Mn as NN atoms and (b)+(c) two possible κ'-phase configurations with 8 Al as NNN atoms and (b) 6 Mn NN atoms or (c) 6 Fe NN atoms respectively.	12
Figure 10	(a) stress-strain curves for a selection of HMnS and the MMnS in this work. (b) Individual strengthening contributions to the YS.	22
Figure 11	(a) flow curves and (b) smoothed instantaneous strain hardening exponent n_H for the steels in Figure 10.	22
Figure 12	Strength-Ductility Diagram with a selection of the HMnS and the MMnS analyzed in this work. The highlighted areas refer to the steel grades in Figure 2.	23

Chapter II - Ab Initio-Based Modelling of the Yield Strength in High-Manganese Steels

Figure 1	FCC-unit cell with 14 lattice positions for matrix atoms and one central interstitial atom.	36
Figure 2	Energetically most favorable cell configurations.	38
Figure 3	Comparison of calculated and experimental values for σ_Y.	40
Figure 4	Contributions of σ_{SS} and σ_{SRO} to yield strength.	41

Figure 5 Proportional contribution of σ_{SS}, σ_{SRO} and σ_{GS} to σ_Y. 42
Figure 6 Impact of C on (a) σ_{SRO}, σ_{SS}; and (b) E_{random} and E_{SRO}. 42
Figure 7 Impact of Mn on (a) σ_{SRO}, σ_{SS}; and (b) E_{random} and E_{SRO}. 43
Figure 8 Comparison of models of σ_Y for the steels used in this paper. 45

Chapter III - Combined deformation twinning and short-range ordering causes serrated flow in High-Manganese steels

Fig. 1 Engineering stress-strain curves at RT and 150 °C of: (a) X60Mn18_RX and X60Mn18_pRX, (b) X30MnAl17-1_RX and X30MnAl17-1_REC. 52
Fig. 2 EBSD maps of the X60Mn18_pRX steel after 0% ((a)-(c)) and 5% ((d)-(f)) tensile strain at RT: (a, d) Image Quality (IQ) map, (b,e) phase distribution map (austenite (blue), α'-martensite (green)) and (c, f) Grain Orientation Spread (GOS) map. ND, TA and TD denote normal direction, tensile axis and transversal direction, respectively. 52
Fig. 3 ForeScatter Detector (FSD) image (a) and EBSD map (b) with colorcoding according to the Inverse Pole Figure (IPF) in rolling direction (RD) of the X30MnAl17-1_REC alloy before tensile testing. Σ3-boundaries in the EBSD maps with IPF colorcoding are highlighted in white. 53
Fig. 4 EBSD IQ maps (a, b,d,e) with IPF colorcoding overlay parallel to the TA (c, f) of X60Mn18_RX alloy (a-c) and X30MnAl17-1_RX alloy (d-f) before the onset of serrated flow (after (a) 2% elongation and 0% (d) elongation respectively) and after 5% elongation at RT (b-c, e-f) respectively (after the onset of serrated flow of the X60Mn18_RX alloy). The white circles in (a) and (b) highlight grains that undergo significant deformation twinning during elongation from 2% to 5%. The circles in dark green highlight areas where the poor local detection rate, probably due to a deterioration of the surface quality as a result of the tensile test, did not allow for a more accurate determination of deformation twins. 53
Fig. 5 EBSD maps (a, b) with colorcoding according to the IPF parallel to the TA and EBSD-IQ maps (c, d) for the X30MnAl17-1_RX alloy after 30% elongation at RT (a, c) and at 150 °C (b, d). The approximated TVF is given in (c,d). 54
Fig. 6 EBSD maps after 40% elongation at RT with colorcoding according to the IPF parallel to the TA for the (a-c) X30MnAl17-1_RX alloy and (d-f) X60Mn18_RX alloy. Σ3-boundaries in the maps with IPF coloration are highlighted in white. (a)+(b) and (d)+(e) show the microstructure of a larger area to offer an overview, while (c) and (f) are in-detail maps of small areas. 54
Fig. 7 True stress-true strain curves and work-hardening rate (WHR)-true strain curves of the X30MnAl17-1 and X60Mn18 steels at (a) RT and (b) 150 °C. The corresponding engineering stress-strain curves are given in Fig. 1. 54
Fig. 8 Schematic of the generation and propagation of deformation bands resulting in serrated flow in high-manganese TWIP steels. 56

Chapter IV - On the Influence of Grain Size on the TWIP/TRIP-Effect and Texture Development in High-Manganese Steels

Fig. 1	Average grain size d_{avg} and grain size distribution as determined using the line-intercept method for the (a) fine-grained and (b) coarse-grained alloys.	62
Fig. 2	(a) Engineering stress-strain curves, (b) flow curves, (c) evolution of the strain hardening exponent n_H over true strain and (d) WHR curves of the four tested alloy conditions.	62
Fig. 3	IPFs parallel to TA and texture indices T for the austenitic phase of the four tested material states before deformation (0%, top row), after 20% elongation (middle row) and after fracture (bottom row).	63
Fig. 4	Texture evolution in austenite of the four tested material states before deformation (0%, top row), after 20% elongation (middle row) and after fracture (bottom row), ODF sections at $\varphi_2 = 45°$.	63
Fig. 5	Definition of texture components relevant for the HMnS in this work.	63
Fig. 6	Volume fractions f of the main texture components in (a) X60Mn17_FG, (b) X60Mn17_CG (c) X30MnAl17-1_FG and (d) X30MnAl17-1_CG before deformation (0%), after 20% elongation and after fracture.	64
Fig. 7	(a)-(f) Image Quality (IQ) EBSD maps with overlayed IPF colorcoding relative to TA for the (a) X30MnAl17-1_FG, (b) X30MnAl17-1_CG, (c) X60Mn17_FG and (d) X60Mn17_CG alloys after 20% uniaxial deformation and for the (e) X60Mn17_CG alloy after elongation to fracture with corresponding (f) EBSD phase map. The yellow ellipse in (e)+(f) highlights a crack close to the fracture surface. Σ3-grain boundaries in (a)-(e) are highlighted in white.	64
Fig. 8	Volume fraction evolution during deformation of texture components in the (a) X30MnAl17-1 and (c) X60Mn17 alloy as well as calculated positions of first-order deformation twins in the ODF section at $\varphi_2 = 45°$ for the (b) X30MnAl17-1_CG alloy after fracture and (d) the X60Mn17_CG alloy after 20% elongation.	65

Chapter V – Strain-Rate-Dependent Deformation Behavior and Mechanical Properties of a Multi-Phase Medium-Manganese Steel

Figure 1	The processing route for the X6MnAl12-3 MMnS.	72
Figure 2	(**a**,**c**) Optical micrographs of the X6MnAl12-3 MMnS (**a**) after 50% cold rolling and (**c**) after intercritical annealing. Easily identifiable prior γ grain boundaries in (**a**) and grain boundaries of recrystallized grains in (**c**) are highlighted in blue. (**b**) Secondary electron (SE) image of the microstructure after intercritical annealing, and (**d**) the corresponding Energy Dispersive X-ray Spectroscopy (EDS) analysis of the local Al and Mn contents are shown.	74
Figure 3	(**a**) Engineering stress-strain and (**b**) true stress-true strain curves of the X6MnAl12-3 alloy tested at different strain rates. (**c**) Overview of the strain-rate-dependent mechanical properties.	75

Figure 4	Electron backscatter diffraction (EBSD) phase maps of the investigated MMnS (**a**) before deformation and after straining to ε_{eng} of (**b**) 2%, (**c**) 10% and (**d**) 20% at 0.001 1/s. Green areas indicate a body-centered cubic crystal structure, α and/or α', whereas blue areas indicate face-centered cubic austenite, γ.	76
Figure 5	γ phase fractions (blue) as determined by EBSD measurements after tensile testing to fracture at (**a**) 0.00001 1/s, (**b**) 0.001 1/s, (**c**) 1.0 1/s, and (**d**) 230 1/s. Green areas indicate a body-centered cubic crystal structure, α and/or α'.	77
Figure 6	Flow curve and work-hardening rate (WHR) of the X6MnAl12-3 alloy tested at 0.00001 1/s, 0.001 1/s, 1.0 1/s and 230 1/s, respectively.	78
Figure 7	EBSD maps of the X6MnAl12-3 alloy prior to deformation (**a**,**b**) with inverse pole figure (IPF) color coding relative to the rolling direction (RD) for (**a**) α and α' and (**b**) γ. Grain orientation spread (GOS) maps for (**c**) α and α', (**d**) γ and (**e**) the kernel average misorientation (KAM) map are shown. White areas in (**a**-**d**) correspond to (**a**,**c**) γ and (**b**,**d**) α or α', respectively.	79
Figure 8	EBSD maps of the X6MnAl12-3 alloy at the end of the discontinuous elastic-plastic transition with (**a**,**b**) IPF color coding relative to the tensile axis (TA) for (**a**) α and α' and (**b**) γ. Corresponding KAM maps for (**c**) α and α' and (**d**) γ. White areas in (a-d) correspond to (**a**,**c**) γ and (**b,d**) α or α', respectively.	80
Figure 9	EBSD IPF maps for 0.001 1/s after (**a**) 20% ε_{eng} and (**c**) ε_f, as well as for the microstructure after straining until fracture at (**e**) 0.00001 1/s, (**g**) 1.0 1/s and (**i**) 230 1/s. Corresponding EBSD maps with color coding according to KAM values of α and α' in (**b**,**f**,**h**) and (**j**) are shown. White areas in the KAM maps correspond to γ.	81
Figure 10	Visualization of local strain rate distribution in a tensile test sample during the discontinuous elastic-plastic transition using in-situ DIC during tensile testing at (**a**) 0.001 1/s and (**b**) 0.00001 1/s. White arrows highlight the propagation of localized peaks in strain rate during straining.	82
Figure 11	Visualization of local strain rate distribution in a tensile test sample prior to necking initiation using in-situ DIC during tensile testing at (**a**) 0.001 1/s and (**b**) 0.00001 1/s. White arrows highlight the propagation of localized peaks in strain rate during straining.	83
Figure 12	Summary of the evolution of γ phase fraction (**a**) during straining at 0.001 1/s and (**b**) comparison of strain-rate-dependent γ phase fractions after fracture.	84
Figure 13	Impact of the strain-rate-dependent strength of α and α' relative to γ ($\Delta\sigma$) on the microstructural evolution during straining at different strain rates.	85

Appendix I - The Impact of Microstructural Characteristics and Testing Parameters on the Formability of High-Manganese Steels

Figure 1 (a) FLC for RX and PS material as determined by both LF and SM method respectively, (b) stress-strain diagram for the RX material and (c) corresponding flow curve with work-hardening rate (WHR). (d)-(f) show the strain paths and FLC for (d) the RX material, (e) the PS material and (f) the PS material starting from 20% pre-straining. 92

Figure 2 (a) EBSD map with colorcoding according to the inverse pole figure and Σ3 grain boundaries highlighted in white after 20% elongation at 0.1 1/s (ND – normal direction, TA – tensile axis, TD – transversal direction); (b)-(e) determination of onset of critical necking for the biaxial strain state (b)+(c) using the SM method and (d)+(e) LF method for (b)+(d) the PS and (c)+(e) RX material, respectively. 93

Appendix II - On the mechanical and corrosion properties of a precipitation-strengthened medium manganese austenitic stainless steel

Figure 1 Microstructure of the developed MMn-stainless steel. a) SEM image of the as-annealed state containing precipitates, b) grain size distribution and average grain size determined by line-intercept method taking annealing twins into account, c) color-coding for the EBSD map before deformation (shown in d), and phase maps (e) before deformation, (f) after 20% elongation and (g) after fracture, showing austenite (blue), ferrite or α'-martensite (green) and ε-martensite (red). TA: Tensile Axis. RD, ND and TD are Rolling, Normal and Transversal Directions, respectively. 98

Figure 2 Tensile properties in comparison to conventional AISI 304 austenitic stainless and HMn-TWIP steels. a) Engineering stress-strain curves, and b) work hardening rate (WHR) curves. 98

Figure 3 Recorded Polarization curves in 5%NaCl for the developed MMn-stainless steel compared to conventional austenitic stainless and HMn-TWIP steels. 99

Appendix III - Impact of warm rolling on microstructure and mechanical properties of high manganese steels

Figure 1 EBSD-IQ maps of 50 % warm rolled material at a) 200 °C, b) 400 °C and c) 500 °C. Blue lines indicate deformation twin boundaries (60° <111>). 103

Figure 2 Engineering stress-strain curves of 50 % warm rolled material at 200 °C, 400 °C and 500 °C in comparison to a recrystallized (Rx) material state (50% cold rolled and annealed for 30 min at 700 °C). 103

List of Tables

Chapter II - Ab Initio-Based Modelling of the Yield Strength in High-Manganese Steels

Table 1	Cell configurations of lowest ordering energy ΔE_{Ckl}.	37
Table 2	Chemical composition of HMnS used in this study in wt. %; grain size d_m in µm; experimentally determined and calculated yield strength $\sigma_{Y,exp}$ and $\sigma_{Y,calc}$ in MPa, experimental data of alloys marked with * are taken from [14].	39
Table 3	Solid solution hardening models in the literature.	45

Chapter III - Combined deformation twinning and short-range ordering causes serrated flow in High-Manganese steels

Table 1	Chemical composition, SFE, average grain size and heat treatment of the alloys tested in this work.	52
Table 2	Occurrence and onset of serrated flow as shown in Fig. 7.	55

Chapter IV - On the Influence of Grain Size on the TWIP/TRIP-Effect and Texture Development in High-Manganese Steels

Table 1	Summary of the tested material states with respective heat treatment, chemical composition and SFE.	61
Table 2	Summary of mechanical properties of the tested material states as determined by quasistatic tensile tests. The listed values for each alloy state are the averages of all conducted tensile tests.	62
Table 3	Phase fractions conducted from X-ray diffraction measurements for the four tested material states.	64

Chapter V - Strain Rate-Dependent Deformation Behavior and Mechanical Properties of a Multi-Phase Medium-Manganese Steel

Table 1	A_{c1}, A_{c3}, and nominal chemical composition of the X6MnAl12-3 MMnS.	72
Table 2	Impact of an increase in strain rate for low, medium and high strain rates (cf. Figure 3).	75

Appendix II - On the mechanical and corrosion properties of a precipitation-strengthened medium manganese austenitic stainless steel

Table 1	Chemical composition in wt.% for the steel grade under investigations.	97

Appendix III - Impact of warm rolling on microstructure and mechanical properties of high manganese steels

Table 1	Chemical composition of the processed Fe-23Mn-0.3C-1Al high manganese steel	102
Table 2	Mechanical properties of the investigated steel depending on the material condition	104

Chapter I
Introduction

In light of demanding requirements regarding vehicle emissions and fuel efficiency (cf. Figure 1), significant research efforts have been made to develop affordable lightweight concepts for formable steels in the automotive industry. In conventionally used steel grades like ferritic interstitial-free (IF) and high-strength low-alloy (HSLA) steels, an increase in strength is achieved at the cost of ductility and vice versa. Accordingly, the strength and ductility of those steel grades cannot be adjusted independently. On the other hand, the mechanical properties of fully austenitic stainless steels or multi-phase steels containing significant phase fractions of austenite are largely dependent on the work-hardening rate (WHR). High-manganese steels (HMnS) containing more than 12 wt.% Mn belong to the second and third generation of such Advanced High Strength Steels (AHSS). Due to their remarkable combination of high ultimate tensile strength (UTS) and high total elongation (TE) that in some cases exceed 50,000 MPa%, HMnS are both suited for crash-relevant car parts and for lightweight concepts widely employed in the automotive industry. [1–6]

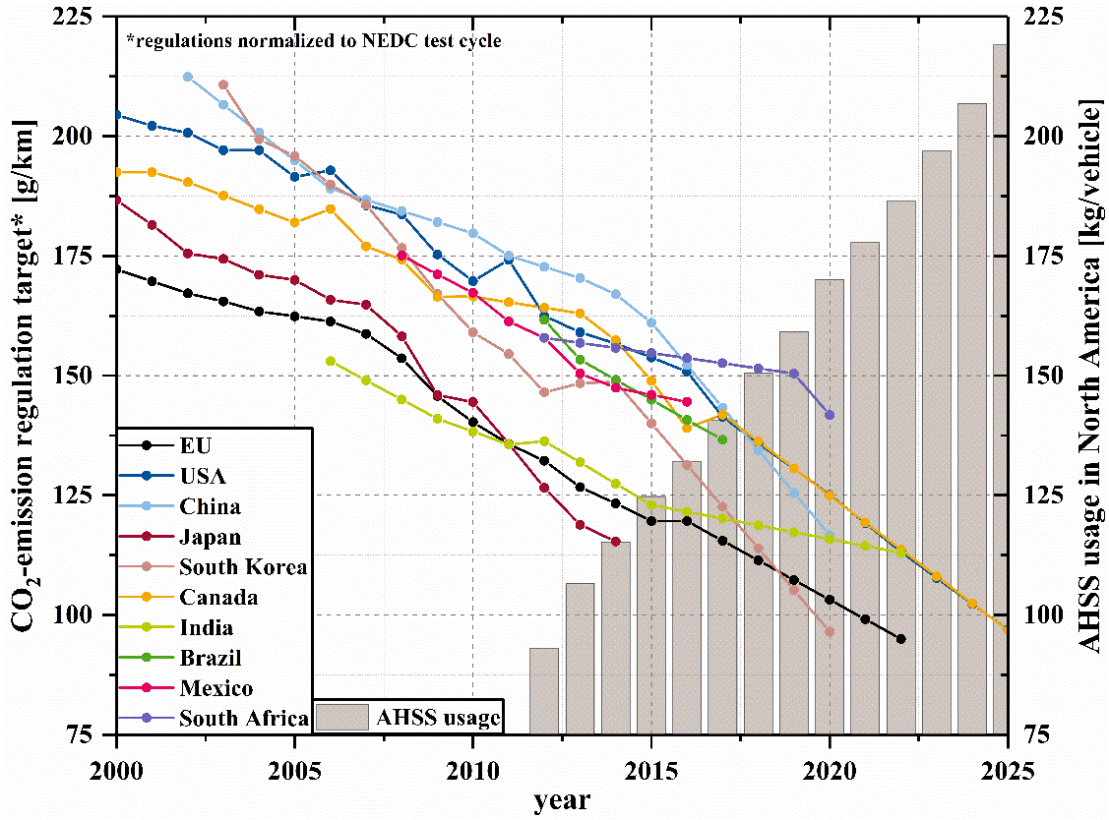


Figure 1: Current and projected world-wide CO_2-regulations and use of AHSS for passenger vehicles in North America; based on [5,6].

Within the group of austenitic steels, HMnS are a special case as the strain hardening behavior can be adjusted by controlling the activation of secondary deformation mechanisms in addition to dislocation glide. The high WHR of HMnS is a result of the material's ability to develop high dislocation densities in combination with the activation of such additional deformation mechanisms. As a result, a broad range of strength-ductility combinations can be achieved (cf. Figure 2). [4,7–9]

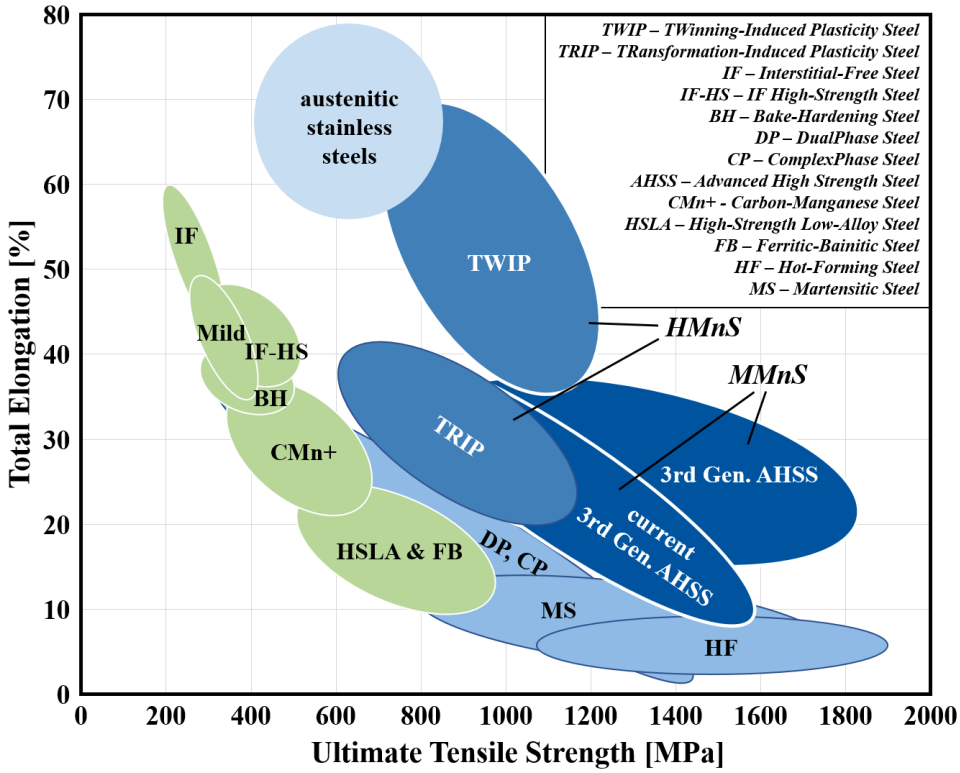


Figure 2: Strength-Ductility Diagram of steel grades commonly used for automotive applications; based on [6].

For HMnS, the deformation mechanism is mostly adjusted by controlling the stacking fault energy (SFE), an intrinsic material parameter that is influenced by alloying additions of the main alloying elements C, Mn, Al and Si, as well as the temperature. The secondary deformation mechanisms in HMnS include deformation-induced phase transformation (TRIP – TRansformation-Induced Plasticity), deformation twinning (TWIP – TWinning-Induced Plasticity) and extensive planar dislocation glide, which induces a high density of glide bands (SRIP – Slip Band Refinement-Induced Plasticity). The TWIP effect is activated at SFE values in the range of 12-55 mJ/m² while the TRIP effect prevails below 18 mJ/m². At high SFE values above 55 mJ/m², deformation twinning is suppressed in favor of the SRIP effect. [1,9–13]

As Al reduces the alloy's density significantly, Al is also beneficial for raising the material's specific strength, thus increasing the application potential for lightweight concepts. Since Mn and C are effective austenite stabilizers, a fully austenitic microstructure can be achieved cost-

effectively without the use of expensive alloying elements such as Ni, Mo and V (cf. Figure 3), which are often used in austenitic stainless steels. [1,2,14,15]

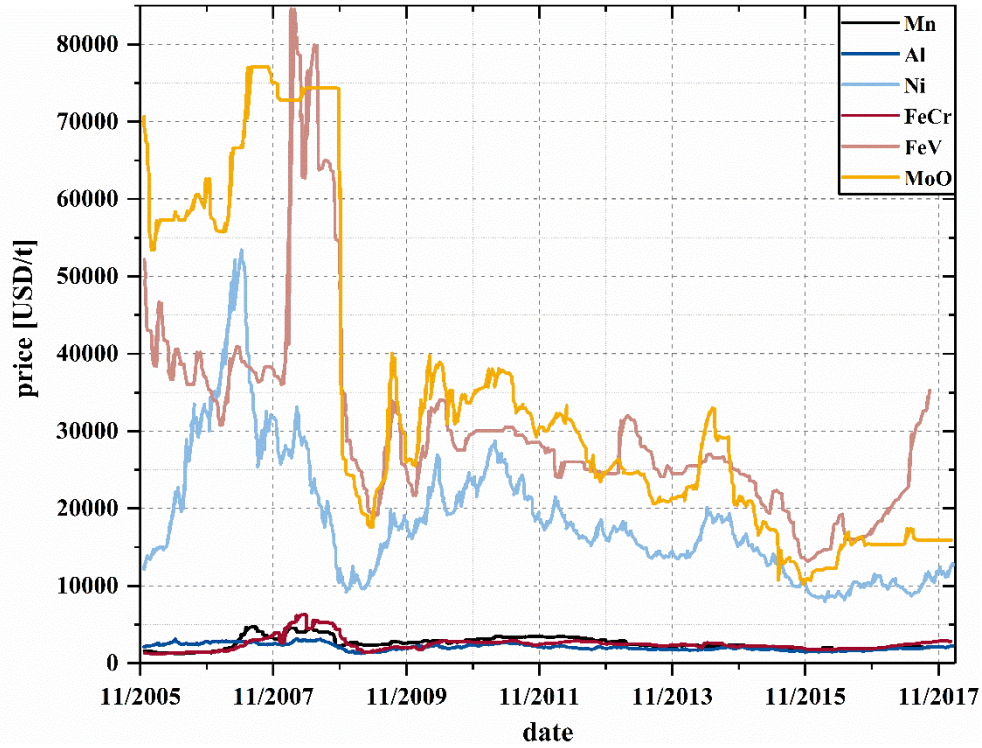


Figure 3: Price development of Mn, Al, Ni, FeCr, FeV and MoO, which are commonly used in HMnS and austenitic stainless steels; derived from [16].

Although the combination of high UTS and high TE results in a high total energy absorption potential of HMnS, design criteria of crash-relevant parts in the automotive industry limit the total available deformation volume significantly below the total elongation of HMnS. Accordingly, only a fraction of the total energy absorption potential can be realized. In the past, thermomechanical approaches (including cold rolling with subsequent recovery- [7,8,17] or reversion-annealing [9] as well as the production of ultrafine-grained recrystallized microstructures [18]) and novel alloy design concepts (including the use of microalloying elements [19,20] and κ'-phase precipitation [21,22]) have been employed in order to increase the yield strength (YS) of fully austenitic HMnS. However, the thermomechanical treatments do not result in recrystallized microstructures, which are common for HMnS due to good reproducibility and predictability of mechanical properties. [1,3,7,9,17]

In fact, some research effort has instead shifted to steels with reduced Mn-content of 3-12 wt.%. Those medium-manganese steels (MMnS) often consist of multi-phase microstructures with phase fractions of ferrite, austenite and martensite. While the YS of MMnS can be increased by increasing the phase fractions of ferrite and martensite, the control of the microstructure and phase fractions requires sophisticated control of complex heat treatments and as such, is a focus of ongoing research. [1,23–28]

1.1 Fundamentals

The following sections summarize the current state of research on HMnS and MMnS, as far as it is relevant to the inquiries conducted within the scope of this thesis. Accordingly, the focus is on the deformation mechanisms accommodating plastic deformation in austenite γ. Additionally, scientific literature on the impact of grain size and short-range ordering on the YS and activation of secondary deformation mechanisms is reviewed, as is the contribution of common alloying elements in HMnS on solid solution strengthening.

1.1.1 Accommodation of Plastic Deformation in Austenite

The majority of plastic deformation in HMnS is accommodated by dislocation slip on the four non-parallel closest-packed {111} slip planes in at least one of three possible <1$\bar{1}$0> slip directions each, resulting in a set of 12 possible slip systems in the face centered cubic (fcc) crystal of γ. The energy of a dislocation depends on the value of its squared Burgers vector, $b = \frac{a_\gamma}{2}[1\bar{1}0]$, with a_γ being the lattice parameter of γ. A dislocation dissociation into two Shockley partial dislocations can occur, if the summed value of the squared Burgers vectors of the partial dislocation pair is lower than for the perfect dislocation:

$$\frac{a_\gamma}{2}[1\bar{1}0] = \frac{a_\gamma}{6}[2\bar{1}\bar{1}] + \frac{a_\gamma}{6}[1\bar{2}1]$$

The partial dislocation pair glides on {111} slip planes in <112> direction, as the combination of displacement vectors of the Shockley partials results in dislocation movement in $[1\bar{1}0]$ direction. However, the $[2\bar{1}\bar{1}]$ and $[1\bar{2}1]$ displacement vectors of the partial dislocations are not lattice vectors. Accordingly, slip of the leading partial dislocation introduces an intrinsic stacking fault, which is removed by slip of the trailing partial dislocation (cf. Figure 4). An additional energy barrier composed of the surface energy of the stacking fault area needs to be overcome for the dissociation of a perfect dislocation to occur. The separation width of the partial dislocations is a function of the force balance between the attractive force of this stacking fault energy (SFE) and the repulsive forces between the partial dislocations. Low SFE values result in a relatively large separation width. HMnS usually have relatively low SFE values below 50 mJ/m² and accordingly, the spacing between the partials is comparably large. While perfect screw dislocations can slip in multiple {111} planes because the dislocation line is parallel to the Burgers vector, partial dislocations exist in only a single {111} slip plane. Accordingly, partial dislocations must recombine before cross-slip events can occur, for which

a large partial separation width is a hindrance. For HMnS, this results in pronounced planar dislocation glide and high dislocation densities, which induces the formation of dislocation cells. Dislocation cells are intragranular areas with boundaries of highly-dense dislocation walls, which separate zones with different combinations of active slip systems. With increasing plastic deformation and the subsequent increase in dislocation density, those dislocation cells are refined. [1,29–32]

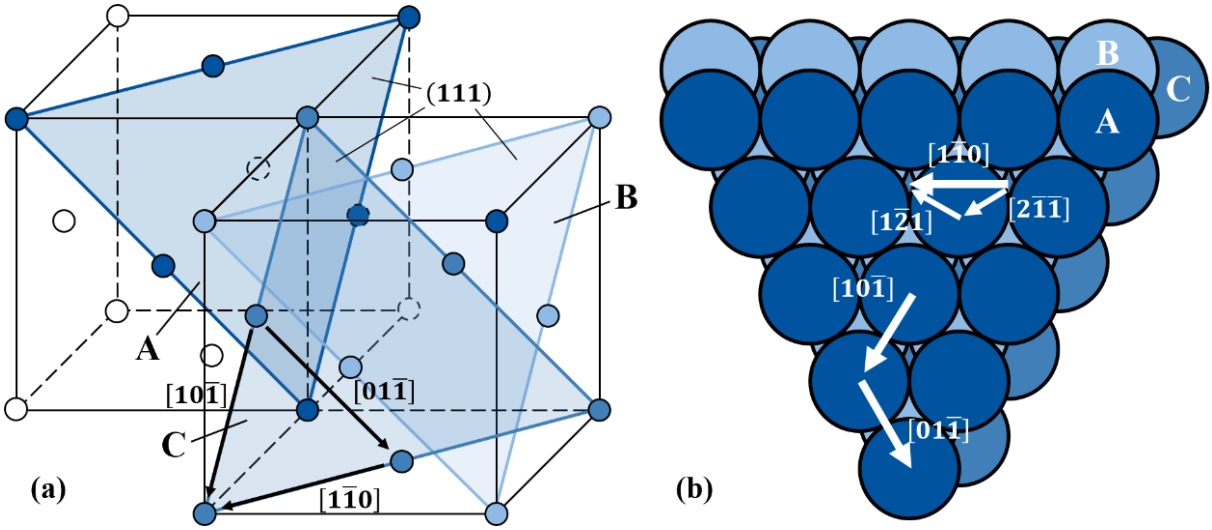


Figure 4: (a) slip systems in fcc and (b) stacking sequence of {111} planes with dislocation dissociation reaction.

A stacking fault can also be introduced into a crystal structure by inserting (extrinsic stacking fault) or removing (intrinsic stacking fault) parts of a close-packed {111} layer. Although this type of intrinsic stacking fault is geometrically identical to the stacking fault introduced by the dissociation of a perfect dislocation into two Shockley partials, the boundary line of this intrinsic stacking fault is made up of Frank partial dislocations with the Burgers vector $\frac{a_\gamma}{3}[111]$. As Frank partials are edge dislocations with a directional vector normal to the slip plane, they are unable to glide and are called “sessile”, whereas Shockley partials are “glissile”. [1,29]

1.1.1.1 Impact of the Chemical Composition on the Stacking Fault Energy

The SFE is primarily a function of the material’s chemical composition and the temperature. As such, it is frequently calculated using subregular solution thermodynamic models, in which the SFE γ_{SF} is modelled as the difference in Gibbs free energy between the hexagonal close-packed (hcp) crystal lattice of a one-layer nucleus of ε-martensite (ε), which is considered to be a representation of an intrinsic stacking fault, and γ:

$$\gamma_{SF} = 2\rho_{sur}\left(\Delta G_{chem}^{\gamma\rightarrow\varepsilon} + \Delta G_{mag}^{\gamma\rightarrow\varepsilon}\right) + 2\sigma^{\gamma/\varepsilon}$$

The chemical composition affects the interfacial energy between γ and ε $\sigma^{\gamma/\varepsilon}$, the molar surface energy ρ_{sur} along the {111} slip plane, the contribution of chemical interaction $\Delta G_{chem}^{\gamma\rightarrow\varepsilon}$ and the contribution of the transformation of magnetic state $\Delta G_{mag}^{\gamma\rightarrow\varepsilon}$. Accordingly, the influence of individual alloying elements on the SFE depends on the overall chemical composition. The general tendencies of the impact of the commonly used alloying elements in HMnS C, Mn, Al and Si can be deduced from numerous theoretical and experimental approaches in literature. C increases $\Delta G_{chem}^{\gamma\rightarrow\varepsilon}$ and accordingly, γ_{SF} in general. Additionally, it also reduces the Néel temperature T_N^{γ}, which determines the magnetic transition from antiferromagnetic to paramagnetic state [33]. As the Young's modulus E is higher in the paramagnetic state - and thus, at increased temperature ("Young's modulus anomaly" [1]) - the decrease of T_N^{γ} induced by C leads to a relative increase of E, the Shear modulus G and subsequently of the SFE. The impact of Mn on the SFE is primarily determined by the strong and complex interaction of C and Mn. While the same is true for Al, the interaction is such that overall, the addition of Al increases the SFE by approximately 8 mJ/m² per wt.% Al. On the other hand, there is no clear consensus on the impact of Si on the SFE. In general, one major problem for accurate thermodynamic predictions is the lack of interaction parameters for the hcp phase in the Fe-Si-C system, which results in a lack of available interaction parameters for the calculation of γ_{SF}. Experimentally determined stacking fault separation widths and more recent thermodynamic models indicate a slight decline of the SFE with increasing Si alloying content. [10–12,34,35]

1.1.1.2 TWinning-Induced Plasticity (TWIP)

The TWIP effect occurs in HMnS with relatively low SFE values between 12 mJ/m² and 55 mJ/m². Deformation twinning in fcc is a crystallographic shear displacement in <112> direction with shear value $\frac{\sqrt{2}}{2}$, that corresponds to a 180° rotation of parts of the crystal lattice around the normal of a {111} mirror plane. Accordingly, there are 12 possible {111}<112> twin systems in γ. The shear displacement is accommodated by coordinated slip of partial dislocations with identical <112>-type Burgers vectors on successive twinning planes. The formation of a twin nucleus requires a three-layer stacking fault, which can be emitted from dislocation reactions or suitable interfaces, e.g. grain boundaries. A possible dislocation reaction, which has been observed by transmission electron microscopy (TEM), is the dissociation of two coplanar dislocations into three Shockley partials on adjacent slip planes [36]:

$$\frac{a_\gamma}{2}[\bar{1}01] + \frac{a_\gamma}{2}[\bar{1}10] = 3 * \frac{a_\gamma}{6}[\bar{2}11]$$

For those dislocation reactions and for the subsequent twin formation and growth to occur, a critical stress is necessary, which depends on the partial dislocation separation width. Twin formation and twin growth proceeds with partial dislocation glide on three successive slip planes, which induces the three-layer stacking fault that serves as a twin nucleus, as shown in Figure 5.

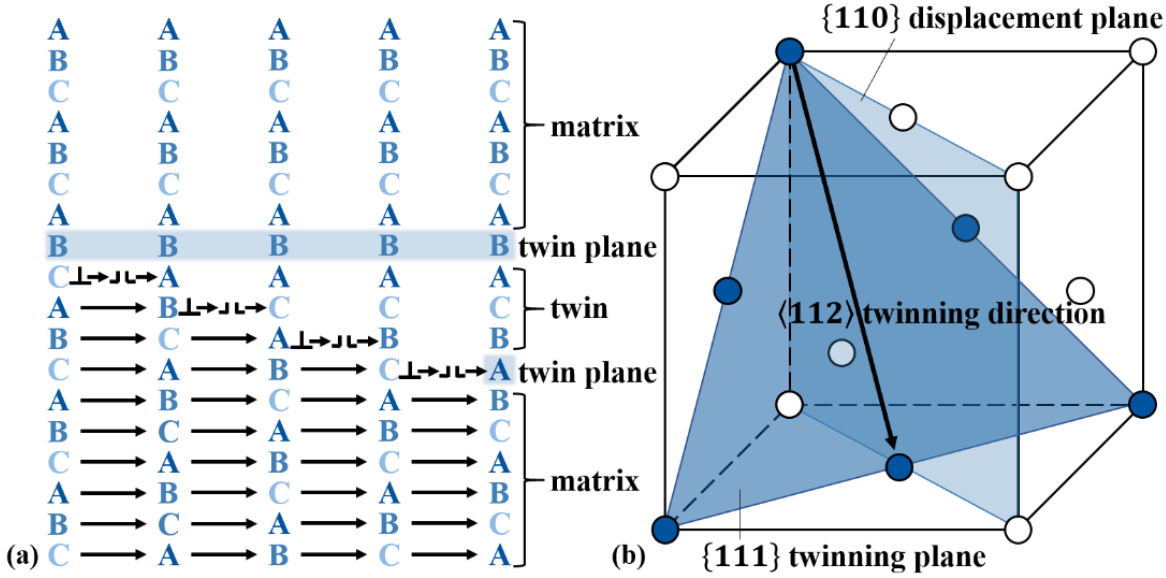


Figure 5: (a) perfect dislocations on subsequent slip planes dissociate into Shockley partials, which changes the stacking sequence of crystal lattice planes and subsequently results in a three-layer twin nucleus [30]; (b) crystallographic twin-matrix relationship.

Twin boundaries function as obstacles to dislocation glide. Accordingly, the generation of additional twin boundaries during deformation results in a dynamic Hall-Petch effect that increases the strain hardening by reducing the mean free path of dislocation movement [1]. As a result, at the critical twinning stress, which marks the onset of deformation twinning during deformation, the strain hardening curve exhibits a pronounced increase.

The strong orientation-dependence of deformation twinning can be explained in terms of the importance of the Schmid factor m on dislocation movement. The Schmid factor describes the importance of the critical resolved shear stress acting on a single grain as a function of the angle between external force F, slip plane and slip direction (cf. Figure 6(a)). The Schmid factors of the leading and trailing partial dislocations involved in twin formation are usually different, as the slip directions are not identical. If the Schmid factor of the leading partial is lower, the partial separation width will be reduced because movement of the trailing partial dislocation is easier. This effect can also be described by the concept of an effective SFE, which in this scenario would be higher than the thermodynamically calculated SFE. In the case of a higher Schmid factor of the leading partial, the difference between the Schmid factors of leading and

trailing partial dislocation can be used to qualitatively describe the decrease of the effective SFE due to an increased partial separation width. Additionally, the Schmidt factors of the slip systems of the grains also influence the dislocation density. In order to ensure strain compatibility with neighboring grains, grains with lower Schmid factors usually have a higher dislocation density, which reduces the effective SFE due to dislocation interactions. The resulting increased intragranular stress promotes deformation twinning, as well. Overall, these aspects lead to a pronounced deformation twinning of grains with orientations close to a <111> orientation parallel to the tensile axis (<111>||TA, TA – tensile axis) and a suppression of twinning in grains with orientations close to <100>||TA. Deformation twins in the <111>||TA-fiber usually have orientations close to the <100>||TA-fiber. In addition, the Schmid factors of the slip systems in <100>||TA-oriented grains are significantly higher than the Schmid factors of the twin systems. The opposite is true for <111>||TA-oriented grains (cf. Figure 6(b)). [37–39]

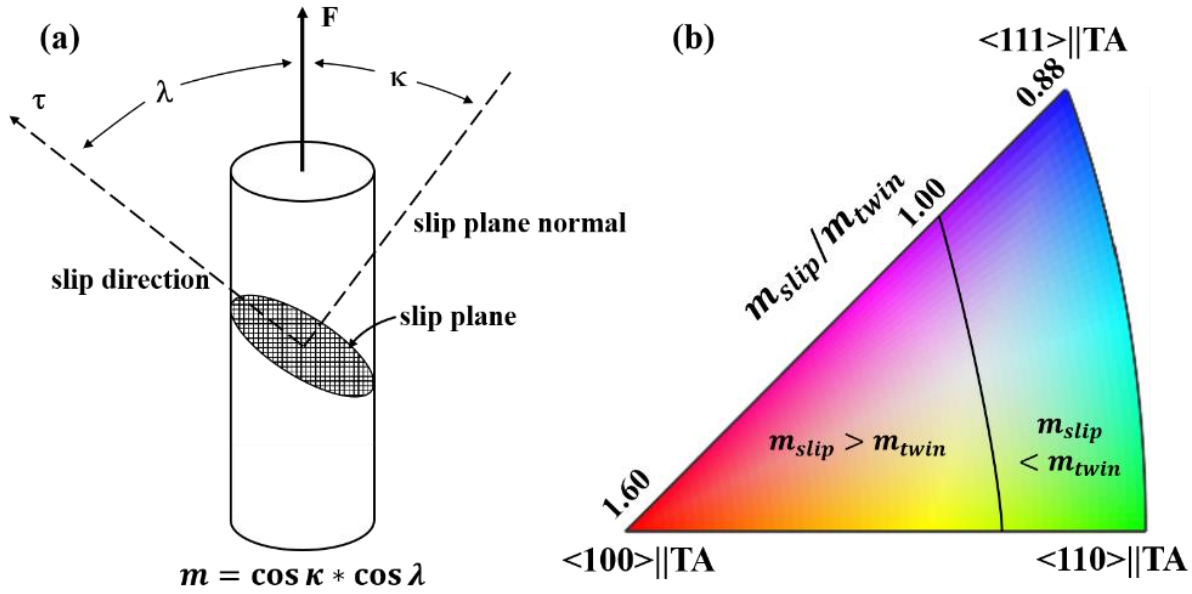


Figure 6: (a) definition of m; (b) orientation dependence of m for slip and twinning in fcc, based on [37].

While the importance of the SFE on the critical stress necessary for twinning is generally accepted, the impact of grain size on deformation twinning is a point of ongoing discussion. There are conflicting findings as to whether the grain size suppresses deformation twinning. However, most authors agree that if the twin volume fraction (TVF) is reduced in smaller grains, deformation twinning is not completely suppressed. [1,37,40,41]

In any case, TEM experiments and texture measurements have shown that the overall maximum TVF in HMnS is lower than 0.3. Simulation approaches using visco-plastic self-consistent (VPSC) and crystal plasticity (CP) models show similar results. [8,42–44]

1.1.1.3 TRansformation-Induced Plasticity (TRIP)

A deformation-induced phase transformation from γ to martensite can occur in HMnS and MMnS, which results in either the hcp-type ε-martensite in HMnS or α'-martensite (α') with a distorted body centered cubic (bcc) crystal structure in MMnS. The $\gamma \rightarrow \alpha'$ transformation follows the Kurdjumov-Sachs (K-S) $\left(\{111\}_\gamma \parallel \{110\}_{\alpha'}, \langle 110\rangle_\gamma \parallel \langle 111\rangle_{\alpha'}\right)$ orientation relationship (OR), while the transformation to ε $\gamma \rightarrow \varepsilon(\rightarrow \alpha')$ follows the Shoji-Nishiyama (S-N) $\left(\{111\}_\gamma \parallel \{0001\}_\varepsilon, \langle 110\rangle_\gamma \parallel \langle 1120\rangle_\varepsilon\right)$ OR. If $\varepsilon \rightarrow \alpha'$ occurs, ε and α' share the Bogers-Burgers (B-B) $(\{0001\}_\varepsilon \parallel \{110\}_{\alpha'}, \langle 1120\rangle_\varepsilon \parallel \langle 111\rangle_{\alpha'})$ OR. Similar to the impact of twin boundaries in TWIP steels, the phase boundaries introduced by martensite act as obstacles to dislocation movement. While ε can accommodate some plastic deformation via dislocation slip or deformation twinning, plastic deformation in α'-containing alloys is primarily localized in γ or at $\gamma - \alpha'$ phase boundaries. Accordingly, the presence of α' reduces the material's ductility significantly. [43,45–49]

Similar to the twinning model, the $\gamma \rightarrow \varepsilon$ transformation can be described by the Mahajan-Chin mechanism, which involves the passing of Shockley partial dislocations on every second plane. As the generation of such a five-layer stacking fault (cf. Figure 7(a)) requires a higher stacking fault separation width than the generation of a three-layer twin nucleus, the SFE values of high-manganese TRIP steels are usually below 18 mJ/m². [2,50]

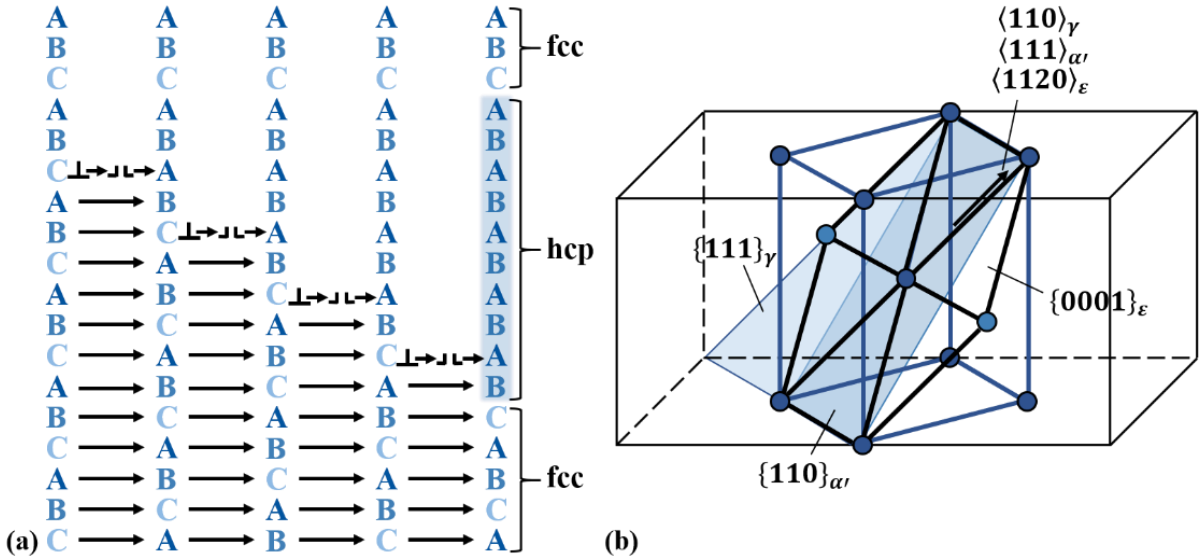


Figure 7: (a) perfect dislocations on every other slip plane dissociate into Shockley partials, which changes the stacking sequence of crystal lattice planes and subsequently results in a five-layer hcp nucleus (based on [30]); (b) OR between γ, ε and α'.

The nucleation of α' involves numerous dislocation reactions and accordingly, occurs at areas of high dislocation density such as intersections of slip bands or ε laths. [45,48]

1.1.1.4 Slip Band Refinement-Induced Plasticity (SRIP)

The Al content of high-manganese TWIP and TRIP steels is usually below 3 wt.% [1]. As Al reduces the alloy's density significantly, the development of HMnS for automotive applications has led to a class of alloys with increased Al contents of up to 12 wt.%. The increased Al content leads to SFE values upwards of 55 mJ/m² and the subsequent suppression of both TRIP and TWIP effect. However, these lightweight-HMnS still display high work-hardening rates (WHR) compared to TRIP and TWIP steels and despite their high SFE values, these alloys still exhibit pronounced planar glide during plastic deformation. [13,51–53]

The pronounced planar dislocation slip leads to the formation of slip bands that usually extend through the entire grain but are stopped at grain boundaries. With increasing strain, the density of slip bands increases, the distance between slip bands decreases and intersections of slip bands occur [13,51–53]. Initially, the high WHR of lightweight-HMnS was explained in terms of an effect like the dynamic Hall-Petch effect in TWIP and TRIP steels, where the intersection of slip bands create an obstacle to dislocation movement and thus, create Taylor lattice-like subdivisions inside the grain. As the slip bands do not extend beyond grain boundaries, the slip bands were called "microbands" and the strain hardening mechanism was named Microband-Induced Plasticity (MBIP) [52,53]. However, considering more recent findings, this terminology and the underlying description of the deformation mechanism is somewhat inaccurate. TEM experiments have shown that dislocation movement is not obstructed at intersected slip bands and accordingly, a subdivision of the grain and a subsequent dynamic Hall-Petch effect do not take place. Instead, long-range stress fields of dislocations in slip bands and on coplanar slip planes in combination with high dislocation densities due to a suppression of cross-slip contribute to the alloy's strength. As the slip band distance decreases during deformation, this effect was termed as Slip Band Refinement-Induced Plasticity (SRIP) [13,51].

1.1.2 Textures in High-Manganese Steels

The deformation of metals with fcc crystal structure and high SFE values are characterized by dislocation slip on the {111} planes in <110> direction and easy activation of cross-slip, because of the low stacking fault separation width that is associated with high SFE values. The pronounced dislocation slip and grain rotations during cold rolling lead to the development of the {112}<111>Copper (Cu), {123}<634>S and the {110}<112>Brass (B) texture components. Due to the high volume fraction of Cu, this type of texture is referred to as Cu-type texture [1]. The definition of common texture components in HMnS and their positions in

the $\varphi_2 = 45°$ and $\varphi_2 = 65°$ sections of the orientation distribution function (ODF) are shown in Figure 8.

(a)

Component	Symbol	Miller indices	Euler angles [°] (φ_1,Φ, φ_2)	Fiber
Copper (Cu)	▽	{112}<111>	(90,35,45)	/
S	⊗	{123}<634>	(59,37,63)	/
Brass (B)	▲	{110}<112>	(55,90,45)	<111>‖TA
Goss (G)	□	{110}<100>	(90,90,45)	/
Rotated Copper (RtCu)	◀	{112}<110>	(0,35,45)	<111>‖TA
Rotated Goss (RtG)	⬡	{110}<110>	(0,90,45)	<100>‖TA
Cube (C)	●	{001}<100>	(45,0,45)	<100>‖TA

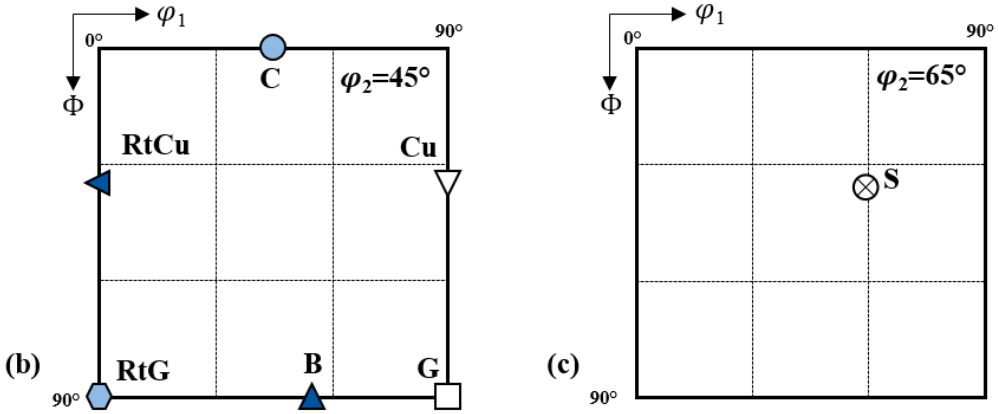


Figure 8: (a) selection of texture components relevant to the deformation behavior of HMnS and their position in (b) the $\varphi_2 = 45°$ ODF section and (c) the $\varphi_2 = 65°$ ODF section.

In fcc metals with lower SFE values, TWIP and/or TRIP is activated and cross-slip is more difficult. This results in the development of a Brass-type texture, which features the B and {110}<100>Goss (G) texture components, whereas the evolution of Cu and S is suppressed. As the SFE values of SRIP steels are high compared to high-manganese TWIP steels, their cold rolling texture initially resembles a Cu-type texture before transitioning to a Brass-type texture. However, Cu and S are still prominent. [1,13,42,54]

The recrystallization texture of HMnS consists of the main texture components that were formed during prior deformation, albeit significantly decreased in intensity. At the same time, the texture index decreases, which is also reflected by the increase in volume fraction of randomly oriented grains. The overall weakening of the texture retained from cold rolling is due to a very homogeneous recrystallization behavior without strong preference for specific orientations. Instead, preferred nucleation sites are in regions of high dislocation density such as shear bands. [54–56]

During uniaxial tension of fcc metals, dislocation glide on {111}<110> slip systems initiates grain rotations that result in the development of grain orientations on or close to the <111>‖TA-fiber, to which both B and {112}<110>Rotated Copper (RtCu) belong. Additionally, a weaker

<100>||TA-fiber develops, as deformation twinning occurs preferably in grains belonging to the <111>||TA-fiber and the orientations of the resulting deformation twins are close to the <100>||TA-fiber. The <100>||TA-fiber primarily consists of the {110}<110>Rotated Goss (RtG) and {001}<100>Cube (C) texture components. Due to the OR of the $\gamma \rightarrow \varepsilon(\rightarrow \alpha')$ transformations, this type of texture evolution is also found in high-manganese TRIP steels. [1,13,39,42,46,57]

1.1.3 Short-Range Ordering and κ′-phase

The high concentration of alloying elements in HMnS result in the frequent occupation of interstitial and matrix lattice sites of γ. Due to interactions between carbon and the surrounding atoms, there are atom arrangements that are energetically preferential for carbon. Ab-initio calculations using density functional theory (DFT) show that this is the case for Mn atoms as nearest neighbors (NN) and Al atoms as next-nearest neighbor (NNN). Accordingly, the distribution of C in the austenitic matrix is guided by the presence of alloying elements, rather than being completely random. This leads to the formation of short-range ordered zones with the size of one or a few elementary cells. Some of the most stable configurations for C result from the presence of Al as corner atoms of an elementary cell, as shown in Figure 9, which is also a frequently reported structure of κ'-carbides of type $(Al, Mn)_3 AlC_x$ in HMnS with Al content of more than 3 wt.%. [51,58–61]

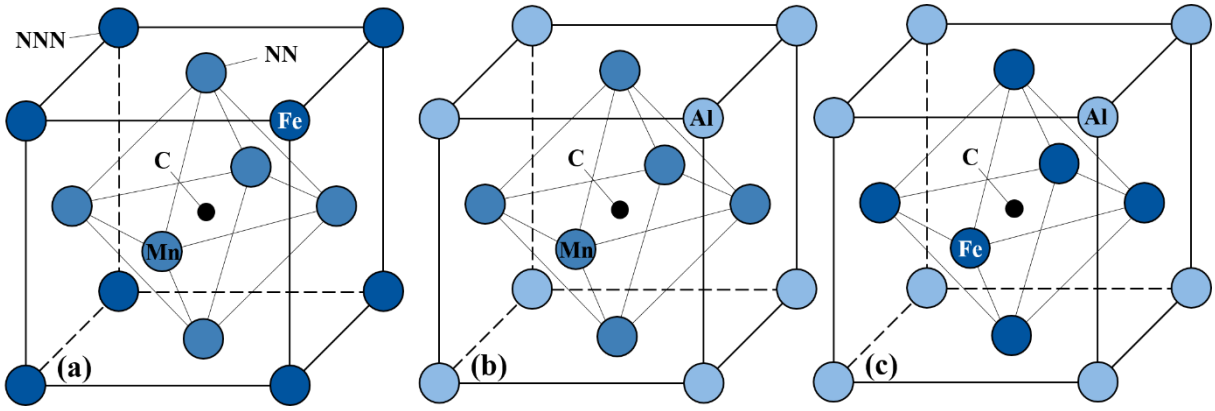


Figure 9: Position of C in central octahedral interstitial site of an fcc elementary cell for (a) energetically preferential SRO configuration with 6 Mn as NN atoms and (b)+(c) two possible κ'-phase configurations with 8 Al as NNN atoms and (b) 6 Mn NN atoms or (c) 6 Fe NN atoms respectively.

Due to the nanoscale nature and coherency of those zones with the matrix, the existence of SRO is very difficult to prove experimentally. However, small angle neutron scattering (SANS) experiments [62] and Mössbauer spectroscopy [1] indicate the presence of SRO zones. Additionally, TEM experiments have revealed intermediate stages between κ'-carbides and SRO zones [51], so called long-range ordered (LRO) zones between 2 nm and 5 nm.

Various effects in HMnS have been linked to the impact of SRO zones. The pronounced planar dislocation slip has been theorized to be a result of a glide plane softening that occurs when SRO zones are cut [1,51,52]. Additionally, Bake-Hardening heat treatments have yielded in significant strength increases when used in HMnS [63]. Attempts to model the yield strength of HMnS which included a strength increase due to SRO zones have resulted in reasonable regression parameters [64]. The impact of SRO on the activation of secondary deformation mechanisms is still an ongoing point of discussion, in which some researchers have elaborated on the possibility of short-range (SR) jumps of C atoms into Mn-rich regions, which could lead to a pinning of dislocation movement and a subsequent increase of the stacking fault separation width w_{SF} [38,65].

1.1.4 Strain Localization Phenomena in High- and Medium-Manganese Steels

The occurrence of serrated flow phenomena has frequently been observed in fully austenitic HMnS by using in-situ digital image correlation (DIC) techniques during tensile testing. Serrated flow in the past has been connected to the initiation and propagation of macroscopic Portevin-Le Châtelier (PLC)-like deformation bands, in which most of the plastic deformation during tensile tests is localized. While the addition of Al reportedly suppresses serrated flow at room temperature (RT), serrated flow has also been observed at elevated temperature in Al-alloyed HMnS. [12,65–67]

There is no clear consensus on the origin of serrated flow in HMnS. Some authors focus on the impact of SR jumps of C atoms into preferential positions after the destruction of SRO clusters by dislocation slip of leading partial dislocations. The subsequent local strength increase supposedly induces a pinning effect of the trailing partial dislocation and dislocation movement requires an increase in stress, which leads to stress spikes in the flow curve [64,68]. Others correlate the activation of secondary deformation mechanisms to the rapid increase of the WHR, which accompanies the spikes in the flow curve [38,65,69,70]. However, most authors point out that the mechanism of the classic PLC effect in ferritic steels, which relies on long-range diffusion of C to strain fields of dislocations, is most likely not responsible for the serrated flow in HMnS, as the diffusion speed of C in γ at RT is very low compared to ferrite (α) [1,29,64,68].

While there have been a few studies on the serrated flow in MMnS, it is not nearly as common as in HMnS. Similar to the occurrence in HMnS, the authors attribute the occurrence to the activation of additional deformation mechanisms next to dislocation glide [71,72]. However, a form of strain localization commonly observed in cold-rolled and intercritically-annealed

MMnS is a discontinuous elastic-plastic transition, which is accompanied by the initiation and propagation of Lüders bands [73]. The discontinuous elastic-plastic transition phase is due to the ultrafine-grained (UFG) multi-phase microstructure after intercritical annealing, which results in different levels of flow stresses for each phase. Accordingly, plastic deformation in MMnS is accompanied by strain localization phenomena on a microstructural scale. [74–76]

1.1.5 Heat Treatment of High- and Medium-Manganese Steels

As most industrial applications for HMnS and MMnS require sheet material, rolling and particularly cold rolling is a conventional step in the processing route. Afterwards, tailored heat treatments are employed to achieve good combinations of strength and ductility. However, those heat treatments can be vastly different for HMnS and MMnS, as HMnS are usually fully austenitic while MMnS possess complex multi-phase microstructures, which require carefully designed process routes. [1,2,73]

For HMnS, relatively low annealing temperatures of 650 – 700 °C and annealing times as low as 5 min already lead to fully recrystallized microstructures after cold rolling. This is due to a very high initial growth rate of nuclei at triple junctions, shear bands and grain boundaries in the heavily-deformed cold-rolled microstructure with very high dislocation density. Because of this heterogeneous nucleation behaviour and a rapidly decreasing growth rate of nuclei, an inhomogeneous grain size distribution is commonly found in HMnS [1,54–56,77]. Fully recrystallized HMnS in general have rather low YS, which is problematic for the application in crash-relevant automotive parts with relatively low deformation volume [3]. Consequently, recovery annealing and reversion annealing heat treatments have been developed to retain the high strength of the cold-rolled material state while reducing the dislocation density to increase the residual formability in comparison to the cold-rolled material state. Both heat treatments follow this concept but are applied for HMnS with different active secondary deformation mechanisms. Recovery annealing in TWIP steels is conducted at moderate temperatures of 550 – 630 °C, where mechanically-induced twins from cold rolling are thermally stable while recrystallization is mostly suppressed due to the low annealing temperature [7–9,17]. In reversion annealing for TWIP/TRIP steels on the other hand, lower annealing temperatures of approximately 350 °C (below the austenitization temperature) are used to retain ε-martensite in addition in the cold-rolled microstructure while decreasing the dislocation density [9,46,49].

The reduced alloying contents of the γ stabilizers C and Mn and increased contents of Al in MMnS cause very low γ phase fractions or even fully α'-martensitic microstructures after

recrystallization heat treatments, resulting in very low ductility. Instead, intercritical annealing at approximately 550 – 800 °C in the α-γ two-phase region after cold rolling is used to effectively partition C and Mn to γ. As a result, γ remains stable during cooling, resulting in an UFG microstructure. At the same time, the stability and resulting phase fraction of γ heavily depends on the temperature and annealing time during intercritical annealing, allowing for an effective adjustment of the SFE of γ and accordingly, for a tailored activation of secondary deformation mechanisms. On the one hand, increasing the annealing temperature increases the γ phase fraction during annealing. However, the γ stability is reduced at the same time, as the total amount of C and Mn atoms is partitioned over a higher phase fraction of γ. If the annealing temperature is too high, the γ stability is not sufficiently high during cooling and a $\gamma \rightarrow \alpha'$ transformation occurs. On the other hand, temperatures at the lower end of the α-γ two-phase region result in a low γ phase fraction after cooling, which results in low ductility. Additionally, as the diffusion speed of C and Mn is heavily dependent on the annealing temperature, longer annealing durations are necessary for an effective elemental partitioning. [24,26–28,71,73,76,78,79]

1.2 Objectives and Scope of the Thesis

While there have been a significant number of contributions studying the strain hardening behavior of fully recrystallized high-manganese steels (HMnS) and intercritically-annealed medium-Mn steels (MMnS), a comprehensive study on the isolated impact of different micro- and nanostructural features on the deformation behavior and mechanical properties of HMnS and MMnS has not been brought forward. To this end, this thesis has the objective of analyzing the influence of short-range ordering (SRO) on a nanoscale and of the microstructure on a microscale on both the strain-hardening behavior and the yield strength (YS). Special scope of this work is the interplay between these characteristics and their combined influence on the deformation behavior. In this regard, the underlying assumption of this work, that the work-hardening rate (WHR) and the YS can be adjusted independently, is analyzed.

For this purpose, in Chapter II “Ab Initio-Based Modelling of the Yield Strength in High-Manganese Steels”, a linear model for the calculation of the YS of HMnS was developed, including the strengthening contribution of SRO, solid solution strengthening and the impact of grain size. A stoichiometry-based function for a given chemical composition of a HMnS was used to determine a distribution of substitutional alloying elements in the material. Subsequently, results from calculations based on the density functional theory (DFT) were employed in evaluating the most likely positions of C atoms and the respective ordering energy of the most stable distribution of C atoms. The contribution of local hardening phenomena induced by SRO to the YS of HMnS was calculated by comparing the ordering energy levels of a random C distribution and the most likely C distribution. Finally, a linear regression model of the individual contributions of C, Mn and Al was employed to calculate the solid-solution strengthening in HMnS, taking SRO into account.

In Chapter III “Combined deformation twinning and short-range ordering causes serrated flow in high-manganese steels”, the description of the impact of SRO is continued by introducing the concept of SRO-assisted deformation twinning and its impact on the deformation behavior of two high-manganese TWIP/TRIP steels. In this context, the suppression of serrated flow in Al-alloyed HMnS at room temperature (RT) and in HMnS with non-recrystallized initial microstructure at testing temperatures below 150 °C was analyzed. Targeted heat treatments were conducted to adjust the initial microstructure of both tested alloys, in order to generate a material state with fully recrystallized microstructure and a material state with recovery-annealed or partially-recrystallized microstructure. Quasistatic tensile tests were conducted at RT and at 150 °C to analyze the impact of testing temperature on the occurrence of serrated

flow. Additionally, the evolution of twin volume fraction (TVF) during the tensile tests at different testing temperatures was detected using Electron Backscatter Diffraction (EBSD) experiments during interrupted tensile tests. Special scope of Chapter III was the analysis of the impact of SRO and the activation of secondary deformation mechanisms on the occurrence of serrated flow.

While Chapter II and Chapter III focused on the impact of SRO on the YS and deformation behavior of HMnS, the focus of Chapter IV "On the Influence of Grain Size on the TWIP/TRIP-Effect and Texture Development in High-Manganese Steels" is on the impact of grain size on the YS and deformation behavior of two high-manganese TWIP/TRIP steels. Scope of this work is the dependence of the evolution of martensite phase fraction and TVF on the initial grain size in recrystallized HMnS. To this end, two different recrystallization temperatures and durations were employed to achieve initial recrystallized material states with a fine-grained microstructure and a coarse-grained microstructure for each alloy. Quasistatic tensile tests at RT were conducted to determine the dependence of the YS and of the WHR on the initial grain size. Macrotexture analysis and EBSD experiments during interrupted tensile tests and after fracture were employed to correlate the evolution of WHR with the grain-size dependent activation of secondary deformation mechanisms. The texture analysis was supported by X-ray diffraction (XRD) measurements to detect the evolution of the γ, ε and α' phase fractions.

The focus of Chapter V "Strain-Rate-Dependent Deformation Behavior and Mechanical Properties of a Multi-Phase Medium-Manganese Steel" is the impact of the initial microstructure on the deformation behavior of a MMnS. Special scope is the strain-rate dependence of strain partitioning in the microstructural constituents, strain localization phenomena at different strain rates, the occurrence of serrated flow at very low strain rates and the activation of the TRIP effect in the tested X6MnAl12-3 alloy. To this end, an intercritical annealing was conducted with subsequent in-situ digital image correlation (DIC) tensile tests over a wide range of strain rates from 0.00001 1/s to 230 1/s to analyze the strain-rate-dependent mechanical properties of the alloy. EBSD experiments were performed to characterize the initial microstructure as well as the evolution of strain partitioning and activation of the TRIP effect during interrupted tensile tests and after fracture for different strain rates. Furthermore, the elemental partitioning of Mn and Al on γ, α and α' respectively was investigated using Energy-Dispersive X-ray Spectroscopy (EDS). Overall, the findings were analyzed in context of the concept of microstructural homogeneity, which had previously been introduced for HMnS in Chapter III.

1.3 Results and Contribution to Original Knowledge

This study investigated the impact of micro- and nanostructural characteristics on the deformation behavior and mechanical properties of high-manganese steels (HMnS) and medium-manganese steels (MMnS). The focus of the work was the analysis of the interplay of the impacts of individual characteristics on the yield strength (YS) and work-hardening rate (WHR), as well as the interplay between different material characteristics on a micro- and nanoscale.

To this end, the impact of short-range ordering (SRO) on both YS and WHR was analyzed. Starting on the nanoscale, the distribution of C atoms was calculated using density-functional theory-based (DFT) simulations that yielded the value of the ordering energy of C as a function of the surrounding Fe, Mn and Al atoms. By using a stoichiometric distribution of those alloying elements in combination with a distribution function of C, which was determined based on the ordering energy, the strengthening contribution of SRO in a HMnS including the contribution of Al was quantified on the macroscale. Three findings stood out: Firstly, the contribution of SRO was most significant for the HMnS with high C and Al contents. Secondly, the contribution of SRO resulted in significant increases of the YS of up to 65 MPa, nearly 20% of the total YS of the tested alloys. Thirdly, the YS and the individual solid-solution strengthening contributions of C, Mn and Al to the YS were predicted with satisfactory accuracy and yielded reasonable regression parameters, when taking the impact of SRO on the YS into account. Accordingly, the concept of using DFT simulation data for the calculation of macroscopic material properties proved to be an expedient approach and showed promise for further applications.

Furthermore, the scale-bridging approach of connecting the impact of SRO to mechanical properties of HMnS was reinforced by analyzing the deformation behavior of two high-manganese TWIP/TRIP (TWIP – TWinning-Induced Plasticity/TRIP- TRansformation-Induced Plasticity) steels with very similar stacking fault energy (SFE) values during tensile testing at room temperature (RT) and at 150 °C. The experimental determination of the twin volume fraction (TVF) revealed that the amount of deformation twins in the Al-alloyed HMnS was significantly lower. In this context, the scale-bridging concept of SRO-assisted deformation twinning was introduced: During deformation, SRO clusters are sheared due to the movement of a leading partial dislocation. The misplacement of C atoms out of SRO clusters induces an energetically unfavorable position. Short-range (SR) jumps of those C atoms into more preferential close-by Mn- and Al-rich surroundings restore a more stable configuration, leading

to a pinning effect of those restored SRO clusters on the trailing partial dislocation. Consequently, this increases the stacking fault separation width w_{SF} and subsequently induces a more pronounced activation of the TWIP effect. Due to the negative impact of Al on the diffusion speed of C in γ and the increasing effect of Al on the lattice parameter, the frequency of such SR jumps is lower in Al-alloyed HMnS, resulting in lower TVF compared to Al-free HMnS. Electron Backscatter Diffraction (EBSD) measurements after deformation at 150 °C confirmed that the TVF was higher than at RT, which is due to the increased diffusion speed at higher testing temperature. Therefore, this study connected the theoretical approach of SRO-assisted deformation twinning with the experimental validation of higher TVF at increased testing temperatures in Al-alloyed HMnS.

Following up on the concept of SRO-assisted deformation twinning, a scale-bridging mechanism was introduced which offers an explanation for the occurrence of serrated flow in high-manganese TWIP steels. As such, the initiation and propagation of macroscopic deformation bands in HMnS was related to the activation of secondary deformation mechanisms on a microstructural scale as well as the concept of microstructural homogeneity. Based on the experimental findings, two necessary requirements for the occurrence of serrated flow were identified. Firstly, a local stress peak induced by the orientation-dependent activation of the TWIP mechanism was found to be necessary to initiate the generation of a deformation band. Secondly, it was shown that the propagation of deformation bands is facilitated by the propagation of the stress localization, which requires a sufficiently homogeneous microstructure to allow for the accommodation of stress and strain in neighboring grains. The mixture of softer and harder microstructural constituents in non-recrystallized material states was found to result in a heterogeneous microstructure, which impedes the propagation of stress localization and as such, suppresses serrated flow. Accordingly, the analysis of the serrated flow behavior yielded a model that connected nanostructural characteristics with the activation of secondary deformation mechanisms on a microstructural scale and the formation and propagation of deformation bands on a macroscale.

In addition to the analysis of the impact of SRO on the activation of secondary deformation mechanisms, a comprehensive study on the impact of the initial grain size in two high-manganese TWIP/TRIP steels revealed a significant grain size-dependence of the YS and the activation of secondary deformation mechanisms, which translated into pronounced grain size-dependent evolutions of the WHR and the deformation texture during quasistatic tensile tests. The reduction in grain size resulted in a significant increase of the YS of approximately 100 MPa. A combined approach of EBSD experiments, X-ray diffraction (XRD) measurements and

macrotexture analysis during interrupted tensile tests enabled the correlative multi-scale study on the impact of grain size on the deformation behavior. The EBSD measurements revealed that the activation of the TWIP and TRIP effects was more pronounced in the coarse-grained alloy states. This was also supported by the XRD measurements which showed a significantly higher phase fraction of ε- and α'-martensite compared to the fine-grained initial state. The macrotexture measurements were in agreement with the EBSD and XRD measurements, revealing that the pronounced TWIP and TRIP effect in the coarse-grained material states induced a relative softening of the <111>||TA-fiber (TA – tensile axis) compared to the <100>||TA-fiber. Additionally, the concept of SRO-assisted deformation twinning was further supported by the measurement of the TVF, martensite phase fractions and the volume fractions of the texture components, which indicated a partial suppression of the TWIP/TRIP effect in the HMnS containing Al. The differences in martensite phase fraction were also put into context of the differences in TVF, as twin-twin intersections are effective nucleation sites for ε and α'. Finally, the grain size-dependent evolution of the WHR was in agreement with the activation of the secondary deformation mechanisms, highlighting the impact of the microstructure on the macroscopic mechanical properties.

The findings on the impact of the initial microstructure on the macroscopic mechanical properties and deformation behavior in HMnS were also put into context of an analysis regarding the deformation behavior of an intercritically-annealed X6MnAl12-3 MMnS. Special scope of that study was the strain-rate-dependent strain partitioning in the microstructure, which consisted of 45% recrystallized or reverted Mn-rich γ as well as 55% Al-rich α and lamellar α', and the resulting impact on the macroscopic mechanical properties. The strain-rate sensitivity of the macroscopic mechanical properties was shown to be a result of the highly strain-rate-dependent deformation behavior on the microscale. The concept of the strain-rate-dependent strength of α and α' relative to γ $\Delta\sigma$ was used to explain the resulting differences in the accommodation of plastic deformation at different strain rates and the partial suppression of the TRIP effect at very low and very high strain rates. At very low strain rates, where serrated flow was observed, a higher fraction of the total plastic deformation was accommodated by α and α' and $\Delta\sigma$ was lower. Overall, the interplay of the activation of the TRIP effect and the strain-rate-dependent $\Delta\sigma$ was suitable to explain the impact of a change in strain rate at very low, medium and high strain rates.

Although the alloying concepts and process routes of the HMnS and MMnS analyzed in this study were vastly different, some similarities in their mechanical response to straining were

found. In both cases, the initial microstructure did not only significantly influence the YS, but also the mechanical response to plastic deformation. Intercritical annealing of cold-rolled MMnS resulted in an ultrafine-grained (UFG) multi-phase microstructure, where each microstructural constituent had different critical stresses for plastic deformation, comparable to partially-recrystallized or recovery-annealed HMnS. As a result, the mixture of harder and softer microstructural constituents in the MMnS led to a pronounced strain-rate-dependent $\Delta\sigma$ as well as a strain-rate-dependent activation of the TRIP effect. This effect is comparable to the aspect of microstructural homogeneity in HMnS, which was found to be a necessary requirement for the occurrence of serrated flow in fully austenitic HMnS. Accordingly, serrated flow was found to be strain-rate-dependent in the MMnS and occurred only for very low strain rates, where the low $\Delta\sigma$ enabled a homogeneous strain partitioning. However, tailoring the strain partitioning behavior in MMnS is very difficult, as the pronounced elemental partitioning of C, Mn and Al during intercritical annealing limits the process window of a target γ phase fraction in combination with a desired SFE. In combination with the observed strain-rate dependence of the activation of secondary deformation mechanisms, this means that the process design for MMnS with regards to both metallurgy and forming is very complex compared to HMnS and requires an individual layout for each new alloy.

To summarize the findings of this work, it was shown that the interplay between SRO and the activation of secondary deformation mechanisms is of critical importance for an accurate description of the deformation behavior of HMnS and MMnS. The significant impact of the initial microstructure is highlighted by the remarkable increase of the YS in the case of the not fully-recrystallized X60Mn18_pRX and X30MnAl17-1_REC alloys (cf. Figure 10). The contribution of the microstructure to the YS in Figure 10(b) includes (i) grain size effects, (ii) the impact of not fully-recrystallized initial microstructures and (iii) the impact of a multi-phase microstructure. The residual ductility of the X30MnAl17-1_REC and X60Mn18_pRX alloys was higher than 15% (cf. Figure 10(a)), allowing for further plastic deformation, e.g. during sheet forming processes. Similarly, the UFG multi-phase microstructure of the MMnS also resulted in a high YS in combination with an elongation to fracture of more than 35%. As Figure 10(b) highlights, the contribution of SRO clusters to the YS needs to be considered as well, reaching up to 60 MPa. This contribution is especially beneficial in the case of the fully-recrystallized HMnS, as this fraction of the YS constitutes nearly 20% of the overall YS.

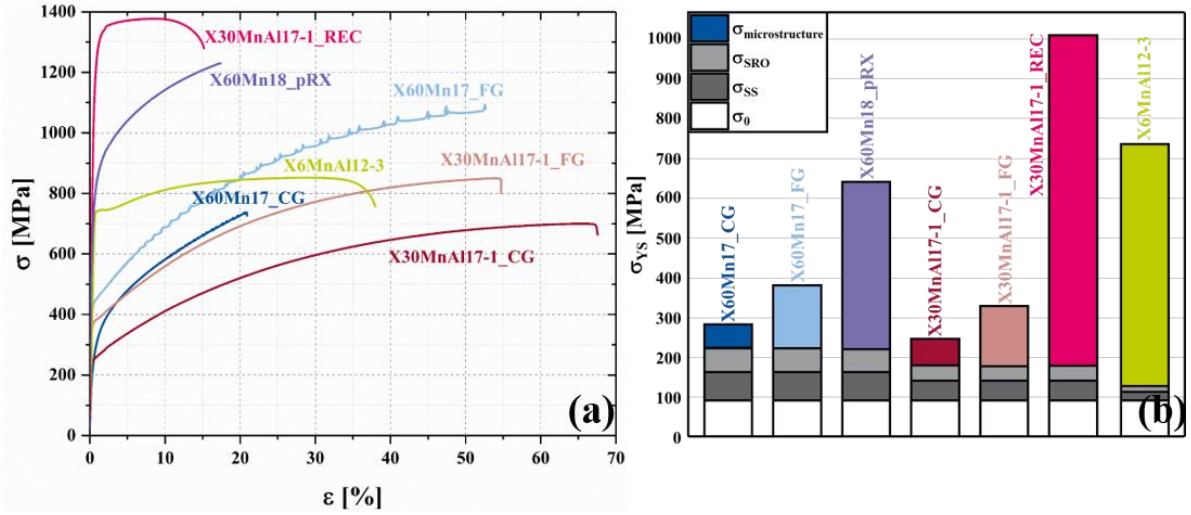


Figure 10: (a) stress-strain curves for a selection of HMnS and the MMnS in this work. (b) Individual strengthening contributions to the YS.

It was not possible to adjust the YS and WHR of TWIP/TRIP steels independently by adjusting the initial microstructure (cf. Figure 11). As the state of SRO clusters after partial recrystallization, recovery annealing or complete recrystallization is very similar, the contribution of SRO to the YS or its effect on the WHR cannot be adjusted significantly, either. However, it was shown that SRO clusters assist in the activation of secondary deformation mechanisms, thus increasing the WHR. In the case of grain size, the fine-grained microstructure of the HMnS partially suppressed the activation of the secondary deformation mechanisms. This is reflected by higher values of the instantaneous strain hardening exponent n_H from Holloman's equation $n_H = \frac{d \ln \sigma_{true}}{d \ln \varepsilon_{true}}$ for the fully recrystallized coarse-grained materials at $\varepsilon_{true} > 0.05$ (cf. Figure 11(b)).

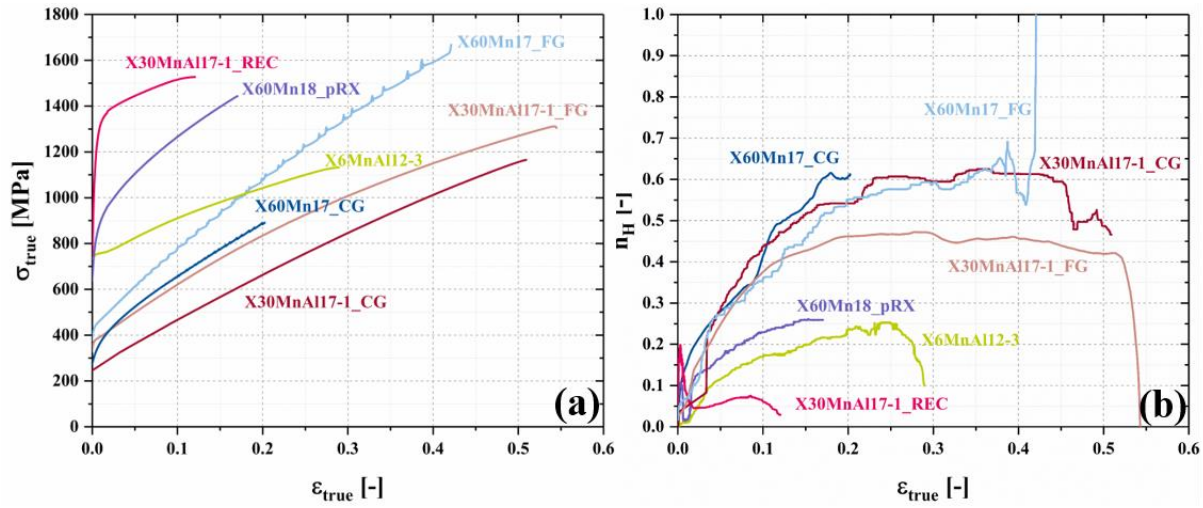


Figure 11: (a) flow curves and (b) smoothed instantaneous strain hardening exponent n_H for the steels in Figure 10.

As the example of the X30MnAl17-1 alloy highlights, the WHR can be adjusted by tailoring the initial microstructure of HMnS. Therefore, it is possible to achieve strength-ductility

combinations of TWIP steels, austenitic stainless steels and the third generation of Advanced High Strength Steels (AHSS) (cf. Figure 12).

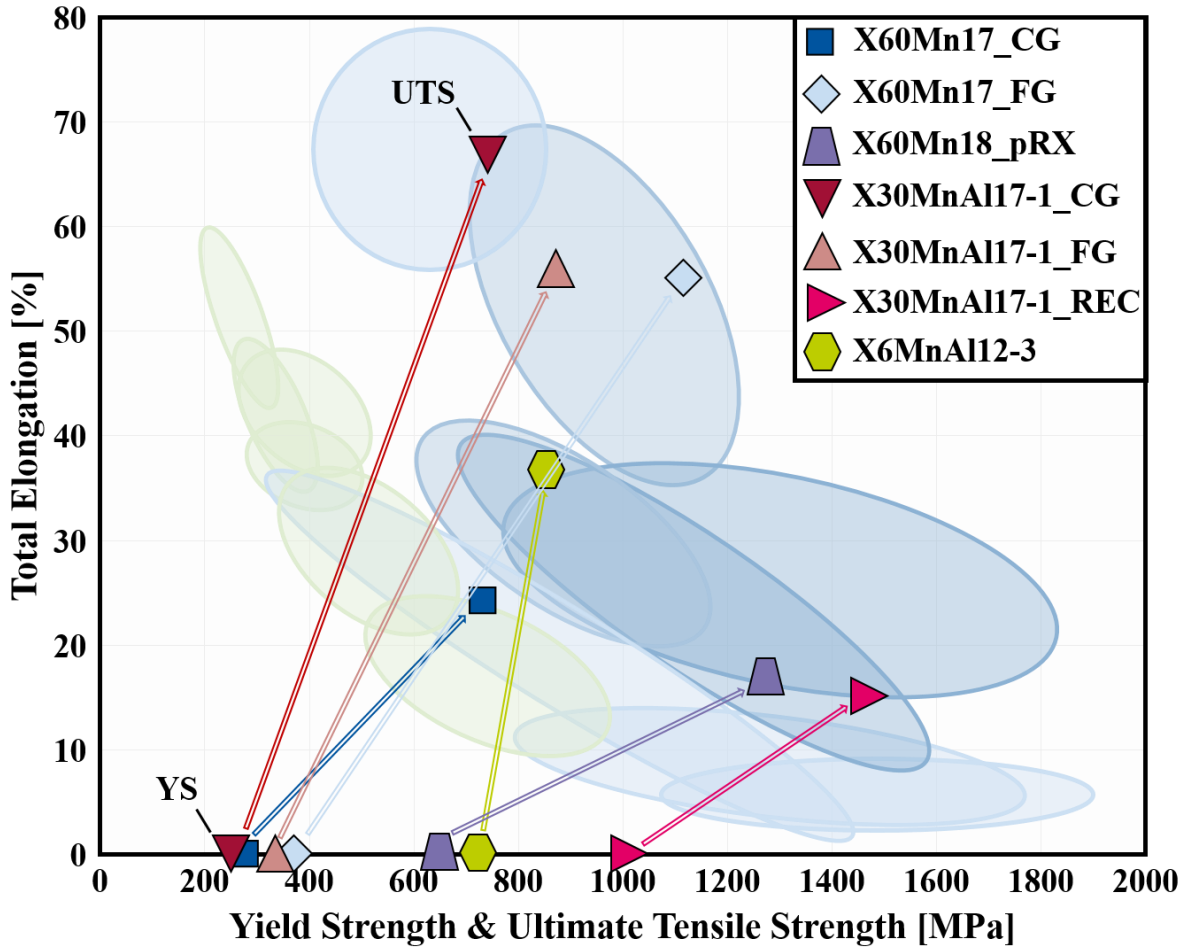


Figure 12: Strength-Ductility Diagram with a selection of the HMnS and the MMnS analyzed in this work. The highlighted areas refer to the steel grades in Figure 2.

To conclude, this study revealed that SRO clusters and a fine-grained initial microstructure both remarkably increase the YS. SRO clusters affect the deformation behavior by assisting in the activation of the secondary deformation mechanisms, which increases the WHR. On the other hand, a reduction in grain size and non-recrystallized initial microstructures partially suppresses the activation of the TWIP and TRIP effect, resulting in a lower n_H. Compared to fully recrystallized HMnS, the UFG microstructure of the MMnS results in an appreciably high YS. Due to the multi-phase microstructure, the strain partitioning behavior critically affects the activation of the TRIP mechanism, the WHR and the resulting mechanical properties. Overall, it can be concluded that the YS and the WHR cannot be adjusted independently by SRO clusters and tailored initial microstructures.

References

[1] B.C. DeCooman, Y. Estrin, S.K. Kim: Twinning-induced plasticity (TWIP) steels. Acta Materialia 142 (2018), 283–362, DOI: 10.1016/j.actamat.2017.06.046.

[2] B.C. DeCooman: High Mn TWIP steel and medium Mn steel; in: R. Rana, S.B. Singh (Eds.): Automotive Steels: Design, Metallurgy, Processing and Applications. Elsevier 2017, 317–385, DOI: 10.1016/B978-0-08-100638-2.00011-0.

[3] M. Bambach, L. Conrads, M. Daamen, O. Güvenç, G. Hirt: Enhancing the crashworthiness of high-manganese steel by strain-hardening engineering, and tailored folding by local heat-treatment. Materials & Design 110 (2016), 157–168, DOI: 10.1016/j.matdes.2016.07.065.

[4] O. Bouaziz, S. Allain, C.P. Scott, P. Cugy, D. Barbier: High manganese austenitic twinning induced plasticity steels: A review of the microstructure properties relationships. Current Opinion in Solid State and Materials Science 15 (2011), 141–168, DOI: 10.1016/j.cossms.2011.04.002.

[5] The International Council on Clean Transportation: 2017 Global update: Light-duty vehicle greenhouse gas and fuel economy standards. www.theicct.org/publications/2017-global-update-LDV-GHG-FE-standards. [14.11.2018; 08:50].

[6] WorldAutoSteel: Advanced High Strength Steels Application Guidelines Version 6.0. https://www.worldautosteel.org/downloads/599700/. [14.11.2018; 09:21].

[7] O. Bouaziz, D. Barbier: Benefits of Recovery and Partial Recrystallization of Nano-Twinned Austenitic Steels. Adv. Eng. Mater. 11 (2013), 976-979, DOI: 10.1002/adem.201300045.

[8] C. Haase, L.A. Barrales-Mora, F. Roters, D.A. Molodov, G. Gottstein: Applying the texture analysis for optimizing thermomechanical treatment of high manganese twinning-induced plasticity steel. Acta Materialia 80 (2014), 327–340, DOI: 10.1016/j.actamat.2014.07.068.

[9] F. Berrenberg, C. Haase, L.A. Barrales-Mora, D.A. Molodov: Enhancement of the strength-ductility combination of twinning-induced/transformation-induced plasticity steels by reversion annealing. Materials Science and Engineering: A 681 (2017), 56–64, DOI: 10.1016/j.msea.2016.10.109.

[10] D.T. Pierce, J.A. Jiménez, J. Bentley, D. Raabe, C. Oskay, J.E. Wittig: The influence of manganese content on the stacking fault and austenite/ε-martensite interfacial energies in Fe–Mn–(Al–Si) steels investigated by experiment and theory. Acta Materialia 68 (2014), 238–253, DOI: 10.1016/j.actamat.2014.01.001.

[11] A. Saeed-Akbari, J. Imlau, U. Prahl, W. Bleck: Derivation and Variation in Composition-Dependent Stacking Fault Energy Maps Based on Subregular Solution Model in High-Manganese Steels. Metallurgical and Materials Transactions A 40 (2009), 3076–3090, DOI: 10.1007/s11661-009-0050-8.

[12] A. Saeed-Akbari, L. Mosecker, A. Schwedt, W. Bleck: Characterization and Prediction of Flow Behavior in High-Manganese Twinning Induced Plasticity Steels: Part I. Mechanism Maps and Work-Hardening Behavior. Metallurgical and Materials Transactions A 43 (2012), 1688–1704, DOI: 10.1007/s11661-011-0993-4.

[13] C. Haase, C. Zehnder, T. Ingendahl, A. Bikar, F. Tang, B. Hallstedt, W. Hu et al.: On the deformation behavior of κ-carbide-free and κ-carbide-containing high-Mn light-weight steel. Acta Materialia 122 (2017), 332–343, DOI: 10.1016/j.actamat.2016.10.006.

[14] W. Bleck: Werkstoffkunde Stahl: für Studium und Praxis, 3rd ed., Verlag Mainz, Aachen 2010.

[15] W. Bleck: Spezielle Werkstoffkunde der Stähle: für Studium und Praxis, 2nd ed., Verlag Mainz, Aachen 2012.

[16] Infomine Inc.: Commodity and Metal Prices. http://www.infomine.com/Investment/metal-prices/. [20.07.2018; 08:57].

[17] C. Haase, T. Ingendahl, O. Güvenç, M. Bambach, W. Bleck, D.A. Molodov, L.A. Barrales-Mora: On the applicability of recovery-annealed Twinning-Induced Plasticity steels: Potential and limitations. Materials Science and Engineering: A 649 (2016), 74–84, DOI: 10.1016/j.msea.2015.09.096.

[18] P. Kusakin, A. Belyakov, R. Kaibyshev, D.A. Molodov: Ultrafine-Grained Structure and Mechanical Properties of a High-Mn Twinning Induced Plasticity Steel. Materials Science Forum 838-839 (2016), 392–397, DOI: 10.4028/www.scientific.net/MSF.838-839.392.

[19] C. Scott, B. Remy, J.-L. Collet, A. Cael, C. Bao, F. Danoix, B. Malard, C. Curfs: Precipitation strengthening in high manganese austenitic TWIP steels. International Journal of Materials Research 102 (2011), 538–549, DOI: 10.3139/146.110508.

[20] H.-W. Yen, M. Huang, C.P. Scott, J.-R. Yang: Interactions between deformation-induced defects and carbides in a vanadium-containing TWIP steel. Scripta Materialia 66 (2012), 1018–1023, DOI: 10.1016/j.scriptamat.2012.02.002.

[21] J.D. Yoo, S.W. Hwang, K.-T. Park: Factors influencing the tensile behavior of a Fe–28Mn–9Al–0.8C steel. Materials Science and Engineering: A 508 (2009), 234–240, DOI: 10.1016/j.msea.2008.12.055.

[22] W. Song, W. Zhang, J. von Appen, R. Dronskowski, W. Bleck: κ-Phase Formation in Fe-Mn-Al-C Austenitic Steels. steel research international 86 (2015), 1161–1169, DOI: 10.1002/srin.201400587.

[23] Z.H. Cai, B. Cai, H. Ding, Y. Chen, R.D.K. Misra: Microstructure and deformation behavior of the hot-rolled medium manganese steels with varying aluminum-content. Materials Science and Engineering: A 676 (2016), 263–270, DOI: 10.1016/j.msea.2016.08.119.

[24] Z.H. Cai, H. Ding, R.D.K. Misra, Z.Y. Ying: Austenite stability and deformation behavior in a cold-rolled transformation-induced plasticity steel with medium manganese content. Acta Materialia 84 (2015), 229–236, DOI: 10.1016/j.actamat.2014.10.052.

[25] Z.C. Li, H. Ding, R.D.K. Misra, Z.H. Cai: Microstructure-mechanical property relationship and austenite stability in medium-Mn TRIP steels: The effect of austenite-reverted transformation and quenching-tempering treatments. Materials Science and Engineering: A 682 (2017), 211–219, DOI: 10.1016/j.msea.2016.11.048.

[26] S.-J. Lee, S. Lee, B.C. DeCooman: Mn partitioning during the intercritical annealing of ultrafine-grained 6% Mn transformation-induced plasticity steel. Scripta Materialia 64 (2011), 649–652, DOI: 10.1016/j.scriptamat.2010.12.012.

[27] S. Lee, B.C. DeCooman: Annealing Temperature Dependence of the Tensile Behavior of 10 pct Mn Multi-phase TWIP-TRIP Steel. Metallurgical and Materials Transactions A 45 (2014), 6039–6052, DOI: 10.1007/s11661-014-2540-6.

[28] B.B. He, B. Hu, H.W. Yen, G.J. Cheng, Z.K. Wang, H.W. Luo, M.X. Huang: High dislocation density-induced large ductility in deformed and partitioned steels. Science (New York, N.Y.) 357 (2017), 1029–1032, DOI: 10.1126/science.aan0177.

[29] G. Gottstein: Materialwissenschaft und Werkstofftechnik: Physikalische Grundlagen, 4th ed., Springer Berlin Heidelberg, Berlin, Heidelberg 2014.

[30] C. Haase: Texture and Microstructure Evolution during Deformation and Annealing of High-Manganese TWIP Steels. Dissertation, Aachen 2016.

[31] I. Gutierrez-Urrutia, D. Raabe: Multistage strain hardening through dislocation substructure and twinning in a high strength and ductile weight-reduced Fe–Mn–Al–C steel. Acta Materialia 60 (2012), 5791–5802, DOI: 10.1016/j.actamat.2012.07.018.

[32] I. Gutierrez-Urrutia, D. Raabe: Microbanding mechanism in an Fe–Mn–C high-Mn twinning-induced plasticity steel. Scripta Materialia 69 (2013), 53–56, DOI: 10.1016/j.scriptamat.2013.03.010.

[33] J.-E. Jin, M. Jung, C.-Y. Lee, J. Jeong, Y.-K. Lee: Néel temperature of high Mn austenitic steels. Metals and Materials International 18 (2012), 419–423, DOI: 10.1007/s12540-012-3006-2.

[34] A. Dumay, J.-P. Chateau, S. Allain, S. Migot, O. Bouaziz: Influence of addition elements on the stacking-fault energy and mechanical properties of an austenitic Fe–Mn–C steel. Materials Science and Engineering: A 483-484 (2008), 184–187, DOI: 10.1016/j.msea.2006.12.170.

[35] R. Xiong, H. Peng, H. Si, W. Zhang, Y. Wen: Thermodynamic calculation of stacking fault energy of the Fe–Mn–Si–C high manganese steels. Materials Science and Engineering: A 598 (2014), 376–386, DOI: 10.1016/j.msea.2014.01.046.

[36] S. Mahajan, G.Y. Chin: Formation of deformation twins in f.c.c. crystals. Acta Metallurgica 21 (1973), 1353–1363, DOI: 10.1016/0001-6160(73)90085-0.

[37] I. Gutierrez-Urrutia, S. Zaefferer, D. Raabe: The effect of grain size and grain orientation on deformation twinning in a Fe–22wt.% Mn–0.6wt.% C TWIP steel. Materials Science and Engineering: A 527 (2010), 3552–3560, DOI: 10.1016/j.msea.2010.02.041.

[38] M. Koyama, T. Sawaguchi, K. Tsuzaki: Deformation Twinning Behavior of Twinning-induced Plasticity Steels with Different Carbon Concentrations – Part 2: Proposal of Dynamic-strain-aging-assisted Deformation Twinning. ISIJ International 55 (2015), 1754–1761, DOI: 10.2355/isijinternational.ISIJINT-2015-070.

[39] H. Beladi, I.B. Timokhina, Y. Estrin, J. Kim, B.C. DeCooman, S.K. Kim: Orientation dependence of twinning and strain hardening behaviour of a high manganese twinning induced plasticity steel with polycrystalline structure. Acta Materialia 59 (2011), 7787–7799, DOI: 10.1016/j.actamat.2011.08.031.

[40] O. Bouaziz, S. Allain, C. Scott: Effect of grain and twin boundaries on the hardening mechanisms of twinning-induced plasticity steels. Scripta Materialia 58 (2008), 484–487, DOI: 10.1016/j.scriptamat.2007.10.050.

[41] M.A. Meyers, O. Vöhringer, V.A. Lubarda: The onset of twinning in metals: a constitutive description. Acta Materialia 49 (2001), 4025–4039, DOI: 10.1016/S1359-6454(01)00300-7.

[42] S. Dancette, L. Delannay, K. Renard, M.A. Melchior, P.J. Jacques: Crystal plasticity modeling of texture development and hardening in TWIP steels. Acta Materialia 60 (2012), 2135–2145, DOI: 10.1016/j.actamat.2012.01.015.

[43] S.L. Wong, M. Madivala, U. Prahl, F. Roters, D. Raabe: A crystal plasticity model for twinning- and transformation-induced plasticity. Acta Materialia 118 (2016), 140–151, DOI: 10.1016/j.actamat.2016.07.032.

[44] C.Y. Sun, N. Guo, M.W. Fu, S.W. Wang: Modeling of slip, twinning and transformation induced plastic deformation for TWIP steel based on crystal plasticity. International Journal of Plasticity 76 (2016), 186–212, DOI: 10.1016/j.ijplas.2015.08.003.

[45] L. Bracke, L. Kestens, J. Penning: Transformation mechanism of α′-martensite in an austenitic Fe–Mn–C–N alloy. Scripta Materialia 57 (2007), 385–388, DOI: 10.1016/j.scriptamat.2007.05.003.

[46] S. Pramanik, A.A. Gazder, A.A. Saleh, E.V. Pereloma: Nucleation, coarsening and deformation accommodation mechanisms of ε-martensite in a high manganese steel. Materials Science and Engineering: A 731 (2018), 506–519, DOI: 10.1016/j.msea.2018.06.024.

[47] F. Maresca, V.G. Kouznetsova, M.G.D. Geers, W.A. Curtin: Contribution of austenite-martensite transformation to deformability of advanced high strength steels: From atomistic mechanisms to microstructural response. Acta Materialia 156 (2018), 463–478, DOI: 10.1016/j.actamat.2018.06.028.

[48] X.-S. Yang, S. Sun, X.-L. Wu, E. Ma, T.-Y. Zhang: Dissecting the mechanism of martensitic transformation via atomic-scale observations. Scientific reports 4 (2014), 6141, DOI: 10.1038/srep06141.

[49] Y. Lü, B. Hutchinson, D.A. Molodov, G. Gottstein: Effect of deformation and annealing on the formation and reversion of ε-martensite in an Fe–Mn–C alloy. Acta Materialia 58 (2010), 3079–3090, DOI: 10.1016/j.actamat.2010.01.045.

[50] S. Mahajan, M.L. Green, D. Brasen: A model for the FCC→HCP transformation, its applications, and experimental evidence. Metallurgical Transactions A 8 (1977), 283–293, DOI: 10.1007/BF02661642.

[51] E. Welsch, D. Ponge, S.M. Hafez Haghighat, S. Sandlöbes, P. Choi, M. Herbig, S. Zaefferer, D. Raabe: Strain hardening by dynamic slip band refinement in a high-Mn lightweight steel. Acta Materialia 116 (2016), 188–199, DOI: 10.1016/j.actamat.2016.06.037.

[52] J.D. Yoo, K.-T. Park: Microband-induced plasticity in a high Mn–Al–C light steel. Materials Science and Engineering: A 496 (2008), 417–424, DOI: 10.1016/j.msea.2008.05.042.

[53] D. Hua, L. Huaying, W. Zhiqiang, H. Mingli, L. Haoze, X. Qibin: Microstructural Evolution and Deformation Behaviors of Fe-Mn-Al-C Steels with Different Stacking Fault Energies. steel research int. 84 (2013), 1288–1293, DOI: 10.1002/srin.201300052.

[54] L. Bracke, K. Verbeken, L. Kestens, J. Penning: Microstructure and texture evolution during cold rolling and annealing of a high Mn TWIP steel. Acta Materialia 57 (2009), 1512–1524, DOI: 10.1016/j.actamat.2008.11.036.

[55] C. Haase, M. Kühbach, L.A. Barrales-Mora, S.L. Wong, F. Roters, D.A. Molodov, G. Gottstein: Recrystallization behavior of a high-manganese steel: Experiments and simulations. Acta Materialia 100 (2015), 155–168, DOI: 10.1016/j.actamat.2015.08.057.

[56] Y. Lü, D.A. Molodov, G. Gottstein: Recrystallization kinetics and microstructure evolution during annealing of a cold-rolled Fe–Mn–C alloy. Acta Materialia 59 (2011), 3229–3243, DOI: 10.1016/j.actamat.2011.01.063.

[57] D. Barbier, N. Gey, S. Allain, N. Bozzolo, M. Humbert: Analysis of the tensile behavior of a TWIP steel based on the texture and microstructure evolutions. Materials Science and Engineering: A 500 (2009), 196–206, DOI: 10.1016/j.msea.2008.09.031.

[58] T.A. Timmerscheidt, R. Dronskowski: An Ab Initio Study of Carbon-Induced Ordering in Austenitic Fe-Mn-Al-C Alloys. steel research international 88 (2017), 1600292, DOI: 10.1002/srin.201600292.

[59] P. Dey, R. Nazarov, B. Dutta, M. Yao, M. Herbig, M. Friák, T. Hickel, D. Raabe, J. Neugebauer: Ab initio explanation of disorder and off-stoichiometry in Fe-Mn-Al-C κ carbides. Phys. Rev. B 95 (2017), 419, DOI: 10.1103/PhysRevB.95.104108.

[60] M.J. Yao, P. Dey, J.-B. Seol, P. Choi, M. Herbig, R.K.W. Marceau, T. Hickel, J. Neugebauer, D. Raabe: Combined atom probe tomography and density functional theory investigation of the Al off-stoichiometry of κ-carbides in an austenitic Fe–Mn–Al–C low density steel. Acta Materialia 106 (2016), 229–238, DOI: 10.1016/j.actamat.2016.01.007.

[61] A.P. Bentley: Ordering in Fe-Mn-Al-C austenite. J Mater Sci Lett 5 (1986), 907–908, DOI: 10.1007/BF01729270.

[62] W. Song, D. Bogdanovski, A. Yildiz, J. Houston, R. Dronskowski, W. Bleck: On the Mn–C Short-Range Ordering in a High-Strength High-Ductility Steel: Small Angle Neutron Scattering and Ab Initio Investigation. Metals 8 (2018), 44, DOI: 10.3390/met8010044.

[63] S. Wesselmecking, W. Song, Y. Ma, T. Roesler, H. Hofmann, W. Bleck: Strain Aging Behavior of an Austenitic High-Mn Steel. steel research int. 89 (2018), 1700515, DOI: 10.1002/srin.201700515.

[64] J.-H. Kang, T. Ingendahl, J. von Appen, R. Dronskowski, W. Bleck: Impact of short-range ordering on yield strength of high manganese austenitic steels. Materials Science and Engineering: A 614 (2014), 122–128, DOI: 10.1016/j.msea.2014.07.016.

[65] S. Allain, O. Bouaziz, T. Lebedkina, M. Lebyodkin: Relationship between relaxation mechanisms and strain aging in an austenitic FeMnC steel. Scripta Materialia 64 (2011), 741–744, DOI: 10.1016/j.scriptamat.2010.12.039.

[66] L. Chen, Y. Zhao, X. Qin: Some aspects of high manganese twinning-induced plasticity (TWIP) steel, a review. Acta Metallurgica Sinica (English Letters) 26 (2013), 1–15, DOI: 10.1007/s40195-012-0501-x.

[67] K. Renard, P.J. Jacques: On the relationship between work hardening and twinning rate in TWIP steels. Materials Science and Engineering: A 542 (2012), 8–14, DOI: 10.1016/j.msea.2012.01.123.

[68] S.-J. Lee, J. Kim, S.N. Kane, B.C.D. Cooman: On the origin of dynamic strain aging in twinning-induced plasticity steels. Acta Materialia 59 (2011), 6809–6819, DOI: 10.1016/j.actamat.2011.07.040.

[69] T.A. Lebedkina, M.A. Lebyodkin, J.-P. Chateau, A. Jacques, S. Allain: On the mechanism of unstable plastic flow in an austenitic FeMnC TWIP steel. Materials Science and Engineering: A 519 (2009), 147–154, DOI: 10.1016/j.msea.2009.04.067.

[70] M.C. Jo, J.H. Choi, H. Lee, A. Zargaran, J.H. Ryu, S.S. Sohn, N.J. Kim et al.: Effects of solute segregation on tensile properties and serration behavior in ultra-high-strength high-Mn TRIP steels. Materials Science and Engineering: A 740-741 (2019), 16–27, DOI: 10.1016/j.msea.2018.10.065.

[71] Y. Ma: Medium-manganese steels processed by austenite-reverted-transformation annealing for automotive applications. Materials Science and Technology 33 (2017), 1713–1727, DOI: 10.1080/02670836.2017.1312208.

[72] X.G. Wang, L. Wang, M.X. Huang: In-situ evaluation of Lüders band associated with martensitic transformation in a medium Mn transformation-induced plasticity steel. Materials Science and Engineering: A 674 (2016), 59–63, DOI: 10.1016/j.msea.2016.07.054.

[73] Y.-K. Lee, J. Han: Current opinion in medium manganese steel. Materials Science and Technology 31 (2015), 843–856, DOI: 10.1179/1743284714Y.0000000722.

[74] P.J. Gibbs, B.C. de Cooman, D.W. Brown, B. Clausen, J.G. Schroth, M.J. Merwin, D.K. Matlock: Strain partitioning in ultra-fine grained medium-manganese transformation induced plasticity steel. Materials Science and Engineering: A 609 (2014), 323–333, DOI: 10.1016/j.msea.2014.03.120.

[75] M.I. Latypov, S. Shin, B.C. de Cooman, H.S. Kim: Micromechanical finite element analysis of strain partitioning in multiphase medium manganese TWIP+TRIP steel. Acta Materialia 108 (2016), 219–228, DOI: 10.1016/j.actamat.2016.02.001.

[76] X. Tan, D. Ponge, W. Lu, Y. Xu, X. Yang, X. Rao, Di Wu et al.: Carbon and strain partitioning in a quenched and partitioned steel containing ferrite. Acta Materialia 165 (2019), 561–576, DOI: 10.1016/j.actamat.2018.12.019.

[77] L.A. Barrales-Mora, Y. Lü, D.A. Molodov: Experimental Determination and Simulation of Annealing Textures in Cold Rolled TWIP and TRIP Steels. steel research international 82 (2011), 119–126, DOI: 10.1002/srin.201000261.

[78] M. Haupt, A. Dutta, D. Ponge, S. Sandlöbes, M. Nellessen, G. Hirt: Influence of Intercritical Annealing on Microstructure and Mechanical Properties of a Medium Manganese Steel. Procedia Engineering 207 (2017), 1803–1808, DOI: 10.1016/j.proeng.2017.10.942.

[79] J. Emo, P. Maugis, A. Perlade: Austenite growth and stability in medium Mn, medium Al Fe-C-Mn-Al steels. Computational Materials Science 125 (2016), 206–217, DOI: 10.1016/j.commatsci.2016.08.041.

Chapter II

Ab Initio-Based Modelling of the Yield Strength in High-Manganese Steels

S. Sevsek and W. Bleck
Metals 8 (1) (2018) 34
https://doi.org/10.3390/met8010034

Chapter II describes a scale-bridging modelling approach of the impact of nano-sized short-range ordered clusters on the macroscopic yield strength. Simulations based on the density functional theory result in the calculation of the ordering energy of different configurations of C-Mn-Al clusters, which are used to determine the distribution of C atoms in various high-manganese steels. The ordering energy contributions are incorporated into a regression model to determine the yield strength and the individual solid solution strengthening contributions of C, Mn and Al. In combination with the impact of grain size, the developed model for the calculation of the yield strength in high-manganese steels showed good agreement with experimental results.

metals

MDPI

Article

Ab Initio-Based Modelling of the Yield Strength in High-Manganese Steels

Simon Sevsek * and Wolfgang Bleck

Steel Institute, RWTH Aachen University, Intzestraße 1, 52072 Aachen, Germany; bleck@iehk.rwth-aachen.de
* Correspondence: simon.sevsek@iehk.rwth-aachen.de; Tel.: +49-241-80-90138

Received: 15 November 2017; Accepted: 3 January 2018; Published: 5 January 2018

Abstract: An ab initio-based model for the strength increase by short-range ordering of C-Mn-Al clusters has been developed. The model is based on ab initio calculations of ordering energies. The impact of clusters on the yield strength of high-manganese austenitic steels (HMnS) is highly dependent on the configurational structure of the cells that carbon atoms will position themselves as interstitial atoms. The impact of the alloying elements C, Mn, and Al on the potential and actual increase in yield strength is analyzed. A model for the calculation of yield strengths of HMnS is derived that includes the impact of short-range ordering, grain size refinement, and solid solution strengthening. The model is in good agreement with experimental data and performs better than other models that do not include strengthening by short-range ordering.

Keywords: short-range ordering; yield strength; high-manganese steel

1. Introduction

High Mn austenitic steels (HMnS) offer great combinations of hardness and ductility with a wide range of possible applications in various industries, such as the automotive industry [1–3]. Depending on the stacking fault energy, which is a result of alloying content, temperature, deformation grade, and other factors, HMnS exhibit a variety of different active deformation modes [4–7]. Those deformation modes include transformation induced plasticity (TRIP), twinning-induced plasticity (TWIP) or pronounced planar glide in combination with the formation of dislocation cells that is sometimes referred to as microband-induced plasticity (MBIP) [1,8–10]. The mode of deformation significantly influences the level of work hardening and plays a major role in determining the mechanical properties [7]. One of those material characteristics is the material's yield strength (YS). In the past, various attempts have been made to model the YS of HMnS based on the chemical composition using linear regression [5,11–13]. However, these models often imply negative solid-solution strengthening by some of the alloying elements, like Mn, that are usually attributed to positive strengthening effects [2,14,15].

Interactions of carbon-metal pairs [16–18] and clusters are described by the concept of short-range ordering (SRO) phenomena [19] in HMnS and might offer an explanation for an additional increase in strength that might lead to a defective linear regression when using standard methods to calculate the impact of solid solution strengthening [14,20,21]. Short-range ordered clusters are a result of local differences in ordering energies that make particular unit cell configurations preferential to inhibit a carbon atom [22]. Ab initio calculations employing density-functional theory (DFT) have been shown to be suitable for calculations of ordering energies in HMnS for several chemical compositions. For example, thermodynamic predictions of κ-phase stability [23], interface energies [24], stacking fault energies [25], and hydrogen trap sites [26] showed good agreement with the experimental data.

Cell models [27] have been used to determine the location of carbon atoms in relation to the matrix or substitutional alloying atoms. Other studies show that the interaction of carbon atoms with

each other is very repulsive and, thus, influences the diffusion behavior [4,25,28–30], which also points to a coordination of carbon atoms in octahedral sites dependent of surrounding solute atoms. Additionally, the position of C also influences the stacking fault energy of the material [31].

Short-range ordering has also been used to explain the pronounced planar glide that HMnS exhibit because of glide plane softening that occurs when short-range ordered C-Mn clusters are destroyed by dislocation stresses reorienting the carbon atom from its octahedral position to a tetrahedral position. This phenomenon also explains the serrated flow curves that can be found during tensile testing of HMnS, as the back stresses of dislocation pile-ups lead to an increase in strength. The reorientation of the carbon atom then leads to a temporary destruction of the short-range ordered cluster and as a result, a rapid drop in strength because of subsequent softening of this glide plane [32]. However, short-range ordering can be restored by short-range jumps of C back from the tetrahedral site to its initial octahedral site [1,2]. Those short-range jumps might be activated by temperature, but already occur at low temperatures where diffusion processes are usually negligible [1,32].

In this study, a basic cell model for the nearest-neighboring atoms of a central octahedral carbon atom is expanded to include the corner atoms of an elementary cell of an austenitic face-centered cubic (FCC) unit cell, which can be described as the second-nearest neighbors of the central octahedral site in an austenitic cell [27]. Results of ab initio calculations are employed to show that the position of Mn and Al being coordinated as a nearest neighbor or second-nearest neighbor to a central carbon atom is of major importance to the energy level of the system [33]. It is assumed that this also holds true in the case of a central interstitial nitrogen atom [2,33,34] but, in this work, the authors will focus solely on carbon. Based on the calculated ordering energies, the yield strength of HMnS is a result of a combination of short-range ordered clusters, regular solid-solution hardening, grain size effects, and the base strength of an austenitic lattice [14,35].

2. Materials and Methods

Many models for the calculation of the yield strength of austenitic steels have been published in the past. Those models generally employ two mechanisms to describe the yield strength: a strengthening by grain size reduction, the Hall-Petch effect, and the alloying elements' contribution to the material's strength [15,36,37]. Many of those models have used databases with significant amounts of different alloys to employ a linear regression in order to get parameters that determine the effect of alloying elements on the yield strength of the austenitic steel. Assuming that SRO in HMnS influences the yield strength σ_Y significantly, a term describing this effect has to be added to the equation [14], resulting in:

$$\sigma_Y = \sigma_0 + \sigma_{SS} + \sigma_{GS} + \sigma_{SRO} \quad (1)$$

where σ_0 is the base strength of a pure austenitic iron lattice and is assumed to be 90 MPa [14]. σ_{SS} is the contribution of alloying elements to the change in yield strength relative to a pure austenitic lattice. Since this paper focuses on HMnS with the main alloying elements C, Mn, and Al, those elements are assumed to be the main contributors to solid solution strengthening and the contributions of other alloying elements are neglected. It is assumed that this does not lead to a large mistake in calculating σ_{SS} because, apart from Mn and Al, no substitutional alloying element exceeds alloying contents of more than 1 wt. %.

σ_{SRO} is the change in yield strength stemming from the existence of short-range ordered regions in the material. Based on the work of [14], this contribution to yield strength can be calculated as:

$$\sigma_{SRO} = M\tau_{SRO} = M\left(\frac{E_{Order}}{b^3}\right) = M\left(\frac{E_{random} - E_{SRO}}{b^3}\right) \quad (2)$$

where $M = 3.06$ is the Taylor-factor for fcc with $b = \frac{\alpha_\gamma}{\sqrt{2}}$ being the magnitude of the Burgers vector and the lattice parameter in austenite in Å depending on the molar fractions x_i of the alloying elements and temperature in K [38]:

$$\alpha_\gamma = \left(\begin{array}{c} 3.5780 + 0.033x_C + 0.00095x_{Mn} - 0.0002x_{Ni} \\ + 0.0006x_{Cr} + 0.0056x_{Al} + 0.0031x_{Mo} + 0.0018x_V \end{array} \right) \times \left(1 + 2.065 \times 10^{-9} \times (\mathrm{T} - 300)\right) \quad (3)$$

Looking at Equation (3), the temperature dependence of the lattice parameter is assumed to be linear.

σ_{GS} describes the strengthening by grain refinement in accordance with the Hall-Petch effect and can be formulated as:

$$\sigma_{GS} = k_y d^{-1/2} \quad (4)$$

Even though k_y depends on the cooling procedure and the carbon content [39], the value $k_y = 11.3\ \mathrm{MPa\ mm}^{1/2}$ seems to be a reasonable assumption for HMnS in general, based on the findings in the literature [1,2,14,39–41].

As can be seen in Figure 1, one unit cell consists of 14 atoms situated on the lattice positions of the FCC bracket and one central octahedral interstitial site, where a single carbon atom can be situated.

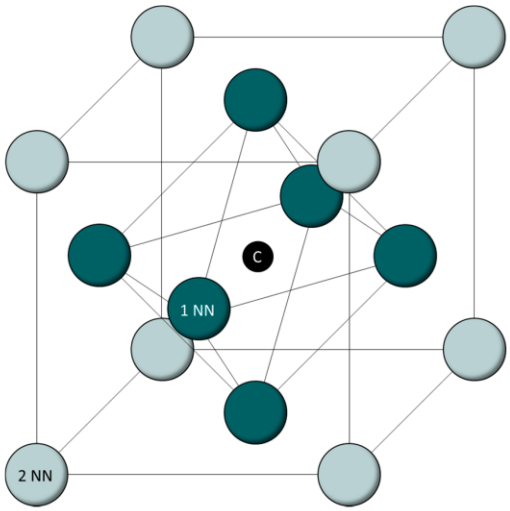


Figure 1. FCC-unit cell with 14 lattice positions for matrix atoms and one central interstitial atom.

First-nearest neighbors (1NN) are the six direct neighbors of the carbon atom. In Figure 1, they are shown in green. Second-nearest neighbors (2NN) in this model are the grey atoms on the corners of the FCC lattice. Although third-nearest neighbors (3NN) can be included in first-principle calculations, a recent study has shown that neither 3NN Al atoms nor 3NN Mn atoms have a positive impact o the ordering energy [33]. To reduce the complexity of the calculations and limit the amount of possible cell configurations, the presence of 3NN alloying atoms is not accounted for in the analysis carried out in this paper. Instead, it is assumed that the material is the sum of FCC-unit cells that do not impact each other. This is obviously not true in reality, but for the purposes of this study, which is aimed at providing a basic model to connect ab initio calculations with experimental results, it is suitable, since it leads to reduced mathematical complexities. The term "cell configuration" is used to describe the combination of alloying atoms and matrix atoms in the cell. "Coordination sphere" is used throughout this paper to refer to the position of atoms relative to the central carbon atom.

The configurations of the cells based on the alloying contents for this 14-cell model are calculated according to [27]:

$$n_{kl} = \frac{14!}{(14 - k - l)!k!l!} \theta_{Fe}^{(14-k-l)} \theta_{Mn}^{k} \theta_{Al}^{l} \quad (5)$$

where n_{kl} is the fraction of all cells that have a configuration with k Mn atoms and l Al atoms with θ_i being the molar fraction of Fe, Mn, and Al, denying the existence of other substitutional alloying elements and ignoring C, since carbon is an interstitial alloying element. Since diffusion rates of substitutional atoms in austenitic steels are very low, it is assumed that the distribution of substitutional elements according to Equation (5) is fixed and that the carbon atom is distributed in accordance with a minimum ordering energy. For clusters of nitrogen and chromium, this approach has been shown to be a realistic approximation, since the presence of nitrogen does not negatively influence the homogeneous distribution of chromium [34]. Cells of type n_{kl} that contain a carbon atom are classified as n_{Ckl}. It should be noted that the assumption that substitutional atoms are distributed according to minimum ordering energies with respect to the presence of a central carbon atom is a very strong assumption, which is unlikely to be true in reality. However, without this assumption, the calculation of ordering energies ΔE_{Ckl} is not possible since ab initio results are presently not available for those unfavorable configurations.

The ordering energy ΔE_{Ckl} of a cell with k Mn atoms, l Al atoms and a central carbon atom is the combination of two energy contributions in comparison to a FCC-unit cell consisting only of Fe atoms and a central interstitial carbon atom. First, the energy required to bring a carbon atom in solution ΔE_{Sol} in a FCC-unit cell with respect to the presence of k Mn atoms and l Al atoms in the first two coordination spheres. The second factor is the change in energy level ΔE_{Lat} resulting from a lattice distortion due to the presence of Mn and Al:

$$\Delta E_{Ckl} = \Delta E_{Sol} + \Delta E_{Lat} \tag{6}$$

Ab initio calculations show that Al is preferentially situated in the second coordination sphere and Mn has a positive effect on the ordering energy level if it sits on a lattice position as a 1NN [22,25,33]. According to those studies, this means that the difference in ordering energy is so profound that the likelihood of a cell configuration that contains 1NN Al atoms instead of 2NN Al atoms or 2NN Mn atoms instead of 1NN Mn atoms is very low. Accordingly, for further calculations in this work and to reduce the model's complexity, it is assumed that for any number of Mn atoms up to six, they will always be 1NN and for any number of Al atoms up to 8, they will always be 2NN.

Using the calculated ordering energies ΔE_{Ckl} from [33], the six cells with the lowest ordering energies are listed in Table 1 and shown in Figure 2.

Table 1. Cell configurations of lowest ordering energy ΔE_{Ckl}.

Cell Name n_{Ckl}	k Mn Atoms	l Al Atoms	ΔE_{Ckl} [eV]
n_{C08}	0	8	−1.2867
n_{C18}	1	8	−1.1524
n_{C28}	2	8	−1.0559
n_{C07}	0	7	−0.9304
n_{C68}	6	8	−0.9287
n_{C38}	3	8	−0.9233

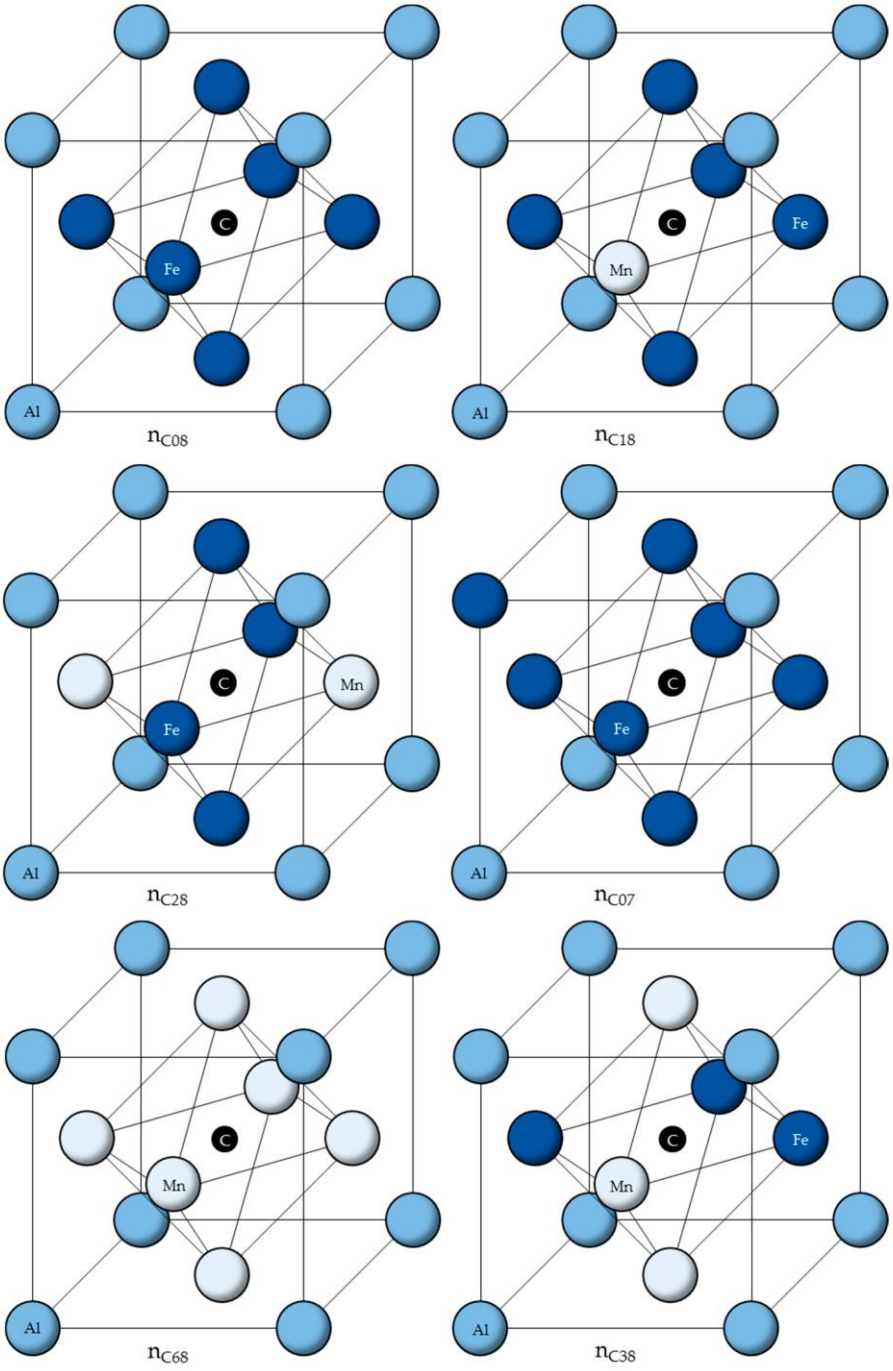


Figure 2. Energetically most favorable cell configurations.

In Equation (2), E_{random} describes the energy state of an unordered alloying system. In this case, a single carbon atom is situated in the central octahedral sites of a randomly chosen FCC-unit cell. This distribution is based on the assumption that there are no preferential octahedral sites, so neither the presence of Mn nor Al influences the position of carbon atoms. Thus, it can be assumed that, for the calculation of E_{random}, the likelihood of the presence of carbon is the same for each type of cell.

Using the random C distribution for E_{random}, E_{random} is calculated according to:

$$E_{random} = \sum_{k=0}^{14} \sum_{l=0}^{14} n_{Ckl,random} \Delta E_{Ckl}, \text{ for } k + l \leq 14 \text{ and } k, l \geq 0 \quad (7)$$

$$n_{Ckl,random} = n_{kl} \times \theta_C \quad (8)$$

Since $\sum n_{kl} = 1$, this method of determining $n_{Ckl,random}$ ensures that carbon is distributed homogeneously in the material, as well as ensuring that every available carbon atom is situated in an octahedral site of a cell.

Contrary to the homogeneous distribution of carbon for E_{random}, the distribution of C for the calculation of E_{SRO} is based on the calculated ordering energies [33]. Since the differences in ordering energy between different cell configurations are significant, as is shown in Table 1, it is assumed that carbon is always situated in the most favorable cell that has not already been assigned a carbon atom. Assuming that at higher temperatures, for example during recrystallization annealing, the diffusion of carbon as an interstitial alloying element is possible, carbon will diffuse to positions with minimal ordering energy in order to minimize the system's Gibbs energy. This means that the cells selected for saturation with carbon are the cells with the lowest ΔE_{Ckl} until $n_{Ckl,SRO} = \theta_C$.

The calculation of ordering energies in the model presented within this work was performed via ab initio simulations based on quantum-mechanical structure optimizations employing density-functional theory (DFT) within the Vienna ab initio Simulation Package (VASP) [33]. The quantum-mechanical structure optimizations are performed based on calculations of lowest-energy states of the electron structure and thus, are conducted at 0 K. Results from ab initio approaches employing DFT have offered good results that are in line with experimental evidence. For example, Mössbauer spectroscopy [17], atom-probe tomography (APT) [42], in situ synchrotron X-ray diffraction measurements [23], and correlative TEM/APT approaches [43] have shown that results from ab initio simulations employing DFT are applicable to systems containing nano-sized κ-carbides that are usually formed during isothermal annealing at temperatures of 600 °C and above. Generally speaking, the effect of temperature changes on the lattice parameter and on intrinsic material properties that derive from electron effects like electrical conductivity is often approximated to be linear [44]. The serrated flow curves of many high-manganese TWIP steels usually occur at temperatures of up to about 200 °C. At higher temperatures, this dynamic strain aging-like effect is either very small or is not detected at all [2,7].

In order to model the temperature dependence of σ_{SRO}, the ab initio results are fitted using a linear approximation of a decrease in σ_{SRO} between 0 K and 500 K. For this purpose, it is assumed that the fact that no serrated flow curve is expected at 500 K can be interpreted as a result of no significant strength increase by short-range ordered clusters.

Based on those assumptions and equations, $\sigma_{Y,calc}$ in MPa was calculated using Equations (2), (3), and (7) for 13 different HMnS with known average grain sizes d_m in µm, listed in Table 2. The alloying contents are given in wt. %.

Table 2. Chemical composition of HMnS used in this study in wt. %; grain size d_m in µm; experimentally determined and calculated yield strength $\sigma_{Y,exp}$ and $\sigma_{Y,calc}$ in MPa, experimental data of alloys marked with * are taken from [14].

Alloy	C	Mn	Al	d_m	$\sigma_{Y,exp}$	$\sigma_{Y,calc}$
X60MnAl17-1	0.56	17.00	1.35	8	328	356
X50MnAl15-1 *	0.49	15.40	1.30	27	294	281
X30MnAl22-1	0.33	22.46	1.21	18	277	275
X30MnAl17-1	0.32	16.80	1.47	17	255	276
X70Mn24	0.71	23.50	0.01	16	334	334
X60Mn23	0.57	23.21	0.01	10	328	334
X50Mn30 *	0.50	30.00	0.00	30	276	273
X50Mn22	0.54	21.95	0.00	14	328	311
X50Mn18 *	0.53	17.90	0.01	8	356	341
X30Mn28	0.28	28.00	0.00	9	291	294
X30Mn23	0.32	22.79	0.01	10	284	291
X30Mn22 *	0.31	22.28	0.00	3	381	384
X30Mn13 *	0.30	12.74	0.01	10	266	274

Experimental yield strength data was taken from the literature [5,14]. Additionally, quasistatic tensile tests have been carried out using a Zwick Z250 tensile testing machine of the AllroundLine by Zwick Roell (Ulm, Germany).

σ_{SS} has been calculated using a linear approximation to explain the differences between experimental and calculated values for the yield strength using the following equation that is a direct result of Equation (1):

$$\sigma_{SS,exp} = \sigma_{Y,exp} - \sigma_{\gamma-Fe} - \sigma_{GS} - \sigma_{SRO} \quad (9)$$

This way, $\sigma_{SS,exp}$ was determined for all steels in Table 2. A regression analysis was performed with respect to the alloying contents of C, Mn, and Al.

The regression analysis lead to the following equation to calculate σ_{SS} with respect to the alloying contents χ_i in weight percent:

$$\sigma_{SS} = 84.55\chi_C + 1.35\chi_{Mn} + 0.44\chi_{Al} \quad (10)$$

Overall, the lattice distortion effect of carbon is by far the strongest contribution to solid solution hardening. This is in accordance with calculations of the misfit of C in an octahedral site using the crystallographic correlation $\frac{r_{OL}}{r_{Fe}} = 0.41$. Comparing the size of the octahedral site to the size of a carbon atom shows that a carbon atom is approximately 8% bigger than the octahedral site, leading to a lattice distortion. Using the lattice parameter calculated according to Equation (3), this size difference can be calculated to approximately 0.03 nm. Comparing this value with the lattice distortion effects by Al and Mn in an austenitic steel according to [45], which are 0.000065 $\frac{nm}{wt.\ \%\ Mn}$ and 0.00095 $\frac{nm}{wt.\ \%\ Al}$ respectively, the difference in contributions between C and Mn and Al in Equation (10) appear to be reasonable.

3. Results and Discussion

Figure 3 shows that the calculations for the yield strength $\sigma_{Y,calc}$ using the proposed model show good agreement with the experimental data.

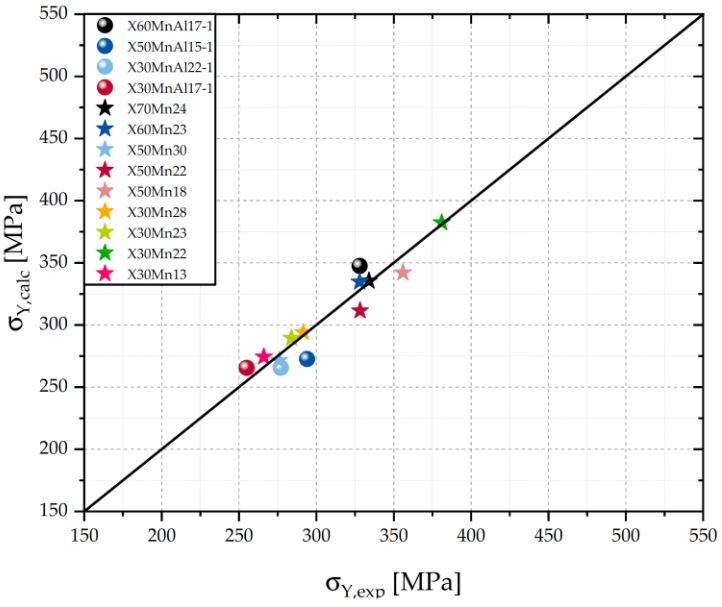


Figure 3. Comparison of calculated and experimental values for σ_Y.

The calculations used in this work lead to differences between $\sigma_{Y,calc}$ and $\sigma_{Y,exp}$ that are smaller than 10%. Those small differences between $\sigma_{Y,calc}$ and $\sigma_{Y,exp}$ might be a result of a negligence of other

alloying elements that participate in solid solution hardening, minor inaccuracies of the measurement of the alloying contents, or d_m.

Since σ_{SRO} can also be understood as a deviation from linear solid solution hardening behavior, a close relationship between σ_{SS} and σ_{SRO} seems logical. Higher alloying contents of C, Mn, and Al lead to a higher solid solution strengthening, but also to more carbon atoms integrated in Mn-C, Al-C, and Mn-Al-C clusters, as well as a higher amount of cells with more Al atoms in the second coordination sphere or Mn atoms in the first coordination sphere according to Equation (5).

The individual contributions of solid solution hardening σ_{SS} and σ_{SRO} are illustrated in Figure 4.

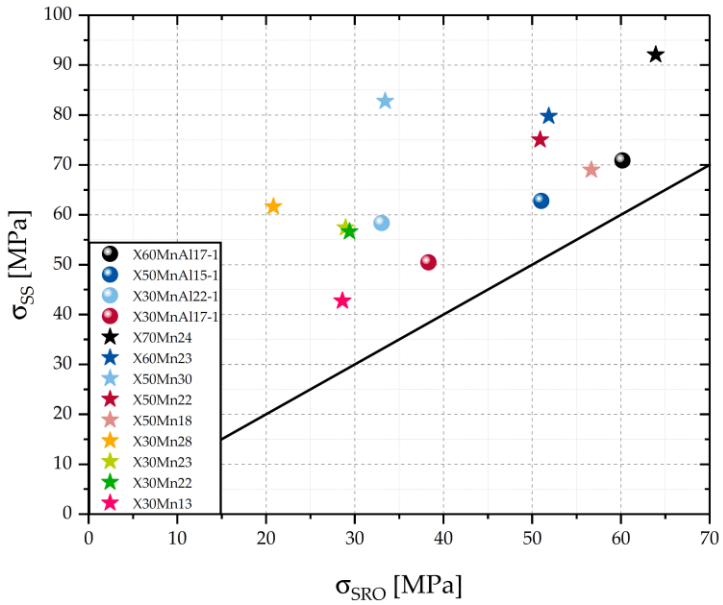


Figure 4. Contributions of σ_{SS} and σ_{SRO} to yield strength.

The strengthening effect of short-range ordered clusters σ_{SRO} is dependent on the chemical composition. For the steel compositions analyzed within the scope of this work, σ_{SRO} at room temperature is approximately in the range of 20 MPa for X30Mn28, containing 0.28 wt. % C and 28.00 wt. % Mn, and 65 MPa for X60MnAl17-1, containing 0.56 wt. % C, 17.00 wt. % Mn, and 1.35 wt. % Al.

Based on Figure 4, one could think, that the connection between σ_{SS} and σ_{SRO} is approximately linear. However, it needs to be kept in mind that the calculation of σ_{SS} is based on linear approximations as well. Additionally, it should be pointed out that although the contribution of σ_{SS} to σ_Y is always greater than that of σ_{SRO}, the proportion between σ_{SS} and σ_{SRO} does not seem to follow a linear trend based on chemical composition. This is illustrated by the line in Figure 4 that represents a relation of $\frac{\sigma_{SS}}{\sigma_{SRO}} = 1$. To further point out the differences in the contributions to σ_Y, the individual contributions of σ_{GS}, σ_{SS}, and σ_{SRO} are portrayed in Figure 5.

According to Figure 5, the contribution of σ_{SRO} to σ_Y is significant. The proportional contribution of σ_{SRO} to σ_Y is in the range of 7.1% for X30Mn28 up to 19.1% for X70Mn24. Since a grain size effect on σ_{SRO} is not assumed in this work, the impact of σ_{SRO} for a given steel composition with larger grain size is higher than for the same steel composition with finer grains. Correspondingly, the proportional contribution of σ_{SRO} that is portrayed in Figure 5 is higher for compositions with larger grains and thus, with smaller grain size strengthening effects σ_{GS}.

The comparison of σ_{SS} and σ_{SRO} for the steels X30Mn13 and X30Mn22 could lead to the conclusion that an increase in Mn content does not significantly influence σ_{SRO}. On the other hand, by comparing X30Mn22 with X30Mn28, it does appear that Mn actually reduces σ_{SRO}. Accordingly, based on these calculations, no clear tendency of the impact of a single alloying element on σ_{SRO} can be found.

For a more detailed analysis, the impact of C and Mn on σ_{SRO} is portrayed in Figures 6 and 7 with regards to the development of σ_{SRO}, σ_{SS}, E_{random}, and E_{SRO} for steels with and without Al.

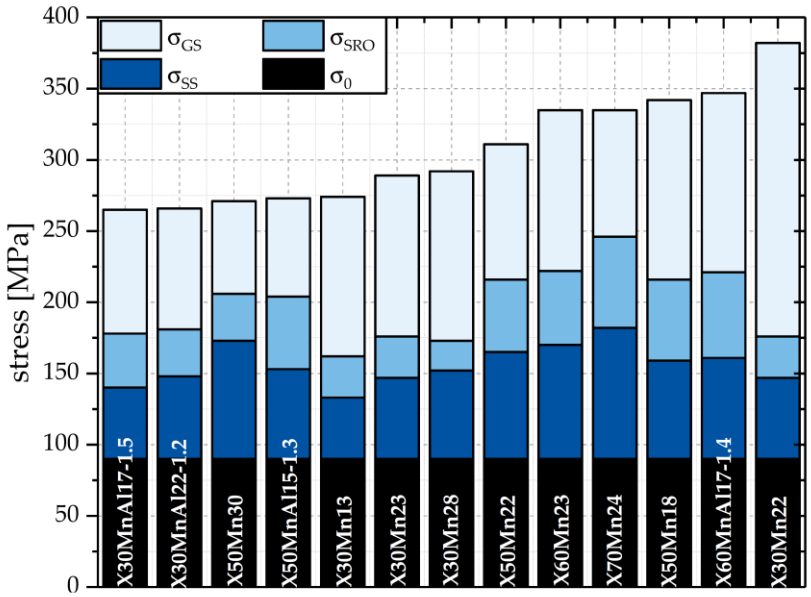


Figure 5. Proportional contribution of σ_{SS}, σ_{SRO}, and σ_{GS} to σ_Y.

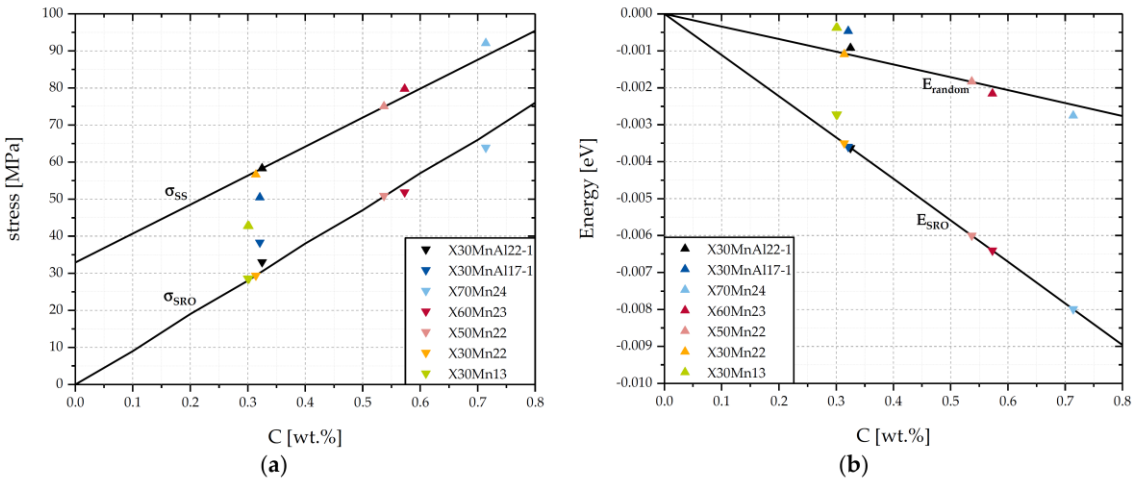


Figure 6. Impact of C on (**a**) σ_{SRO}, σ_{SS}; and (**b**) E_{random} and E_{SRO}.

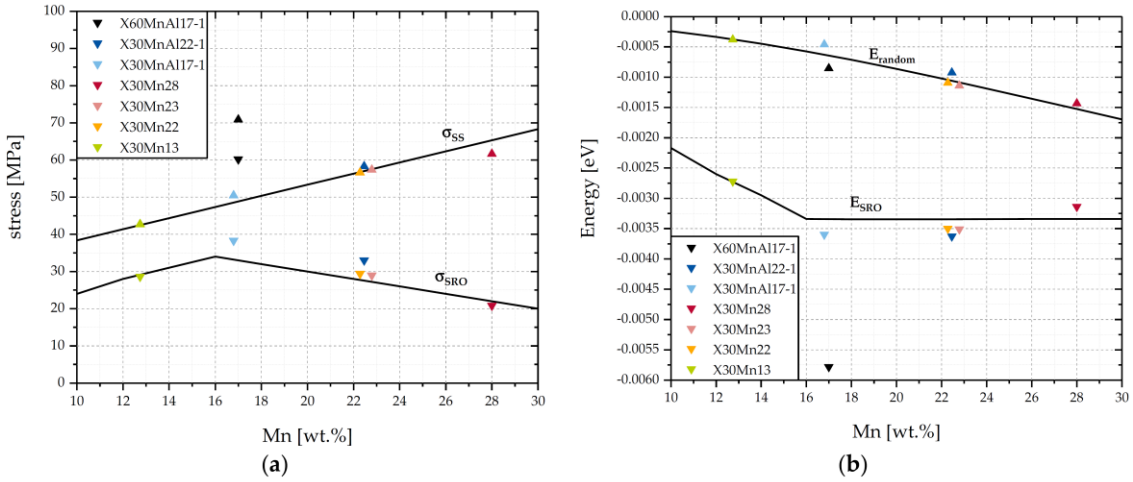


Figure 7. Impact of Mn on (**a**) σ_{SRO}, σ_{SS}; and (**b**) E_{random} and E_{SRO}.

Figure 6 analyzes a steel with a constant Mn content of 22 wt. % with increasing C content from 0.0 wt. % up to 0.8 wt. %. Additionally, seven steels that were studied in this work were selected to illustrate the impact of changes in Mn content and Al content.

According to Figure 6a, σ_{SRO} and σ_{SS} increase approximately linearly with C content. This can be explained by an increasing number of cells with carbon atoms. In theory, this increase in σ_{SRO} will only occur as long as there are cells with a preferential structure available, which leads to a decrease in ordering energy E_{SRO}, as can be seen in Figure 6b. If no preferential cells were available, C atoms would have to be situated in non-preferential cells with $\Delta E_{Ckl} > 0$ eV. To a small degree, this effect is included in the calculation of E_{random} because C is assumed to be homogeneously distributed among all cells, including those with positive and, thus, unfavorable values of ΔE_{Ckl}. This explains the lower rate of decrease of E_{random} in Figure 6b compared to E_{SRO}. However, σ_{SRO} will always remain positive because, according to Equation (2), as long as E_{random} is bigger than E_{SRO}, σ_{SRO} will be positive. This premise is always fulfilled by using the assumption in this work, that carbon will be situated in the cells of lowest possible ordering energy first and that the distribution of alloying elements for the calculation of E_{random} and E_{SRO} is the same.

Looking at Figure 6a, the steels with Al, X30MnAl22-1 and X30MnAl17-1, show positive deviations for the calculated values of σ_{SRO} and X30MnAl17-1 shows a negative deviation for σ_{SS}. In the case of solid solution strengthening for X30MnAl17-1, this can be explained by the low Mn content of 16.80 wt. % compared to the 22.00 wt. % used as a basis of calculation of σ_{SS} in Figure 6. Accordingly, X70Mn24 and X60Mn23 show slightly higher values for than σ_{SS} it would be the case for 22.00 wt. % Mn.

The increase of σ_{SRO} can be explained by the impact of the introduction of new cell configurations containing Al atoms. According to Table 1, n_{C08} is the lowest possible energy configuration. However, since the Al content of the steels in this study is very low, only very few cells with the configuration n_{C08} are available. The majority of Al atoms is in cells also containing Mn atoms. According to [33], the introduction of Al atoms as a 2NN into cells with Mn atoms as 1NN does not necessarily lead to a lower ordering energy, but is rather dependent of the number of 1NN Mn atoms. The molar fraction of Mn in a steel containing 22 wt. % Mn obviously depends on the wt. % of the other alloying elements. For the X30MnAl22-1, the molar fraction of Mn is approximately 0.23. According to Equation (5), the most common cell configuration is expected to be n_{30}. The ordering energy of the cell configuration n_{C30} is $\Delta E_{C30} = -0.0501$ eV. This means that this cell configuration is preferential to a pure iron FCC-unit cell. Increasing the number of Al atoms in this cell configuration to 1 and 2 respectively results in $\Delta E_{C31} = -0.0082$ eV and $\Delta E_{C32} = 0.0338$ eV. Both cell configurations are not preferential with respect to n_{C30} which according to previous assumptions means that the cells n_{C31} and

n_{C32} will not contain a carbon atom as long as there are other more preferential cell configurations like n_{30} that do not already contain a carbon atom. In turn, E_{SRO} will not be negatively influenced by cell configurations like n_{C31} and n_{C32}. However, E_{random} will include the negative impact of unfavorable cell configurations which will lead to an increase of E_{random} and a total increase of σ_{SRO}.

Overall, it can be said that the positive impact of Al on σ_{SRO} is a result of an introduction of favorable cell configurations containing Al atoms that inhibit a carbon atom and the avoidance of cell configurations of unfavorable cell configurations.

Figure 7 analyzes a steel with a constant C content of 0.3 wt. % with increasing Mn content from 10 wt. % up to 30 wt. %. Seven steels with varying Al and C content were added to the diagram.

Contrary to the impact of C that is documented in Figure 6, a local maximum of σ_{SRO} at approximately 16 wt. % Mn is observed. Looking at Figure 7b, this can be explained by the stagnation of E_{SRO} for Mn contents of 16 wt. % and higher. At the same time, E_{random} is decreasing, leading to a smaller difference between E_{random} and E_{SRO} and accordingly to a lower σ_{SRO}.

The stagnation of E_{SRO} can be explained by considering the method of calculation for σ_{SRO}. For Al-free steels, the energetically optimal cell is n_{60}. As long as $\theta_C < n_{C60}$, an increase in the amount of C atoms will decrease E_{SRO}. This is due to the underlying assumption that C atoms will be situated in preferential cells of lowest possible ordering energy. At $\theta_C = n_{C60}$, all C atoms are situated in cells of optimal configuration and thus, E_{SRO} is minimized. Due to the way E_{random} is calculated in Equation (7), E_{random} continues to decrease at $\theta_C > n_{C60}$. As a result, σ_{SRO} decreases.

In accordance with Figure 6a, Figure 7a shows that additions of Al and C increase σ_{SRO} significantly.

The contribution of solid solution hardening σ_{SS} increases linearly with the Mn and C content, as it is to be expected considering Equation (10).

To conclude, unlike for the addition of C, Mn additions do not always increase σ_{SRO}. This is a result of a stagnation of E_{SRO} because of a saturation of preferential cells with carbon. In theory, the same effect should be noticeable for C and Al, as well. However, because of the comparably low alloying contents of those elements, it is very unlikely that a point of saturation will be reached in common alloys.

This decrease in σ_{SRO} can be understood as the impact of the deviation from linear solid solution hardening. If the ratio of Mn atoms to Fe atoms becomes increasingly larger and the amount of cells with randomly-distributed Mn increases, the impact of an actual ordering of Mn decreases since fewer cells are brought into short-range ordering to minimize the ordering energy.

Overall, the change of E_{Order} with varying contents of alloying elements can be understood as the effectiveness of an alloy addition of those elements with respect to the increase in strength by short-range ordering. Since it is assumed that σ_{SS} follows a linear trend and σ_{GS} is fixed, $\left|\frac{\delta E_{Order}}{\delta X_i}\right|$ is an indicator for the effectiveness of an addition of an alloying element. A higher $\left|\frac{\delta E_{Order}}{\delta X_i}\right|$ means a greater efficiency in employing an addition of the alloying element i. Looking at Figures 6 and 7, C and Al both appear to be more efficient than Mn in increasing the yield strength by short-range ordering.

In order to compare the accuracy of the model used in this work to calculate σ_Y with other descriptive models, $\sigma_{Y,model}$ according to models by Pickering [15], Lorenz [15], Bouaziz [11], De Cooman [2], and Choi [46] has been calculated. The equations used for $\sigma_{Y,model}$ are listed in Table 3. The coefficients used for the alloying contents are in $\frac{\text{MPa}}{\text{wt. \%}}$, coefficients for grain size influence are in $\text{MPam}^{0.5}$ unless stated otherwise. It needs to be pointed out that although all of the models are for austenitic steels, only the models of Bouaziz, De Cooman, and Choi are specifically for HMnS. Additionally, some of the models include coefficients for the Hall-Petch effect while others neglect them. In order to be able to compare the models, the grain size effect has been calculated according to Equation (4) and added to the model calculations of Choi and Bouaziz.

Table 3. Solid solution hardening models in the literature.

Model	$\sigma_{Y,model}$
Pickering	$68 + 493N + 354C + 3.7Cr + 14Mo + 20Si + 0.22d^{-1/2}$
Lorenz	$40 + 450N + 525C + 2Mn + 8.4Cr + 22Mo + 5Cu + 0.77d^{-1/2}$
Bouaziz	$228 + 137C - 2Mn + \sigma_{GS}$
De Cooman	$189 + 413/\sqrt{(d[\mu m])}$
Choi	$97 + 279C - 1.5Mn + 49.6Si + 20.5Al + \sigma_{GS}$

Figure 8 compares $\sigma_{Y,model}$ with $\sigma_{Y,calc}$ and $\sigma_{Y,exp}$.

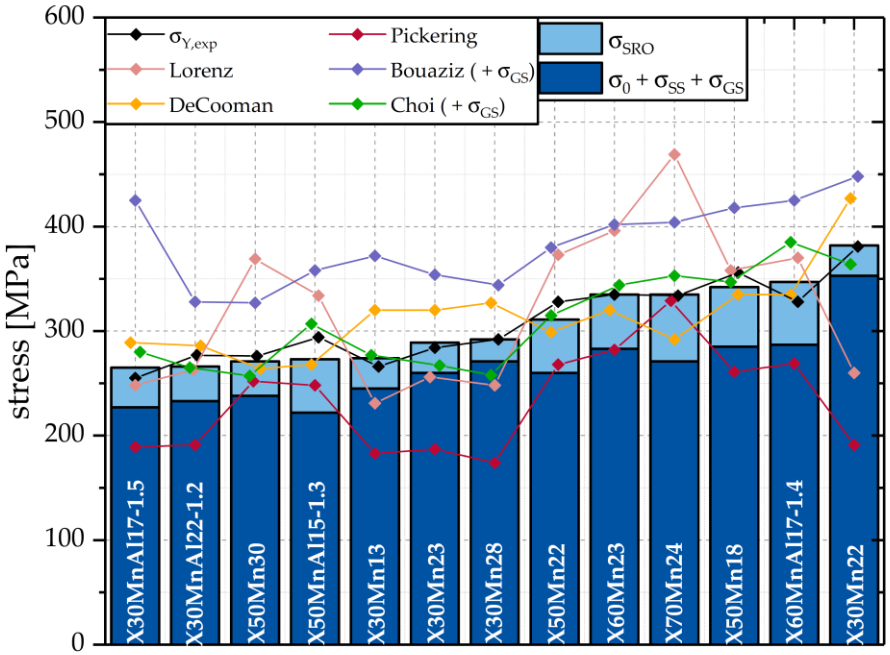


Figure 8. Comparison of models of σ_Y for the steels used in this paper.

Due to the difference in the steel concepts those models were developed for, significant deviations from $\sigma_{Y,exp}$ can be seen. Those deviations are a result of a focus on other alloying elements. For example, Pickering does not consider the impact of Mn on yield strength. Nevertheless, the models of Choi [46] and De Cooman [2] offer reasonable results, but are not as close to the experimental data as the model developed in this work. Additionally, the model by De Cooman does not take compositional variances into account, while the model of Choi considers the impact of Mn on yield strength to be negative.

The models of Pickering and Lorenz are not applicable to HMnS based on the results of the calculations. The model by Bouaziz tends to overestimate the yield strength.

4. Conclusions

A basic ab initio-based model for the calculation of σ_Y has been developed. The model shows good agreement with the experimental values. Discrepancies between experimental $\sigma_{Y,exp}$ and calculation results $\sigma_{Y,calc}$ are smaller than 10%. While many complexity-reducing assumptions have been made that lead to inaccuracies when calculating σ_{SRO}, this model portrays that the general concept of combining ab initio simulations with experimental data can lead to feasible results on a macroscopic scale. This is also shown by the calculated positive impact of Mn and Al on yield strength by solid solution strengthening in a reasonable range.

The impact of the alloying content of C, Mn, and Al on the strengthening by short-range ordering was analyzed. For the given steel compositions with fully austenitic microstructures in this work,

the values for σ_{SRO} are as high as approximately 65 MPa. This significant strengthening leads to a proportional contribution to σ_Y of nearly 20%.

While an increase in C and Al increases σ_{SRO} as long as a sufficient number of atoms of substitutional alloying elements are available to form preferential cell structures, a limiting factor for the effectiveness of strength increases by Mn was found.

The impact of short-range ordered clusters during deformation needs to be evaluated. A higher amount of more stable, energetically favorable clusters might not only lead to an increase in σ_{SRO} and σ_Y, it might also impact the beginning of serrations in the flow curve, as well as their amplitude if the serrations are resulting from short-distance carbon atom jumps associated with the cutting of clusters.

Acknowledgments: The authors are thankful for the financial support from Deutsche Forschungsgemeinschaft (DFG) within the Project C2: "Material Properties of High Mn-Steels" of the Collaborative Research Centre (SFB) 761 "Steel-ab initio". The provision of experimental data by Sebastian Wesselmecking (Steel Institute, RWTH Aachen University) is very much appreciated as well as the provision of ab initio calculation results by Dronskowski, Tobias Timmerscheidt, and Dmitri Bogdanovski (Department of Inorganic Chemistry, RWTH Aachen University) of Project A1: "ab initio Quantum chemistry of the Fe-Mn-C system" of SFB 761 "Steel-ab initio".

Author Contributions: Simon Sevsek analyzed the data. Simon Sevsek and Wolfgang Bleck wrote the paper.

Conflicts of Interest: The authors declare no conflict of interest.

References

1. De Cooman, B.C.; Kwon, O.; Chin, K.-G. State-of-the-knowledge on TWIP steel. *Mater. Sci. Technol.* **2012**, *28*, 513–527. [CrossRef]
2. De Cooman, B.C. High Mn TWIP steel and medium Mn steel. In *Automotive Steels: Design, Metallurgy, Processing and Applications*, 1st ed.; Rana, R., Singh, S.B., Eds.; Woodhead Publishing: Cambridge, UK, 2017; pp. 317–385. ISBN 9780081006382.
3. Haase, C.; Ingendahl, T.; Güvenc, O.; Bambach, M.; Bleck, W.; Molodov, D.A.; Barrales-Mora, L.A. On the applicability of recovery-annealed Twinning-Induced Plasticity steels: Potential and limitations. *Mater. Sci. Eng. A* **2016**, *649*, 74–84. [CrossRef]
4. Abbasi, A.; Dick, A.; Hickel, T.; Neugebauer, J. First-principles investigation of the effect of carbon on the stacking fault energy of Fe–C alloys. *Acta Mater.* **2011**, *59*, 3041–3048. [CrossRef]
5. Bouaziz, O.; Zurob, H.; Chehab, B.; Embury, J.D.; Allain, S.; Huang, M. Effect of chemical composition on work hardening of Fe–Mn–C TWIP steels. *Mater. Sci. Technol.* **2011**, *27*, 707–709. [CrossRef]
6. Tewary, N.K.; Ghosh, S.K.; Chatterjee, S. Effect of Al Content in Low Carbon High Manganese TWIP Steel. *Key Eng. Mater.* **2016**, *706*, 16–22. [CrossRef]
7. Bäumer, A.; Jimenez, J.A.; Bleck, W. Effect of temperature and strain rate on strain hardening and deformation mechanisms of high manganese austenitic steels. *Int. J. Mater. Res.* **2010**, *101*, 705–714. [CrossRef]
8. Choi, K.; Seo, C.-H.; Lee, H.; Kim, S.K.; Kwak, J.H.; Chin, K.G.; Park, K.-T.; Kim, N.J. Effect of aging on the microstructure and deformation behavior of austenite base lightweight Fe–28Mn–9Al–0.8C steel. *Scr. Mater.* **2010**, *63*, 1028–1031. [CrossRef]
9. Gutierrez-Urrutia, I.; Raabe, D. Microbanding mechanism in an Fe–Mn–C high-Mn twinning-induced plasticity steel. *Scr. Mater.* **2013**, *69*, 53–56. [CrossRef]
10. Liu, F.; Dan, W.J.; Zhang, W.G. Strain hardening model of TWIP steels with manganese content. *Mater. Sci. Eng. A* **2016**, *674*, 178–185. [CrossRef]
11. Bouaziz, O.; Allain, S.; Scott, C.P.; Cugy, P.; Barbier, D. High manganese austenitic twinning induced plasticity steels: A review of the microstructure properties relationships. *Curr. Opin. Solid State Mater. Sci.* **2011**, *15*, 141–168. [CrossRef]
12. Bouaziz, O. Strain-hardening of twinning-induced plasticity steels. *Scr. Mater.* **2012**, *66*, 982–985. [CrossRef]
13. Ohkubo, N.; Miyakusu, K.; Uematsu, Y.; Kimura, H. Effect of Alloying Elements on the Mechanical Properties of the Stable Austenitic Stainless Steel. *ISIJ Int.* **1994**, *34*, 764–772. [CrossRef]
14. Kang, J.-H.; Ingendahl, T.; von Appen, J.; Dronskowski, R.; Bleck, W. Impact of short-range ordering on yield strength of high manganese austenitic steels. *Mater. Sci. Eng. A* **2014**, *614*, 122–128. [CrossRef]
15. Sieurin, H.; Zander, J.; Sandström, R. Modelling solid solution hardening in stainless steels. *Mater. Sci. Eng. A* **2006**, *415*, 66–71. [CrossRef]

16. Oda, K.; Fujimura, H.; Ino, H. Local interactions in carbon-carbon and carbon-M (M: Al, Mn, Ni) atomic paris in FCC gamma-iron. *J. Phys. Condens. Matter* **1994**, *6*, 679–692. [CrossRef]
17. Bentley, A.P. Ordering in Fe–Mn–Al–C austenite. *J. Mater. Sci. Lett.* **1986**, *5*, 907–908. [CrossRef]
18. McLellan, R.B.; Dunn, W.W. A quasi-chemical treatment of interstitial solid solutions: It application to carbon austenite. *J. Phys. Chem. Solids* **1969**, *30*, 2631–2637. [CrossRef]
19. Pelton, A.D.; Kang, Y.-B. Modeling short-range ordering in solutions. *Int. J. Mater. Res.* **2007**, *98*, 907–917. [CrossRef]
20. Honeycombe, R.W.K. The effect of temperature and alloying additions on the deformation of metal crystals. *Progress Mater. Sci.* **1961**, *9*, 95–120. [CrossRef]
21. Oda, K.; Kondo, N.; Shibata, K. X-ray Absorption Fine Structure Analysis of Interstitial (C, N)-Substitutional (Cr) Complexes in Austenitic Stainless Steels. *ISIJ Int.* **1990**, *30*, 625–631. [CrossRef]
22. Von Appen, J.; Dronskowski, R. Carbon-Induced Ordering in Manganese-Rich Austenite—A Density-Functional Total-Energy and Chemical-Bonding Study. *Steel Res. Int.* **2011**, *82*, 101–107. [CrossRef]
23. Song, W.; Zhang, W.; von Appen, J.; Dronskowski, R.; Bleck, W. k-Phase Formation in Fe–Mn–Al–C Austenitic Steels. *Steel Res. Int.* **2015**, *86*, 1161–1169. [CrossRef]
24. Raabe, D.; Roters, F.; Neugebauer, J.; Gutierrez-Urrutia, I.; Hickel, T.; Bleck, W.; Schneider, J.M.; Wittig, J.E.; Mayer, J. Ab initio-guided design of twinning-induced plasticity steels. *MRS Bull.* **2016**, *41*, 320–325. [CrossRef]
25. Medvedeva, N.I.; Park, M.S.; van Aken, D.C.; Medvedeva, J.E. First-principles study of Mn, Al and C distribution and their effect on stacking fault energies in fcc Fe. *J. Alloys Compd.* **2014**, *582*, 475–482. [CrossRef]
26. Timmerscheidt, T.; Dey, P.; Bogdanovski, D.; von Appen, J.; Hickel, T.; Neugebauer, J.; Dronskowski, R. The Role of κ-Carbides as Hydrogen Traps in High-Mn Steels. *Metals* **2017**, *7*, 264. [CrossRef]
27. McLellan, R.B. Cell models for interstitial solid solutions. *Acta Metall.* **1982**, *30*, 317–322. [CrossRef]
28. Bhadeshia, H.K.D.H. Diffusion of carbon in austenite. *Met. Sci.* **1981**, *15*, 477–479. [CrossRef]
29. McLellan, R.B.; Ko, C. The C–C interaction energy in iron-carbon solid solutions. *Acta Metall.* **1987**, *35*, 2151–2156. [CrossRef]
30. McLellan, R.B.; Ko, C. The diffusion of carbon in austenite. *Acta Metall.* **1988**, *36*, 531–537. [CrossRef]
31. Gholizadeh, H.; Draxl, C.; Puschnig, P. The influence of interstitial carbon on the g-surface in austenite. *Acta Metall.* **2013**, *61*, 341–349. [CrossRef]
32. Lee, S.-J.; Kim, J.; Kane, S.N.; DeCooman, B.C. On the origin of dynamic strain aging in twinning-induced plasticity steels. *Acta Metall.* **2011**, *59*, 6809–6819. [CrossRef]
33. Timmerscheidt, T.; Dronskowski, R. An Ab Initio Study of Carbon-Induced Ordering in Austenitic Fe–Mn–Al–C Alloys. *Steel Res. Int.* **2017**, *88*, 1–10. [CrossRef]
34. Sumin, V.V.; Chimid, G.; Rashev, T.; Saryivanov, L. The Neutron-Spectroscopy Proof of the Strong Cr–N Interactions in Nitrogen Stainless Steels. *Mater. Sci. Forum* **1999**, *318–320*, 31–40. [CrossRef]
35. Bouaziz, O.; Barbier, D. Benefits of Recovery and partial Recrystallization of Nano-Twinned Austenitic Steels. *Adv. Eng. Mater.* **2013**, *15*, 976–979. [CrossRef]
36. Fiore, N.F.; Bauer, C.L. Binding of solute atoms to dislocations. *Progress Mater. Sci.* **1968**, *13*, 85–134. [CrossRef]
37. Butt, M.Z.; Feltham, P. Solid-solution hardening. *J. Mater. Sci.* **1993**, *28*, 2557–2576. [CrossRef]
38. Saeed-Akbari, A.; Imlau, J.; Prahl, U.; Bleck, W. Derivation and Variation in Composition-Dependent Stacking Fault Energy Maps Based on Subregular Solution Model in High-Manganese Steels. *Metall. Mater. Trans. A* **2009**, *40*, 3076–3090. [CrossRef]
39. Kang, J.-H.; Duan, S.; Kim, S.-J.; Bleck, W. Grain Boundary Strengthening in High Mn Austenitic Steels. *Metall. Mater. Trans. A* **2016**, *47*, 1918–1921. [CrossRef]
40. Kang, S.; Jung, Y.-S.; Jun, J.-H.; Lee, Y.-K. Effects of recrystallization annealing temperature on carbide precipitation, microstructure and mechanical properties in Fe–18Mn–0.6C–1.5Al TWIP steel. *Mater. Sci. Eng. A* **2010**, *527*, 745–751. [CrossRef]
41. De las Cuevas, F.; Reis, M.; Ferraiuolo, A.; Pratolongo, G.; Karjalainen, L.P.; Alkorta, J.; Gil Sevillano, J. Hall-Petch relationship of a TWIP steel. *Key Eng. Mater.* **2010**, *423*, 147–152. [CrossRef]
42. Bartlett, L.N.; van Aken, D.C.; Medvedeva, J.; Isheim, D.; Medvedeva, N.I.; Song, K. An Atom Probe Study of Kappa Carbide Precipitation and the Effect of Silicon Addition. *Metall. Mater. Trans. A* **2014**, *45*, 2421–2435. [CrossRef]

43. Yao, M.J.; Welsch, E.; Ponge, D.; Haghighat, S.; Sandlöbes, S.; Choi, P.; Herbig, M.; Bleskov, I.; Hickel, T.; Lipinska-Chwalek, M.; et al. Strengthening and strain hardening mechanisms in a precipitation-hardened high-Mn lightweight steel. *Acta Mater.* **2017**, *140*, 258–273. [CrossRef]
44. Gottstein, G. *Physikalische Grundlagen der Materialkunde*, 3rd ed.; Springer: Berlin/Heidelberg, Germany, 2007; ISBN 978-3-540-71104-9.
45. Li, M.; Chang, H.; Kao, P.; Gan, D. The effect of Mn and Al contents on the solvus of κ phase in austenitic Fe–Mn–Al–C alloys. *Mater. Chem. Phys.* **1999**, *59*, 96–99. [CrossRef]
46. Choi, W.S.; de Cooman, B.C.; Sandlöbes, S.; Raabe, D. Size and orientation effects in partial dislocation-mediated deformation of twinning-induced plasticity steel micro-pillars. *Acta Mater.* **2015**, *98*, 391–404. [CrossRef]



© 2018 by the authors. Licensee MDPI, Basel, Switzerland. This article is an open access article distributed under the terms and conditions of the Creative Commons Attribution (CC BY) license (http://creativecommons.org/licenses/by/4.0/).

Chapter III

Combined deformation twinning and short-range ordering causes serrated flow in high-manganese steels

S. Sevsek, F. Brasche, C. Haase and W. Bleck
Materials Science & Engineering A 746 (2019) 434-442
https://doi.org/10.1016/j.msea.2019.01.042

Chapter III elaborates on the impact of short-range ordering on the deformation behaviour in two high-manganese TWIP/TRIP steels. Special scope is the analysis of the isolated impact of short-range ordering and deformation twinning on the occurrence of serrated flow. To this end, targeted heat treatments are used to generate partially-recrystallized and recovery-annealed material states in addition to fully recrystallized initial microstructures. Experimental data from quasi in-situ electron backscatter diffraction experiments during interrupted tensile tests suggests that the suppression of serrated flow in the recrystallized, Al-alloyed high-manganese TWIP/TRIP steel is due to a partly suppression of the secondary deformation mechanism. A multi-scale model is introduced, highlighting the critical importance of both the activation of secondary deformation mechanisms as well as a sufficiently homogeneous microstructure that enables the propagation of localized stress peaks in heavily-twinned grains.

Contents lists available at ScienceDirect

Materials Science & Engineering A

journal homepage: www.elsevier.com/locate/msea

Combined deformation twinning and short-range ordering causes serrated flow in high-manganese steels

Simon Sevsek[a,*], Frederike Brasche[b], Christian Haase[a], Wolfgang Bleck[a]

[a] Steel Institute, RWTH Aachen University, Intzestraße 1, 52072 Aachen, Germany
[b] Institute of Physical Metallurgy and Metal Physics, RWTH Aachen University, Kopernikusstraße 14, 52074 Aachen, Germany

ARTICLE INFO

Keywords:
Twinning-induced plasticity
Short-range ordering
High-manganese steel
Serrated flow

ABSTRACT

The isolated impact of deformation twinning and short-range ordering on the serrated flow phenomena in two high-manganese twinning-induced plasticity steels, an X60Mn18 and an X30MnAl17-1 alloy, was studied via quasistatic tensile tests at room temperature and at 150 °C. In order to identify the effect of prior deformation twins, both alloys were investigated in recrystallized and non-recrystallized states. The experimental data suggest that the inhibition of the movement of trailing partial dislocations by short-range ordered clusters results in a promotion of deformation twinning. A multi-scale model is introduced to connect short-range ordering theory, deformation twinning, the formation and propagation of deformation bands and the occurrence of serrated flow.

1. Introduction

High-manganese steels (HMnS) containing more than 15 wt% Mn exhibit significant potential for widespread use in sheet applications in various industries due to their excellent combination of high strength and high ductility [1–7]. This combination is a result of the material's ability to develop very high dislocation densities in combination with the activation of additional deformation mechanisms, such as deformation-induced twinning (TWinning Induced Plasticity – TWIP effect) and/or deformation-induced phase transformation (TRansformation Induced Plasticity – TRIP effect) [4,8–10]. The activation of the respective deformation mechanisms is guided by the steel's stacking fault energy (SFE), which depends on various factors such as the chemical composition and deformation temperature [11,12]. At room temperature (RT), the TWIP effect is usually activated at SFE values in the range of 12–55 mJ/m^2, while the TRIP effect prevails below 18 mJ/m^2. Both deformation twins and martensite laths act as obstacles to the movement of dislocations, reducing the effective mean free path (MFP) and resulting in a so-called dynamic Hall-Petch effect [1,13–16]. At SFE values above 55 mJ/m^2, deformation twinning is suppressed, and plastic deformation is accommodated by planar dislocation glide, which leads to a high density of glide bands. This effect is usually referred to as MicroBand-Induced Plasticity (MBIP) or Slip band Refinement-Induced Plasticity (SRIP) [17].

One aspect that is potentially detrimental to sheet forming processes of HMnS in industrial applications is the occurrence of localized deformation phenomena at room temperature which result in serrated flow curves. The addition of Al is reported to suppress this effect at room temperature. However, at elevated temperatures, serrated flow has also been observed in Al-alloyed HMnS [18–26].

There are several theories related to serrated flow in HMnS. Some of them focus on the energetically favourable positions of C atoms in short-range ordered (SRO) clusters, enabling short-range (SR) jumps of C atoms into preferential octahedral positions [27–29]. Other theories point to deformation twinning as an important mechanism responsible for the serrated flow [18,30]. For instance, Lee et al. [27] argue that C atoms get rearranged into octahedral positions out of the stacking fault plane due to SR jumps. This phenomenon occurs when energetically favourable C-Mn clusters are sheared by the movement of the leading partial dislocation of a stacking fault. Kang et al. [28] agree that the destruction of SRO clusters by passing dislocations could lead to a significant glide plane softening that leads to an enhancement of planar glide and a stress plateau in the flow curve. Furthermore, Allain et al. [18] argue that dynamic interactions between solute C atoms and dislocations could also inhibit dislocation glide because of lattice friction effects, which could promote deformation twinning. Koyama et al. [30] also relate their findings to serrated flow, citing the trapping of slowly moving partial dislocations by C atoms as a promoting factor for deformation twinning.

So far, there is no clear consensus on the mechanism responsible for serrated flow. However, the established theories point to a dislocation pinning effect, either by C-Mn SRO clusters or solute C atoms that

* Corresponding author.
E-mail address: simon.sevsek@iehk.rwth-aachen.de (S. Sevsek).

https://doi.org/10.1016/j.msea.2019.01.042
Received 2 October 2018; Received in revised form 22 December 2018; Accepted 10 January 2019
Available online 11 January 2019
0921-5093/ © 2019 Elsevier B.V. All rights reserved.

causes an increased stacking fault separation width w_{SF}. This effect may promote deformation twinning [1,18,27,28,30].

The aim of the present study is to investigate the influence of SRO clusters and deformation twins on the occurrence of serrated flow. To analyse the effect of SR jumps by C atoms into preferential positions in SRO clusters with respect to different chemical compositions and temperature, an X60Mn18 without Al addition and an X30MnAl17-1 alloy containing Al were tested in quasistatic tensile tests at RT and at 150 °C. The upper temperature limit of 150 °C was selected based on the assumption that dynamic recovery processes can be neglected at this temperature. In order to isolate the impact of deformation twinning, the X30MnAl17-1 steel was tested in fully-recrystallized state, i.e. without deformation twins prior to tensile testing, and in recovery-annealed[1] state, i.e. with deformation twins retained from cold-rolling. Furthermore, the influence of grain size and microstructural heterogeneity on serrated flow will be discussed based on the behaviour of the X60Mn18 steel in a partially-recrystallized condition.

2. Experimental methods

The X60Mn18 alloy was strip-cast using a double-roller device with the as-cast thickness of roughly 3 mm followed by in-line hot rolling with a thickness reduction of approximately 20–30% to a strip thickness of 2.2 mm. Afterwards, the strip was cold rolled to a final thickness of 1.1 mm (reduction of 50%). The X30MnAl17-1 alloy was ingot-cast (dimension 140 × 140 × 500 mm^3) with a subsequent homogenization annealing at 1150 °C for 5 h and hot forging at 1150 °C that decreased height and width from 140 mm to 55 mm, followed by an additional homogenization annealing at 1150 °C for 2 h and hot rolling to a sheet thickness of 2.2 mm. Afterwards, the sheet thickness was further reduced by 50% during cold rolling to a final thickness of 1.1 mm. Tensile test specimens with 30 mm initial gauge length and 6 mm gauge width were machined using water jet cutting, followed by mechanical grinding of the samples to guarantee a smooth surface. The tensile axis was perpendicular to the rolling direction (RD). Heat treatments of the specimens were performed in a salt bath furnace to minimize decarburization and oxidation effects during annealing. The heat treatments for the fully-recrystallized (designation RX), partially-recrystallized (designation pRX) and recovery-annealed (designation REC) material states are listed in Table 1 in addition to the chemical compositions of the two HMnS, the respective SFE values at RT and at 150 °C as well as the average grain sizes d_{avg} (in RX-states).

To calculate the temperature-dependent SFE values of both alloys, a subregular solution thermodynamic model was used [36]. At RT, the SFEs of both alloys are very similar and indicate the activation of TRIP and TWIP deformation modes. At 150 °C, the increase in SFE promotes the suppression of the TRIP effect and deformation twinning is predicted to be the predominant secondary deformation mechanism [1].

Quasistatic tensile tests were conducted using a Z250 tensile testing machine by ZwickRoell that was equipped with a contact-type extensometer MultiXtens to measure strain. The strain rate from the beginning of the test until a plastic deformation of 0.2% was kept constant at 0.00025 1/s. At higher strains, the strain rate was increased over a duration of 10 s to a constant strain rate of 0.001 1/s until fracture. A heating chamber setup was employed to perform tensile testing at a temperature of 150 °C.

Electron backscatter diffraction (EBSD) measurements were performed using a Zeiss Sigma scanning electron microscope (SEM) at acceleration voltages of 15 kV and working distances between 10 mm and 20 mm. A step size of 70 nm was used in order to allow for a high effective spatial resolution of the EBSD system. Additionally, a larger overview of the microstructure has been measured in the EBSD maps in Fig. 6, using a step size of 150 nm. The samples were ground with subsequent mechanical polishing using a water-based diamond suspension and finished by electropolishing with 22 V for 20 s, using an electrolyte containing 700 ml ethanol (C_2H_5OH), 100 ml butyl glycol ($C_6H_{14}O_2$) and 78 ml perchloric acid (60%) ($HClO_4$).

The evolution of deformation twins was investigated using quasi in-situ EBSD measurements of the same surface area after interrupted tensile tests in the parallel gauge length of tensile specimens with a reduced gauge length of 12 mm. Post-processing was performed using the *HKL* Channel 5 software and the MATLAB-based MTEX toolbox [37,38]. The post-processing included the removal of wild spikes and a careful noise reduction that considered at least five neighbouring data points. The approximation of twin volume fractions (TVF) was conducted using the image-analysis program ImageJ [39], which was employed in calculating the area fraction of highlighted Σ3-boundaries and relevant, manually coloured grey-level variations in the Image Quality (IQ) maps, which are commonly referred to as deformation twins or twin bundles that are too thin to show individual orientations in EBSD measurements [40,41]. The identification of deformation twins based on grey-level variations was performed by following a multi-step analysis process. The process was used to minimize the chance of misidentifying local deviations in EBSD detection rate as deformation twins. Local deviations could also occur due to poor surface quality of the sample or increased dislocation densities in highly active slip bands. To this end, the shape of the grey-level variation was considered as well as the orientation of the parent grain. Furthermore, slip and twin trace analysis was performed based on the crystallographic directions of all possible slip and twin systems and compared with the visible grey-level variations. The respective Schmid factors of slip and twin systems with compatible crystallographic orientation were calculated and used as a criterion to determine whether the grey-level variation was likely to be a deformation twin. Accordingly, only a fraction of all grey-level variations was identified as deformation twins and highlighted in blue in the EBSD maps. In addition, Σ3-boundaries in the EBSD Image Quality (IQ) maps indexed by the MTEX-code are highlighted in red color. Most of those boundaries could easily be identified as annealing twin boundaries, based on the shape and size of the twins. In cases where this identification was not easily performed, each specific Σ3-boundary underwent the same identification process as the grey-level variations.

3. Results

The results of the quasistatic tensile tests are shown in Fig. 1.

In fully-recrystallized condition, both alloys show serrated flow except for the X30MnAl17-1_RX alloy tested at RT. Neither X60Mn18_pRX nor X30MnAl17-1_REC show serrated flow.

The microstructures of the X60Mn18_pRX before tensile testing and after 5% elongation are shown in Fig. 2.

The heat treatment at 555 °C for 16 min led to a phase fraction of approximately 5% α'-martensite which was retained from cold rolling (Fig. 2(b)). Additionally, some deformation twins can be identified in the IQ maps (a,d). However, a significant fraction of the microstructure was recrystallized, as can be recognized by the low grain orientation spread (GOS) values in Fig. 2(c). Straining to 5% resulted in an increase of α'-martensite content to 8%, and only a small increase in TVF.

In contrast, microstructural imaging of the X30MnAl17-1_REC alloy in Fig. 3 shows a high density of deformation twins after recovery annealing prior to tensile testing.

The changes of the microstructural features during the interrupted tensile tests of the X60Mn18_RX alloy and the X30MnAl17-1_RX alloy are shown in Fig. 4.

[1] Recovery annealing of cold-rolled TWIP and TWIP/TRIP steels was shown to be an effective method to generate steels with high yield strength and appreciable ductility, meeting the requirements for crash-relevant automotive parts. Mechanically induced twins remain thermally stable during recovery annealing at moderate temperatures (550–630 °C), contributing to a high yield strength during further deformation. Simultaneously, the dislocation density is reduced, resulting in improved formability. [31–35].

Table 1
Chemical composition, SFE, average grain size and heat treatment of the alloys tested in this work.

Designation	Heat treatment	C (wt%)	Mn (wt%)	Al (wt%)	SFE at RT (mJ/m^2)	SFE at 150 °C (mJ/m^2)	d_{avg} (μm)
X60Mn18_RX	700 °C, 60 min	0.569	17.42	0.003	16.6	41.3	5
X60Mn18_pRX	555 °C, 16 min						–
X30MnAl17-1_RX	700 °C, 60 min	0.321	16.80	1.470	16.5	42.5	7
X30MnAl17-1_REC	550 °C, 5 min						–

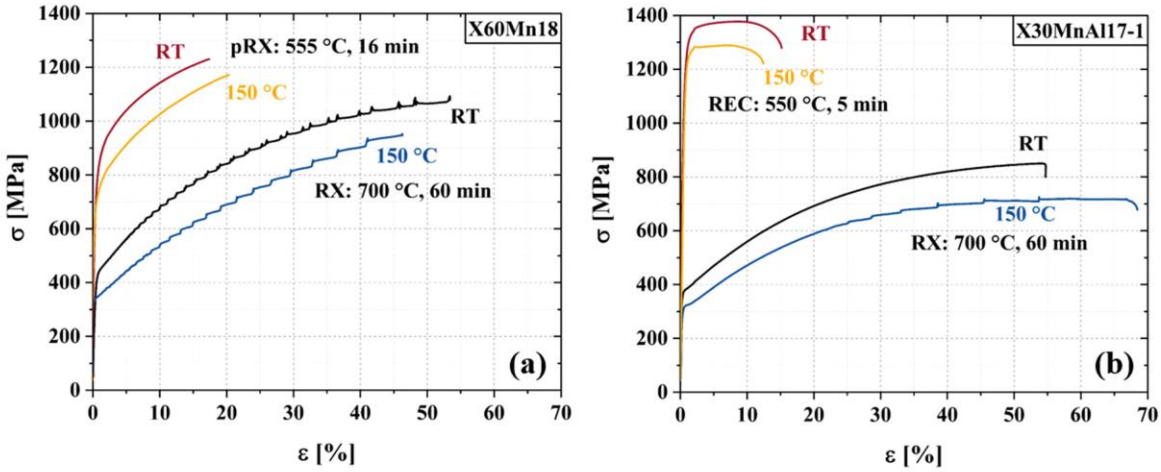


Fig. 1. Engineering stress-strain curves at RT and 150 °C of: (a) X60Mn18_RX and X60Mn18_pRX, (b) X30MnAl17-1_RX and X30MnAl17-1_REC.

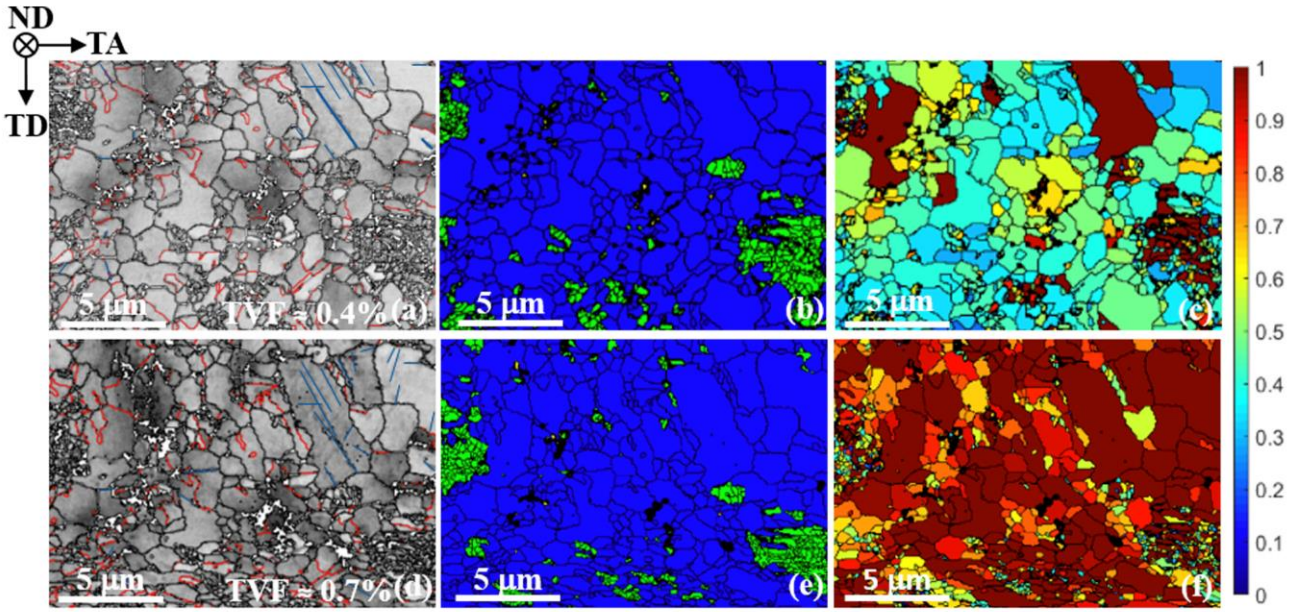


Fig. 2. EBSD maps of the X60Mn18_pRX steel after 0% ((a)-(c)) and 5% ((d)-(f)) tensile strain at RT: (a, d) Image Quality (IQ) map, (b,e) phase distribution map (austenite (blue), α'-martensite (green)) and (c, f) Grain Orientation Spread (GOS) map. ND, TA and TD denote normal direction, tensile axis and transversal direction, respectively.

For the X60Mn18_RX alloy, the tensile test was interrupted before the onset of serrated flow at 2% elongation and right after the onset of serrated flow at 5% elongation. Since the X30MnAl17-1_RX alloy did not show serrated flow at RT, the initial microstructure before tensile testing and the microstructure after 5% elongation is shown. While the TVF of the X60Mn18_RX alloy increased noticeably, the TVF in the X30MnAl17-1_RX alloy did not increase a lot and is significantly lower than in the X60Mn18_RX alloy.

Fig. 5 shows EBSD maps for the X30MnAl17-1_RX alloy after 30% elongation at RT (a,c), where no serrated flow occurs, and 150 °C (b,d), after the onset of serrated flow.

With the increase in testing temperature, the TVF in the X30MnAl17-1_RX alloy increased from approximately 1.5% at RT to about 2.8% at 150 °C.

The difference in TVF for the X60Mn18_RX alloy (a) and the X30MnAl17-1_RX alloy (b) after 40% elongation at RT is shown in the EBSD map in Fig. 6.

While only some grains of the X30MnAl17-1_RX alloy contain deformation twins after 40% elongation (Fig. 6(b)), most grains of the X60Mn18_RX alloy, which are not aligned along the < 100 > ||TA-fiber, (Fig. 6(a)) contain deformation twins. Additionally, the direction of the deformation twins in the X60Mn18_RX alloy indicate that

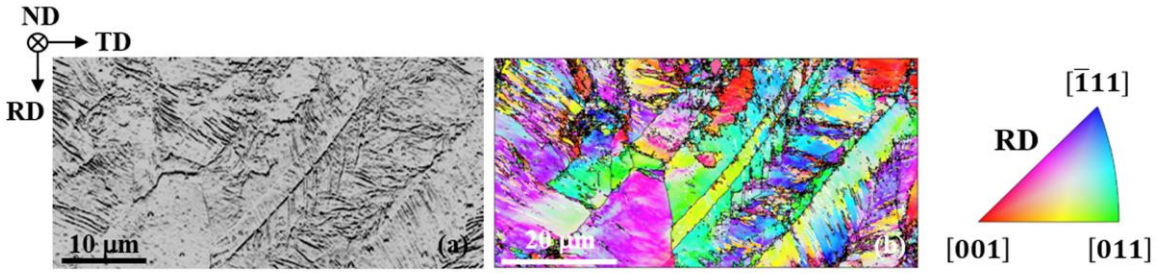


Fig. 3. ForeScatter Detector (FSD) image (a) and EBSD map (b) with colorcoding according to the Inverse Pole Figure (IPF) in rolling direction (RD) of the X30MnAl17-1_REC alloy before tensile testing. Σ3-boundaries in the EBSD maps with IPF colorcoding are highlighted in white.

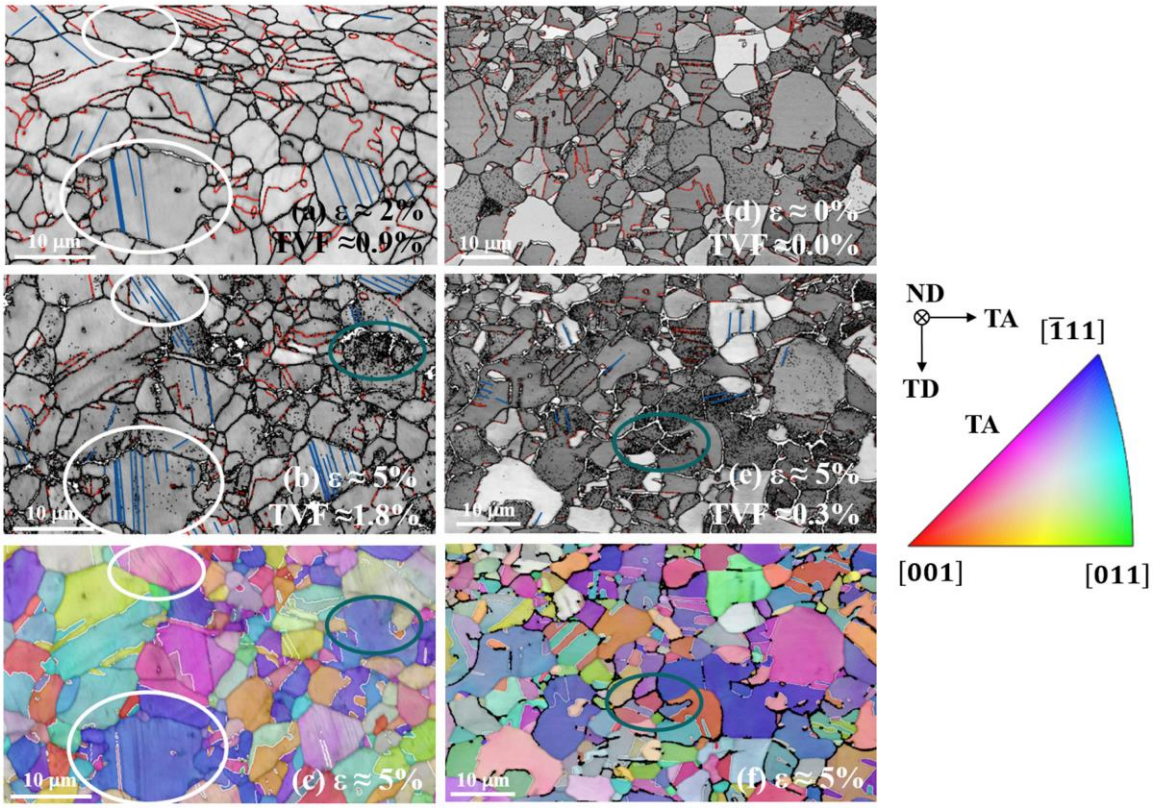


Fig. 4. EBSD IQ maps (a, b,d,e) with IPF colorcoding overlay parallel to the TA (c, f) of X60Mn18_RX alloy (a-c) and X30MnAl17-1_RX alloy (d-f) before the onset of serrated flow (after (a) 2% elongation and 0% (d) elongation respectively) and after 5% elongation at RT (b-c, e-f) respectively (after the onset of serrated flow of the X60Mn18_RX alloy). The white circles in (a) and (b) highlight grains that undergo significant deformation twinning during elongation from 2% to 5%. The circles in dark green highlight areas where the poor local detection rate, probably due to a deterioration of the surface quality as a result of the tensile test, did not allow for a more accurate determination of deformation twins.

multiple twin systems are active. The resulting TVF of approximately 7.4% is significantly higher than the TVF of the X30MnAl17-1_RX alloy at about 2.1%.

4. Discussion

There are several theoretical approaches that discuss the occurrence of serrated flow in HMnS, as has been stated in the introduction. To investigate the role of short-range ordered (SRO) clusters and deformation twinning, two HMnS were tested in different material states with the aim of separating the potential impact of SRO clusters and deformation twinning on serrated flow.

Although the chemical composition and processing route until heat treatment of the X30MnAl17-1_RX and X30MnAl17-1_REC alloys are identical, the onset of serrated flow is different, as highlighted by spikes in the work-hardening rate (WHR) curve in Fig. 7. At RT (Fig. 7(a)), only the X60Mn18_RX alloy shows serrated flow. At 150 °C (Fig. 7(b)), both alloys in RX condition have serrated flow curves. The alloys in pRX/REC condition do not show serrated flow at either RT or 150 °C. The occurrence and onset of serrated flow are summarized in Table 2 for all material states and testing temperatures.

As given in Table 2, the pRX and REC states do not show serrated flow. The main difference between the RX and pRX/REC conditions is the evolution of the twin volume fraction (TVF) during deformation, as indicated by the calculated TVFs in Figs. 2, 4, 5 and 6. Accordingly, the suppression of serrated flow in the REC/pRX states might be due to a lower density of newly-formed deformation twins compared to the RX states. It has been shown that the twin density evolution during further deformation is drastically reduced in recovery-annealed TWIP steels [33]. The work of Lebedkina et al. [42] also points to the impact of deformation twinning on serrated flow by employing EBSD experiments to show that the peaks in serrated flow curves might be related to the activation of new twinning systems. In contrast, since the chemical composition of the RX and pRX/REC material states is the same, the

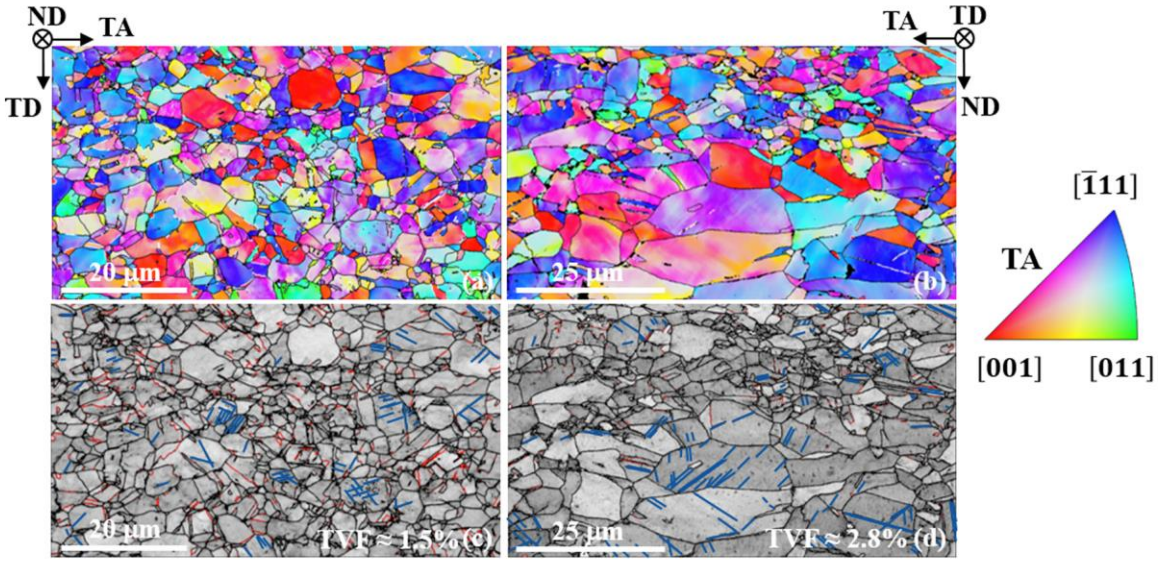


Fig. 5. EBSD maps (a, b) with colorcoding according to the IPF parallel to the TA and EBSD-IQ maps (c, d) for the X30MnAl17-1_RX alloy after 30% elongation at RT (a, c) and at 150 °C (b, d). The approximated TVF is given in (c,d).

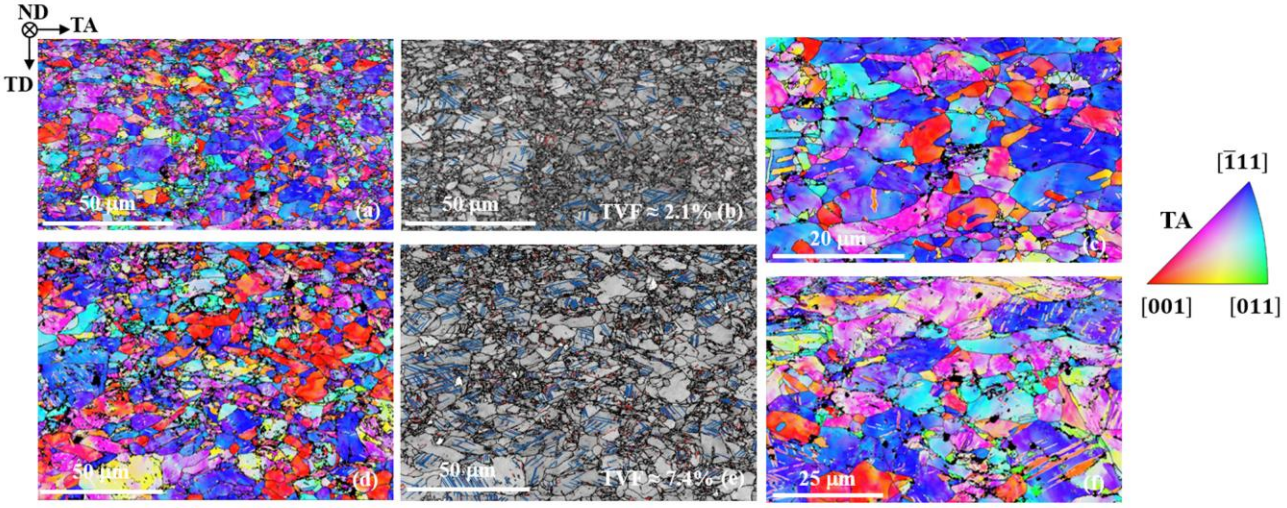


Fig. 6. EBSD maps after 40% elongation at RT with colorcoding according to the IPF parallel to the TA for the (a-c) X30MnAl17-1_RX alloy and (d-f) X60Mn18_RX alloy. Σ3-boundaries in the maps with IPF coloration are highlighted in white. (a) + (b) and (d) + (e) show the microstructure of a larger area to offer an overview, while (c) and (f) are in-detail maps of small areas.

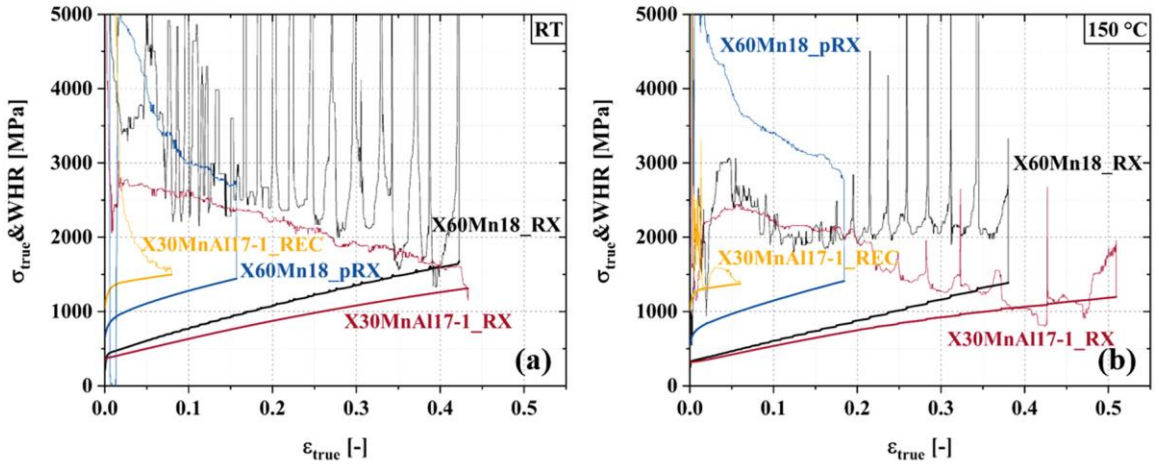


Fig. 7. True stress-true strain curves and work-hardening rate (WHR)-true strain curves of the X30MnAl17-1 and X60Mn18 steels at (a) RT and (b) 150 °C. The corresponding engineering stress-strain curves are given in Fig. 1.

Table 2
Occurrence and onset of serrated flow as shown in Fig. 7.

Designation	Temperature	Serrated Flow	Onset strain
X60Mn18_RX	RT	+	≈ 3%
	150 °C	+	≈ 5%
X60Mn18_pRX	RT	–	–
	150 °C	–	–
X30MnAl17-1_RX	RT	–	–
	150 °C	+	≈ 25%
X30MnAl17-1_REC	RT	–	–
	150 °C	–	–

state of SRO clusters prior to deformation is very similar. This assumption is based on the findings of previously published internal friction experiments, which show that the formation of SRO clusters is based on point defect complexes involving C atoms. Recovery annealing heat treatments at 550 °C led to a re-establishment of the initial state of internal friction peaks, suggesting a reformation of SRO clusters that were previously destroyed by dislocation movement [27]. Additionally, bake-hardening heat treatments of HMnS for 20 min at 170 °C have resulted in significant strength increases, which have been linked to the re-establishment of SRO clusters [43]. As the temperature of the heat treatments in this work is at least 550 °C, the reformation of SRO clusters in the X60Mn18_pRX and X30MnAl17-1_REC alloys is very likely. Accordingly, if serrated flow occurred exclusively due to the shearing of SRO clusters facilitating subsequent glide plane softening and promotion of planar glide, the onset of serrated flow should be similar for the RX and pRX/REC conditions. To conclude, deformation twinning could be the reason for the occurrence of serrated flow in the X60Mn18_RX alloy, while serrated flow is suppressed in the X60Mn18_pRX alloy.

The difference in the occurrence of serrated flow in the X30MnAl17-1_RX and X60Mn18_RX alloys at RT could be explained in terms of different volume fractions of deformation twins formed during tensile testing. Although the SFE of both alloys is almost identical (c.f. Table 1), Figs. 4 and 6 show that the density of newly formed deformation twins in the Al-alloyed X30MnAl17-1_RX is lower. As Al decreases the shear modulus G of HMnS [44] and the stacking fault separation width w_{SF} is correlated to G [45], the decreased w_{SF} will result in a lower probability of twin nucleation in the X30MnAl17-1 alloy. On the one hand, this does not explain why serrated flow occurs at 150 °C in the X30MnAl17-1_RX alloy, as an increase in testing temperature usually leads to higher SFE values and a subsequent decrease in twin density [30]. On the other hand, despite the increase in SFE, the TVF increases after tensile testing at 150 °C as shown in Fig. 5, which could be due to an increase of w_{SF} induced by the pinning of the trailing partial dislocation by C atoms, which are more mobile at higher temperatures. Whereas long-range diffusion of C in HMnS at low temperatures is unlikely to occur because of the low diffusivity of C in γ-Fe at RT, SR jumps of C atoms into preferential lattice positions provide a reasonable mechanism to explain short-range movement of C atoms. After C atoms have been misplaced into tetrahedral sites by the shearing of SRO clusters due to the movement of a leading partial dislocation, the energetic preference of C to be situated in near octahedral sites induces the repositioning of C [27,28]. The possibility of such SR jumps has previously been elaborated on with ab-initio based simulations and subsequent TEM experiments, as performed by Hickel et al. [46], showing that nanodiffusion of C in stacking faults is possible. The activation barrier for SR jumps is further reduced in the case of C diffusion along dislocation cores [46,47], which is likely to occur for C atoms that are situated in stacking faults. The frequency of SR jumps is correlated to the diffusion rate of C in austenite, D_C^{γ} [45]. Hence, SR jumps are more likely to occur at 150 °C than at RT. As the addition of Al in HMnS decreases D_C^{γ} [1] and increases the matrix lattice parameter α_{γ} significantly [48], the frequency of SR jumps will be lower in Al-alloyed steels. This means that SRO-assisted deformation twinning at RT is suppressed in Al-alloyed HMnS but possible in HMnS without Al addition, explaining the lower TVF (c.f. Fig. 4) of Al-alloyed HMnS. At 150 °C, SRO-assisted deformation twinning occurs in Al-alloyed HMnS and increases the TVF relative to the TVF at RT. Additionally, the increase of the SFE from 16.5 mJ/m^2 to 42.5 mJ/m^2, as given in Table 1, could support the increase of TVF due to the fact that the TRIP effect is not competing with the TWIP effect at 150 °C, which could result in a higher TVF [49,50].

Based on the findings discussed in the previous paragraphs, the following observations can be made: (i) Serrated flow occurs only in the material states that show significant deformation twinning. (ii) The onset of serrated flow at 150 °C for the Al-alloyed material is due to an increase in TVF. This can be explained with the higher frequency of SR jumps of C atoms into SRO clusters, which pin the trailing partial dislocation and increases w_{SF}.

While the previous paragraphs have pointed out that deformation twinning is a necessary – although not a sufficient - requirement for the occurrence of serrated flow in high-Mn TWIP steels, the following remarks are dedicated to explaining the formation and propagation of deformation bands. As the Schmid factors of dislocation glide systems and deformation twinning systems are orientation-dependent, the critical stress necessary for deformation twinning is orientation-dependent as well, leading to a heterogeneous twinning behaviour on the microstructural scale. Grains with orientations close to the $<111>$||TA-fiber typically exhibit pronounced deformation twinning, while the low Schmid factor of the twin systems compared to the high Schmid factor of glide systems in grains of the $<100>$||TA-fiber results in a low TVF in those grains [40,41]. As a result, SRO-assisted deformation twinning primarily occurs in favourably oriented grains and thus, local differences in TVF will lead to local stress gradients. Without the activation of additional deformation mechanisms, the active stresses in grains of any orientation are reasonably close, as deformation in fcc metals is easily accommodated by dislocation slip on the 12 available $\{111\}<110>$ slip systems. Deformation twinning leads to a dynamic Hall-Petch effect and subsequent stress accumulation at grain boundaries of heavily twinned grains. In fully-recrystallized microstructures, this results in the activation of additional glide and twin systems in neighbouring grains as well as the activation of more dislocation sources, which results in local hardening phenomena and the propagation of local stresses. This type of microstructural phenomena could be termed “localized activation of additional deformation mechanisms”. It can be assumed that a low TVF, as is the case for the X30MnAl17-1_RX alloy at RT, does not result in a sufficient increase in local stress and thus, an activation of deformation twinning or additional slip systems in neighbouring grains could not occur. In general, the total TVF in high-Mn TWIP steels is typically not significantly higher than 10% [1], while some studies report a TVF as low as approximately 5% [33]. In this context, the increase in TVF of nearly 100% for the X30MnAl17-1_RX alloy after 30% elongation at 150 °C compared to deformation at RT (Fig. 5) highlights the importance of deformation twinning for the occurrence of serrated flow. In fact, when comparing the EBSD maps of the X30MnAl17-1_RX, which does not show serrated flow at RT, and X60Mn18_RX alloys after 40% elongation at RT in Fig. 6, it is noteworthy that deformation twinning is mostly limited to a few grains with $<111>$||TA orientation in the X30MnAl17-1_RX alloy, while the majority of grains in the X60Mn18_RX alloy show a significant amount of deformation twins. This observation is also in line with the estimated TVF for the X30MnAl17-1_RX alloy after 40% elongation at RT and 30% elongation at 150 °C (Figs. 5(d) and 6(b)).

Very weak (almost random) textures have been reported frequently for austenitic fully-recrystallized HMnS, which means that grains with favourable orientation for deformation twinning are usually in close proximity to grains with less favourable orientation [51,52]. Thus, deformation twinning initially leads to local stress inhomogeneities. In

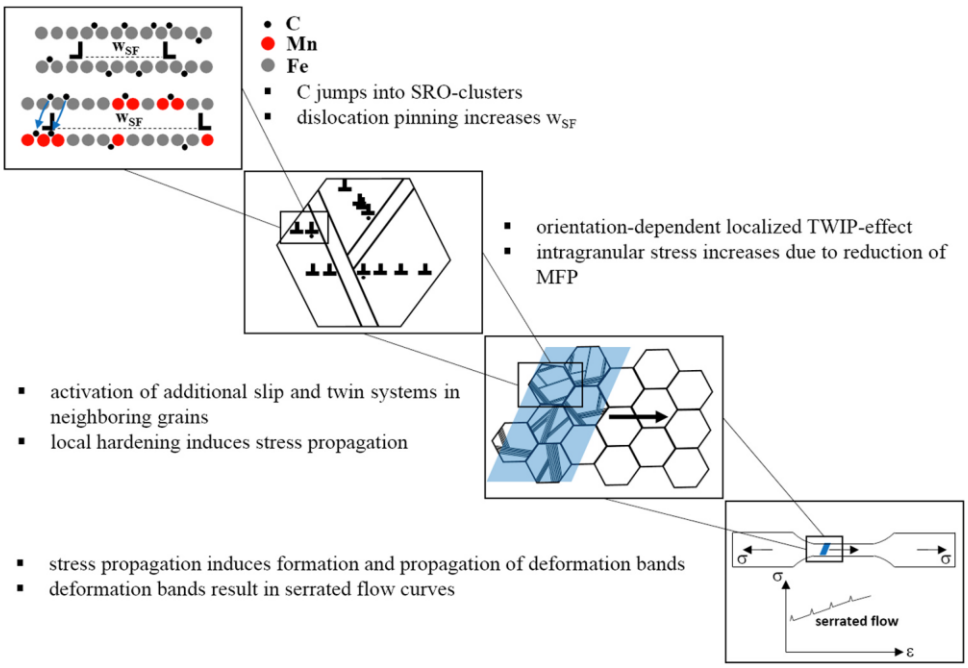


Fig. 8. Schematic of the generation and propagation of deformation bands resulting in serrated flow in high-manganese TWIP steels.

microstructures with a mixture of soft and hard constituents, such as partially-recrystallized microstructures, the stress propagation is hindered. In the case of the X60Mn18_pRX alloy, this inhomogeneous microstructure is due to the existence of a large spread of average grain sizes, as well as fractions of non-recrystallized grains and martensite (Fig. 2). In addition to a lower density of newly formed deformation twins, this explains the suppression of serrated flow. This microstructural requirement for the propagation of stress localization could be termed “microstructural homogeneity”. Although numerous studies on the occurrence of serrated flow in high-Mn TWIP steels have been published, to the best of the authors' knowledge, the importance of the microstructure for the initiation and propagation of deformation bands has not been addressed. However, a recent study on the serrated flow behaviour of a high-Mn TRIP steel showed that the initiation and progression of the martensitic transformation during tensile testing could occur sequentially at segregated Mn-bands, which are common in HMnS [53]. Therefore, it can be stated that the impact of microstructure on the localized activation of secondary deformation mechanisms and the occurrence of serrated flow is similar to the findings on TWIP steels in the present work.

The following scale-bridging progression of mechanisms for the formation and propagation of deformation bands and the resulting occurrence of serrated flow in HMnS is proposed: The rearrangement of C atoms by SR jumps into preferential positions in SRO clusters induces deformation twinning due to the pinning of the trailing partial dislocation and the subsequent increase of w_{SF}. The orientation-dependence of deformation twinning leads to a selective activation of deformation twinning in preferred grains, which in turn causes the activation of new dislocation sources, glide systems and twin systems in neighbouring grains. On a macroscopic level, this leads to local deformation phenomena in the form of deformation bands, which are detectable as serrated flow in HMnS. In recovery-annealed microstructures, the low density of newly formed deformation twins is not sufficient to activate additional twin and glide systems in neighbouring grains. Similarly, the suppression of serrated flow by alloying addition of Al can be explained by the decreased frequency of SR jumps due to a reduction in C diffusivity, which results in a lower TVF. At 150 °C, the diffusivity of C is increased and enables SRO-assisted deformation twinning. In partially-recrystallized microstructures, the microstructural heterogeneity due to a mixture of soft and hard constituents hinders the propagation of localized stress and suppresses serrated flow. A schematic for the generation and propagation of deformation bands as proposed in this work is shown in Fig. 8.

5. Conclusions

The impact of short-range ordered (SRO) clusters and deformation twinning on the onset of serrated flow in high-manganese twinning-induced plasticity (TWIP) steels was investigated by means of quasi-static tensile tests at room temperature and at 150 °C for recovery-annealed, partially-recrystallized and fully-recrystallized alloys. The following conclusions can be drawn:

- For the generation of deformation bands, the localized activation of additional deformation mechanisms is necessary. Local stress peaks induced by SRO-assisted deformation twinning in grains with favourable orientation cause the activation of additional glide and twin systems in neighbouring grains, which induces a propagating stress localization.
- Neither the SRO-based theory nor the deformation twinning-based theory is capable of explaining serrated flow in high-Mn TWIP steels exclusively. Whereas the SRO-based theory is not suited to describe the suppression of serrated flow in recovery-annealed and partially-recrystallized alloys at room temperature, the deformation-twinning based theory does not explain the increase of twin volume fraction and onset of serrated flow at 150 °C for the fully-recrystallized X30MnAl17-1 alloy.
- Serrated flow is suppressed in the partially-recrystallized and recovery-annealed alloys tested in this work. At room temperature, the fully-recrystallized state of the X30MnAl17-1 alloy does not show serrated flow, while the fully-recrystallized X60Mn18 alloy does. At 150 °C, serrated flow occurs for both fully-recrystallized alloys. In the case of the X30MnAl17-1 alloy, this is due to a higher twin volume fraction at 150 °C than at room temperature, which is a result of an increased C diffusivity that enhances SRO-assisted deformation twinning.
- For homogeneous microstructures, such as fully-recrystallized microstructures, localized activation of additional deformation

mechanisms facilitates the formation and propagation of deformation bands and serrated flow in high-Mn TWIP steels. For heterogeneous microstructures, such as partially-recrystallized and recovery-annealed microstructures, this effect is suppressed due to inhibited propagation of deformation bands.

Acknowledgements

The authors are grateful for the financial support of the Deutsche Forschungsgemeinschaft (DFG) within the Collaborative Research Centre (SFB) 761 “Steel – ab initio”.

Conflict of interest

None.

Contributors

Simon Sevsek performed the experiments. All authors participated in the analysis of experimental data and contributed in the writing process.

Data availability

The raw data required to reproduce these findings cannot be shared at this time as the data also forms part of an ongoing study. The processed data required to reproduce these findings cannot be shared at this time due to legal or ethical reasons.

References

[1] B.C. DeCooman, Y. Estrin, S.K. Kim, Twinning-induced plasticity (TWIP) steels, Acta Mater. 142 (2018) 283–362, https://doi.org/10.1016/j.actamat.2017.06.046.
[2] B.C. DeCooman, High Mn TWIP steel and medium Mn steel, in: R. Rana, S.B. Singh (Eds.), Automotive Steels: Design, Metallurgy, Processing and Applications, Woodhead Publishing, 2017, pp. 317–385.
[3] B.C. DeCooman, O. Kwon, K.-G. Chin, State-of-the-knowledge on TWIP steel, Mater. Sci. Technol. 28 (5) (2012) 513–527, https://doi.org/10.1179/1743284711Y.0000000095.
[4] J.K. Choi, S.-.G. Lee, Y.-.H. Park, I.-.W. Han, J.W. Morris Jr., High manganese austenitic steel for cryogenic applications, in: Proceedings of the Twenty-second International Offshore and Polar Engineering Conference, Rhodes, Greece, 2012, pp. 29–35.
[5] S. Allain, J.P. Chateau, O. Bouaziz, A physical model of the twinning-induced plasticity effect in a high manganese austenitic steel, Mater. Sci. Eng., A 387–389 (2004) 143–147, https://doi.org/10.1016/j.msea.2004.01.060.
[6] O. Bouaziz, Strain-hardening of twinning-induced plasticity steels, Scr. Mater. 66 (12) (2012) 982–985, https://doi.org/10.1016/j.scriptamat.2011.11.029.
[7] O. Bouaziz, S. Allain, C.P. Scott, P. Cugy, D. Barbier, High manganese austenitic twinning induced plasticity steels: a review of the microstructure properties relationships, Curr. Opin. Solid State Mater. Sci. 15 (4) (2011) 141–168, https://doi.org/10.1016/j.cossms.2011.04.002.
[8] L. Mosecker, A. Saeed-Akbari, Nitrogen in chromium-manganese stainless steels: a review on the evaluation of stacking fault energy by computational thermodynamics, Sci. Technol. Adv. Mater. 14 (3) (2013) 33001, https://doi.org/10.1088/1468-6996/14/3/033001.
[9] S.K. Paul, N. Stanford, T. Hilditch, Austenite plasticity mechanisms and their behavior during cyclic loading, Int. J. Fatigue 106 (2018) 185–195, https://doi.org/10.1016/j.ijfatigue.2017.10.005.
[10] A. Abbasi, A. Dick, T. Hickel, J. Neugebauer, First-principles investigation of the effect of carbon on the stacking fault energy of Fe-C alloys, Acta Mater. 59 (8) (2011) 3041–3048, https://doi.org/10.1016/j.actamat.2011.01.044.
[11] D.T. Pierce, J.A. Jiménez, J. Bentley, D. Raabe, C. Oskay, J.E. Wittig, The influence of manganese content on the stacking fault and austenite/ε-martensite interfacial energies in Fe–Mn–(Al–Si) steels investigated by experiment and theory, Acta Mater. 68 (2014) 238–253, https://doi.org/10.1016/j.actamat.2014.01.001.
[12] L. Mosecker, D.T. Pierce, A. Schwedt, M. Beighmohamadi, J. Mayer, W. Bleck, J.E. Wittig, Temperature effect on deformation mechanisms and mechanical properties of a high manganese C+N alloyed austenitic stainless steel, Mater. Sci. Eng., A 642 (2015) 71–83, https://doi.org/10.1016/j.msea.2015.06.047.
[13] D.R. Steinmetz, T. Jäpel, B. Wietbrock, P. Eisenlohr, I. Gutierrez-Urrutia, A. Saeed-Akbari, T. Hickel, F. Roters, D. Raabe, Revealing the strain-hardening behavior of twinning-induced plasticity steels: theory, simulations, experiments, Acta Mater. 61 (2) (2013) 494–510, https://doi.org/10.1016/j.actamat.2012.09.064.
[14] O. Bouaziz, S. Allain, C. Scott, Effect of grain and twin boundaries on the hardening mechanisms of twinning-induced plasticity steels, Scr. Mater. 58 (6) (2008) 484–487, https://doi.org/10.1016/j.scriptamat.2007.10.050.
[15] J.-H. Kang, T. Ingendahl, W. Bleck, A constitutive model for the tensile behaviour of TWIP steels: composition and temperature dependencies, Mater. Des. 90 (2016) 340–349, https://doi.org/10.1016/j.matdes.2015.10.126.
[16] S.L. Wong, M. Madivala, U. Prahl, F. Roters, D. Raabe, A crystal plasticity model for twinning- and transformation-induced plasticity, Acta Mater. 118 (2016) 140–151, https://doi.org/10.1016/j.actamat.2016.07.032.
[17] C. Haase, C. Zehnder, T. Ingendahl, A. Bikar, F. Tang, B. Hallstedt, W. Hu, W. Bleck, D.A. Molodov, On the deformation behavior of κ-carbide-free and κ-carbide-containing high-Mn light-weight steel, Acta Mater. 122 (2017) 332–343, https://doi.org/10.1016/j.actamat.2016.10.006.
[18] S. Allain, O. Bouaziz, T. Lebedkina, M. Lebyodkin, Relationship between relaxation mechanisms and strain aging in an austenitic FeMnC steel, Scr. Mater. 64 (8) (2011) 741–744, https://doi.org/10.1016/j.scriptamat.2010.12.039.
[19] B. Aydemir, H.K. Zeytin, G. Guven, Investigation of portevin-Le Chatelier effect of hot-rolled Fe-13Mn-0.2C-1Al-1Si TWIP steel, Mater. Tehnol. 50 (4) (2016) 511–516, https://doi.org/10.17222/mit.2015.034.
[20] L. Chen, H.-S. Kim, S.-K. Kim, B.C. de Cooman, Localized deformation due to Portevin-LeChatelier effect in 18Mn-0.6C TWIP austenitic steel, ISIJ Int. 47 (12) (2007) 1804–1812, https://doi.org/10.2355/isijinternational.47.1804.
[21] L.G. Hector, P.D. Zavattieri, Nucleation and propagation of portevin-Le Châtelier bands in austenitic steel with twinning induced plasticity, Experimental and Applied Mechanics, Springer, New York, NY, 2011, pp. 855–863.
[22] S. Hoffmann, W. Bleck, B. Berme, In situ characterization of deformation behavior of austenitic high manganese steels, Steel Res. Int. 83 (4) (2012) 379–384, https://doi.org/10.1002/srin.201100311.
[23] J. Kim, Y. Estrin, B.C. de Cooman, Application of a dislocation density-based constitutive model to Al-alloyed TWIP steel, Metall. Mat. Trans. A 44 (9) (2013) 4168–4182, https://doi.org/10.1007/s11661-013-1771-2.
[24] K. Renard, S. Ryelandt, P.J. Jacques, Characterisation of the portevin-Le Châtelier effect affecting an austenitic TWIP steel based on digital image correlation, Mater. Sci. Eng., A 527 (12) (2010) 2969–2977, https://doi.org/10.1016/j.msea.2010.01.037.
[25] A. Saeed-Akbari, A.K. Mishra, J. Mayer, W. Bleck, Characterization and prediction of flow behavior in high-manganese twinning induced plasticity steels: Part II. Jerky flow and instantaneous strain rate, Metall. Mater. Trans. A 43 (5) (2012) 1705–1723, https://doi.org/10.1007/s11661-011-1070-8.
[26] W. Song, D. Bogdanovski, A. Yildiz, J. Houston, R. Dronskowski, W. Bleck, On the Mn–C short-range ordering in a high-strength high-ductility steel: small angle neutron scattering and Ab initio investigation, Metals 8 (1) (2018) 44, https://doi.org/10.3390/met8010044.
[27] S.-J. Lee, J. Kim, S.N. Kane, B.C. DeCooman, On the origin of dynamic strain aging in twinning-induced plasticity steels, Acta Mater. 59 (17) (2011) 6809–6819, https://doi.org/10.1016/j.actamat.2011.07.040.
[28] J.-H. Kang, T. Ingendahl, J. von Appen, R. Dronskowski, W. Bleck, Impact of short-range ordering on yield strength of high manganese austenitic steels, Mater. Sci. Eng., A 614 (2014) 122–128, https://doi.org/10.1016/j.msea.2014.07.016.
[29] S. Sevsek, W. Bleck, Ab initiobased modelling of the yield strength in high-manganese steels, Metals 8 (1) (2018) 34, https://doi.org/10.3390/met8010034.
[30] M. Koyama, T. Sawaguchi, K. Tsuzaki, Deformation twinning behavior of twinning-induced plasticity steels with different carbon concentrations – Part 2: proposal of dynamic-strain-aging-assisted deformation twinning, ISIJ Int. 55 (8) (2015) 1754–1761, https://doi.org/10.2355/isijinternational.ISIJINT-2015-070.
[31] O. Bouaziz, D. Barbier, Benefits of recovery and partial recrystallization of nano-twinned austenitic steels, Adv. Eng. Mater. 15 (10) (2013) 976–979, https://doi.org/10.1002/adem.201300045.
[32] C. Haase, T. Ingendahl, O. Güvenc, M. Bambach, W. Bleck, D.A. Molodov, L.A. Barrales-Mora, On the applicability of recovery-annealed twinning-induced plasticity steels: potential and limitations, Mater. Sci. Eng., A 649 (2016) 74–84, https://doi.org/10.1016/j.msea.2015.09.096.
[33] C. Haase, L.A. Barrales-Mora, F. Roters, D.A. Molodov, G. Gottstein, Applying the texture analysis for optimizing thermomechanical treatment of high manganese twinning-induced plasticity steel, Acta Mater. 80 (2014) 327–340, https://doi.org/10.1016/j.actamat.2014.07.068.
[34] F. Berrenberg, C. Haase, L.A. Barrales-Mora, D.A. Molodov, Enhancement of the strength-ductility combination of twinning-induced/transformation-induced plasticity steels by reversion annealing, Mater. Sci. Eng., A 681 (2017) 56–64, https://doi.org/10.1016/j.msea.2016.10.109.
[35] F. Brasche, C. Haase, L.A. Barrales-Mora, D.A. Molodov, Comparative study of the influence of reversion- and recovery- annealing on the mechanical behavior of high-manganese steels with varying stacking fault energy, Steel Res. Int. 89 (9) (2018) 1700377, https://doi.org/10.1002/srin.201700377.
[36] A. Saeed-Akbari, J. Imlau, U. Prahl, W. Bleck, Derivation and variation in composition-dependent stacking fault energy maps based on subregular solution model in high-manganese steels, Metall. Mater. Trans. A 40 (13) (2009) 3076–3090, https://doi.org/10.1007/s11661-009-0050-8.
[37] R. Hielscher, H. Schaeben, A novel pole figure inversion method: specification of the MTEX algorithm, J. Appl. Crystallogr 41 (6) (2008) 1024–1037, https://doi.org/10.1107/S0021889808030112.
[38] F. Bachmann, R. Hielscher, H. Schaeben, Texture analysis with MTEX – free and open source software toolbox, SSP 160 (2010) 63–68, https://doi.org/10.4028/www.scientific.net/SSP.160.63.
[39] C.A. Schneider, W.S. Rasband, K.W. Eliceiri, NIH Image to ImageJ: 25 years of Image analysis, Nat. Methods 9 (7) (2012) 671–675, https://doi.org/10.1038/nmeth.2089.
[40] D. Barbier, N. Gey, N. Bozzolo, S. Allain, M. Humbert, EBSD for analysing the

twinning microstructure in fine-grained TWIP steels and its influence on work hardening, J. Microsc. 235 (1) (2009) 67–78, https://doi.org/10.1111/j.1365-2818.2009.03182.x.
[41] I. Gutierrez-Urrutia, D. Raabe, Dislocation and twin substructure evolution during strain hardening of an Fe–22wt% Mn–0.6wt% C TWIP steel observed by electron channeling contrast imaging, Acta Mater. 59 (16) (2011) 6449–6462, https://doi.org/10.1016/j.actamat.2011.07.009.
[42] T.A. Lebedkina, M.A. Lebyodkin, J.-P. Chateau, A. Jacques, S. Allain, On the mechanism of unstable plastic flow in an austenitic FeMnC TWIP steel, Mater. Sci. Eng., A 519 (1–2) (2009) 147–154, https://doi.org/10.1016/j.msea.2009.04.067.
[43] S. Wesselmecking, W. Song, Y. Ma, T. Roesler, H. Hofmann, W. Bleck, Strain aging behavior of an austenitic high-Mn steel, Steel Res. Int. 89 (9) (2018) 1700515, https://doi.org/10.1002/srin.201700515.
[44] G. Ghosh, G.B. Olson, The isotropic shear modulus of multicomponent Fe-base solid solutions, Acta Mater. 50 (10) (2002) 2655–2675, https://doi.org/10.1016/S1359-6454(02)00096-4.
[45] G. Gottstein, Materialwissenschaft und Werkstofftechnik: Physikalische Grundlagen, 4th ed., Springer-Verlag Berlin Heidelberg, Berlin, Heidelberg, 2014.
[46] T. Hickel, S. Sandlöbes, R.K.W. Marceau, A. Dick, I. Bleskov, J. Neugebauer, D. Raabe, Impact of nanodiffusion on the stacking fault energy in high-strength steels, Acta Mater. 75 (2014) 147–155, https://doi.org/10.1016/j.actamat.2014.04.062.
[47] D.E. Jiang, E.A. Carter, Carbon dissolution and diffusion in ferrite and austenite from first principles, Phys. Rev. B 67 (21) (2003) 1045, https://doi.org/10.1103/PhysRevB.67.214103.
[48] M.C. Li, H. Chang, P.W. Kao, D. Gan, The effect of Mn and Al contents on the solvus of κ phase in austenitic Fe-Mn-Al-C alloys, Mater. Chem. Phys. 59 (1) (1999) 96–99, https://doi.org/10.1016/S0254-0584(99)00026-7.
[49] A. Dumay, J.P. Chateau, S. Allain, S. Migot, O. Bouaziz, Influence of addition elements on the stacking-fault energy and mechanical properties of an austenitic Fe–Mn–C steel, Mater. Sci. Eng., A 483–484 (2008) 184–187, https://doi.org/10.1016/j.msea.2006.12.170.
[50] J. Kim, B.C. DeCooman, On the stacking fault energy of Fe-18 Pct Mn-0.6 Pct C-1.5 Pct Al twinning-induced plasticity steel, Metall. Mat. Trans. A 42 (4) (2011) 932–936, https://doi.org/10.1007/s11661-011-0610-6.
[51] C. Haase, M. Kühbach, L.A. Barrales-Mora, S.L. Wong, F. Roters, D.A. Molodov, G. Gottstein, Recrystallization behavior of a high-manganese steel: experiments and simulations, Acta Mater. 100 (2015) 155–168, https://doi.org/10.1016/j.actamat.2015.08.057.
[52] C. Haase, Texture and Microstructure Evolution during Deformation and Annealing of High-manganese TWIP Steels (PhD dissertation), Aachen, 2016.
[53] M.C. Jo, J.H. Choi, H. Lee, A. Zargaran, J.H. Ryu, S.S. Sohn, N.J. Kim, S. Lee, Effects of solute segregation on tensile properties and serrated behavior in ultra-high-strength high-Mn TRIP steels, Mater. Sci. Eng., A 740–741 (2019) 16–27, https://doi.org/10.1016/j.msea.2018.10.065.

Chapter IV

On the Influence of Grain Size on the TWIP/TRIP-Effect and Texture Development in High-Manganese Steels

S. Sevsek, F. Brasche, D. Molodov and W. Bleck
Materials Science & Engineering A 754 (2019) 152-160
https://doi.org/10.1016/j.msea.2019.03.072

Chapter IV analyzes the changes in deformation texture for two high-manganese TWIP/TRIP steels with different initial grain sizes. Quasistatic tensile tests reveal that the yield strength and initial work-hardening rate can be significantly increased by decreasing the initial grain size. A correlative analysis of electron backscatter diffraction experiments, macrotexture and phase fraction measurements during interrupted tensile tests shows that the TWIP and TRIP effect is more pronounced in the coarse-grained material state. This induces a relative softening of the <111>||TA-fiber, which shows favorable orientations for deformation twinning, compared to the <100>||TA-fiber. Due to the more pronounced TWIP and TRIP effect, the rate of the decline of the work-hardening rate during further plastic deformation is lower in the coarse-grained material state.

Contents lists available at ScienceDirect

Materials Science & Engineering A

journal homepage: www.elsevier.com/locate/msea

On the influence of grain size on the TWIP/TRIP-effect and texture development in high-manganese steels

Simon Sevsek[a,*], Frederike Brasche[b], Dmitri A. Molodov[b], Wolfgang Bleck[a]

[a] Steel Institute, RWTH Aachen University, Intzestraße 1, 52072, Aachen, Germany
[b] Institute of Physical Metallurgy and Metal Physics, RWTH Aachen University, Kopernikusstraße 14, 52056, Aachen, Germany

ARTICLE INFO

Keywords:
High-manganese steel
Grain size
Twinning-induced plasticity
Transformation-induced plasticity
Texture development

ABSTRACT

The impact of grain size on the work-hardening rate of two high-manganese steels with nearly identical stacking fault energy values of approximately 16.6 mJ m^{-2} (X60Mn17 alloy) and 16.5 mJ m^{-2} (X30MnAl17-1 alloy) was analyzed via macro-texture and micro-texture measurements as well as quasistatic tensile tests and phase analysis. Both alloys exhibited differences in twin volume fraction and volume fraction of the martensitic phase. The twin volume fraction increased with grain size. The X30MnAl17-1 alloy with Al and lower C content showed a lower overall twin volume fraction than the X60Mn17 alloy without Al. Additionally, the phase fractions of ε-martensite and α′-martensite were very low in the X30MnAl17-1 alloy. The increased grain size and the subsequent increase in twin volume fraction led to a relative decrease of the volume fraction of grains with < 111 > -orientation parallel to the tensile axis for both alloys.

1. Introduction

The remarkable mechanical properties of fully austenitic high-manganese TWIP (TWinning-Induced Plasticity) and TRIP (TRansformation-Induced Plasticity) steels with 12–30 wt% Mn and stacking fault energy (SFE) values in the range of 12–55 mJ m^{-2} can be attributed to high dislocation densities and the activation of additional deformation mechanisms such as deformation twinning [1–7]. Pronounced planar dislocation glide leads to a lower probability of dislocation annihilation and the combination with gradual grain refinement via deformation twinning - the so-called dynamic Hall-Petch effect – results in high work-hardening rates (WHR) [8–11]. In high-manganese steels (HMnS) that exhibit the TRIP effect, the strain-induced transformation of austenite to ε-martensite (hexagonal close packed) or α′-martensite (body centered cubic) increases the WHR and can retard local necking [1,12–14]. Accordingly, the product of ultimate tensile strength and total elongation for HMnS in some cases exceeds 50,000 MPa% [5,15]. Those properties make high-manganese TWIP/TRIP steels a point of interest for crash-relevant car parts [1]. However, a low yield strength (YS), as is common for HMnS, is detrimental to the performance for conventionally-designed crash-relevant parts because the available deformation volume of such parts is low compared to the total elongation of HMnS [5,15,16]. Thus, increasing the YS is of high significance for the application potential of HMnS.

Conventional approaches to increase the YS in HMnS include the reduction of grain size, the use of alloying (e.g. C, Si) and microalloying elements (e.g. V, Nb) or the application of recovery annealing heat treatments to retain the heavily-twinned, fine-grained microstructure after cold-rolling [5,16–24]. While the addition of alloying elements can increase the YS, it also changes the SFE and the WHR [25,26]. Although the increase of the YS via grain refinement is well documented in HMnS, the magnitude of impact on the evolution of WHR during the uniaxial tensile test in TWIP/TRIP steels is still not fully understood, although there are several studies on the impact of grain size on deformation twinning [5,8,23,24,27–33].

In the past, attempts have been made to determine the solid solution strengthening contribution of various alloying elements, most often based on experimental data and linear regression models. Those models often imply negative solid-solution strengthening parameters for Mn, which is usually thought of as an element with a positive impact on solid solution strengthening [1,6,34–37]. This led to the development of new models, which perceived the concept of short-range ordering (SRO) as an additional contribution to the YS of HMnS [38,39]. SRO is the concept of interactions of carbon-metal pairs which result in local differences of ordering energies and make certain cell configurations more favorable to inhibit a central C atom [40–43]. Ab-initio calculations employing density-functional theory (DFT) have been utilized to determine the differences in ordering energies [44,45]. Results from

* Corresponding author.
E-mail address: simon.sevsek@iehk.rwth-aachen.de (S. Sevsek).

https://doi.org/10.1016/j.msea.2019.03.072
Received 4 January 2019; Received in revised form 8 March 2019; Accepted 15 March 2019
Available online 20 March 2019
0921-5093/ © 2019 Elsevier B.V. All rights reserved.

those approaches have shown good agreement with experimental data, e.g. from Mössbauer spectroscopy, atom-probe tomography (APT), small-angle neutron scattering (SANS) and in-situ synchrotron X-ray diffraction [43,46–49]. While the influence of SRO on the WHR in HMnS has been described as enhancing planar glide, its impact on secondary deformation mechanisms such as deformation twinning is still a point of debate [50–52].

Analyzing the texture of a material is a powerful tool to investigate the material's response to deformation or heat treatment. The dependence of the activation of deformation twinning on the Schmid factor along with strong rotations of the grains leads to a texture evolution during uniaxial tensile tests that is dominated by grains with orientations close to the < 111 > ||TA- (TA – tensile axis) or < 100 > ||TA-fiber [28,53–55]. The typical recrystallization texture of high-manganese TWIP steels contains similar texture components as the deformation texture but is strongly weakened in intensity [5,56–58].

The aim of this study is to analyze the impact of grain size on the activation of the secondary deformation mechanisms in two TWIP/TRIP HMnS (X60Mn17 and X30MnAl17-1) and the effect on mechanical properties. To this end, phase analyses and macro-texture measurements were performed by X-ray diffraction (XRD) to analyze the evolution of phase fractions of ε- and α′-martensite during uniaxial tensile tests in a fine-grained and a coarse-grained state. Quasistatic, uniaxial tensile tests were employed to evaluate the mechanical properties.

2. Experimental methods

The X60Mn17 alloy was produced via strip-casting with an as-cast thickness of approximately 3 mm, using a double-roller device, followed by in-line hot-rolling with a thickness reduction of roughly 20–30% to a strip thickness of 2.2 mm. A subsequent cold-rolling process with a thickness reduction of 50% led to a final strip thickness of 1.1 mm. The X30MnAl17-1 alloy was ingot-cast with ingot dimensions of 140 mm × 140 mm x 500 mm. Subsequently, a homogenization annealing at 1150 °C for 5 h and hot forging at 1150 °C from 140 mm × 140 mm–55 mm × 55 mm was employed, followed by an additional homogenization annealing at 1150 °C for 2 h and hot-rolling to a sheet thickness to 2.2 mm. The following cold-rolling thickness reduction of 50% resulted in a final thickness of 1.1 mm.

Tensile test specimens with 30 mm initial gauge length and 6 mm gauge width were machined using water jet cutting. The TA was perpendicular to the rolling direction (RD). Heat treatments of the tensile test specimens to achieve the fine-grained (designation FG) and coarse-grained (designation CG) microstructures were performed in a salt bath furnace. Average grain sizes d_{avg} and the grain size distribution were determined with the line-intercept method using optical microscopy images of the microstructure after etching with a Klemm-solution, taking annealing twins into account. The chemical composition regarding the alloying elements with relevant alloying contents of both HMnS in wt%, the respective SFE values that were calculated using a subregular solution thermodynamic model [7] and the heat treatments for the respective material states are given in Table 1.

Metallographic preparation for Electron Backscatter Diffraction (EBSD), XRD and macro-texture measurements was performed by means of mechanical grinding with SiC paper up to 4000 grit with subsequent mechanical polishing using 3 µm and 1 µm diamond suspension. Electropolishing was then performed at 22 V using an electrolyte containing 700 ml ethanol (C_2H_5OH), 100 ml butyl glycol ($C_6H_{14}O_2$) and 78 ml perchloric acid (60%) ($HClO_4$). The duration of electropolishing was 20 s for EBSD measurements and 2 min for the XRD measurements, respectively.

EBSD analysis was performed on the sheet surface of tensile test specimen with 12 mm gauge length and 2 mm gauge width, using a Zeiss Sigma scanning electron microscope (SEM) at an acceleration voltage of 15 kV and a working distance between 15 mm and 20 mm, a step size of 70 nm and utilizing a post-processing routine employing the HKL Channel 5 software, as well as the MTEX toolbox. A noise reduction was employed by removing wild spikes and considering at least 5 neighboring data points. Phase analysis and XRD measurements were conducted on the mid-layer of the sheet thickness using a Bruker D8 Advance X-ray diffractometer equipped with a HI-STAR area detector operating at 30 kV and 25 mA to acquire three incomplete (0–85°) {111}-, {200}- and {220}-pole figures, which were used to calculate the corresponding orientation distribution function (ODF) via the MATLAB-based MTEX toolbox [59,60]. Volume fractions of the texture components were calculated by using a radius of 15° around the ideal position.

Uniaxial, quasistatic tensile tests were conducted using a Z250 tensile testing machine by ZwickRoell. For each alloy state in the same condition, at least 3 tensile tests were conducted. Strains were measured with the contact-type extensometer MultiXtens by ZwickRoell. The strain rate from the beginning up to 0.2% yielding was kept constant at 0.00025 1/s, after which the strain rate was increased to 0.001 1/s over the duration of 10 s and then kept constant until fracture. The WHR throughout this manuscript is defined as $\frac{d\sigma_{true}}{d\varepsilon_{true}}$ and as such, is the slope of the flow curve [1,5,11]. To describe the evolution of the WHR with increasing true strain, the strain hardening exponent n_H from Holloman's equation has been calculated for any given true strain, using the relationship $n_H = \frac{d \ln \sigma_{true}}{d \ln \varepsilon_{true}}$.

3. Results

Fig. 1 shows the grain size distribution and the average grain size d_{avg} for all material states as determined by using the line-intercept method.

The selected heat treatments led to a logarithmic distribution of grain diameters with significant differences in the grain size of each state of alloy. At the same time, d_{avg} of the fine-grained and coarse-grained material states are similar. Both fine-grained material states show average grain sizes of approximately 4 µm, although the grain size distribution of the X30MnAl17-1_FG alloy is narrower but shows one distinct runaway value with a grain diameter of 24 µm. The average grain size of the X60Mn17_CG alloy (16 µm) was slightly lower than that of the X30MnAl17-1_CG alloy (22 µm). Overall, the increase in annealing temperature and annealing duration resulted in significant differences between the average grain size for both alloys.

The results of the quasistatic tensile tests are shown in Fig. 2.

The results for each material state were reproducible. Fig. 2(a) shows that the coarse-grained X60Mn17 alloy had a significantly reduced elongation to fracture (ε_f) of 20.2% compared to the X60Mn17_FG alloy with 52.9%, while ε_f for the X30MnAl17-1_CG condition was slightly increased to 69.2% from 62.7% for the X30MnAl17-1_FG condition. In both cases, the grain refinement led to a

Table 1
Summary of the tested material states with respective heat treatment, chemical composition and SFE.

Designation	Heat treatment	C [wt%]	Mn [wt%]	Al [wt%]	Si [wt.%]	SFE [mJ/m^2]
X60Mn17_FG	700 °C, 60 min	0.569	17.42	0.003	0.09	16.6
X60Mn17_CG	950 °C, 90 min					
X30MnAl17-1_FG	700 °C, 60 min	0.321	16.80	1.470	0.03	16.5
X30MnAl17-1_CG	900 °C, 90 min					

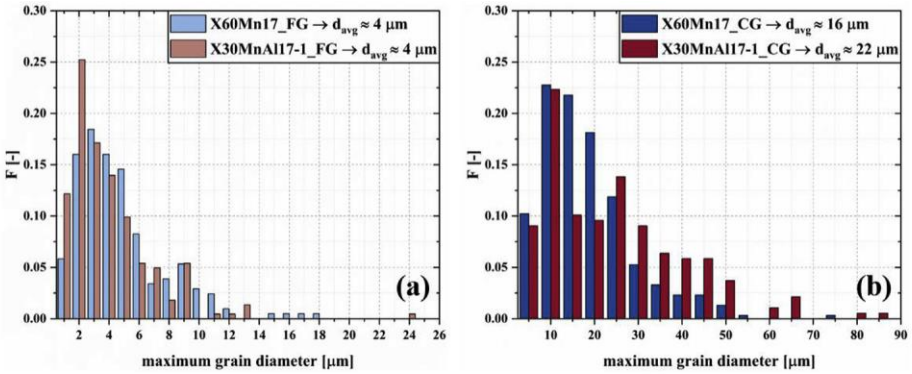


Fig. 1. Average grain size d_{avg} and grain size distribution as determined using the line-intercept method for the (a) fine-grained and (b) coarse-grained alloys.

significantly higher yield strength (YS) and ultimate tensile strength (UTS). For the X60Mn17 alloy, the YS and UTS increased by $\Delta\sigma_{YS,\,X60Mn17} = 184\,MPa$ and $\Delta\sigma_{UTS,\,X60Mn17} = 306\,MPa$ respectively. The impact of the reduction in grain size was less pronounced for the X30MnAl17-1 alloy at $\Delta\sigma_{YS,\,X30MnAl17-1} = 84\,MPa$ and $\Delta\sigma_{UTS,\,X30MnAl17-1} = 138\,MPa$. Additionally, the fine-grained states displayed a higher initial WHR, as can be seen in Fig. 2(d). This is also highlighted by the evolution of n_H with increasing strain, as shown in Fig. 2(c). At early stages of deformation ($\varepsilon_{true} < 0.05$), n_H is higher for the fine-grained material states. During further plastic deformation, n_H increases for both material states, but more significantly for the coarse-grained material states. As a result, n_H is higher for the coarse-grained material states in both alloys at approximately $\varepsilon_{true} > 0.05$. Both states of the X60Mn17 alloy showed serrated flow curves, which is common for high-manganese TWIP steels that do not contain Al [5]. None of the tested alloy states exhibited a significant necking behavior before fracture. An overview of the mechanical properties of the tested material states is given in Table 2.

The macro-texture evolution of the four material states is shown in Fig. 3 as inverse pole figures (IPF) relative to the tensile axis (TA) for the fully recrystallized states (0%), after 20% elongation and after fracture (ε_f). Additionally, the texture indices T and the respective elongation to fracture ε_f for the specific samples are given.

The IPFs indicate that while the recrystallization texture (0%) was very weak, the macro-texture evolution during tensile straining (20% and ε_f) was dominated by a stronger $< 111 >$ ||TA- and a softer $< 100 >$ ||TA-fiber. This is also visible in the corresponding

Table 2
Summary of mechanical properties of the tested material states as determined by quasistatic tensile tests. The listed values for each alloy state are the averages of all conducted tensile tests.

Designation	YS [MPa]	UTS [MPa]	ε_f [%]
X60Mn17_FG	384.7	1073.1	52.9
X60Mn17_CG	280.5	766.7	20.2
X30MnAl17-1_FG	328.9	842.8	62.7
X30MnAl17-1_CG	245.1	704.8	69.2

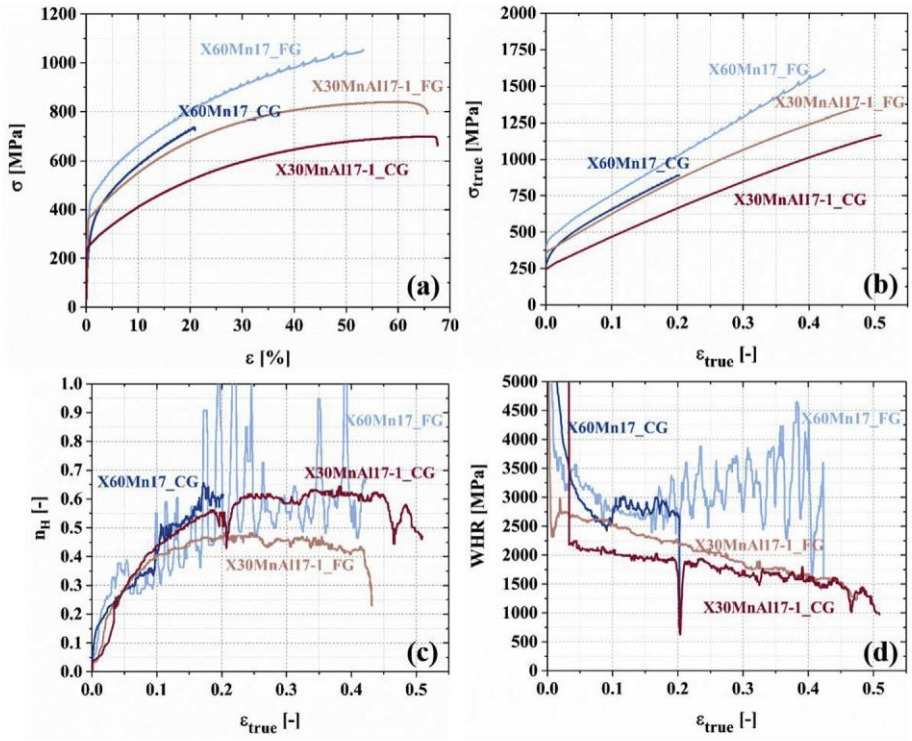


Fig. 2. (a) Engineering stress-strain curves, (b) flow curves, (c) evolution of the strain hardening exponent n_H over true strain and (d) WHR curves of the four tested alloy conditions.

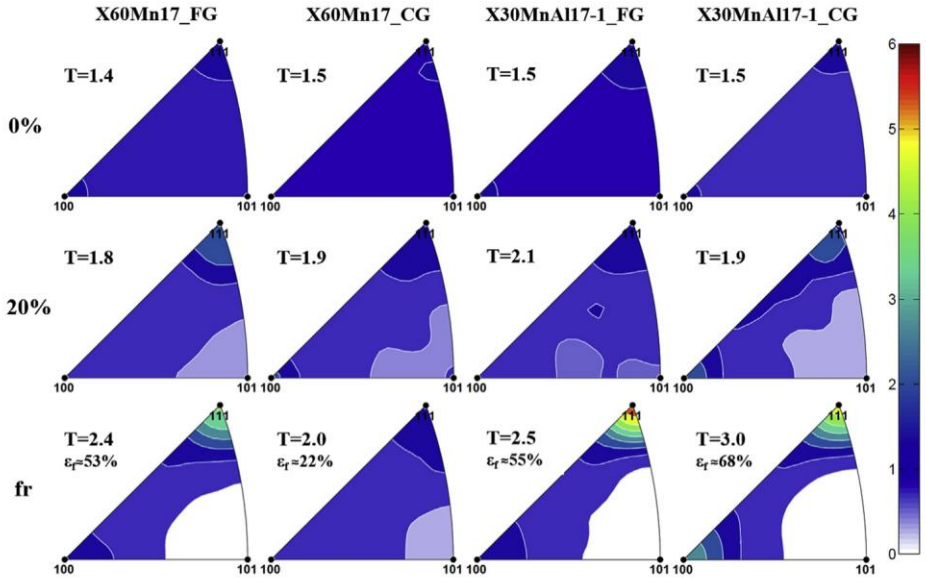


Fig. 3. IPFs parallel to TA and texture indices T for the austenitic phase of the four tested material states before deformation (0%, top row), after 20% elongation (middle row) and after fracture (bottom row).

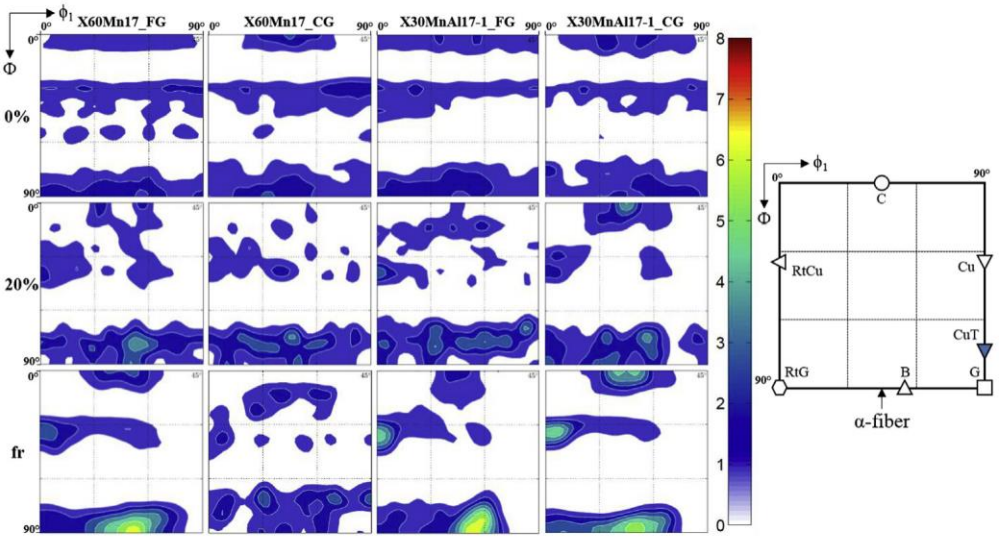


Fig. 4. Texture evolution in austenite of the four tested material states before deformation (0%, top row), after 20% elongation (middle row) and after fracture (bottom row), ODF sections at $\phi_2 = 45°$.

orientation distribution function (ODF) sections at $\phi_2 = 45°$, shown in Fig. 4.

The definition of texture components used in Fig. 4 can be found in Fig. 5 [21,22].

While all tested alloys showed a weak but complete α-fiber in the recrystallized state, the {110} < 100 > Goss (G) texture component softened during elongation, leading to an incomplete α-fiber at fracture that was dominated by the {110} < 112 > Brass (B) texture component. Additionally, the intensity of the {112} < 110 > Rotated Copper (RtCu) texture component increased, as well as the intensity of the {001} < 100 > Cube (C) and {110} < 110 > Rotated Goss (RtG) texture components. The X60Mn17_CG alloy was an exception as the texture remained very weak even after fracture. Since the total elongation of the X60Mn17_CG alloy was only slightly over 20%, differences between the texture at 20% elongation and ε_f were marginal (cf. Table 2), as is also indicated by the low increase of the texture index from T = 1.9 at 20% elongation to T = 2.0 at ε_f. The evolution of the volume fractions f of the main texture components is illustrated in Fig. 6, revealing results corresponding to the ODF sections shown in Fig. 4.

Component	Symbol	Miller indices	Euler angles [°] (ϕ_1,Φ,ϕ_2)
Brass (B)	△	{110}<122>	(55,90,45)
Goss (G)	□	{110}<100>	(90,90,45)
Cube (C)	○	{001}<100>	(45,0,45)
Copper (Cu)	▽	{112}<111>	(90,35,45)
Rotated Copper (RtCu)	◁	{112}<110>	(0,35,45)
CopperTwin(CuT)	▼	{552}<115>	(90,74,45)
Rotated Goss (RtG)	⬡	{110}<110>	(0,90,45)
α-fiber	<110> parallel to ND → includes B, G and RtG		

Fig. 5. Definition of texture components relevant for the HMnS in this work.

With increasing elongation, the volume fractions of the B and RtCu texture component significantly increased for all alloys and conditions except X60Mn17_CG, in which the B texture component slightly decreased. The volume fractions of C and RtG texture components slightly increased or remained at a similar level. In contrast to that, G and Cu texture components decreased in volume fraction.

The in-detail EBSD IPF-maps in Fig. 7 are excerpts of larger EBSD maps with the focus of comparing the twinning behavior of the (a)

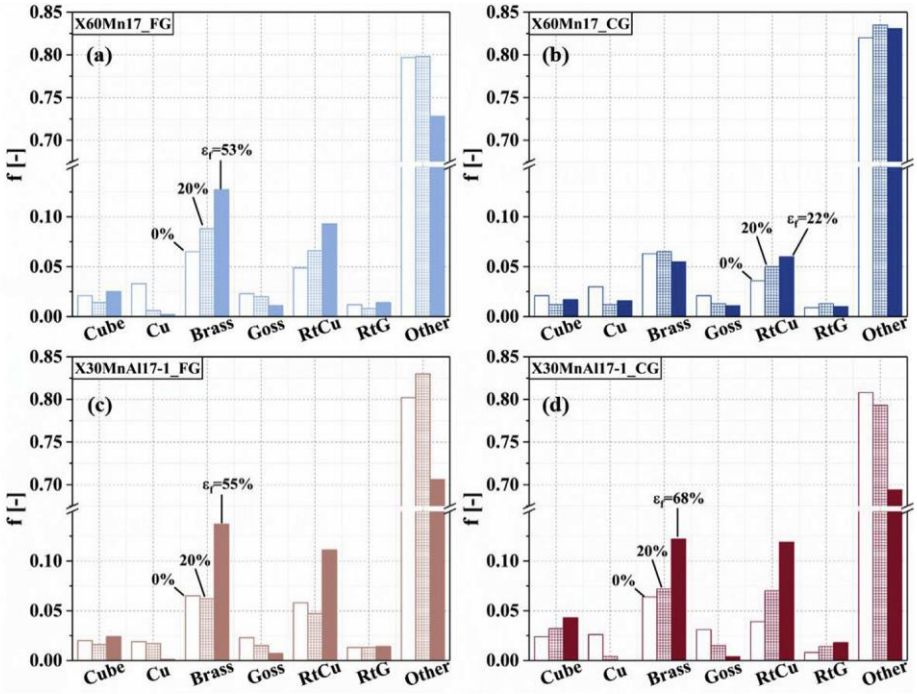


Fig. 6. Volume fractions f of the main texture components in (a) X60Mn17_FG, (b) X60Mn17_CG (c) X30MnAl17-1_FG and (d) X30MnAl17-1_CG before deformation (0%), after 20% elongation and after fracture.

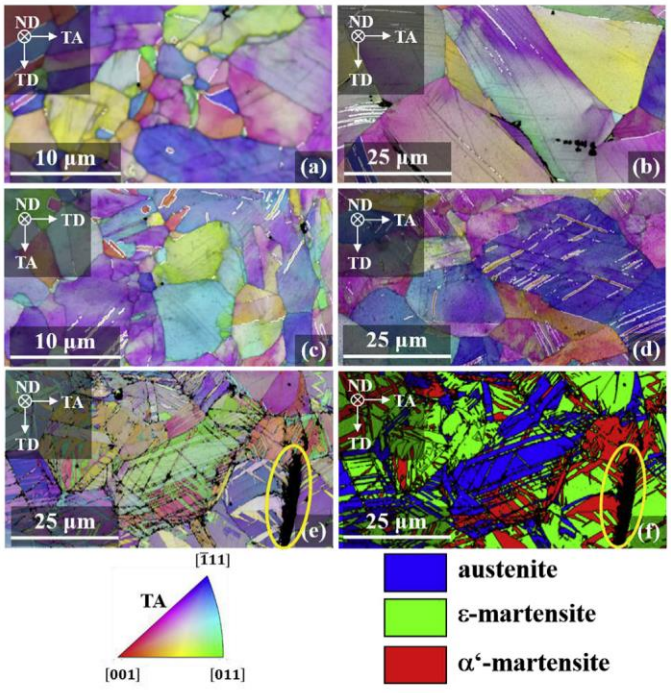


Fig. 7. (a)–(f) Image Quality (IQ) EBSD maps with overlayed IPF colorcoding relative to TA for the (a) X30MnAl17-1_FG, (b) X30MnAl17-1_CG, (c) X60Mn17_FG and (d) X60Mn17_CG alloys after 20% uniaxial deformation and for the (e) X60Mn17_CG alloy after elongation to fracture with corresponding (f) EBSD phase map. The yellow ellipse in (e) + (f) highlights a crack close to the fracture surface. Σ3-grain boundaries in (a)–(e) are highlighted in white. (For interpretation of the references to color in this figure legend, the reader is referred to the Web version of this article.)

X30MnAl17-1_FG and (c) X60Mn17_FG alloys with a coarse-grained (b) X30MnAl17-1 and (d) X60Mn17 after 20% uniaxial deformation. In addition, for the X60Mn17_CG alloy, the microstructure after fracture is shown in Fig. 7(e) + (f).

Comparing the quantity of detected boundaries between grains with Σ3 CSL (Coincidence Site Lattice) orientation relationship in Fig. 7(a)–(e), the EBSD measurements indicate that the coarse-grained alloys included more deformation twins, while the number of Σ3-grain boundaries was the lowest for the X30MnAl17-1_FG alloy. Although Σ3-grain boundaries could also be an indication of annealing twins, the shape and size of the majority of twins in Fig. 7(a)–(d) is indicative of deformation twins. As annealing twins develop during heat treatments at high temperatures, they typically have straight boundaries and are larger than deformation twins, which are usually very thin and tapered [61]. The EBSD phase map in Fig. 7(f) for the X60Mn17_CG alloy shows that a significant fraction of ε-martensite and α′-martensite is present after elongation to fracture. As highlighted in Fig. 7(f), microcracks close to the fracture surface were formed at phase boundaries of ε- and α′ during deformation.

The results of the phase analyses conducted from X-ray diffraction are summarized in Table 3.

The XRD results show that (i) the phase fractions of ε-martensite and

Table 3
Phase fractions conducted from X-ray diffraction measurements for the four tested material states.

Designation	elongation	Phase fraction [%]		
		Austenite	ε-martensite	α′-martensite
X60Mn17_FG	0%	99	1	< 1
	20%	92	3	5
	ε_f (53%)	84	10	6
X60Mn17_CG	0%	95	1	4
	20%	80	13	7
	ε_f (22%)	65	24	11
X30MnAl17-1_FG	0%	98	2	< 1
	20%	97	3	< 1
	ε_f (55%)	97	3	< 1
X30MnAl17-1_CG	0%	98	2	< 1
	20%	98	2	< 1
	ε_f (68%)	98	2	< 1

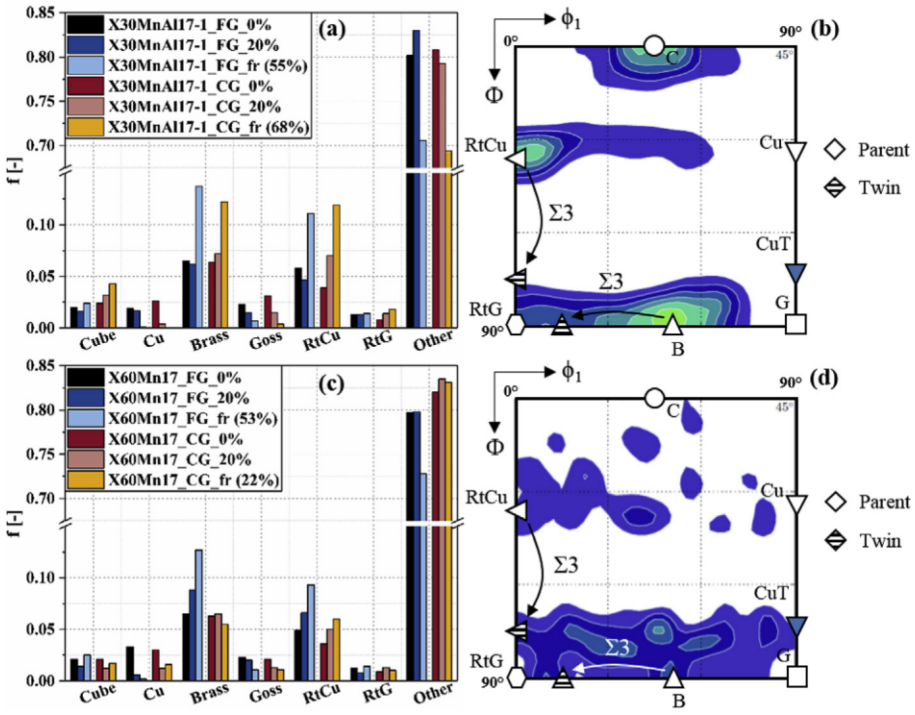


Fig. 8. Volume fraction evolution during deformation of texture components in the (a) X30MnAl17-1 and (c) X60Mn17 alloy as well as calculated positions of first-order deformation twins in the ODF section at $\varphi_2 = 45°$ for the (b) X30MnAl17-1_CG alloy after fracture and (d) the X60Mn17_CG alloy after 20% elongation.

α′-martensite were higher in the X60Mn17 alloy than in the X30MnAl17-1 alloy and (ii) that those phase fractions were higher for the X60Mn17_CG condition than in the X60Mn17_FG condition.

4. Discussion

As stated in the introduction, the low YS of many HMnS is problematic in cases of crash-relevant applications [15,16]. Accordingly, the impact of a conventional method to increase the YS like grain refinement on the mechanical properties of TWIP/TRIP HMnS is of special interest. In the following passages, first, the presented results of the tensile tests and EBSD measurements will be used to discuss the influence of grain size on the WHR and YS for the X60Mn17 and X30MnAl17-1 alloys. Afterwards, the macro-texture measurements will be analyzed with respect to the observed differences in twin volume fraction.

Fig. 2(a) shows that the decrease in d_{avg} from 16 µm in the X60Mn17_CG alloy to 4 µm in the X60Mn17_FG alloy led to a significant increase in YS. The same observation was made for the Al-alloyed HMnS, where the higher annealing temperature and annealing time increased d_{avg} from 4 µm to 22 µm. The differences in grain size resulted in different initial levels of the WHR and n_H after yielding (cf. Fig. 2(c)+(d)), which can be explained by a reduced initial mean free path (MFP) of dislocation movement after the elastic-plastic transition. This induced different dislocation-generation rates and a higher dislocation density in the fine-grained alloys at the start of plastic deformation [10,62,63]. On the other hand, the strain hardening exponent n_H of both coarse-grained alloy states is higher than for the fine-grained alloys at $\varepsilon_{true} > 0.05$ (cf. Fig. 2(c)). A rapid increase in WHR is commonly explained in terms of the activation of a secondary hardening mechanism, such as the TWIP or TRIP effect, which induces a reduction of the MFP [5,10,64]. This is in agreement with Fig. 7, where the EBSD IPF-maps indicate that after 20% uniaxial deformation, the twin density of the coarse-grained conditions (cf. Fig. 7(b)+(d)) was higher, although all alloys showed the TWIP effect. Accordingly, the n_H curves (cf. Fig. 2(c)) indicated that the initially higher WHR in the fine-grained alloys, which is due to grain refinement, is compensated by an additional hardening mechanism in the coarse-grained alloys. For the X30MnAl17-1_CG alloy, the higher strain hardening exponent n_H at $\varepsilon_{true} > 0.05$ (cf. Fig. 2(c)) compared to the fine-grained material state resulted in a very similar WHR at $\varepsilon_{true} > 0.4$ (cf. Fig. 2(d)). Since the coarse-grained alloy state exhibited a lower flow stress (cf. Fig. 2(b)), this resulted in a higher elongation to fracture compared to the fine-grained alloy state. Additionally, the XRD measurements (cf. Table 3) indicated that the ε-martensite and α′-martensite phase fractions were significantly higher for the X60Mn17_CG condition compared to the fine-grained material. Accordingly, the TWIP and TRIP effect were more active in the coarse-grained material in the sense that the volume fraction of twins and the phase fraction of martensite were substantially higher. This led to higher values of n_H. In contrast to the X60Mn17 alloy and despite similar SFE values (cf. Table 1), the phase fractions of ε-martensite and α′-martensite did not increase significantly during plastic deformation in the X30MnAl17-1 alloy. Accordingly, the X30MnAl17-1 alloy could also be classified as a TWIP alloy to clearly distinguish the deformation behavior from the TWIP/TRIP X60Mn17 alloy. The decrease in ε_f for the X60Mn17_CG alloy can be explained in terms of the high phase fractions of ε-martensite and α′-martensite at a relatively low elongation to fracture. Especially α′-martensite is significantly harder than austenite, which is due to the tetragonal distortion of the body centered cubic cell of α′-martensite [61], and influences the strain partitioning behavior, leading to the preferential accommodation of plastic deformation in austenite [65]. While the TRIP effect can have a positive impact on ductility, rapidly occurring $\gamma \rightarrow \varepsilon$ and $\gamma \rightarrow \varepsilon \rightarrow \alpha'$ transformations lead to an early saturation or conclusion of the austenite transformation. This can lead to crack initiation at phase boundaries (cf. Fig. 7(f)) [66], which in turn leads to preliminary fracture [1,13,14,67]. This is also reflected by the sharp drop in the WHR curves prior to fracture for the X60Mn17 alloys in Fig. 2(d).

The macro-texture evolution shown by means of ODF sections in Fig. 4 is in accordance with the frequently reported development of a stronger $<111>$ ||TA- and a softer $<100>$ ||TA-fiber with the main

texture components being B and RtCu (< 111 > ||TA) as well as RtG and C (< 100 > ||TA). Dislocation glide leads to a rotation of grains to orientations on the < 111 > ||TA- and < 100 > ||TA fibers. Subsequently, the Schmid factor for twinning is high in < 111 > ||TA oriented grains. Twinning in grains with orientations close to < 111 > ||TA results in twin orientations close to < 100 > ||TA [28,53–55]. Comparing the volume fractions of the texture components after deformation of the X30MnAl17-1_FG and X30MnAl17-1_CG conditions (Fig. 8(a)), the coarse-grained material shows a stronger increase of C and RtG texture components, indicating an increase in twin volume fraction, as both C and RtG are components of the < 100 > ||TA-fiber.

The relatively lower volume fraction of B in the X30MnAl17-1_CG alloy compared the fine-grained condition (cf. Fig. 8(a) + (b)), can be explained in terms of a higher fraction of grains of this orientation that exhibit deformation twinning. Fig. 8(b) + (d) show the calculated positions of first-order deformation twins in the ODF section at $\varphi_2 = 45°$ for the B and RtCu texture components. Due to the use of a 15° radius around the ideal position to calculate the volume fraction of each texture component, the volume fraction of RtG is increased by a fraction of deformation twins formed in B-oriented grains, which appear in the $\varphi_2 = 45°$ ODF section at $\Phi = 90°$ and slightly higher φ_1-values then the RtG texture component. Similarly, this is also the case for deformation twins in RtCu-oriented grains, which appear in the $\varphi_2 = 45°$ ODF section at $\varphi_1 = 0°$ and slightly lower Φ-values then the RtG texture component. Comparing the ODF sections at $\varphi_2 = 45°$ after fracture for the X30MnAl17-1 alloy (cf. Fig. 4), the X30MnAl17-1_CG alloy revealed a slight peak in intensity at the position of deformation twins in B-oriented grains while the X30MnAl17-1_FG alloy did not. Accordingly, this also indicates that the slightly increased volume fraction of RtG and slightly lower volume fraction of B in the X30MnAl17-1_CG compared to the fine-grained condition was due to an increase in twin volume fraction. Comparing the X30MnAl17-1 alloys after 20% elongation, the increased twin volume fraction in the coarse-grained alloy results in a higher volume fraction of C (cf. Figs. 4 and 6(b) and 8(a)) and a stronger < 100 > ||TA-fiber in general, as shown in the IPFs in Fig. 3.

Comparing the X60Mn17 alloy conditions, the volume fraction of the B and RtCu texture components (< 111 > ||TA-fiber) in the coarse-grained material state increased less than in the X30MnAl17-1 alloy. This can be explained by an increase in twin volume fraction for the coarse-grained alloy (similar as in the X30MnAl17-1 alloy) on the one hand and the partial transformation to ε-martensite and α′-martensite on the other hand. The nucleation of martensite is promoted in areas of high dislocation density, such as twin-twin intersections and ε-martensite-twin intersections [1,13,68,69]. Since < 111 > ||TA is a favorable orientation for deformation twinning, more nucleation sites for ε-martensite and α′-martensite are available in grains of such orientation [53]. With increasing deformation, the phase fraction of ε-martensite and α′-martensite increased (cf. Table 3), leading to a reduced phase fraction of austenite and a reduced volume fraction of the < 111 > ||TA-fiber texture components B and RtCu.

The differences in twin volume fraction between the X60Mn17 alloy and the X30MnAl17-1 alloy in the EBSD maps in Fig. 7 can also be discussed in context of the texture evolution in both alloys. The lower relative increase of the < 111 > ||TA-fiber texture components B and RtCu in the X60Mn17 alloy after 20% elongation shown in the corresponding ODFs (cf. Figs. 4 and 8(d)) compared to those of the X30MnAl17-1 alloy indicate a higher twin volume fraction in the Al-free alloy. This is reflected by two findings: Firstly, the shift in intensity in the ODF sections at $\varphi_2 = 45°$ towards the position of first-order deformation twins of RtCu indicates that 20% elongation led to a higher volume fraction of first-order deformation twins in the Al-free HMnS. Secondly, the observation that the intensities around the B texture component increased only slightly suggests that a higher volume fraction of grains exhibited deformation twinning or underwent a martensitic transformation instead of rotating towards the < 111 > ||TA-fiber. Because the nucleation of martensite is promoted at twin-twin intersections, the lower twin volume fraction in the X30MnAl17-1 alloy resulted in lower overall phase fractions of martensite (cf. Table 3). Accordingly, the ductility is not negatively impacted by coarser grains in the X30MnAl17-1 alloy, as can be seen in Fig. 2. The difference in twin volume fraction for the X60Mn17 and X30MnAl17-1 alloys can be explained in terms of the impact of SRO [38,39,50,70]. Several authors point to a pinning effect of C and/or SRO clusters on the trailing partial dislocation of a stacking fault, increasing the stacking fault width and facilitating deformation twinning [50–52,70]. Al reduces the diffusion rate of C atoms in austenitic steels and increases the lattice parameter [5,43–48,71–73]. As a result, the distance of short-range jumps of C into preferential lattice positions, the likelihood of short-range jumps and the dislocation-pinning effect of SRO are reduced in Al-alloyed HMnS [39,61,70,74].

To summarize, EBSD and macro-texture analysis showed that the coarse-grained condition of both alloys had a higher twin volume fraction, which in the case of the X60Mn17 alloy conditions resulted in a subsequently increased phase fractions of ε-martensite and α′-martensite. Due to the high hardness of α′-martensite, the elongation to fracture of the coarse-grained X60Mn17 condition was reduced.

5. Conclusions

The impact of grain size on the mechanical properties, deformation mechanisms and texture development of two high-manganese steels (HMnS) was investigated in this study by means of mechanical testing, microstructural and texture analysis. Overall, the following conclusions can be drawn:

- A decrease in average grain size of the tested alloys from 16 µm (X60Mn17_CG) and 22 µm (X30MnAl17-1_CG) to 4 µm (X60Mn17_FG and X30MnAl17-1_FG) led to a considerable increase in yield strength (YS) and ultimate tensile strength (UTS). In the case of the X60Mn17 alloy, the YS increased from 275 MPa to 381 MPa while the elongation to fracture also increased significantly from 22% to 53%. For the X30MnAl17-1 alloy, the decrease in average grain size led to an increase in YS from 245 MPa to 338 MPa, which was accompanied by a small decrease in total elongation from 69% to 63%.
- The work-hardening rate (WHR) after the onset of plastic deformation is higher for the fine-grained material states, which is due to the initially smaller mean free path of dislocation movement. However, the strain hardening exponent n_H is higher in the coarse-grained material states at $\varepsilon_{true} > 0.05$. For the X30MnAl17-1 alloy, this difference in work-hardening behavior results in a higher elongation to fracture in the coarse-grained alloy.
- The higher values of n_H at $\varepsilon_{true} > 0.05$ for the coarse-grained states of both tested HMnS is due to a higher twin volume fraction in the coarse-grained condition, which effectively reduces the mean free path of dislocation movement during plastic deformation. Additionally, the higher twin volume fraction in the X60Mn17_CG condition facilitates the γ→ε- and/or γ→ε→α′-transformation, leading to higher martensitic phase fractions. In the X60Mn17_CG alloy, the high volume fraction of hard α′-martensite leads to early fracture.
- The impact of the influence of grain size on the activation of secondary deformation mechanisms is accompanied by changes in the texture development. The more pronounced TWIP- and/or TRIP-effect in the coarse-grained conditions lead to a relative softening of the < 111 > ||TA-fiber in favor of grains with orientations close to the < 100 > ||TA-fiber.
- This can be explained by a preferred activation of the TRIP and TWIP effect in favorably oriented grains close to the < 111 > ||TA-fiber in austenite. For the TWIP effect, this results in first-order deformation twins close to the < 100 > ||TA-fiber. Accordingly, both secondary deformation mechanisms lower the volume fraction

of austenite grains rotating towards the < 111 > ||TA-fiber during deformation.

Conflicts of interest

The authors declare no conflict of interest.

Contributors

Simon Sevsek conducted the mechanical testing and performed the EBSD measurements. Frederike Brasche conducted the phase analysis and XRD measurements. All authors participated in the analysis of experimental data and contributed in the writing process.

Data availability

The raw data required to reproduce these findings cannot be shared at this time as the data also forms part of an ongoing study. The processed data required to reproduce these findings cannot be shared at this time due to legal or ethical reasons.

Acknowledgements

The authors are grateful for the financial support of the Deutsche Forschungsgemeinschaft within the Collaborative Research Centre (SFB) 761 “Steel – ab initio”.

References

[1] B.C. DeCooman, High Mn TWIP steel and medium Mn steel, in: R. Rana, S.B. Singh (Eds.), Automotive Steels: Design, Metallurgy, Processing and Applications, Woodhead Publishing, 2017, pp. 317–385.
[2] B.C. DeCooman, O. Kwon, K.-G. Chin, State-of-the-knowledge on TWIP steel, Mater. Sci. Technol. 28 (5) (2012) 513–527 https://doi.org/10.1179/1743284711Y.0000000095.
[3] S. Allain, J.P. Chateau, O. Bouaziz, A physical model of the twinning-induced plasticity effect in a high manganese austenitic steel, Mater. Sci. Eng., A 387–389 (2004) 143–147 https://doi.org/10.1016/j.msea.2004.01.060.
[4] D.T. Pierce, J.A. Jiménez, J. Bentley, D. Raabe, C. Oskay, J.E. Wittig, The influence of manganese content on the stacking fault and austenite/ε-martensite interfacial energies in Fe–Mn–(Al–Si) steels investigated by experiment and theory, Acta Mater. 68 (2014) 238–253 https://doi.org/10.1016/j.actamat.2014.01.001.
[5] B.C. DeCooman, Y. Estrin, S.K. Kim, Twinning-induced plasticity (TWIP) steels, Acta Mater. 142 (2018) 283–362 https://doi.org/10.1016/j.actamat.2017.06.046.
[6] O. Bouaziz, S. Allain, C.P. Scott, P. Cugy, D. Barbier, High manganese austenitic twinning induced plasticity steels: a review of the microstructure properties relationships, Curr. Opin. Solid State Mater. Sci. 15 (4) (2011) 141–168 https://doi.org/10.1016/j.cossms.2011.04.002.
[7] A. Saeed-Akbari, J. Imlau, U. Prahl, W. Bleck, Derivation and variation in composition-dependent stacking fault energy maps based on subregular solution model in high-manganese steels, Metall. Mater. Trans. 40 (13) (2009) 3076–3090 https://doi.org/10.1007/s11661-009-0050-8.
[8] O. Bouaziz, S. Allain, C. Scott, Effect of grain and twin boundaries on the hardening mechanisms of twinning-induced plasticity steels, Scripta Mater. 58 (6) (2008) 484–487 https://doi.org/10.1016/j.scriptamat.2007.10.050.
[9] O. Bouaziz, Strain-hardening of twinning-induced plasticity steels, Scripta Mater. 66 (12) (2012) 982–985 https://doi.org/10.1016/j.scriptamat.2011.11.029.
[10] D.R. Steinmetz, T. Jäpel, B. Wietbrock, P. Eisenlohr, I. Gutierrez-Urrutia, A. Saeed-Akbari, T. Hickel, F. Roters, D. Raabe, Revealing the strain-hardening behavior of twinning-induced plasticity steels: theory, simulations, experiments, Acta Mater. 61 (2) (2013) 494–510 https://doi.org/10.1016/j.actamat.2012.09.064.
[11] J.-K. Kim, M.-H. Kwon, B.C. de Cooman, On the deformation twinning mechanisms in twinning-induced plasticity steel, Acta Mater. 141 (2017) 444–455 https://doi.org/10.1016/j.actamat.2017.09.043.
[12] O. Grässel, L. Krüger, G. Frommeyer, L.W. Meyer, High strength Fe–Mn–(Al, Si) TRIP/TWIP steels development - properties - application, Int. J. Plast. 16 (10–11) (2000) 1391–1409 https://doi.org/10.1016/S0749-6419(00)00015-2.
[13] S. Pramanik, A.A. Gazder, A.A. Saleh, E.V. Pereloma, Nucleation, coarsening and deformation accommodation mechanisms of ε-martensite in a high manganese steel, Mater. Sci. Eng., A 731 (2018) 506–519 https://doi.org/10.1016/j.msea.2018.06.024.
[14] Y. Lü, B. Hutchinson, D.A. Molodov, G. Gottstein, Effect of deformation and annealing on the formation and reversion of ε-martensite in an Fe–Mn–C alloy, Acta Mater. 58 (8) (2010) 3079–3090 https://doi.org/10.1016/j.actamat.2010.01.045.
[15] M. Bambach, L. Conrads, M. Daamen, O. Güvenç, G. Hirt, Enhancing the crashworthiness of high-manganese steel by strain-hardening engineering, and tailored folding by local heat-treatment, Mater. Des. 110 (2016) 157–168 https://doi.org/10.1016/j.matdes.2016.07.065.
[16] C. Haase, T. Ingendahl, O. Güvenc, M. Bambach, W. Bleck, D.A. Molodov, L.A. Barrales-Mora, On the applicability of recovery-annealed Twinning-Induced Plasticity steels: potential and limitations, Mater. Sci. Eng., A 649 (2016) 74–84 https://doi.org/10.1016/j.msea.2015.09.096.
[17] O. Bouaziz, D. Barbier, Benefits of recovery and partial recrystallization of nano-twinned austenitic steels, Adv. Eng. Mater. 15 (10) (2013) 976–979 https://doi.org/10.1002/adem.201300045.
[18] F. Brasche, C. Haase, L.A. Barrales-Mora, D.A. Molodov, Comparative study of the influence of reversion- and recovery- annealing on the mechanical behavior of high-manganese steels with varying stacking fault energy, Steel Res. Int. 07 (2017) 1700377 https://doi.org/10.1002/srin.201700377.
[19] S. Kang, J.-G. Jung, M. Kang, W. Woo, Y.-K. Lee, The effects of grain size on yielding, strain hardening, and mechanical twinning in Fe–18Mn–0.6C–1.5Al twinning-induced plasticity steel, Mater. Sci. Eng., A 652 (2016) 212–220 https://doi.org/10.1016/j.msea.2015.11.096.
[20] J.-H. Kang, S. Duan, S.-J. Kim, W. Bleck, Grain boundary strengthening in high Mn austenitic steels, Metall. Mater. Trans. 47 (5) (2016) 1918–1921 https://doi.org/10.1007/s11661-016-3399-5.
[21] C. Haase, L.A. Barrales-Mora, F. Roters, D.A. Molodov, G. Gottstein, Applying the texture analysis for optimizing thermomechanical treatment of high manganese twinning-induced plasticity steel, Acta Mater. 80 (2014) 327–340 https://doi.org/10.1016/j.actamat.2014.07.068.
[22] F. Berrenberg, C. Haase, L.A. Barrales-Mora, D.A. Molodov, Enhancement of the strength-ductility combination of twinning-induced/transformation-induced plasticity steels by reversion annealing, Mater. Sci. Eng., A 681 (2017) 56–64 https://doi.org/10.1016/j.msea.2016.10.109.
[23] S. Takaki, D. Akama, N. Nakada, T. Tsuchiyama, Effect of grain boundary segregation of interstitial elements on Hall-petch coefficient in steels, Mater. Trans. 55 (1) (2014) 28–34 https://doi.org/10.2320/matertrans.MA201314.
[24] G. Dini, R. Ueji, A. Najafizadeh, Grain size dependence of the flow stress of TWIP steel, Inside MS 654–656 (2010) 294–297 https://doi.org/10.4028/www.scientific.net/MSF.654-656.294.
[25] A. Dumay, J.P. Chateau, S. Allain, S. Migot, O. Bouaziz, Influence of addition elements on the stacking-fault energy and mechanical properties of an austenitic Fe–Mn–C steel, Mater. Sci. Eng., A 483–484 (2008) 184–187 https://doi.org/10.1016/j.msea.2006.12.170.
[26] A. Saeed-Akbari, L. Mosecker, A. Schwedt, W. Bleck, Characterization and prediction of flow behavior in high-manganese twinning induced plasticity steels: Part I. Mechanism maps and work-hardening behavior, Metall. Mater. Trans. 43 (5) (2012) 1688–1704 https://doi.org/10.1007/s11661-011-0993-4.
[27] F.d.l. Cuevas, M. Reis, A. Ferraiuolo, G. Pratolongo, L.P. Karjalainen, J. Alkorta, J. Gil Sevillano, Hall-Petch relationship of a TWIP steel, Key Eng. Mater. 423 (2010) 147–152 https://doi.org/10.4028/www.scientific.net/KEM.423.147.
[28] I. Gutierrez-Urrutia, S. Zaefferer, D. Raabe, The effect of grain size and grain orientation on deformation twinning in a Fe–22wt.% Mn–0.6wt.% C TWIP steel, Mater. Sci. Eng., A 527 (15) (2010) 3552–3560 https://doi.org/10.1016/j.msea.2010.02.041.
[29] M.A. Meyers, O. Vöhringer, V.A. Lubarda, The onset of twinning in metals: a constitutive description, Acta Mater. 49 (19) (2001) 4025–4039 https://doi.org/10.1016/S1359-6454(01)00300-7.
[30] I. Gutierrez-Urrutia, D. Raabe, Grain size effect on strain hardening in twinning-induced plasticity steels, Scripta Mater. 66 (12) (2012) 992–996 https://doi.org/10.1016/j.scriptamat.2012.01.037.
[31] R. Ueji, N. Tsuchida, D. Terada, N. Tsuji, Y. Tanaka, A. Takemura, K. Kunishige, Tensile properties and twinning behavior of high manganese austenitic steel with fine-grained structure, Scripta Mater. 59 (9) (2008) 963–966 https://doi.org/10.1016/j.scriptamat.2008.06.050.
[32] L. Chen, Y. Zhao, X. Qin, Some aspects of high manganese twinning-induced plasticity (TWIP) steel, a review, Acta Metall. Sin. 26 (1) (2013) 1–15 https://doi.org/10.1007/s40195-012-0501-x.
[33] Z.Y. Liang, Y.Z. Li, M.X. Huang, The respective hardening contributions of dislocations and twins to the flow stress of a twinning-induced plasticity steel, Scripta Mater. 112 (2016) 28–31 https://doi.org/10.1016/j.scriptamat.2015.09.003.
[34] O. Bouaziz, H. Zurob, B. Chehab, J.D. Embury, S. Allain, M. Huang, Effect of chemical composition on work hardening of Fe-Mn-C TWIP steels, Mater. Sci. Technol. 27 (3) (2011) 707–709 https://doi.org/10.1179/026708309X12535382371852.
[35] N. Ohkubo, K. Miyakusu, Y. Uematsu, H. Kimura, Effect of alloying elements on the mechanical properties of the stable Austenitic stainless steel, ISIJ Int. 34 (9) (1994) 764–772 https://doi.org/10.2355/isijinternational.34.764.
[36] H. Sieurin, J. Zander, R. Sandström, Modelling solid solution hardening in stainless steels, Mater. Sci. Eng., A 415 (2006) 66–71 https://doi.org/10.1016/j.msea.2005.09.031.
[37] W.S. Choi, B.C. de Cooman, S. Sandlöbes, D. Raabe, Size and orientation effects in partial dislocation-mediated deformation of twinning-induced plasticity steel micro-pillars, Acta Mater. 98 (2015) 391–404 https://doi.org/10.1016/j.actamat.2015.06.065.
[38] J.-H. Kang, T. Ingendahl, J. von Appen, R. Dronskowski, W. Bleck, Impact of short-range ordering on yield strength of high manganese austenitic steels, Mater. Sci. Eng., A 614 (2014) 122–128 https://doi.org/10.1016/j.msea.2014.07.016.
[39] S. Sevsek, W. Bleck, Ab initio-based modelling of the yield strength in high-manganese steels, Metals 8 (1) (2018) 34 https://doi.org/10.3390/met8010034.
[40] K. Oda, H. Fujimura, H. Ino, Local interactions in carbon-carbon and carbon-M (M: Al,Mn,Ni) atomic paris in FCC gamma-iron, J. Phys. Condens. Matter 6 (3) (1994) 679–692 https://doi.org/10.1088/0953-8984/6/3/008.
[41] K. Oda, N. Kondo, K. Shibata, X-ray absorption fine structure analysis of interstitial

(C, N)-Substitutional (Cr) complexes in austenitic stainless steels, ISIJ Int. 30 (8) (1990) 625–631 https://doi.org/10.2355/isijinternational.30.625.
[42] A.D. Pelton, Y.-B. Kang, Modeling short-range ordering in solutions, Int. J. Mater. Res. 98 (10) (2007) 907–917 https://doi.org/10.3139/146.101554.
[43] A.P. Bentley, Ordering in Fe-Mn-Al-C austenite, J. Mater. Sci. Lett. 5 (9) (1986) 907–908 https://doi.org/10.1007/BF01729270.
[44] T. Timmerscheidt, R. Dronskowski, An ab initio study of carbon-induced ordering in austenitic Fe-Mn-Al-C alloys, Steel Res. Int. 88 (1) (2017) 1–10 https://doi.org/10.1002/srin.201600292.
[45] J. von Appen, R. Dronskowski, Carbon-induced ordering in manganese-rich austenite - a density-functional total-energy and chemical-bonding study, Steel Res. Int. 82 (2) (2011) 101–107 https://doi.org/10.1002/srin.201000260.
[46] W. Song, W. Zhang, J. von Appen, R. Dronskowski, W. Bleck, k-Phase Formation in Fe-Mn-Al-C Austenitic Steels, steel res, interactions 86 (10) (2015) 1161–1169 https://doi.org/10.1002/srin.201400587.
[47] L.N. Bartlett, D.C. van Aken, J. Medvedeva, D. Isheim, N.I. Medvedeva, K. Song, An atom probe study of kappa carbide precipitation and the effect of silicon addition, Metall. Mater. Trans. 45 (5) (2014) 2421–2435 https://doi.org/10.1007/s11661-014-2187-3.
[48] M.J. Yao, E. Welsch, D. Ponge, S.M.H. Haghighat, S. Sandlöbes, P. Choi, M. Herbig, I. Bleskov, T. Hickel, M. Lipinska-Chwalek, P. Shanthraj, C. Scheu, S. Zaefferer, B. Gault, D. Raabe, Strengthening and strain hardening mechanisms in a precipitation-hardened high-Mn lightweight steel, Acta Mater. 140 (2017) 258–273 https://doi.org/10.1016/j.actamat.2017.08.049.
[49] W. Song, D. Bogdanovski, A. Yildiz, J. Houston, R. Dronskowski, W. Bleck, On the Mn–C short-range ordering in a high-strength high-ductility steel: small angle neutron scattering and ab initio investigation, Metals 8 (1) (2018) 44 https://doi.org/10.3390/met8010044.
[50] S.-J. Lee, J. Kim, S.N. Kane, B.C. DeCooman, On the origin of dynamic strain aging in twinning-induced plasticity steels, Acta Mater. 59 (17) (2011) 6809–6819 https://doi.org/10.1016/j.actamat.2011.07.040.
[51] S. Allain, O. Bouaziz, T. Lebedkina, M. Lebyodkin, Relationship between relaxation mechanisms and strain aging in an austenitic FeMnC steel, Scripta Mater. 64 (8) (2011) 741–744 https://doi.org/10.1016/j.scriptamat.2010.12.039.
[52] M. Koyama, T. Sawaguchi, K. Tsuzaki, Deformation twinning behavior of twinning-induced plasticity steels with different carbon concentrations – Part 2: proposal of dynamic-strain-aging-assisted deformation twinning, ISIJ Int. 55 (8) (2015) 1754–1761 https://doi.org/10.2355/isijinternational.ISIJINT-2015-070.
[53] I. Gutierrez-Urrutia, D. Raabe, Dislocation and twin substructure evolution during strain hardening of an Fe–22wt.% Mn–0.6wt.% C TWIP steel observed by electron channeling contrast imaging, Acta Mater. 59 (16) (2011) 6449–6462 https://doi.org/10.1016/j.actamat.2011.07.009.
[54] D. Barbier, N. Gey, S. Allain, N. Bozzolo, M. Humbert, Analysis of the tensile behavior of a TWIP steel based on the texture and microstructure evolutions, Mater. Sci. Eng., A 500 (1–2) (2009) 196–206 https://doi.org/10.1016/j.msea.2008.09.031.
[55] A.A. Saleh, E.V. Pereloma, A.A. Gazder, Microstructure and texture evolution in a twinning-induced-plasticity steel during uniaxial tension, Acta Mater. 61 (7) (2013) 2671–2691 https://doi.org/10.1016/j.actamat.2013.01.051.
[56] C. Haase, M. Kühbach, L.A. Barrales-Mora, S.L. Wong, F. Roters, D.A. Molodov, G. Gottstein, Recrystallization behavior of a high-manganese steel: experiments and simulations, Acta Mater. 100 (2015) 155–168 https://doi.org/10.1016/j.actamat.2015.08.057.
[57] L. Bracke, K. Verbeken, L. Kestens, J. Penning, Microstructure and texture evolution during cold rolling and annealing of a high Mn TWIP steel, Acta Mater. 57 (5) (2009) 1512–1524 https://doi.org/10.1016/j.actamat.2008.11.036.
[58] Y. Lü, D.A. Molodov, G. Gottstein, Recrystallization kinetics and microstructure evolution during annealing of a cold-rolled Fe–Mn–C alloy, Acta Mater. 59 (8) (2011) 3229–3243 https://doi.org/10.1016/j.actamat.2011.01.063.
[59] F. Bachmann, R. Hielscher, H. Schaeben, Texture analysis with MTEX – free and open source software toolbox, SSP 160 (2010) 63–68 https://doi.org/10.4028/www.scientific.net/SSP.160.63.
[60] R. Hielscher, H. Schaeben, A novel pole figure inversion method: specification of the MTEX algorithm, J. Appl. Crystallogr. 41 (6) (2008) 1024–1037 https://doi.org/10.1107/S0021889808030112.
[61] G. Gottstein, Materialwissenschaft und Werkstofftechnik: Physikalische Grundlagen, fourth ed., Springer-Verlag Berlin Heidelberg, Berlin, Heidelberg, 2014.
[62] F. Roters, D. Raabe, G. Gottstein, Work hardening in heterogeneous alloys—a microstructural approach based on three internal state variables, Acta Mater. 48 (17) (2000) 4181–4189 https://doi.org/10.1016/S1359-6454(00)00289-5.
[63] J.-H. Kang, T. Ingendahl, W. Bleck, A constitutive model for the tensile behaviour of TWIP steels: composition and temperature dependencies, Mater. Des. 90 (2016) 340–349 https://doi.org/10.1016/j.matdes.2015.10.126.
[64] S.L. Wong, M. Madivala, U. Prahl, F. Roters, D. Raabe, A crystal plasticity model for twinning- and transformation-induced plasticity, Acta Mater. 118 (2016) 140–151 https://doi.org/10.1016/j.actamat.2016.07.032.
[65] M.I. Latypov, S. Shin, B.C. de Cooman, H.S. Kim, Micromechanical finite element analysis of strain partitioning in multiphase medium manganese TWIP + TRIP steel, Acta Mater. 108 (2016) 219–228 https://doi.org/10.1016/j.actamat.2016.02.001.
[66] M. Madivala, A. Schwedt, S.L. Wong, F. Roters, U. Prahl, W. Bleck, Temperature dependent strain hardening and fracture behavior of TWIP steel, Int. J. Plast. 104 (2018) 80–103 https://doi.org/10.1016/j.ijplas.2018.02.001.
[67] P.J. Gibbs, B.C. de Cooman, D.W. Brown, B. Clausen, J.G. Schroth, M.J. Merwin, D.K. Matlock, Strain partitioning in ultra-fine grained medium-manganese transformation induced plasticity steel, Mater. Sci. Eng., A 609 (2014) 323–333 https://doi.org/10.1016/j.msea.2014.03.120.
[68] S. Lee, B.C. de Cooman, Tensile behavior of intercritically annealed 10 pct Mn multi-phase steel, Metall. Mater. Trans. 45 (2) (2014) 709–716 https://doi.org/10.1007/s11661-013-2047-6.
[69] S. Lee, B.C. de Cooman, Annealing temperature dependence of the tensile behavior of 10 pct Mn multi-phase TWIP-TRIP steel, Metall. Mater. Trans. 45 (13) (2014) 6039–6052 https://doi.org/10.1007/s11661-014-2540-6.
[70] S. Sevsek, F. Brasche, C. Haase, W. Bleck, Combined deformation twinning and short-range ordering causes serrated flow in high-manganese steels, Mater. Sci. Eng., A 746 (2019) 434–442 https://doi.org/10.1016/j.msea.2019.01.042.
[71] N.I. Medvedeva, M.S. Park, D.C. van Aken, J.E. Medvedeva, First-principles study of Mn, Al and C distribution and their effect on stacking fault energies in fcc Fe, J. Alloy. Comp. 582 (2014) 475–482 https://doi.org/10.1016/j.jallcom.2013.08.089.
[72] T. Timmerscheidt, P. Dey, D. Bogdanovski, J. von Appen, T. Hickel, J. Neugebauer, R. Dronskowski, The role of κ-carbides as hydrogen traps in high-Mn steels, Metals 7 (7) (2017) 264 https://doi.org/10.3390/met7070264.
[73] D.E. Jiang, E.A. Carter, Carbon dissolution and diffusion in ferrite and austenite from first principles, Phys. Rev. B 67 (21) (2003) 1045 https://doi.org/10.1103/PhysRevB.67.214103.
[74] M.C. Li, H. Chang, P.W. Kao, D. Gan, The effect of Mn and Al contents on the solvus of κ phase in austenitic Fe-Mn-Al-C alloys, Mater. Chem. Phys. 59 (1) (1999) 96–99 https://doi.org/10.1016/S0254-0584(99)00026-7.

Chapter V

Strain-Rate-Dependent Deformation Behavior and Mechanical Properties of a Multiphase Medium-Manganese Steel

S. Sevsek, C. Haase and W. Bleck
Metals 9 (3) (2019) 344
https://doi.org/10.3390/met9030344

Chapter V investigates the strain-rate dependence of the deformation behavior and mechanical properties of an intercritically-annealed medium-manganese steel with a multiphase microstructure consisting of 45% recrystallized or reverted γ as well as 55% recrystallized α and lamellar α'. In-situ tensile tests using digital image correlation reveal that the strain localization behavior shows a strong dependence on the strain rate, as serrated flow only occurs at very low strain rates. The new concept of the strain-rate-dependent strength of α and α' relative to γ is introduced in order to explain the different mechanisms of strain accommodation on a microstructural scale, including the strain-rate dependence of the activation of the TRIP effect. Overall, the strain-rate dependence of the macroscopic mechanical properties can be explained by the strain-rate-dependent deformation behavior on the microscale.

metals

MDPI

Article

Strain-Rate-Dependent Deformation Behavior and Mechanical Properties of a Multi-Phase Medium-Manganese Steel

Simon Sevsek *, Christian Haase and Wolfgang Bleck

Steel Institute, RWTH Aachen University, 52072 Aachen, Germany; christian.haase@iehk.rwth-aachen.de (C.H.); bleck@iehk.rwth-aachen.de (W.B.)

* Correspondence: simon.sevsek@iehk.rwth-aachen.de; Tel.: +49-241-809-0138

Received: 3 March 2019; Accepted: 15 March 2019; Published: 18 March 2019

check for updates

Abstract: The strain-rate-dependent deformation behavior of an intercritically annealed X6MnAl12-3 medium-manganese steel was analyzed with respect to the mechanical properties, activation of deformation-induced martensitic phase transformation, and strain localization behavior. Intercritical annealing at 675 °C for 2 h led to an ultrafine-grained multi-phase microstructure with 45% of mostly equiaxed, recrystallized austenite and 55% ferrite or recovered, lamellar martensite. In-situ digital image correlation methods during tensile tests revealed strain localization behavior during the discontinuous elastic-plastic transition, which was due to the localization of strain in the softer austenite in the early stages of plastic deformation. The dependence of the macroscopic mechanical properties on the strain rate is due to the strain-rate sensitivity of the microscopic deformation behavior. On the one hand, the deformation-induced phase transformation of austenite to martensite showed a clear strain-rate dependency and was partially suppressed at very low and very high strain rates. On the other hand, the strain-rate-dependent relative strength of ferrite and martensite compared to austenite influenced the strain partitioning during plastic deformation, and subsequently, the work-hardening rate. As a result, the tested X6MnAl12-3 medium-manganese steel showed a negative strain-rate sensitivity at very low to medium strain rates and a positive strain-rate sensitivity at medium to high strain rates.

Keywords: medium-manganese steel; TRIP; strain-rate sensitivity; Lüders band; serrated flow; in-situ DIC tensile tests

1. Introduction

Increasing demands for fuel-efficient vehicles led to the development of Advanced High-Strength Steels (AHSS). First generation AHSS usually possess a ferritic matrix and employs phase fractions of harder phases like martensite, bainite, and metastable retained austenite to increase the product of ultimate tensile strength (UTS) and elongation to fracture ε_f < 20 GPa% [1,2]. In search of further improvement of this so-called ECO-Index, the second generation of AHSS with fully austenitic microstructures was developed. Reaching an ECO-Index of >50 GPa%, the remarkable mechanical properties result from very high dislocation densities in combination with the activation of additional deformation mechanisms in addition to dislocation slip which increase the work-hardening rate (WHR) [3,4]. The critical parameter governing the activation of those secondary deformation mechanisms, such as deformation twinning (TWinning-Induced Plasticity–TWIP) and deformation-induced phase transformation (TRansformation-Induced Plasticity–TRIP), is the material's stacking fault energy (SFE), which is primarily a function of the chemical composition [5–8]. As the main alloying element of the second generation AHSS is Mn with alloying contents <35 wt.%, those steels are also termed high-manganese steels (HMnS).

While the total energy-absorption potential of HMnS makes them an attractive option for crash-relevant parts in the automotive industry, several aspects have hindered widespread industrial application. Due to the design criteria of automotive parts, the available deformation volume is rather low, emphasizing the importance of a high yield strength (YS), which HMnS do not possess compared to their UTS [9,10]. Additionally, during quasistatic tensile tests, strain localization phenomena have frequently been observed that result in the propagation of deformation bands in the sample and subsequent serrated flow curves [11–14]. The third generation of AHSS has drawn significant interest, as they have reduced Mn contents of 3–12 wt.% and are described as medium-manganese steels (MMnS). Intercritical annealing (IA) in the two-phase region of austenite (γ) and ferrite (α) is conventionally employed to develop an ultrafine-grained (UFG) multi-phase microstructure consisting of γ, α, and martensite (α'), which increases the YS considerably, while retaining good ductility [1,2]. However, a discontinuous elastic-plastic transition during quasistatic tensile testing has frequently been reported [15].

In the past, there have been numerous efforts to analyze the impact of annealing parameters during the IA on the initial microstructure and the partitioning of alloying elements on the individual phases [1,16–22]. Subsequent studies have dealt with the activation of secondary deformation mechanisms in γ and the strain partitioning in the microstructural constituents of different hardness [23–26]. However, most of the work on the analysis of mechanical properties has been performed within a small range of strain rates in the quasistatic tensile testing regime. On the other hand, for application in crash-relevant automotive parts, understanding the deformation behavior at very high strain rates is critical. It has been observed in the past that the UTS of HMnS and MMnS increases with increasing strain rate at high-speed tensile tests while also retaining good ductility. While microstructural investigations have revealed that adiabatic heating effects during high-speed tensile tests partially suppress the TWIP and TRIP effect, the strain partitioning behavior in multi-phase MMnS has primarily been investigated during quasistatic tensile testing. [2,4,22,23,27–29]

However, the microstructural response in combination with the strain partitioning behavior is especially interesting in the case of MMnS. This is because of possible differences in the response to the plastic deformation at high strain rates of the individual microstructural constituents of the multi-phase microstructure. In this work, the strain rate-dependent mechanical properties and deformation behavior of a X6MnAl12-3 MMnS are investigated. To this end, the strain partitioning behavior on a microstructural scale is investigated by means of interrupted tensile tests at different strain rates coupled with electron backscatter diffraction (EBSD) experiments. Additionally, in-situ digital image correlation (DIC) methods during tensile testing are employed to analyze the strain localization behavior in the specimen with respect to the occurrence of deformation bands.

2. Materials and Methods

The X6MnAl12-3 alloy was ingot-cast in an ALD vacuum induction furnace with ingot dimensions of 140 mm × 140 mm × 500 mm. Afterward, the MMnS was hot-forged at 1150 °C in 3 forging passes to a cross section of 160 mm × 40 mm. Subsequent hot rolling to a sheet thickness of 2.5 mm was performed at 1150 °C with reheating between passes. The MMnS was then homogenization annealed at 1100 °C for 2 h, followed by water quenching and an additional austenitization annealing at 850 °C for 10 min with subsequent water quenching to reduce eigenstrains. Finally, the MMnS was cold-rolled (CR) to a final thickness of 1.25 mm (50% thickness reduction).

Before intercritical annealing (IA) at 675 °C for 2 h in a salt bath furnace (THERMCONCEPT GmbH, Bremen, Germany), tensile test specimens with 30 mm initial gauge length and 6 mm gauge width were machined after cold rolling using water jet cutting. The tensile axis (TA) was perpendicular to the rolling direction (RD). The temperatures for the austenitization annealing and the IA were selected based on previous studies for a MMnS with a very similar chemical composition [22,23]. Additionally, dilatometer measurements were performed after cold rolling to determine A_{c1} and A_{c3}, ensuring that the IA was performed in the α-γ two-phase region and that the temperature for the

austenitization was higher than A_{c3}. A_{c1}, A_{c3}, and the nominal chemical composition of the MMnS tested in this work are summarized in Table 1. The processing route, including the final heat treatment, is summarized in Figure 1.

Table 1. A_{c1}, A_{c3}, and nominal chemical composition of the X6MnAl12-3 MMnS.

Designation	Nominal Chemical Composition [wt.%]			A_{c1} [°C]	A_{c3} [°C]
	C	Mn	Al		
X6MnAl12-3	0.064	11.7	2.9	503	825

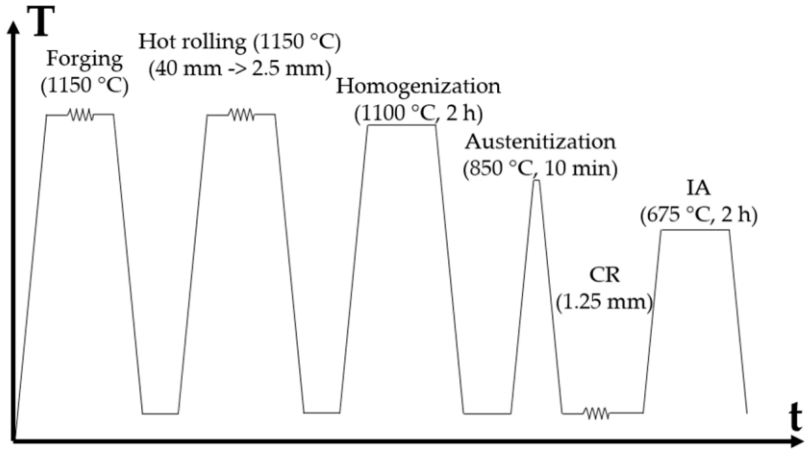


Figure 1. The processing route for the X6MnAl12-3 MMnS.

Tensile testing was performed on two different devices. A minimum number of three tensile tests per strain rate were performed and a representative test result was selected for the diagrams in this work. The tensile tests at constant strain rates $\dot{\varepsilon}$ of 0.00001 1/s, 0.0001 1/s, 0.001 1/s, 0.01 1/s, and 0.1 1/s were conducted using a Z250 tensile testing machine by ZwickRoell (Ulm, Germany). Strains were measured with the contact-type extensometer MultiXtens by ZwickRoell. The Aramis 12 Megapixel DIC system (GOM GmbH, Braunschweig, Germany) was employed during the quasistatic tensile tests to analyze the local $\dot{\varepsilon}$ and the strain distribution in the specimens. For the higher $\dot{\varepsilon}$ of 1.0 1/s, 11 1/s, 140 1/s, and 230 1/s, dynamic tensile test samples with 20 mm gauge length and 6 mm width were used. The dynamic tensile tests were conducted at room temperature on a servo-hydraulic HTM2012 testing machine by ZwickRoell (Ulm, Germany). Strain was measured using a high-speed opto-electronic device. A piezo-electric type load cell was used to measure the applied load. At 140 1/s and 230 1/s, additional strain gauges were attached to the sample shoulders linked in a Wheatstone bridge circuit to reduce the oscillation of the input load signal, which occurs at high testing speeds. In order to determine the flow curves, the force signal was smoothed with a polynomial spline function to eliminate the remaining oscillations.

Optical microscopy was conducted using a 5% Nital etchant. Metallographic preparation for electron backscatter diffraction (EBSD) measurements was performed by means of mechanical grinding with SiC paper up to 4000 grit with subsequent mechanical polishing using 3 µm and 1 µm diamond suspension. Electropolishing was then performed at 28 V for 20 s using an electrolyte containing 700 mL ethanol (C_2H_5OH), 100 mL butyl glycol ($C_6H_{14}O_2$), and 78 mL perchloric acid (60%) ($HClO_4$). EBSD analyses were performed on the sheet surface for two different kinds of specimens. The measurements of the initial microstructure and after fracture were performed on A_{30} tensile test specimens. For the measurements after fracture, the measured area was selected as close to the fracture surface as possible. Interrupted tensile tests of specimens with 12 mm gauge length and 2 mm gauge width were used to analyze the microstructural evolution after 2%, 10%, and 20% elongation, respectively. A Zeiss Sigma scanning electron microscope (SEM) (Carl Zeiss Microscopy

GmbH, Jena, Germany) was used for all SEM experiments. Secondary electron (SE) images were taken at an acceleration voltage of 20 kV and coupled with Energy Dispersive X-ray Spectroscopy (EDS) for line-scans with 20 nm step size. The chemical composition of γ was determined via EDS and was used for the calculation of the SFE, based on a subregular solution thermodynamic model that takes the impact of temperature into account too [7]. For larger-area EBSD measurements before deformation, after 20% uniform elongation at 0.001 1/s and after fracture of the 0.00001 1/s and 0.001 1/s strain rates, an acceleration voltage of 15 kV and a step size of 100 nm were selected. For the other high-resolution (HR) EBSD measurements, an acceleration voltage of 10 kV and a step size of 70 nm was used. The phase fractions given in this manuscript are based on those HR EBSD measurements, however, the phase fractions determined by the large-area EBSD measurements did not deviate significantly. The working distance was between 18 mm and 24 mm and a post-processing routine employing the HKL Channel 5 software (version 5.12j, Oxford Instruments, Abingdon-on-Thames, UK) was utilized, as well as the MATLAB-based MTEX toolbox [30,31]. Noise reduction was employed by removing wild spikes and considering at least 5 neighboring data points.

3. Results

The microstructures of the MMnS after cold-rolling prior to IA and after intercritical annealing at 675 °C for 2 h are shown in Figure 2. After cold-rolling (cf. Figure 2a), a very fine-grained lamellar microstructure was present. Prior γ grain boundaries (GB) were still visible in optical micrographs and separated regions of lamellar martensite. After intercritical annealing (cf. Figure 2c), a high fraction of the lamellar morphology was retained. However, in some areas (highlighted in Figure 2c), a more equiaxed recrystallized grain morphology was present. The SE image in Figure 2b with the corresponding EDS analysis in Figure 2d indicates that elemental partitioning of Al and Mn was present after intercritical annealing. Al-enriched regions showed approximately 3.4 wt.% Al and corresponded with Mn-depleted regions with about 10.5 wt.% Mn. Mn-rich regions showed about 14.0 wt.% Mn and corresponded with Al-depleted regions, where only approximately 2.5 wt.% Al was present. Comparing the microstructure in Figure 2b with the phase fractions from EBSD measurements shown in Figure 4a revealed that the Mn-rich regions correspond to austenite while the Al-rich regions correspond to ferrite and α'-martensite.

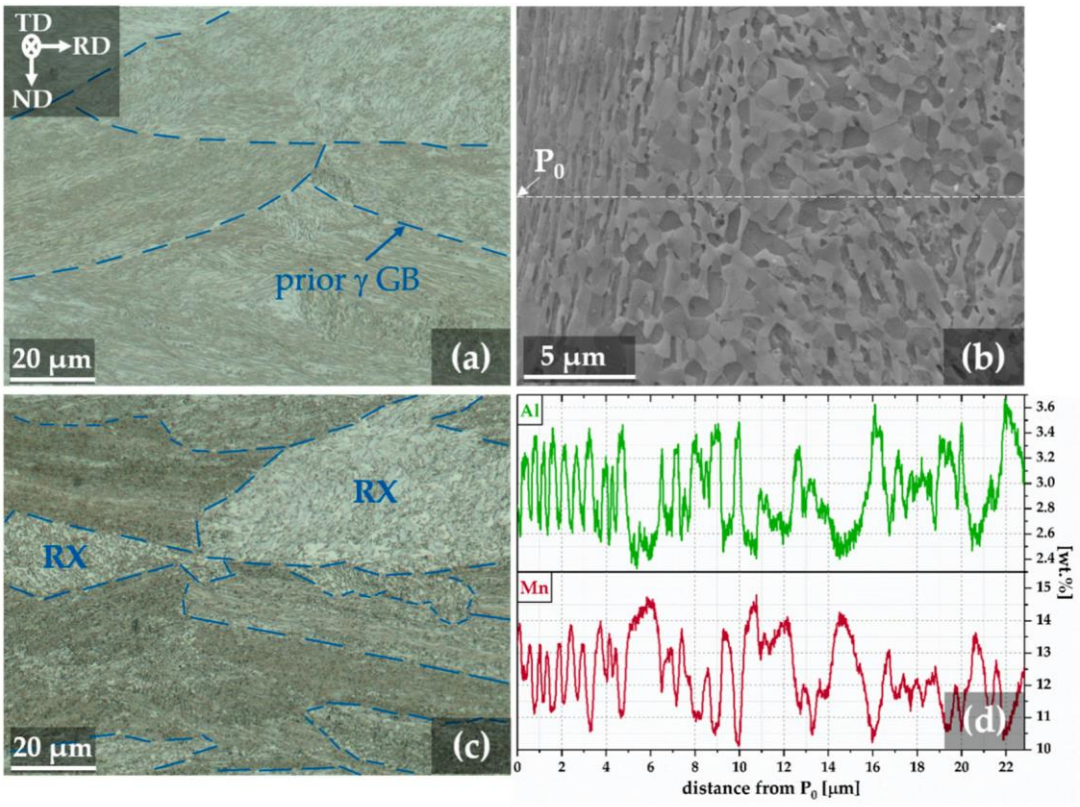


Figure 2. (**a**,**c**) Optical micrographs of the X6MnAl12-3 MMnS (**a**) after 50% cold rolling and (**c**) after intercritical annealing. Easily identifiable prior γ grain boundaries in (**a**) and grain boundaries of recrystallized grains in (**c**) are highlighted in blue. (**b**) Secondary electron (SE) image of the microstructure after intercritical annealing, and (**d**) the corresponding Energy Dispersive X-ray Spectroscopy (EDS) analysis of the local Al and Mn contents are shown.

The strain-rate-dependent mechanical properties as determined by tensile tests are shown in Figure 3, in addition to the strain-rate-dependent YS and stress values corresponding to engineering strains ε_{eng} of 5% and 10%. The mechanical response of the tested X6MnAl12-3 MMnS to an increase of $\dot{\varepsilon}$ can be divided into strain rate changes in the regime of low, medium, and high strain rates, as shown in Table 2. In general, the ductility was affected the most, as the uniform elongation (UE) and ε_f decreased from approximately UE = ε_f = 40% at 0.00001 1/s to about UE = 18% and ε_f = 30% at 1.0 1/s respectively. During dynamic tensile testing ($\dot{\varepsilon} \geq$ 1.0 1/s), the UE was not affected significantly, while ε_f increased slightly to 35% and 32% at 140 1/s and 230 1/s. The YS only decreased slightly from 720 MPa at 0.00001 1/s to 690 MPa at 230 1/s, which equals a variation in YS of less than 5%. The UTS decreased from 875 MPa at 0.00001 1/s to 790 MPa at 1.0 1/s. During the dynamic tensile tests, the UTS increased up to 835 MPa at 230 1/s. At strain rates of 0.0001 1/s and 0.00001 1/s, serrated flow occurred, as shown in Figure 3b. Additionally, Figure 3a shows that at <1.0 1/s, a discontinuous elastic-plastic transition was observed which extended up to approximately 2% ε_{eng}. For the high-speed dynamic tensile tests, the necessary application of the smoothing function for the force data did not allow for accurate observation of the transition phase. However, at 1.0 1/s, the discontinuous elastic-plastic transition was also observed in the raw data of the force signal.

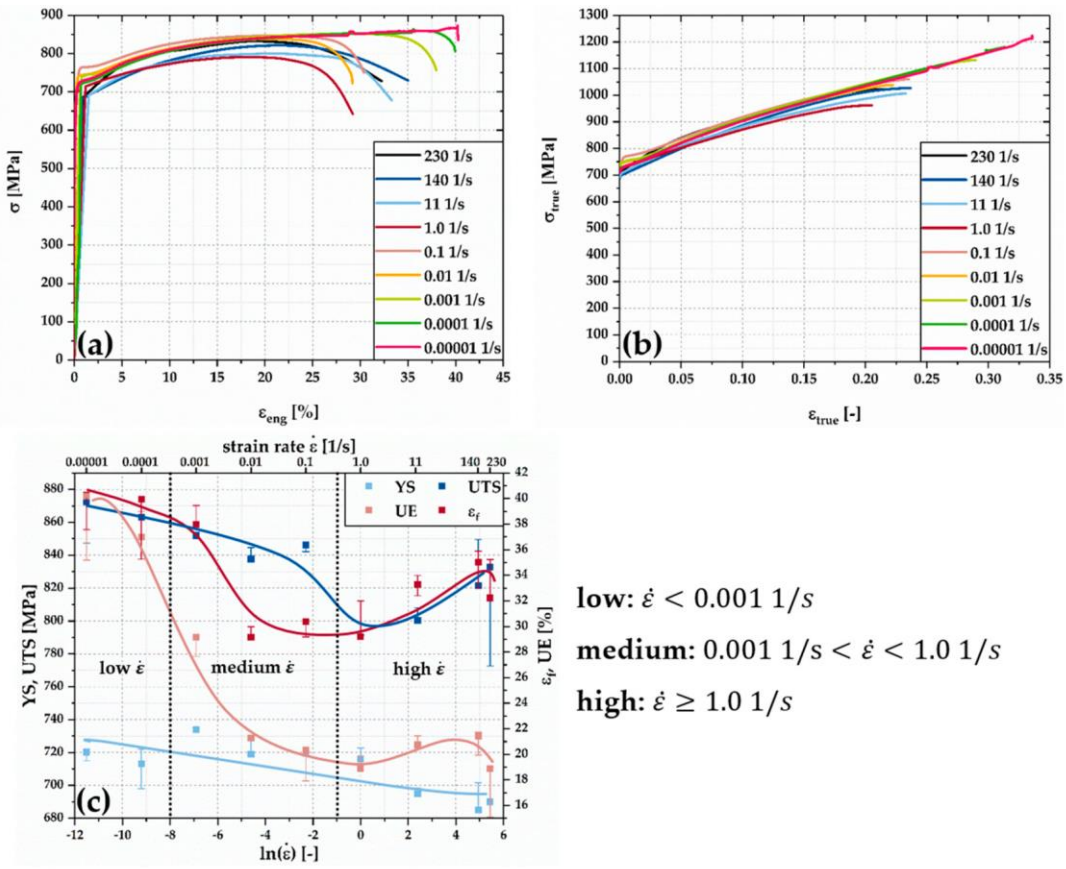


Figure 3. (**a**) Engineering stress-strain and (**b**) true stress-true strain curves of the X6MnAl12-3 alloy tested at different strain rates. (**c**) Overview of the strain-rate-dependent mechanical properties.

Table 2. Impact of an increase in strain rate for low, medium, and high strain rates (cf. Figure 3).

Mechanical Property	Low $\dot{\varepsilon}$	Medium $\dot{\varepsilon}$	High $\dot{\varepsilon}$
YS	↓	↓	↓
UTS	↓	↓	↑
UE	↓	↓	~
ε_f	~	↓	↑

In Figure 4, the initial austenite (γ), ferrite (α), and martensite (α') phase fractions after IA and the evolution of austenite phase fraction during quasistatic tensile testing at 0.001 1/s are shown, as measured by EBSD experiments. After IA at 675 °C for 2 h (cf. Figure 4a), the initial microstructure was lath-like with phase fractions of approximately 45% γ (face-centered cubic) and 55% α and/or recovered α' (body-centered cubic). At the end of the discontinuous elastic-plastic transition after approximately 2% elongation (cf. Figure 4b), no change in the γ phase fraction was detected. During straining at 0.001 1/s to ε_{eng} of 10% (Figure 4c) and 20% (Figure 4d), a significant fraction of γ underwent a martensitic $\gamma \rightarrow \alpha\prime$ phase transformation, resulting in a detected γ phase fraction of 35% and 15% respectively. No ε-martensite was detected.

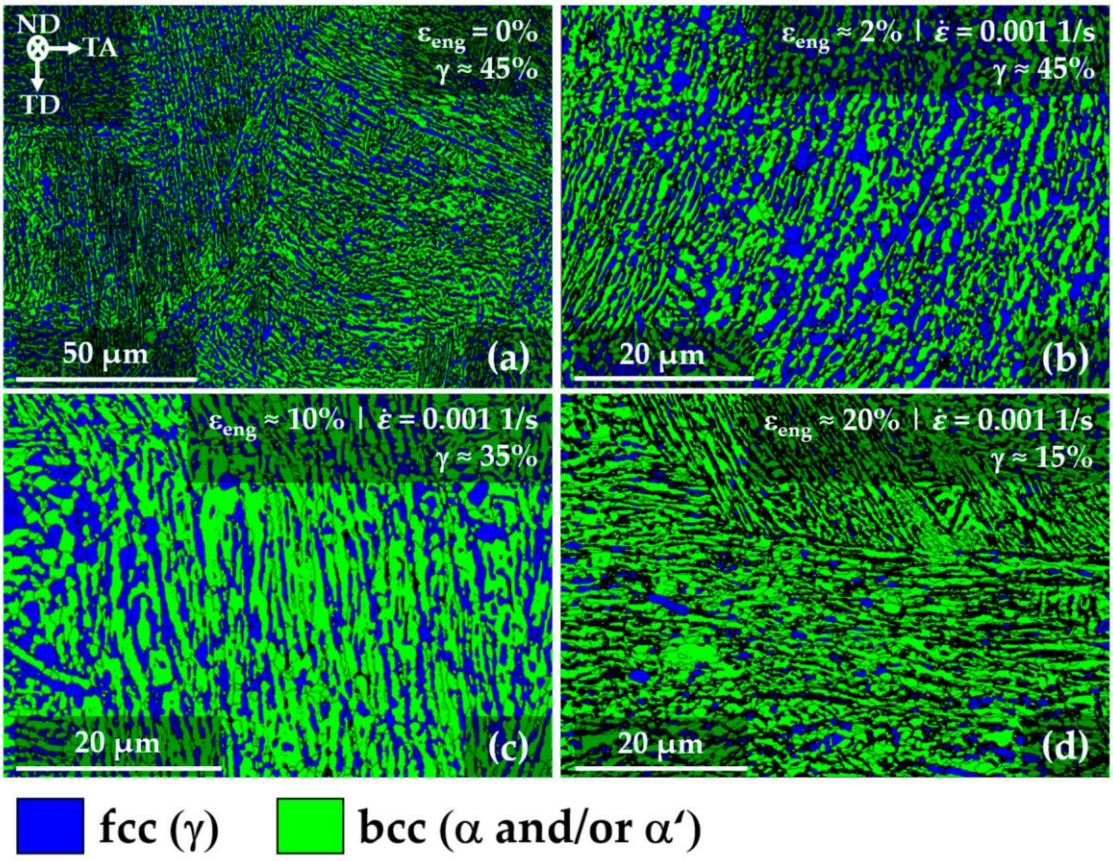


Figure 4. Electron backscatter diffraction (EBSD) phase maps of the investigated MMnS (**a**) before deformation and after straining to ε_{eng} of (**b**) 2%, (**c**) 10%, and (**d**) 20% at 0.001 1/s. Green areas indicate a body-centered cubic crystal structure, α and/or α′, whereas blue areas indicate face-centered cubic austenite, γ.

To investigate the impact of strain rate on the phase transformation, Figure 5 compares the microstructure after tensile testing at different $\dot{\varepsilon}$ until fracture. While the medium $\dot{\varepsilon}$ of 0.001 1/s led to a nearly complete $\gamma \rightarrow \alpha\prime$ transformation at fracture (cf. Figure 5b), both very high strain rates of 1 1/s and 230 1/s (cf. Figure 5c,d) as well as a very low $\dot{\varepsilon}$ of 0.00001 1/s (cf. Figure 5a) facilitated significantly higher retained γ phase fractions of 29% and 25% after fracture, respectively.

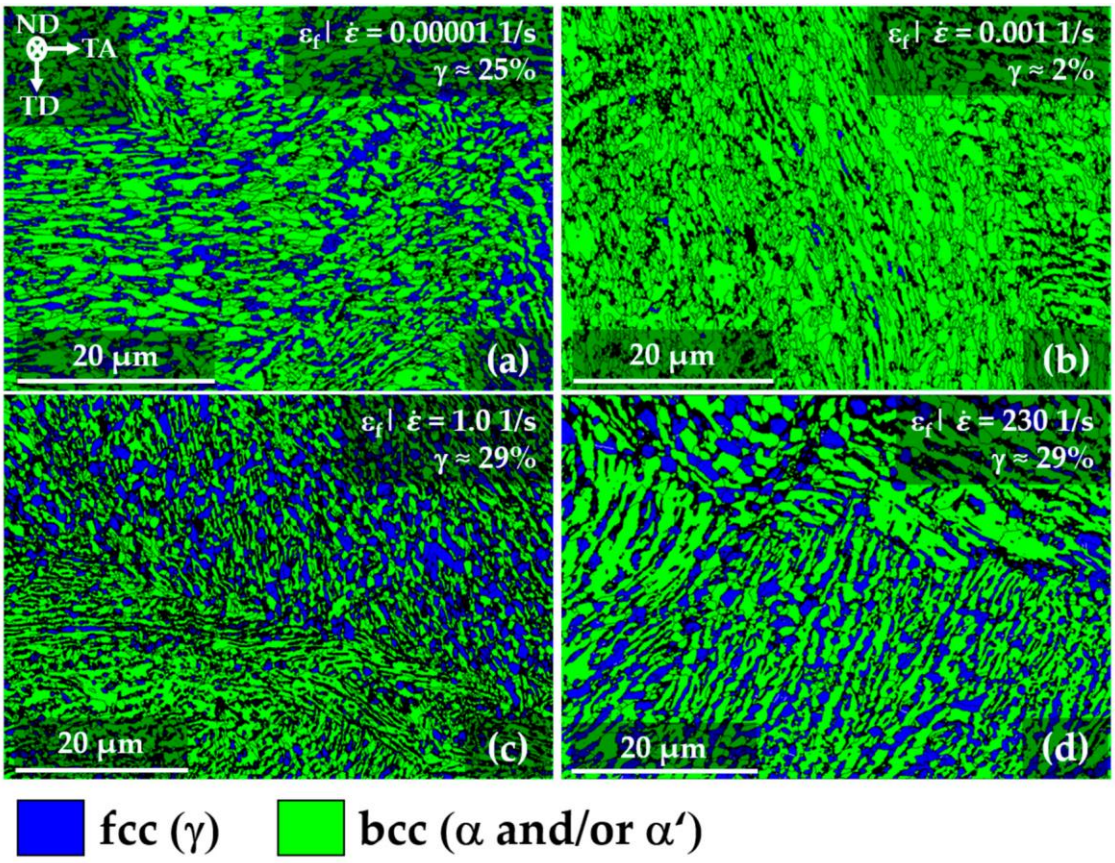


Figure 5. γ phase fractions (blue) as determined by EBSD measurements after tensile testing to fracture at (**a**) 0.00001 1/s, (**b**) 0.001 1/s, (**c**) 1.0 1/s, and (**d**) 230 1/s. Green areas indicate a body-centered cubic crystal structure, α and/or α'.

To highlight the onset of serrated flow at 0.00001 1/s, Figure 6 compares the flow curves and WHR of the tensile tests at 0.00001 1/s, 0.001 1/s, 1.0 1/s, and 230 1/s. While the flow curves at quasistatic strain rates of 0.001 1/s and 0.00001 1/s were almost identical, ε_f at the slower $\dot{\varepsilon}$ of 0.00001 1/s was significantly higher. The WHR during the initial stages of deformation were similar, as both curves dropped significantly during the Lüders band propagation. Afterwards the WHR increased and evolved in a similar way. However, at a true strain of approximately 0.25, the onset of the serrated flow at 0.00001 1/s was highlighted by a peak in the WHR curve, whereas the WHR at 0.001 1/s decreased to the flow curve, and necking was initiated. Similarly, the second serration in the flow curve at ε_{true} of approximately 0.33 marked the onset of the second peak in the WHR curve of the MMnS tested at 0.00001 1/s. Overall, the significantly more pronounced decrease in austenite phase fraction for 0.001 1/s did not result in a higher WHR compared to testing at 0.00001 1/s. Furthermore, tensile testing at 1.0 1/s led to a decrease of the WHR below those of 0.001 1/s and 0.00001 1/s, resulting in a reduction of uniform elongation. Increasing $\dot{\varepsilon}$ from 1.0 1/s to 230 1/s led to a small increase in the WHR to slightly lower levels than for the quasistatic tensile tests, which resulted in an increase in UTS, UE, and ε_f.

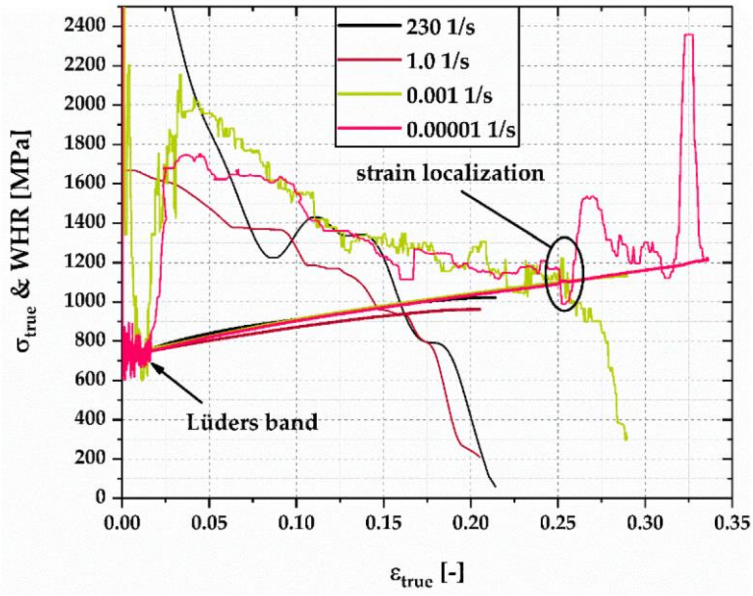


Figure 6. Flow curve and work-hardening rate (WHR) of the X6MnAl12-3 alloy tested at 0.00001 1/s, 0.001 1/s, 1.0 1/s, and 230 1/s, respectively.

Figure 7 shows the EBSD inverse pole figure (IPF) maps and grain orientation spread (GOS) maps for α and α′, as well as γ and the kernel average misorientation (KAM) map. The GOS for α and γ was usually below 1.0 in equiaxed grains, indicating recrystallized grains, whereas the GOS values in lamellar morphologies were 2.0 or higher (cf. Figure 7c,d). The IPF maps in Figure 7 show that the orientation of the γ, α and α′ grains within the lamellar structures did not vary significantly. On the other hand, the regions in the microstructure, where granular grains occurred frequently, did not show any preferred orientations. Those regions also showed significantly lower KAM values (cf. Figure 7e).

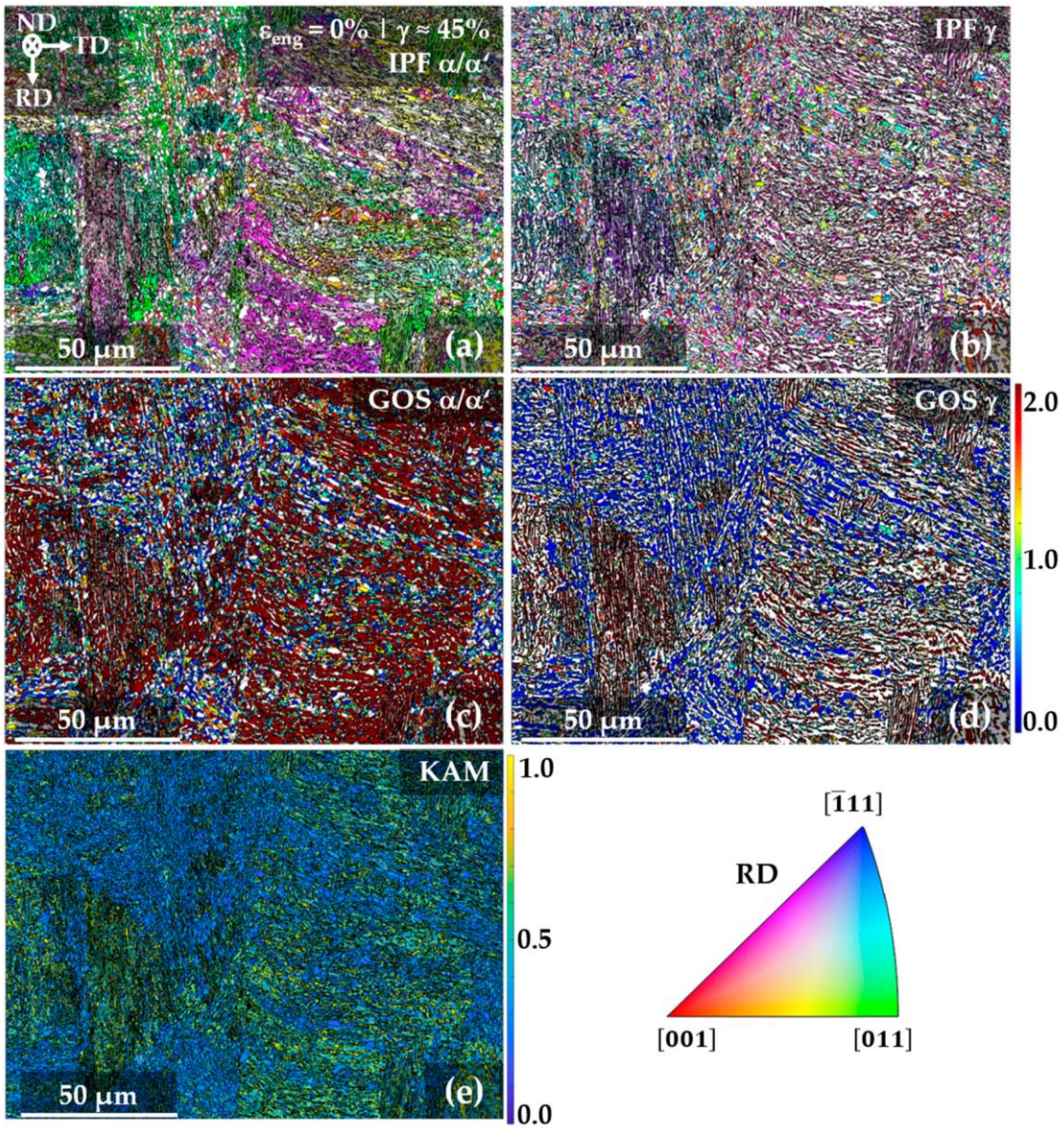


Figure 7. EBSD maps of the X6MnAl12-3 alloy prior to deformation (**a**,**b**) with inverse pole figure (IPF) color coding relative to the rolling direction (RD) for (**a**) α and α′ and (**b**) γ. Grain orientation spread (GOS) maps for (**c**) α and α′, (**d**) γ, and (**e**) the kernel average misorientation (KAM) map are shown. White areas in (**a**–**d**) correspond to (**a**,**c**) γ and (**b**,**d**) α or α′, respectively.

The EBSD IPF maps and KAM maps in Figure 8 show the microstructure of the X6MnAl12-3 alloy after uniform elongation to 2% strain. Comparing the EBSD IPF maps in Figure 8a,b showed that, similar to the undeformed state in Figure 7, the orientation of lamellar α and α′ grains did not deviate much, while the equiaxed γ grains between those lamellae were comparably randomly oriented. However, the KAM values of the γ grains were significantly higher than those of most equiaxed α grains (cf. Figure 8c,d) and also significantly higher than the KAM values of the γ grains in the undeformed state, as shown in Figure 7e.

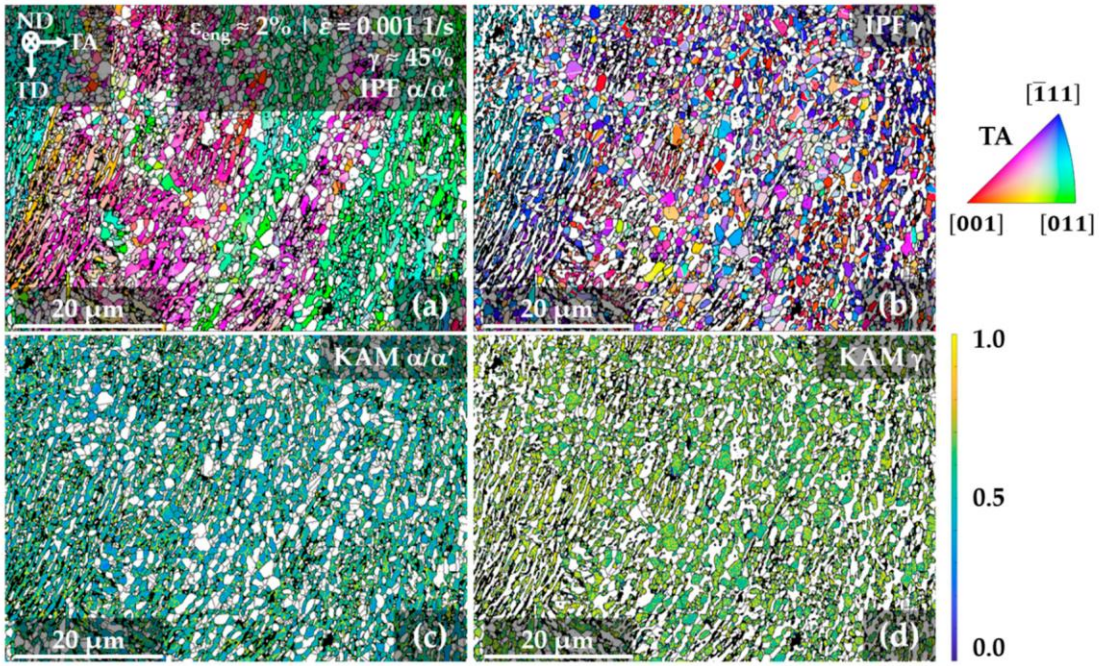


Figure 8. EBSD maps of the X6MnAl12-3 alloy at the end of the discontinuous elastic-plastic transition with (**a**,**b**) IPF color coding relative to the tensile axis (TA) for (**a**) α and α′and (**b**) γ. Corresponding KAM maps are shown for (**c**) α and α′ and (**d**) γ. White areas in (a–d) correspond to (**a**,**c**) γ and (**b**,**d**) α or α′, respectively.

The evolution of the microstructure and the distribution of strain between phases of the X6MnAl12-3 during further straining and after fracture for $\dot{\varepsilon}$ of 0.00001 1/s, 0.001 1/s, 1.0 1/s, and 230 1/s is shown in Figure 9 by means of EBSD IPF maps and KAM maps for α and α′. The EBSD IPF maps in Figure 9 show that the microstructure at higher elongations mainly consisted of blocks of lamellar α and α′ grains, in which the orientations of α and α′ were similar to each other. Comparing the KAM maps of α and α′ grains after fracture for 0.00001 1/s, 1.0 1/s, and 230 1/s (cf. Figure 9b,f,h,j), the KAM values overall decreased with increasing strain rate. The KAM values of α and α′ grains after elongation to fracture at 0.00001 1/s (cf. Figure 9e) and after 20% elongation at 0.001 1/s (cf. Figure 9b) were similar.

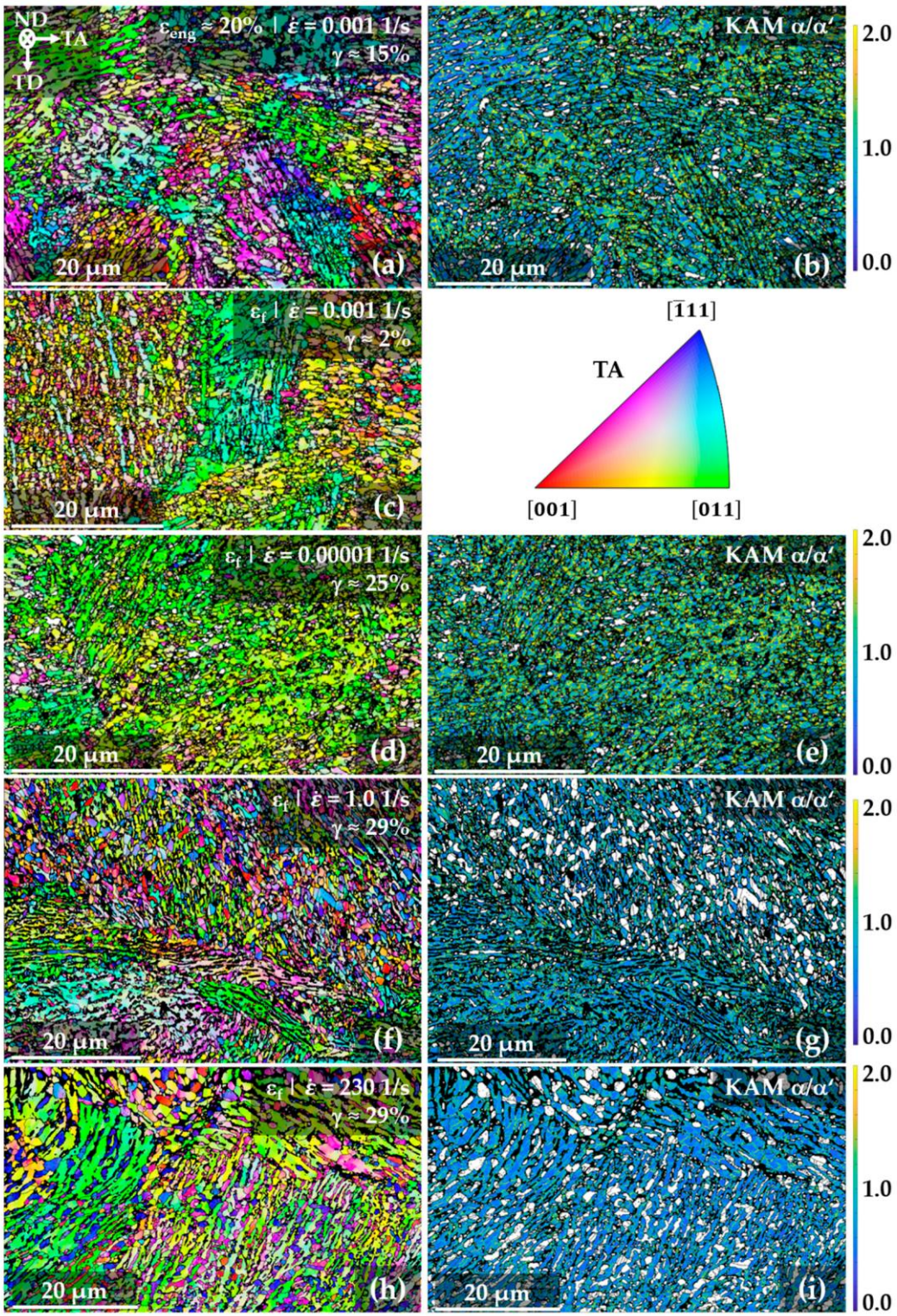


Figure 9. EBSD IPF maps for 0.001 1/s after (**a**) 20% ε_{eng} and (**c**) ε_f, as well as for the microstructure after straining until fracture at (**e**) 0.00001 1/s, (**g**) 1.0 1/s, and (**i**) 230 1/s. Corresponding EBSD maps with color coding according to KAM values of α and α′ in (**b**,**f**,**h**) and (**j**) are shown. White areas in the KAM maps correspond to γ.

The in-situ DIC measurements in Figure 10 show the local strain rate, which indicates localized deformation behavior, on the surface of the tensile test specimen during the discontinuous

elastic-plastic transition for the strain rates of 0.001 1/s and 0.00001 1/s. As shown in Figure 10, the discontinuous yield phenomenon was accompanied by a Lüders-band type of strain localization, which initiates in the clamping sections of the tensile test specimen and subsequently progresses towards the middle of the sample. The bands meet at the end of the Lüders strain at approximately 2.0% ε_{eng}. At higher strains, the plastic deformation proceeded homogeneously.

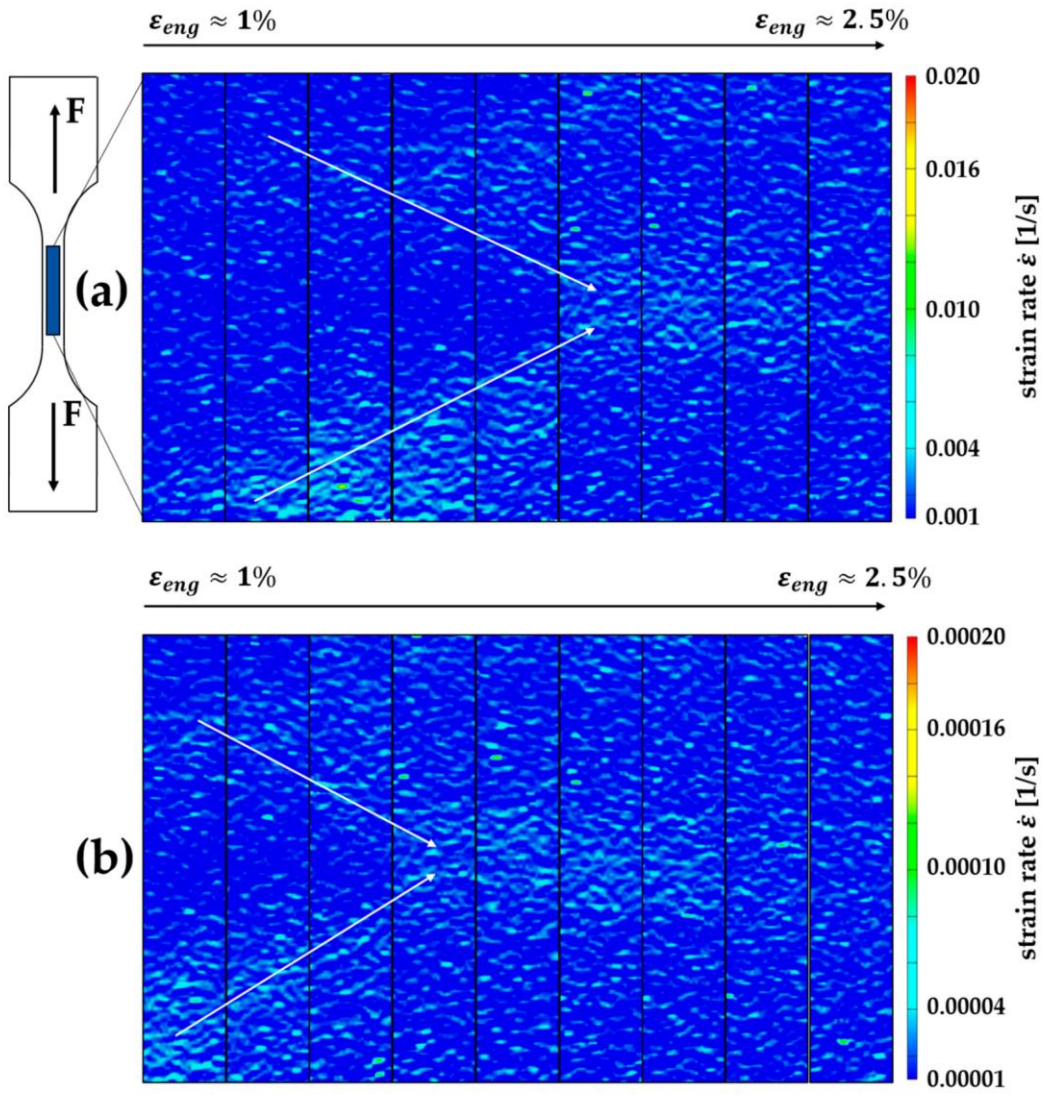


Figure 10. Visualization of local strain rate distribution in a tensile test sample during the discontinuous elastic-plastic transition using in-situ DIC during tensile testing at (**a**) 0.001 1/s and (**b**) 0.00001 1/s. White arrows highlight the propagation of localized peaks in strain rate during straining.

Figure 11 shows the strain localization behavior at high plastic strains for the specimens at 0.001 1/s and 0.00001 1/s. Comparing Figure 11a,b, tensile testing at 0.001 1/s did not lead to pronounced localized deformation behavior before necking, while two "X"-shaped areas ("X-bands") of strain localization occurred before necking during tensile testing at 0.00001 1/s. The onset of those deformation bands coincided with the spikes in the flow curve shown in Figure 6. The deformation bands propagated only in one direction and changed direction at the end of the parallel gauge length (cf. left part of Figure 11b).

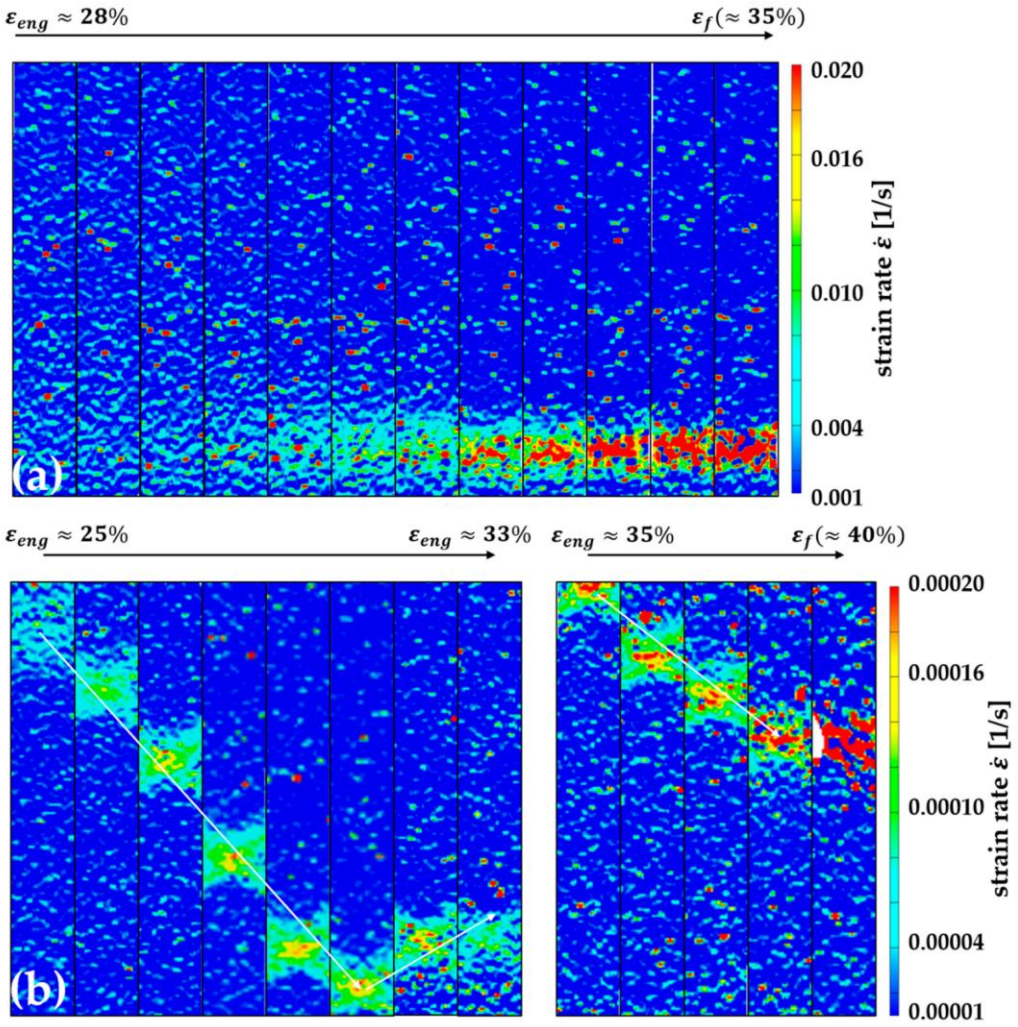


Figure 11. Visualization of the local strain rate distribution in a tensile test sample prior to necking initiation using in-situ DIC during tensile testing at (**a**) 0.001 1/s and (**b**) 0.00001 1/s. White arrows highlight the propagation of localized peaks in strain rate during straining.

4. Discussion

In this work, the strain-rate-dependent mechanical properties and strain localization behavior of an intercritically annealed medium-manganese X6MnAl12-3 steel were investigated.

IA at 675 °C for 2 h after cold rolling led to a mixed microstructure consisting of γ, α, and α′. The distinction between α and α′ can be made based on the lamellar morphology and the GOS values (cf. Figure 7), for which a threshold value of 2 can be used to distinguish recrystallized grains with low internal stress (GOS below 2) and deformed grains with higher internal stress (GOS over 2) [32]. For the purpose of distinguishing between α and α′ in this work, a lamellar morphology in combination with a GOS value over 2 is considered to indicate α′. However, it should be noted that recovered α′ could also show GOS values below 2, as the diffusion of C out of the distorted bcc lattice could reduce the lattice distortion of α′ and accordingly reduce the GOS value. Applying the GOS criterion for γ (cf. Figure 7d) reveals that the majority of γ grains, except lamellar grains of reverted γ situated between α′-lamellae, showed GOS values significantly lower than 1. Whereas the microstructure after cold rolling can be identified as fully martensitic (cf. Figure 2c), IA led to a microstructure consisting of lamellar reverted γ and α and α′ grains as well as recrystallized, mostly equiaxed γ and α grains. Al and Mn were partitioned with Mn being enriched and Al being depleted in γ (cf. Figures 2d and 4a). The approximated Mn and Al contents of 14.0 wt.% and 2.5 wt.% for the

calculation of the SFE using a subregular solution thermodynamic model [7] resulted in an SFE of γ at room temperature (RT) of 10 mJ/m^2. The low alloying content of 0.064 wt.% does not allow for an accurate determination of the actual C content in austenite via EDS. However, it can be assumed that the SFE is not significantly impacted by the partitioning of C to γ because of the very low alloying content of C compared to the significant γ phase fraction of 45% [6–8,33]. Accordingly, for the calculation of the SFE in this work, the C content is approximated to be 0.064 wt.%. This is in line with the findings of experimental approaches using atom probe tomography and EDS on a MMnS with very similar chemical composition and phase fractions after IA [22].

Overall, the high YS in the X6MnAl12-3 alloy, despite the low C content, can be explained by the presence of hard α′ and the ultrafine-grained microstructure, which affects the flow stress significantly [34,35]. In the case of the microstructure of the X6MnAl12-3 alloy after IA, the critical stress required for plastic deformation is different for each α′, α, and γ. Due to the low C content, the critical stress value for γ is significantly lower than for α and especially for α′. As a result, the initial plastic deformation is mainly accommodated by deformation in γ, which is pointed out by the comparison of KAM values for γ, α, and α′ in Figure 8. High KAM values are an indication of the existence of geometrically necessary dislocations [36]. The different critical stress values of γ, α, and α′ for plastic deformation are also the reason for the discontinuous elastic-plastic transition during quasistatic tensile testing. Due to the polynomial function that is used to smooth the oscillating force signal during the analysis of the high-speed dynamic tensile tests, it remains unclear whether the discontinuous elastic-plastic transition also occurs at higher strain rates, as a previous study has found to be the case for a multi-phase MMnS [28].

During deformation, the TRIP effect leads to a reduction in γ phase fraction, as summarized in Figure 12.

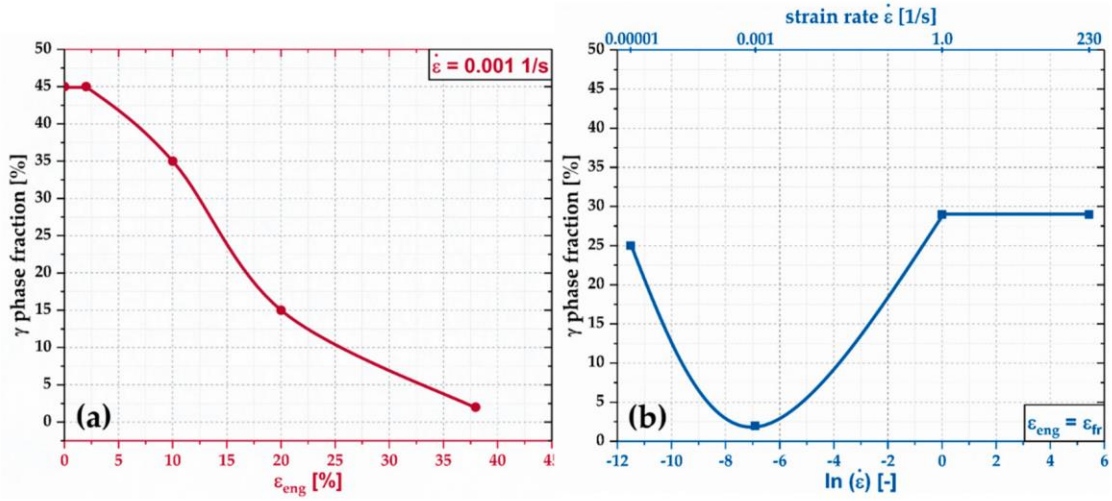


Figure 12. Summary of the evolution of γ phase fraction (**a**) during straining at 0.001 1/s and (**b**) comparison of strain-rate-dependent γ phase fractions after fracture.

The activation of the TRIP effect is determined by the stability of γ, which depends on the chemical composition, temperature and internal stress σ_γ [37]. With progressing plastic deformation, σ_γ increases and reaches a critical level for the activation of the TRIP effect. Accordingly, as shown in Figures 7 and 12, the phase fraction of γ is reduced. As stated in the previous paragraph, the flow stress of multi-phase steels like the X6MnAl12-3 MMnS is determined by the individual effective flow stress of each microstructural component γ, α, and α′. As evidenced by the discontinuous elastic-plastic transition, plastic deformation will be accommodated to different degrees by γ, α, and α′, and intergranular strain accommodation is impeded [24–26]. However, at low $\dot{\varepsilon}$, strain accommodation processes like dislocation generation in neighboring grains can occur over a longer period of time until

the critical stress for initiation of the TRIP effect is reached. As Figures 8 and 12 show, this results in higher phase fractions of γ after fracture for a strain rate of 0.00001 1/s. This is also reflected by the higher KAM values in α and α′ after deformation in Figure 9 for lower strain rates and is in agreement with previous reports of decreasing twin volume fractions with lower strain rates in high-manganese TWIP steels [38], where dislocation activity increased at lower strain rates [39]. Accordingly, the strain-rate sensitivity at low and medium $\dot{\varepsilon}$ of the tested X6MnAl12-3 MMnS on the microscale regarding the activation of secondary deformation mechanisms is high.

At $\dot{\varepsilon} \geq 1.0$ 1/s, adiabatic heating effects can cause drastic temperature increases of up to 100–150 °C in the tensile test specimen during deformation [29,36]. As such, the SFE is increased in-situ to 27–38 mJ/m^2 in γ based on the chemical composition derived from EDS [7], which is higher than the critical value of 18 mJ/m^2, above which the TRIP effect is suppressed or partially suppressed, as has been shown previously for HMnS and multi-phase MMnS [4,27–29,40–42]. Therefore, higher γ phase fractions are present after fracture (cf. Figures 8 and 12). This results in an increase in UTS with increasing strain rate >1.0 1/s (cf. Figure 3c), because strain accommodation processes between γ, α, and α′ do not occur to the same extent as at lower strain rates. This is also reflected by the low KAM values of α and α′ at higher strain rates (cf. Figure 9), as a higher fraction of plastic deformation is accommodated by γ at 1.0 1/s than at lower strain rates.

Following the remarks of the previous paragraphs, the impact of $\dot{\varepsilon}$ on the accommodation of plastic deformation in the X6MnAl12-3 MMnS can be described as a strain-rate-dependent strength of α and α′ relative to γ (Δσ). At high strain rates, strain accommodation processes are partially inhibited, increasing Δσ. At low strain rates, sufficient time for the dislocation generation at grain boundaries of α and α′ is available to accommodate the increased stress level in neighboring γ grains. Accordingly, Δσ is lower than at high strain rates. As a result, the accommodation of plastic deformation is much more homogeneously distributed over γ, α, and α′ at very slow strain rates. Consequently, the TRIP effect, which is activated above a critical stress value for σ_γ, is partially suppressed at very low strain rates. Figure 13 illustrates the strain-rate-dependent microstructural development.

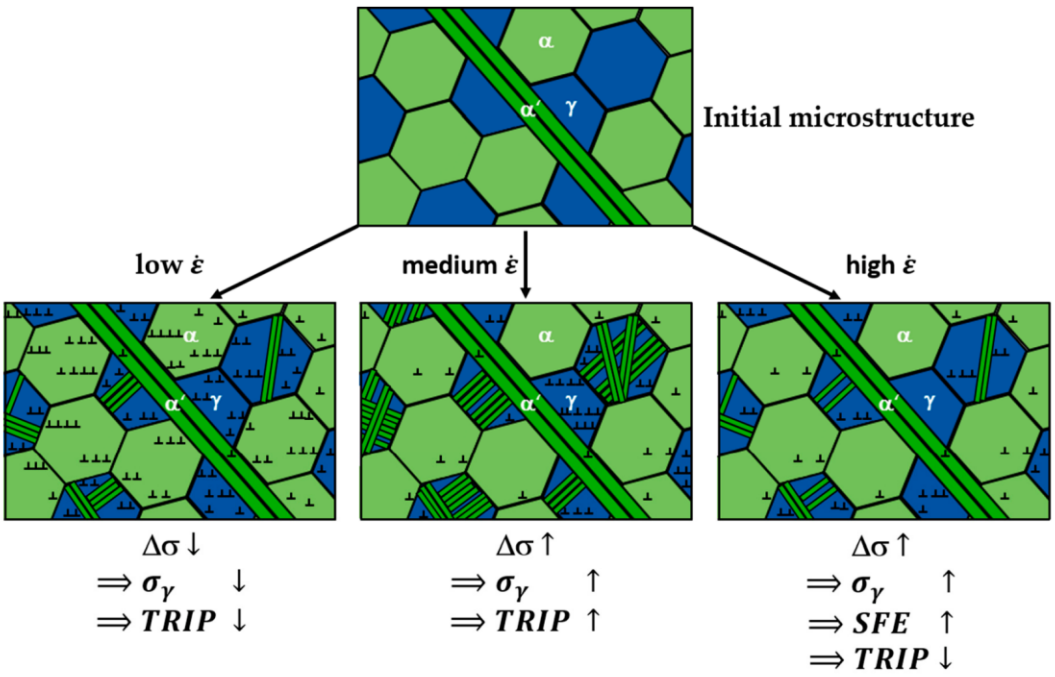


Figure 13. Impact of the strain-rate-dependent strength of α and α′ relative to γ (Δσ) on the microstructural evolution during straining at different strain rates.

The low WHR, UE, and ε_f at 1.0 1/s compared to quasistatic $\dot{\varepsilon}$ (cf. Figure 6) can be explained by three effects. Firstly, adiabatic heating at high $\dot{\varepsilon}$ enables dynamic recovery processes in γ, which decreases the WHR [4,27]. Additionally, the adiabatic heating also increases the SFE of γ and leads to a partial suppression of the TRIP effect during plastic deformation (cf. Figures 4 and 5) [7,8,27–29]. Thirdly, the high $\Delta\sigma$ suppresses the participation of the harder α and α' phases in accommodating plastic deformation to a large extent. Increasing $\dot{\varepsilon}$ >1.0 1/s led to an increase in WHR and, accordingly, to higher UTS and ε_f (cf. Figure 3), which is typically observed in conventional TRIP steels, dual-phase (DP) steels, and high-manganese TWIP steels with positive strain-rate sensitivity [27,43,44], as well as in multi-phase MMnS [28]. However, at 1.0 1/s, this effect is not strong enough to compensate for the partial suppression of the TRIP effect, which results in a low WHR compared to quasistatic $\dot{\varepsilon}$. This minimum in UE and ε_f at medium-high $\dot{\varepsilon}$ has also been previously observed in high-manganese TWIP steels [27]. Comparing the γ phase fractions after elongation to fracture (cf. Figures 5 and 12) reveals that increasing $\dot{\varepsilon}$ >1.0 1/s did not lead to an increase in the retained γ phase fraction, as has also previously been reported in multi-phase MMnS [28]. This is because the adiabatic heating effect primarily occurs during necking so that during the initial stages of plastic deformation, the TRIP effect can still occur. Due to this, the UE does not increase significantly. Overall, the interplay of effects on a microscale leads to a negative strain-rate sensitivity in the quasistatic $\dot{\varepsilon}$ regime with regards to the macroscopic mechanical properties, especially for the UTS, UE and ε_f. At high $\dot{\varepsilon}$, the strain-rate sensitivity is slightly positive, similar to conventional TRIP and DP steels.

Although the α' phase fraction after straining to fracture at 0.00001 1/s is not as high as at 0.001 1/s (cf. Figures 8 and 12), indicating a lower activity of the TRIP effect, the WHR is similar (cf. Figure 6). Usually, the TRIP effect leads to a strong increase in WHR [1,27]. However, as the participation of the harder phases α and α' in accommodating plastic deformation increases at lower strain rates due to a lower relative $\Delta\sigma$, the necessary stress for further straining increases to a similar extent. Accordingly, the WHR in the quasistatic tensile testing regime is not impacted significantly by the strain rate.

Recently, the impact of microstructural heterogeneity and the activation of secondary deformation mechanisms has been found to be of critical importance for the initiation and propagation of deformation bands, resulting in serrated flow curves [14,45]. Following the remarks of the previous paragraphs, the occurrence of serrated flow in the X6MnAl12-3 alloy at very slow strain rates could be due to the enhanced accommodation of plastic deformation by relatively low $\Delta\sigma$, which enables the propagation of deformation bands and the occurrence of serrated flow. Comparing the flow curves of the X6MnAl12-3 alloy at 0.001 1/s and 0.00001 1/s in Figure 6 reveals that the onset of strain localization during plastic deformation at 0.00001 1/s and 0.001 1/s occurs at approximately 28% strain, as is also shown by the in-situ DIC measurements in Figure 11. However, as the propagation of stresses is inhibited by the higher $\Delta\sigma$ at 0.001 1/s, necking is initiated in contrast to the occurrence of the serrated flow at 0.00001 1/s. This also explains the higher total elongation at 0.00001 1/s.

5. Conclusions

The strain-rate-dependent deformation behavior and mechanical properties of a X6MnAl12-3 medium-manganese steel (MMnS) were investigated. Intercritical annealing at 675 °C for 2 h led to an ultrafine-grained multi-phase microstructure consisting of approximately 45% reverted austenite (γ) and 55% recrystallized ferrite (α) and recovered martensite (α'). The following conclusions can be drawn:

- The strain-rate sensitivity of the macroscopic mechanical properties is different for low quasistatic strain rates and high strain rates $\dot{\varepsilon}$, which is due to the high strain-rate sensitivity of the deformation behavior on the microscale. On the microscale, the strain-rate-dependent strength of α and α' relative to γ ($\Delta\sigma$) leads to the observed strain-rate sensitivity of the $\gamma \rightarrow \alpha\prime$ phase transformation (TRIP).

- At low $\dot{\varepsilon}$, $\Delta\sigma$ is relatively small, which enables the accommodation of plastic deformation by α or α' and compensates the negative impact of the partial suppression of the TRIP effect on the work-hardening rate (WHR). At very low $\dot{\varepsilon}$, serrated flow occurs, which is due to the TRIP mechanism in combination with a significant accommodation of plastic deformation by α and α'.
- At high $\dot{\varepsilon}$, plastic deformation is not accommodated by α and α' to a large extent due to a very high $\Delta\sigma$. Additionally, adiabatic heating effects partially suppress the TRIP effect in γ.
- At a medium quasistatic $\dot{\varepsilon}$ (e.g., 0.001 1/s), $\Delta\sigma$ is relatively high, and plastic deformation is primarily accommodated by γ, which induces the pronounced activation of the TRIP mechanism.

Author Contributions: Conceptualization, S.S.; formal analysis, S.S.; investigation, S.S.; project administration, W.B.; supervision, C.H. and W.B.; visualization, S.S.; writing–original draft, S.S.; writing–review & editing, S.S., C.H. and W.B.

Funding: This research was funded by the "Deutsche Forschungsgemeinschaft" (DFG) within the Sonderforschungsbereich (Collaborative Research Center) 761 "Steel–ab initio".

Conflicts of Interest: The authors declare no conflict of interest. The funders had no role in the design of the study; in the collection, analyses, or interpretation of data; in the writing of the manuscript, or in the decision to publish the results.

References

1. Lee, Y.-K.; Han, J. Current opinion in medium manganese steel. *Mater. Sci. Technol.* **2015**, *31*, 843–856. [CrossRef]
2. DeCooman, B.C. High Mn TWIP steel and medium Mn steel. In *Automotive Steels: Design, Metallurgy, Processing and Applications*; Rana, R., Singh, S.B., Eds.; Woodhead Publishing: Cambridge, UK, 2017; pp. 317–385.
3. Bouaziz, O.; Allain, S.; Scott, C.P.; Cugy, P.; Barbier, D. High manganese austenitic twinning induced plasticity steels: A review of the microstructure properties relationships. *Curr. Opin. Solid State Mater. Sci.* **2011**, *15*, 141–168. [CrossRef]
4. DeCooman, B.C.; Estrin, Y.; Kim, S.K. Twinning-induced plasticity (TWIP) steels. *Acta Mater.* **2018**, *142*, 283–362. [CrossRef]
5. Bouaziz, O. Strain-hardening of twinning-induced plasticity steels. *Scr. Mater.* **2012**, *66*, 982–985. [CrossRef]
6. Pierce, D.T.; Jiménez, J.A.; Bentley, J.; Raabe, D.; Oskay, C.; Wittig, J.E. The influence of manganese content on the stacking fault and austenite/ε-martensite interfacial energies in Fe–Mn–(Al–Si) steels investigated by experiment and theory. *Acta Mater.* **2014**, *68*, 238–253. [CrossRef]
7. Saeed-Akbari, A.; Imlau, J.; Prahl, U.; Bleck, W. Derivation and Variation in Composition-Dependent Stacking Fault Energy Maps Based on Subregular Solution Model in High-Manganese Steels. *Metall. Mater. Trans. A* **2009**, *40*, 3076–3090. [CrossRef]
8. Dumay, A.; Chateau, J.P.; Allain, S.; Migot, S.; Bouaziz, O. Influence of addition elements on the stacking-fault energy and mechanical properties of an austenitic Fe–Mn–C steel. *Mater. Sci. Eng. A* **2008**, *483–484*, 184–187. [CrossRef]
9. Bambach, M.; Conrads, L.; Daamen, M.; Güvenç, O.; Hirt, G. Enhancing the crashworthiness of high-manganese steel by strain-hardening engineering, and tailored folding by local heat-treatment. *Mater. Des.* **2016**, *110*, 157–168. [CrossRef]
10. Haase, C.; Barrales-Mora, L.A.; Roters, F.; Molodov, D.A.; Gottstein, G. Applying the texture analysis for optimizing thermomechanical treatment of high manganese twinning-induced plasticity steel. *Acta Mater.* **2014**, *80*, 327–340. [CrossRef]
11. Allain, S.; Bouaziz, O.; Lebedkina, T.; Lebyodkin, M. Relationship between relaxation mechanisms and strain aging in an austenitic FeMnC steel. *Scr. Mater.* **2011**, *64*, 741–744. [CrossRef]
12. Hoffmann, S.; Bleck, W.; Berme, B. In Situ Characterization of Deformation Behavior of Austenitic High Manganese Steels. *Steel Res. Int.* **2012**, *83*, 379–384. [CrossRef]
13. Renard, K.; Ryelandt, S.; Jacques, P.J. Characterisation of the Portevin-Le Châtelier effect affecting an austenitic TWIP steel based on digital image correlation. *Mater. Sci. Eng. A* **2010**, *527*, 2969–2977. [CrossRef]

14. Sevsek, S.; Brasche, F.; Haase, C.; Bleck, W. Combined deformation twinning and short-range ordering causes serrated flow in high-manganese steels. *Mater. Sci. Eng. A* **2019**. [CrossRef]
15. Wang, X.G.; Wang, L.; Huang, M.X. In-situ evaluation of Lüders band associated with martensitic transformation in a medium Mn transformation-induced plasticity steel. *Mater. Sci. Eng. A* **2016**, *674*, 59–63. [CrossRef]
16. Ma, Y.; Song, W.; Bleck, W. Investigation of the Microstructure Evolution in a Fe-17Mn-1.5Al-0.3C Steel via In Situ Synchrotron X-ray Diffraction during a Tensile Test. *Materials* **2017**, *10*, 1129. [CrossRef]
17. Ma, Y. Medium-manganese steels processed by austenite-reverted-transformation annealing for automotive applications. *Mater. Sci. Technol.* **2017**, *33*, 1713–1727. [CrossRef]
18. Lee, S.; DeCooman, B.C. Annealing Temperature Dependence of the Tensile Behavior of 10 pct Mn Multi-phase TWIP-TRIP Steel. *Metall. Mater. Trans. A* **2014**, *45*, 6039–6052. [CrossRef]
19. Lee, S.-J.; Lee, S.; DeCooman, B.C. Mn partitioning during the intercritical annealing of ultrafine-grained 6% Mn transformation-induced plasticity steel. *Scr. Mater.* **2011**, *64*, 649–652. [CrossRef]
20. Cai, Z.H.; Ding, H.; Misra, R.D.K.; Ying, Z.Y. Austenite stability and deformation behavior in a cold-rolled transformation-induced plasticity steel with medium manganese content. *Acta Mater.* **2015**, *84*, 229–236. [CrossRef]
21. Emo, J.; Maugis, P.; Perlade, A. Austenite growth and stability in medium Mn, medium Al Fe-C-Mn-Al steels. *Comput. Mater. Sci.* **2016**, *125*, 206–217. [CrossRef]
22. Benzing, J.T.; Kwiatkowski da Silva, A.; Morsdorf, L.; Bentley, J.; Ponge, D.; Dutta, A.; Han, J.; McBride, J.R.; Van Leer, B.; Gault, B.; Raabe, D.; Wittig, J.E. Multi-scale characterization of austenite reversion and martensite recovery in cold-rolled medium-Mn steel. *Acta Mater.* **2019**, *166*, 512–530. [CrossRef]
23. Dutta, A.; Ponge, D.; Sandlöbes, S.; Raabe, D. Strain partitioning and strain localization in medium manganese steels measured by in situ microscopic digital image correlation. *Materialia* **2019**, *5*, 100252. [CrossRef]
24. Tan, X.; Ponge, D.; Lu, W.; Xu, Y.; Yang, X.; Rao, X.; Wu, D.; Raabe, D. Carbon and strain partitioning in a quenched and partitioned steel containing ferrite. *Acta Mater.* **2019**, *165*, 561–576. [CrossRef]
25. Gibbs, P.J.; de Cooman, B.C.; Brown, D.W.; Clausen, B.; Schroth, J.G.; Merwin, M.J.; Matlock, D.K. Strain partitioning in ultra-fine grained medium-manganese transformation induced plasticity steel. *Mater. Sci. Eng. A* **2014**, *609*, 323–333. [CrossRef]
26. Latypov, M.I.; Shin, S.; DeCooman, B.C.; Kim, H.S. Micromechanical finite element analysis of strain partitioning in multiphase medium manganese TWIP+TRIP steel. *Acta Mater.* **2016**, *108*, 219–228. [CrossRef]
27. Brüx, U.; Frommeyer, G.; Grässel, O.; Meyer, L.W.; Weise, A. Development and characterization of high strength impact resistant Fe-Mn-(Al-, Si) TRIP/TWIP steels. *Steel Res. Int.* **2002**, *73*, 294–298. [CrossRef]
28. Poling, W.A. Tensile Deformation of Third Generation Advanced High Strength Sheet Steels under High Strain Rates. Ph.D. Dissertation, Colorado School of Mines, Golden, CO, USA, 2016. Available online: http://hdl.handle.net/11124/170454 (accessed on 14 March 2019).
29. Rana, R.; De Moor, E.; Speer, J.G.; Matlock, D.K. On the Importance of Adiabatic Heating on Deformation Behavior of Medium-Manganese Sheet Steels. *JOM* **2018**, *70*, 706–713. [CrossRef]
30. Bachmann, F.; Hielscher, R.; Schaeben, H. Texture Analysis with MTEX—Free and Open Source Software Toolbox. *SSP* **2010**, *160*, 63–68. [CrossRef]
31. Hielscher, R.; Schaeben, H. A novel pole figure inversion method: Specification of the MTEX algorithm. *J. Appl. Crystallogr.* **2008**, *41*, 1024–1037. [CrossRef]
32. Field, D.; Bradford, L.; Nowell, M.; Lillo, T. The role of annealing twins during recrystallization of Cu. *Acta Mater.* **2007**, *55*, 4233–4241. [CrossRef]
33. Bouaziz, O.; Zurob, H.; Chehab, B.; Embury, J.D.; Allain, S.; Huang, M. Effect of chemical composition on work hardening of Fe-Mn-C TWIP steels. *Mater. Sci. Technol.* **2011**, *27*, 707–709. [CrossRef]
34. Gutierrez-Urrutia, I.; Zaefferer, S.; Raabe, D. The effect of grain size and grain orientation on deformation twinning in a Fe–22wt.% Mn–0.6wt.% C TWIP steel. *Mater. Sci. Eng. A* **2010**, *527*, 3552–3560. [CrossRef]
35. Dini, G.; Ueji, R.; Najafizadeh, A. Grain Size Dependence of the Flow Stress of TWIP Steel. *MSF* **2010**, *654–656*, 294–297. [CrossRef]
36. Calcagnotto, M.; Ponge, D.; Demir, E.; Raabe, D. Orientation gradients and geometrically necessary dislocations in ultrafine grained dual-phase steels studied by 2D and 3D EBSD. *Mater. Sci. Eng. A* **2010**, *527*, 2738–2746. [CrossRef]

37. Twardowski, R.; Prahl, U. Microstructure based flow curve modeling of high-Mn steels with TWIP and TRIP effect. *Comput. Methods Mater. Sci.* **2012**, *12*, 130–136.
38. Meyers, M.A.; Vöhringer, O.; Lubarda, V.A. The onset of twinning in metals: A constitutive description. *Acta Mater.* **2001**, *49*, 4025–4039. [CrossRef]
39. Li, K.; Yu, B.; Misra, R.D.K.; Han, G.; Tsai, Y.T.; Shao, C.W.; Shang, C.J.; Yang, J.R.; Zhang, Z.F. Strain rate dependence on the evolution of microstructure and deformation mechanism during nanoscale deformation in low carbon-high Mn TWIP steel. *Mater. Sci. Eng. A* **2019**, *742*, 116–123. [CrossRef]
40. Saeed-Akbari, A.; Mosecker, L.; Schwedt, A.; Bleck, W. Characterization and Prediction of Flow Behavior in High-Manganese Twinning Induced Plasticity Steels: Part, I. Mechanism Maps and Work-Hardening Behavior. *Metall. Mater. Trans. A* **2012**, *43*, 1688–1704. [CrossRef]
41. Gutierrez-Urrutia, I.; Raabe, D. Grain size effect on strain hardening in twinning-induced plasticity steels. *Scr. Mater.* **2012**, *66*, 992–996. [CrossRef]
42. Gutierrez-Urrutia, I.; Zaefferer, S.; Raabe, D. Electron channeling contrast imaging of twins and dislocations in twinning-induced plasticity steels under controlled diffraction conditions in a scanning electron microscope. *Scr. Mater.* **2009**, *61*, 737–740. [CrossRef]
43. Kim, J.-H.; Kim, D.; Han, H.N.; Barlat, F.; Lee, M.-G. Strain rate dependent tensile behavior of advanced high strength steels: Experiment and constitutive modeling. *Mater. Sci. Eng. A* **2013**, *559*, 222–231. [CrossRef]
44. Curtze, S.; Kuokkala, V.-T.; Hokka, M.; Peura, P. Deformation behavior of TRIP and DP steels in tension at different temperatures over a wide range of strain rates. *Mater. Sci. Eng. A* **2009**, *507*, 124–131. [CrossRef]
45. Jo, M.C.; Choi, J.H.; Lee, H.; Zargaran, A.; Ryu, J.H.; Sohn, S.S.; Kim, N.J.; Lee, S. Effects of solute segregation on tensile properties and serration behavior in ultra-high-strength high-Mn TRIP steels. *Mater. Sci. Eng. A* **2019**, *740–741*, 16–27. [CrossRef]



© 2019 by the authors. Licensee MDPI, Basel, Switzerland. This article is an open access article distributed under the terms and conditions of the Creative Commons Attribution (CC BY) license (http://creativecommons.org/licenses/by/4.0/).

Appendix I

The Impact of Microstructural Characteristics and Testing Parameters on the Formability of High-Manganese Steels

S. Sevsek, S. Wesselmecking, M. Haupt and W. Bleck
Conference Proceedings of the 4th International Conference on Medium and High Manganese Steels, Aachen, Germany, April 1-3 (2019) 310-313

In Appendix I, the impact of deformation twinning on the sheet formability of a high-manganese steel in Nakajima tests is analyzed. To this end, the impact of pre-straining the alloy to 20% elongation was investigated with respect to the residual formability in different strain states of the forming limit diagram.

The Impact of Microstructural Characteristics and Testing Parameters on the Formability of High-Manganese Steels

Simon Sevsek*[1], Sebastian Wesselmecking[1], Marco Haupt[2], Wolfgang Bleck[1]

[1] *RWTH Aachen University, Steel Institute, 52056 Aachen, Germany, *corresponding author: simon.sevsek@iehk.rwth-aachen.de*

[2] *RWTH Aachen University, Institute of Metal Forming, 52056 Aachen, Germany*

Keywords

Forming limit curve, digital image correlation, twinning-induced plasticity, strain localization

1 Introduction

High-manganese steels (HMnS) with Mn contents of more than 12 wt.% exhibit remarkable mechanical properties that result in a product of strength and ductility higher than 50,000 MPa% (ECO-Index). The mechanical properties are due to very high dislocation densities in combination with the activation of additional deformation mechanisms, such as deformation-induced twinning (TWIP) or deformation-induced phase transformation (TRIP) depending on the material's stacking fault energy (SFE) [Bouaziz 2011] [DeCooman 2018]. Other parameters such as grain size, deformation path and deformation speed also influence the secondary deformation mechanism and subsequently the work-hardening rate (WHR) [Meyers 2001].

The occurrence of strain localization phenomena during quasistatic tensile tests has frequently been reported in HMnS. The strain localization is manifested in form of deformation bands that propagate through the sample, resulting in serrated flow curves. While the ductility of HMnS is not impacted significantly, deformation localization during sheet forming processes could potentially result in premature failure. [DeCooman 2018] [Sevsek 2019]

The scope of this work is to study the sheet formability of a X40MnAl19-1 high-Mn TWIP steel. To this end, Nakajima tests with in-situ digital image correlation (DIC) have been performed and the forming limit curves (FLC) have been determined using two different necking criteria. To study the impact of prior deformation, pre-straining to 20% elongation with subsequent Nakajima tests have been conducted.

2 Experimental

The X40MnAl19-1 alloy (designation based on nominal chemical composition in wt.%) was fully recrystallized (designation RX) before testing. For pre-straining to 20% (designation PS), a sheet of the X40MnAl19-1 alloy of 2.10 mm thickness, approximately 1200 mm length and 566 mm width was strained at 3 mm/min, using a 12 MN servohydraulic tensile testing machine at the Steel Institute (IEHK) at RWTH Aachen University. Nakajima sample geometries were machined using water-jet cutting perpendicular to the rolling direction and tensile direction, respectively. Nakajima tests were performed at a testing speed of 60 mm/min, using the in-situ DIC system GOM Aramis 12M operated at a frequency of 10 Hz. For the determination of

the onset of unstable necking, both the “section method” (SM) as well as the time-dependent “linear best fit” (LF) method have been used [Hotz 2013]. The LF method determines the onset of necking based on a distinct change in local strain rate at the position of fracture initiation during the last 4 seconds before fracture. The SM method on the other hand uses the deformation data along a digital section across the necking area of the last time step before fracture to fit a parabola to the detected major and minor strain, which is then used to approximate the critical strains.

3 Results

The results of the quasistatic tensile tests for the RX material as well as the FLC and strain paths for both RX and PS material are shown in Figure 1.

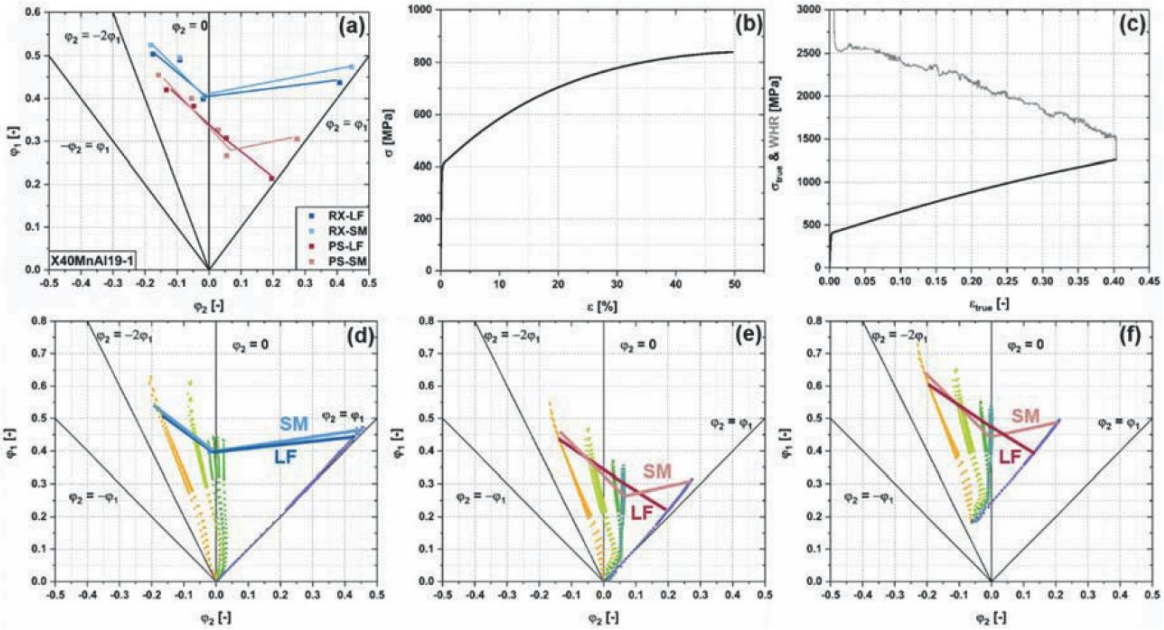


Figure 1: (a) FLC for RX and PS material as determined by both LF and SM method respectively, (b) stress-strain diagram for the RX material and (c) corresponding flow curve with work-hardening rate (WHR). (d)-(f) show the strain paths and FLC for (d) the RX material, (e) the PS material and (f) the PS material starting from 20% pre-straining.

In the case of the RX material, the FLC determined using the LF method was very similar to the FLC determined by using the SM method. For the PS material, both LF method and SM method led to nearly identical FLCs except for the biaxial strain state, where the values determined by the SM method were significantly higher. During the early stages of the Nakajima test, the strain paths of RX and PS revealed significant biaxial pre-strain, which is common in the Nakajima setup. Necking occurred in every strain state except for the biaxial strain state ($\varphi_2=\varphi_1$), which is pointed out by the detection of additional points on the strain paths above the FLC.

As Figure 2 shows, the determination of the onset of necking using either of the two necking criteria during Nakajima tests for the biaxial strain state ($\varphi_2=\varphi_1$) for both the pre-strained (PS) and the fully recrystallized (RX) X40MnAl19-1 alloy was problematic due to inhomogeneous necking behavior. Additionally, electron backscatter diffraction (EBSD) experiments after 20% pre-straining revealed the presence of deformation twins. While the selection of necking criterion did not change the position of the FLC for most stress states as shown in Figure 1, there was a big discrepancy between the determined onset of necking in the biaxial stress state of the pre-strained material state.

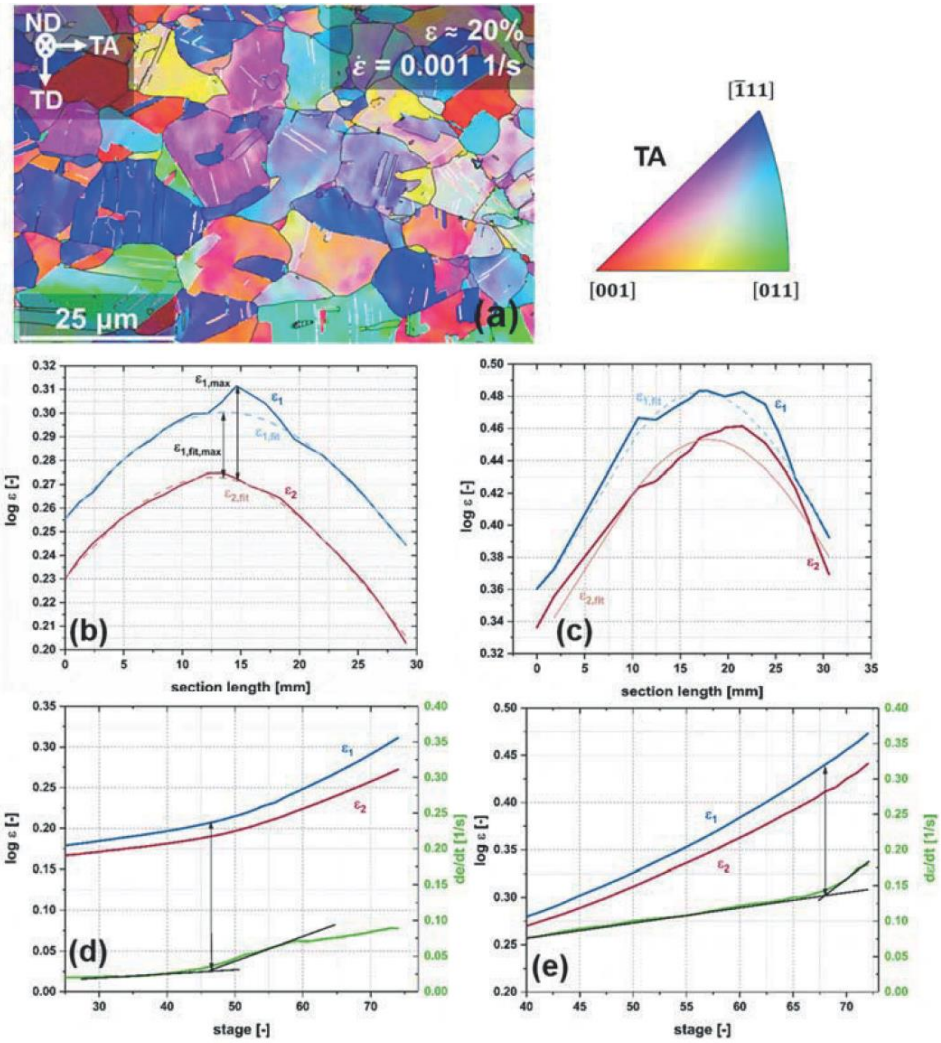


Figure 2: (a) EBSD map with colorcoding according to the inverse pole figure and Σ3 grain boundaries highlighted in white after 20% elongation at 0.1 1/s (ND – normal direction, TA – tensile axis, TD – transversal direction); (b)-(e) determination of onset of critical necking for the biaxial strain state (b)+(c) using the SM method and (d)+(e) LF method for (b)+(d) the PS and (c)+(e) RX material, respectively.

4 Discussion

Previous studies have shown that the activity of the TWIP effect depends on the strain state, as deformation twinning is partly suppressed for $\varphi_2=0$ and even more significantly for $\varphi_2=\varphi_1$ [Weiss 2018]. In general, the forming limit on left side of the forming limit diagram (FLD) is determined by localized necking behavior, whereas the forming limit in the biaxial strain state is usually reached during diffuse necking. As the WHR and accordingly the formability of TWIP steels is increased by deformation twinning, the left side of the forming limit diagram (FLD) is high compared to the right side, where deformation twinning is partly suppressed.

Additionally, serrated flow curves during quasistatic tensile tests in high-Mn TWIP steels have been shown to be related to the TWIP effect. Although strain localization phenomena can be observed as deformation bands during those tests, the total formability is not impacted because local strains can effectively be accommodated on a microstructural level by the activation of additional twin systems and slip systems in neighboring grains [Sevsek 2019]. In the case of the biaxial strain state during

Nakajima tests, the partly suppression of deformation twinning leads to failure without significant necking, as Figures 2(b)+(c) show, because local stress increases cannot be accommodated as effectively.

Comparing Figures 1(d)+(f), the total formability of the PS material considering the pre-straining of 20% is comparable to the RX material with regards to the right side of the FLD, but significantly better for the left side. The overall twin fraction is reported to be relatively low and highly dependent on grain orientation [DeCooman 2018] [Meyers 2001]. As the samples for the Nakajima test were cut perpendicular to the direction of pre-straining, previously unfavorable orientations for twinning are now preferential. Accordingly, increased deformation twinning in the PS material on the left side of the FLD compared to the RX material after deformation equivalent to 20% elongation could be one reason for the good residual formability of the PS material.

Regarding the selection of the method to determine the onset of critical necking, both methods were susceptible to diffuse necking in the biaxial strain state. For the LF method, the diffuse necking behavior induced jumps in the detected strain rate (cf. Figure 2(d)), which led to a premature determination of the critical strain for inhomogeneous deformation, while the occurrence of multiple, small necking zones in the RX material (cf. Figure 2(c)) led to a poor parabola fit.

5 Conclusions

In this study, Nakajima tests for a fully recrystallized and a 20% pre-strained high-Mn TWIP X40MnAl19-1 steel revealed that the low formability in the biaxial strain state compared to the uniform elongation strain state is due to the strain-path dependence of deformation twinning. Accordingly, the residual formability of the pre-strained material depended on the strain path, as well. The analysis of the linear-best-fit time-dependent method and the section method to determine the onset of critical necking revealed that both methods are not robust enough to be used discretionary in cases of diffuse necking behavior.

Acknowledgement

The authors are grateful for the financial support of the Deutsche Forschungsgemeinschaft (DFG) within the Collaborative Research Centre (SFB) 761 “Steel – ab initio”.

References

Bouaziz, O.; Allain, S.; Scott, P.; Cugy, D.; Barbier, D.: High manganese austenitic twinning induced plasticity steels: A review of the microstructure properties relationships. Curr. Opin. Solid State Mater. Sci. 15 (2011) 141–168. https://doi.org/10.1016/j.cossms.2011.04.002.

DeCooman, B.C.; Estrin, Y.; Kim, S.K.: Twinning-induced plasticity (TWIP) steels, Acta Mater. 142 (2018) 283–362. https://doi.org/10.1016/j.actamat.2017.06.046.

Hotz, W.; Merklein, M.; Kuppert, A.; Friebe, H.; Klein, M.: Time dependent FLC determination - Comparison of different algorithms to detect the onset of unstable necking before fracture, Key Engineering Materials 549 (2013) 397–404. https://doi.org/10.4028/www.scientific.net/KEM.549.397.

Meyers, M.A.; Vöhringer, O.; Lubarda, V.A.: The onset of twinning in metals: a constitutive description, Acta Mater. 49 (2001) 4025–4039. https://doi.org/10.1016/S1359-6454(01)00300-7.

Sevsek, S.; Brasche, F.; Haase, C.; Bleck, W.: Combined deformation twinning and short-range ordering causes serrated flow in high-manganese steels, Materials Science and Engineering: A 746 (2019) 434-442. https://doi.org/10.1016/j.msea.2019.01.042.

Weiss, M.; Mester, K.; Taylor, A.; Stanford, N.: A critical assessment of deformation twinning and epsilon martensite formation in austenitic alloys during complex forming operations, Materials Characterization 145 (2018) 423-434. https://doi.org/10.1016/j.matchar.2018.09.003.

Appendix II

On the mechanical and corrosion properties of a precipitation-strengthened medium manganese austenitic stainless steel

T. Allam, **S. Sevsek**, X. Guo, A. Hamada and W. Bleck
Conference Proceedings of the 4th International Conference on Medium and High Manganese Steels, Aachen, Germany, April 1-3 (2019) 365-368

The extended abstract in Appendix II reveals that precipitation hardening in a Chromium-alloyed fully austenitic medium-manganese led to a high yield strength of approximately 600 MPa while retaining a high work-hardening rate, resulting in an ultimate tensile strength of 975 MPa and more than 45% elongation to fracture. Despite carbide precipitation, the corrosion resistance was comparable to stainless steels typically used in industrial applications.

On the mechanical and corrosion properties of a precipitation-strengthened medium manganese austenitic stainless steel

Tarek Allam[1,2,*], Simon Sevsek[1], Xiaofei Guo[1], Atef Hamada[3] and Wolfgang Bleck[1]

[1]*Steel Institute (IEHK), RWTH Aachen University, 52056 Aachen, Germany, tallam@iehk.rwth-aachen.de*

[2]*Metallurgical and Materials Engineering Department, Suez University, Suez, Egypt*

[3]*Egypt-Japan University of Science and Technology, New Borg El-Arab City, Egypt*

[*]*Speaker*

Abstract

A cold-rolled and annealed medium manganese (MMn) stainless steel with improved strength-ductility balance has been developed by utilizing a precipitation-strengthening concept. Recrystallization annealing at 1000 °C for 3 minutes resulted in a fully-recrystallized and extremely fine-grained (~1µm) austenitic microstructure with a substantial amount of Cr-V-based precipitates. The developed steel revealed a yield strength (YS) of 600 MPa, an ultimate tensile strength (UTS) of 975 MPa and more than 45% total elongation (TE). The results demonstrate a comparable TE to the conventional high manganese (HMn) TWIP X60MnAl17-1 steel with an increase of more than 300 MPa in YS and 160 MPa in UTS. Compared to AISI 410 austenitic stainless steel, the developed MMn-stainless steel shows a pronounced increase in YS and UTS with 240 MPa and 250MPa, respectively. Potentio-dynamic polarization measurements in 5%NaCl revealed that the developed steel has a similar open current potential and one order higher corrosion current density than that of 26Cr-19Ni stainless steel, while it shows a distinct positive open current potential and one order lower corrosion current density than that of HMn TWIP Fe-15Mn-2Al-0.5C steel. The excellent mechanical properties and good corrosion resistance of the developed MMn-austenitic stainless steel emphasize its potential to be applied for lightweight concepts of cold-formable components with increased corrosion resistance.

Keywords

MMnS, strain hardening, corrosion properties, austenitic stainless steel, precipitations

1 Introduction

High manganese steels (HMnS) exhibit an excellent combination of ultra-high strength and work hardening capacity (Grässel et al. 2000). As a solution for the low yield strength that limits their industrial application, a processing route consisting of cold rolling followed by a recovery annealing heat treatment has been proposed (Bouaziz et al. 2011). Moreover, various alloying elements have been added to enhance the poor corrosion resistance of HMnS (Kannan et al. 2008). In order to minimize production costs and overcome the processing-related drawbacks, medium manganese steels (MMnS) have been developed. Their duplex microstructure consisting of ferrite and austenite allows even higher yield strengths to be achieved in addition to a considerable work hardening rate, which depends on the amount and stability of the reverted austenite (Suh et al. 2013; Ma et al. 2017). In this contribution, a new medium manganese austenitic stainless steel concept is developed that possesses superior mechanical properties to the conventional stainless steel and enhanced corrosion resistance compared to HMnS. The addition of V was utilized for

precipitation strengthening to achieve high yield strength and to control the grain size during recrystallization annealing treatments.

2 Experimental

The laboratory-produced steel grade was subjected to hot and cold rolling processes to a final thickness of 1.5 mm with 62.5% cold reduction. The chemical composition is listed in Table 1. The microstructure was adjusted in a recrystallization annealing treatment at 1000 °C for 3 minutes in a salt bath. Scanning Electron Microscopy (SEM) equipped with Energy Dispersive Spectrometer (EDS) and Electro Backscattering Diffraction (EBSD) was applied to investigate the developed microstructures. Mechanical properties were evaluated by means of tensile testing at room temperature. The corrosion properties of the investigated material were evaluated by dynamic polarization measurement in 5%NaCl with controlled scanning rate of 0.016 mV/s

Table 1: Chemical composition in wt.% for the steel grade under investigations.

Elements	C	Si	Mn	P	S	Cr	Ni	V	N
Developed-MMn	0.17	0.43	10.4	0.014	0.009	17.7	4.7	1.0	0.267

3 Results

Figure 1a shows that the annealing treatment at 1000°C for 3 minutes resulted in a recrystallized microstructure with an average grain size of approximately 1 μm (cf. Figure 1b taking annealing twins into account), and that the formation of a significant amount of precipitates occurred. The preliminary thermodynamic and kinetics calculations using Thermo-calc® -TCFE9 database and MatCalc-6, respectively, indicated the formation of M23C6 and MN particles that reach their saturation state within the first 300s at 1000°C. Figure 1d shows that recrystallization did not lead to the development of a strong texture and that the microstructure was almost fully austenitic, with less than 1% of ferrite detected during EBSD (cf. Figure 1e). As shown in Fig. 1f, no martensitic phase transformation was observed after 20% elongation. After fracture (cf. Figure 1g), very small fractions of ε-martensite (below 1%) were present. Significant deformation twinning was not observed at any deformation stage.

Tensile tests revealed that the developed MMn-stainless steel showed superior YS and UTS values compared to those of the HMn-TWIP X60MnAl17-1 alloy or the conventional AISI 304 austenitic stainless steel with a comparable TE, as is shown in Figure 2a. The corresponding work hardening rate (WHR) depicted inFigure 2b revealed a higher initial WHR for the developed MMn-stainless steel (~3.4 GPa) than the other grades. However, this high WHR decreased at a higher rate than those of other grades until they became equal at a true stress value of about 1.2 GPa.

The developed MMn steel did not only achieve an improved mechanical property-profile, but it also exhibited an enhanced corrosion resistance, which is comparable to the corrosion behavior of the austenitic steel AISI 310s and superior to the HMn-TWIP X60MnAl17-1 steel. Figure 3 shows the potentio-dynamic polarization curves in addition to the open current potential and corrosion current density values of the developed steel in comparison to the references.

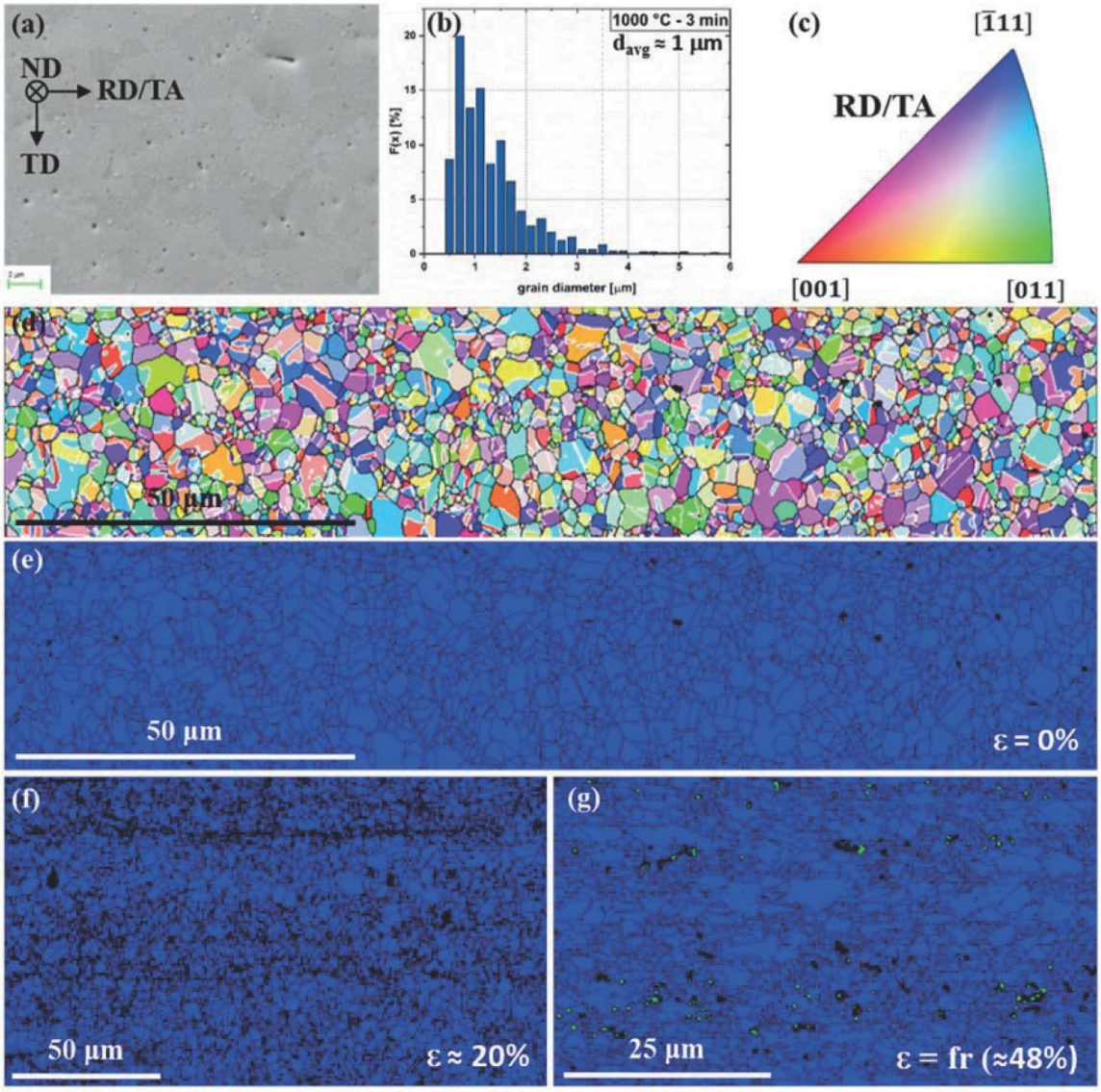


Figure 1: Microstructure of the developed MMn-stainless steel. a) SEM image of the as-annealed state containing precipitates, b) grain size distribution and average grain size determined by line-intercept method taking annealing twins into account, c) color-coding for the EBSD map before deformation (shown in d), and phase maps (e) before deformation, (f) after 20% elongation and (g) after fracture, showing austenite (blue), ferrite or α'-martensite (green) and ε-martensite (red). TA: Tensile Axis. RD, ND and TD are Rolling, Normal and Transversal Directions, respectively.

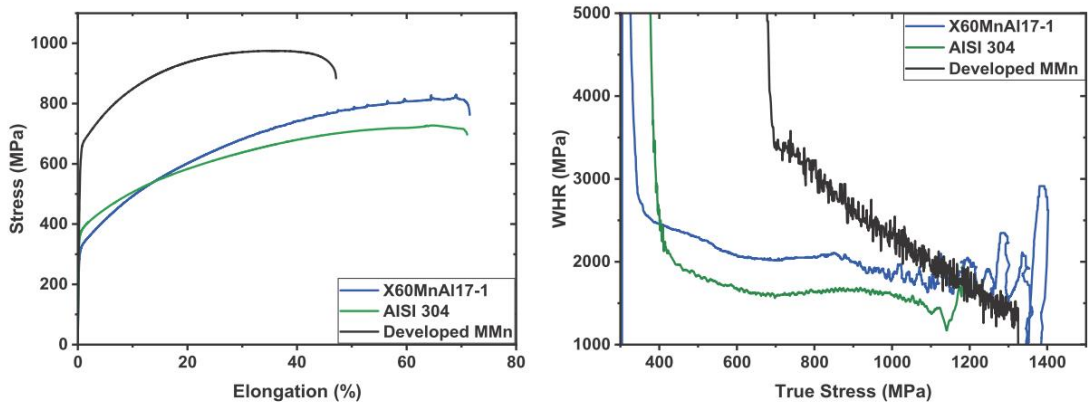
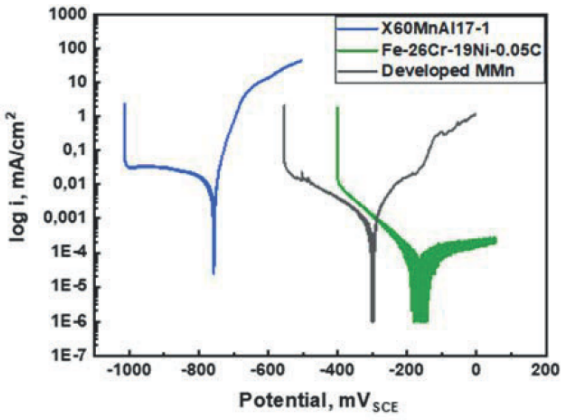


Figure 2: Tensile properties in comparison to conventional AISI 304 austenitic stainless and HMn-TWIP steels. a) Engineering stress-strain and b) work hardening rate (WHR) curves.



Material	Open current potential, mV_{SCE}	Corrosion current density, mA/cm2
X60MnAl17-1	-755	0.00897
Fe-26Cr-19Ni-0.05C (AISI 310s)	-175	0.00003
Developed MMn	-300	0.00079

Figure 3: Recorded Polarization curves in 5%NaCl for the developed MMn-stainless steel compared to conventional austenitic stainless AISI 310s and HMn-TWIPX60MnAl17-1 steels.

4 Summary

A new cold-rolled and annealed MMn-austenitic stainless steel has been developed and investigated in terms of mechanical and corrosion properties. The superior tensile properties and the high initial WHR seem to be due to the very fine-grained microstructure and the formation of different Cr-V-based precipitates. The exact types of precipitates have to be investigated in further studies. Although the stacking fault energy of the developed steel is in the TWIP-range (~25 mJ/m^2 based on a previous study (Hamada and Kömi 2018)), no twins have been observed, even after fracture, emphasizing the role of grain size in controlling the deformation mechanism. We believe that the presence of carbides can deteriorate the corrosion resistance, however, the developed steel with less than 5 wt.% Ni and approximately 18 wt.% Cr still can show comparable corrosion resistance to that of the more expensive (19 wt.%Ni and 26 wt.%) AISI 310s stainless steel.

Acknowledgement

Hamada gratefully acknowledges the STDF- Egypt for supporting the melt production. Allam expresses his gratitude to the DAAD for the personal financial support. DFG within the Collaborative Research Center (SFB) 761 is appreciated for supporting the processing and testing the developed steel grade.

References

Bouaziz, O.; Allain, S.; Scott, C. P.; Cugy, P.; Barbier, D.: High manganese austenitic twinning induced plasticity steels. A review of the microstructure properties relationships. Current Opinion in Solid State and Materials Science, 15 (2011) 4, pp. 141–168.

Grässel, O.; Krüger, L.; Frommeyer, G.; Meyer, L.W: High strength Fe–Mn–(Al, Si) TRIP/TWIP steels development — properties — application. International Journal of Plasticity, 16 (2000) 10-11, pp. 1391–1409.

Hamada, Atef; Kömi, Jukka: Effect of microstructure on mechanical properties of a novel high-Mn TWIP stainless steel bearing vanadium. Materials Science and Engineering: A, 718 (2018), pp. 301–304.

Kannan, M. Bobby; Raman, R. SinghK; Khoddam, S.: Comparative studies on the corrosion properties of a Fe–Mn–Al–Si steel and an interstitial-free steel. Corrosion Science, 50 (2008) 10, pp. 2879–2884.

Ma, Yan; Song, Wenwen; Bleck, Wolfgang: Investigation of the Microstructure Evolution in a Fe-17Mn-1.5Al-0.3C Steel via In Situ Synchrotron X-ray Diffraction during a Tensile Test. Materials, 10 (2017) 10.

Suh, Dong Woo; Ryu, Joo Hyun; Joo, Min Sung; Yang, Hong Seok; Lee, Kyooyoung; Bhadeshia, H. K. D. H.: Medium-Alloy Manganese-Rich Transformation-Induced Plasticity Steels. Metall and Mat Trans A, 44 (2013) 1, pp. 286–293.

Appendix III

Impact of warm rolling on microstructure and mechanical properties of high manganese steels

M. Haupt, M. Müller, C. Haase, **S. Sevsek**, A. Schwedt and G. Hirt
Conference Proceedings of the 4th International Conference on Medium and High Manganese Steels, Aachen, Germany, April 1-3 (2019) 97-100

Scope of Appendix III is to transfer the concept of recovery annealing to the warm rolling process of a high-manganese steel. In this context, the temperature during warm rolling was varied to change the stacking fault energy. The subsequent changes in microstructure and mechanical response to uniaxial deformation were evaluated by means of electron backscatter diffraction measurements and quasistatic tensile testing, respectively. Overall, the yield strength was significantly higher than in the fully recrystallized material, while deformation twinning was activated during tensile testing at room temperature, which led to a notable work-hardening during deformation. As a result, it was possible to adjust the strength-ductility combination of the high-manganese steel based on the temperature during warm rolling.

Impact of warm rolling on microstructure and mechanical properties of high manganese steels

Marco Haupt[1], Max Müller[1], Christian Haase[2], Simon Sevsek[2], Alexander Schwedt[3], Gerhard Hirt[1]

[1]*Institute of Metal Forming, RWTH Aachen University, Germany, haupt@ibf.rwth-aachen.de*

[2]*Steel Institute, RWTH Aachen University, Germany*

[3]*Central Facility for Electron Microscopy, RWTH Aachen University, Germany*

Abstract

In this work, a Fe-23Mn-0.3C-1Al high manganese steel was processed to warm rolled strips using varying rolling temperatures in order to substantially increase the yield strength and maintain a certain ductility. Application of electron backscatter diffraction (EBSD) and uniaxial tensile testing allows for the understanding of the activated deformation mechanisms and their impact on the resulting microstructure and mechanical properties. Compared to the recrystallized state, the results show a significant enhancement of the yield strength. This behaviour is mainly dominated by the change of the active deformation mechanisms during rolling. At lower temperatures deformation twinning is very pronounced, whereas this mechanism is suppressed at temperatures higher than 400 ℃.

Keywords

HMnS, Warm Rolling, Microstructure, Mechanical Properties

1 Introduction

High manganese TWIP steels offer favourable mechanical properties in terms of high tensile strength and high ductility, which is generally of high relevance for crash relevant automotive applications. However, the comparably low yield strength of fully recrystallized high manganese steels represents a crucial disadvantage. Hence, numerous approaches to increase the yield strength of high manganese TWIP steels have been discussed in the literature, such as micro alloying [Scott 2018], partial recrystallization [Bouaziz 2013], grain refinement [Ueji 2008] and recovery annealing [Haase 2016]. Due to present limitations of these approaches, the impact of warm rolling on the mechanical properties of a high manganese steel is investigated in the present study.

The deformation mechanisms activated in high manganese steels are mainly determined by the stacking fault energy (SFE), which is dependent on the chemical composition, grain size and temperature. In the SFE range of 20 to 60 mJ/m² deformation twinning is the predominant deformation mechanism in addition to dislocation glide. Above 60 mJ/m², the deformation mechanism changes mainly to slip [Saed-Akbari 2009]. The concept of warm rolling of high manganese TWIP steels takes advantage of this temperature dependence of the deformation mechanisms and allows for a combination of slip and twinning to achieve superior mechanical properties. By rolling at elevated temperatures and therefore higher SFE, the material benefits from strain hardening due to the slip effect. The twinning mechanism during forming at room temperature, i.e. after prior warm rolling, accordingly enables a certain ductility and work hardening behaviour of the warm rolled high manganese steel.

In order to investigate the impact of warm rolling temperature on the mechanical properties of a high manganese steel, a Fe-23Mn-0.3C-1Al TWIP steel was processed at rolling temperatures ranging from 200 to 500 ℃ in this work. The resulting microstructure was characterised by EBSD measurements, whereas mechanical properties were analysed by uniaxial tensile tests.

2 Experimental Procedure

2.1 Material and processing

A Fe-23Mn-0.3C-1Al high manganese steel alloy was selected for the present study. The respective chemical composition is given in Table 1.

Table 1: Chemical composition of the processed Fe-23Mn-0.3C-1Al high manganese steel

Element	Fe	C	Si	Mn	P	S	Al	Ni	Mo	Cr
wt.%	Bal.	0.322	0.053	22.45	0.008	0.008	0.995	0.027	0.008	0.020

The investigated material was produced by an adapted hot forming route comprising ingot casting, forging and hot rolling. At first, a 100 kg ingot was cast in a vacuum induction furnace. Then the ingot was forged in one heat and three passes at 1150 ℃ to reduce the height from 140 mm to 50 mm. A subsequent annealing treatment at 1150 ℃ for five hours in an argon atmosphere was applied to dissolve micro-segregations. During hot rolling at 1150 ℃, sheet thickness was further reduced to 4.0 mm in seven passes. The occurring oxide-scale was subsequently removed by sandblasting.

Then the hot strips were warm rolled in seven passes to 2.0 mm on a four-high cold-rolling mill. In order to investigate the impact of the warm rolling temperature, the 50 % thickness reduction was conducted at 200 ℃, 400 ℃ and 500 ℃, respectively. The strips were reheated for five minutes in between consecutive rolling passes to ensure consistent rolling temperatures.

2.2 Material characterisation

The resulting microstructure of the warm rolled strips was examined using a JEOL JSM 7000F scanning electron microscope equipped with an EDAX Hikari EBSD detector. The measurements were performed with a step size of 200 nm and an acceleration voltage of 20 kV.

Determination of the mechanical properties in rolling direction at room temperature was achieved by uniaxial tensile tests on a Zwick Z100 universal testing machine at a constant strain rate of 0.001 s^{-1}.

3 Results and Discussion

Figure 1 shows EBSD-IQ maps of the resulting microstructure after warm rolling of the Fe-23Mn-0.3C-1Al high manganese steel at different temperatures. All images display a highly deformed austenitic grain structure. The fraction of twin boundaries (60°<111>), which are indicated in blue colour, decreases significantly at higher warm rolling temperatures. At 400 ℃ warm rolled material still shows a significant fraction of twin boundaries, while practically no twin boundaries are present in the material warm rolled at 500 ℃. This correlation indicates a change of the predominant deformation mechanism during warm rolling from twinning to slip in the temperature range of 400 to 500 ℃. Therefore, it was possible to achieve a height reduction of 50 % primarily based on the slip mechanism during warm rolling at 500 ℃.

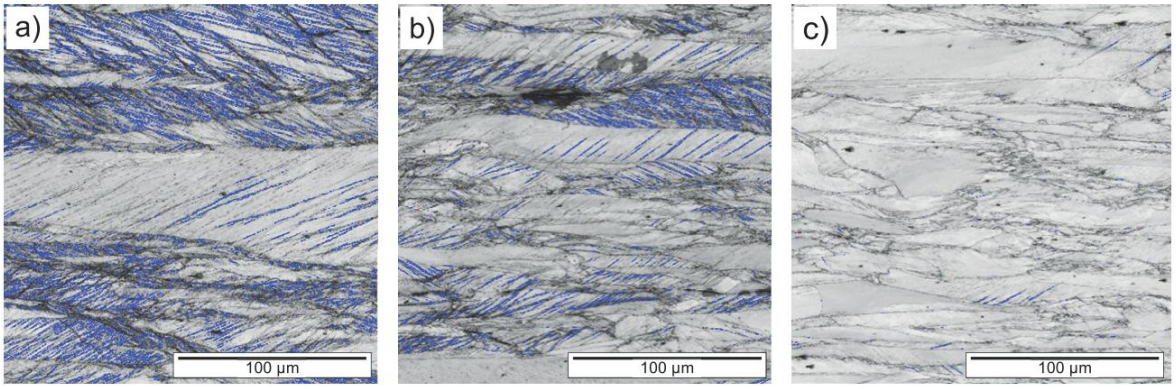


Figure 1: EBSD-IQ maps of 50 % warm rolled material at a) 200 ℃, b) 400 ℃ and c) 500 ℃. Blue lines indicate deformation twin boundaries (60°<111>).

The impact of the observed microstructure on the mechanical properties of the warm rolled material is shown in Figure 2, which shows the corresponding engineering stress-strain curves derived from uniaxial tensile tests. A warm rolling temperature of 200 ℃ results in a very high yield strength of 109 2 MPa and a total elongation (TE) of only 12.0 %. An increased warm rolling temperature leads to a decrease in yield and tensile strength (TS), but to a significant increase in uniform elongation (UE) and total elongation. The material, which was warm rolled at 500 ℃, still exhibits a high yield strength (YS) of 788 MPa but a significantly increased total elongation of 38.5 %. The results of uniaxial tensile tests are summarised in Table 2.

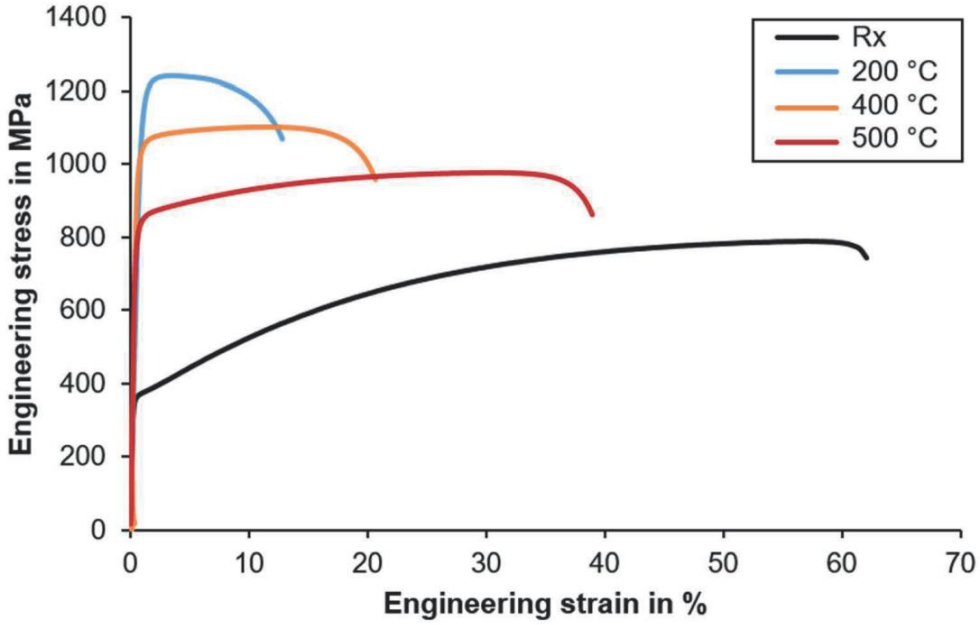


Figure 2: Engineering stress-strain curves of 50 % warm rolled material at 200 ℃, 400 ℃ and 500 ℃ in comparison to a recrystallized (Rx) m aterial state (50% cold rolled and annealed for 30 min at 700 ℃).

All warm rolled materials show a significant work-hardening behaviour at room temperature despite the high deformation applied during the rolling process. This indicates the activation of the twinning mechanism during the tensile tests at room temperature, which causes the notable work-hardening. In comparison to the recrystallized Fe-23Mn-0.3C-1Al high manganese steel, which was annealed for 30 minutes at 700 ℃ after 50% cold rolling, warm r olling leads to a drastic increase in yield and tensile strength at a reasonable decrease of ductility. Despite the strong

work-hardening behaviour of the recrystallized material, the overall strength level of the warm rolled materials exceeds the tensile strength of the recrystallized state.

Table 2: Mechanical properties of the investigated steel depending on the material condition

Material condition	YS in MPa	TS in MPa	UE in %	TE in %
WR at 200 ℃	1092	1242	2.7	12.0
WR at 400 ℃	969	1100	11.3	20.2
WR at 500 ℃	788	975	30.1	38.5
Rx	356	787	56.8	62.1

4 Conclusion

In this work, a Fe-23Mn-0.3C-1Al high manganese TWIP steel was subjected to a processing route comprising ingot casting, forging, hot rolling and warm rolling at various warm rolling temperatures in order to increase the yield strength and maintain a decent ductility. The resulting microstructure and corresponding mechanical properties were analysed. The following conclusions can be drawn:

- The predominant deformation mechanism of a high manganese TWIP steel during rolling can be affected by adjustment of the rolling temperature, which results in a change of the stacking fault energy. EBSD-IQ maps of the investigated material show a drastic decrease of the fraction of twin boundaries after warm rolling at 500 ℃ compared to lower warm rolling temperatures.
- The warm rolled material exhibits excellent mechanical properties due to the combination of slip and twinning. An increased rolling temperature results in an increased elongation and a decreased yield and tensile strength. The twinning mechanism, which is predominant at room temperature, enables a significant work-hardening of the warm rolled material.
- Warm rolling of high manganese TWIP steels is suitable for notably improving the yield strength. The comparison to the recrystallized material state shows an overall advantage of the warm rolled material state regarding mechanical properties. The strength level could be substantially increased while maintaining a reasonable ductility.

Acknowledgement

The authors gratefully acknowledge the financial support of Deutsche Forschungsgemeinschaft (DFG) within the Collaborative Research Centre (SFB) 761 “Stahl - ab initio; Quantenmechanisch geführtes Design neuer Eisenbasiswerkstoffe”.

References

Saeed-Akbari, A. et al.: Derivation and variation in composition-dependent stacking fault energy maps based on subregular solution model in high-manganese steels. Metall and Mat Trans A, 40 (2009), pp3076–3090

Bouaziz, O.; Barbier, D.: Benefits of recovery and partial recrystallization of nano-twinned austenitic steels. Adv.Eng.Mater.,15 (2013), p976-979

Haase, C. et al.: On the applicability of recovery-annealed twinning-induced plasticity steels: Potential and limitations. Materials Science & Engineering A, 649 (2016), pp74–84

Scott, C. et al.: Precipitation strengthening in high manganese austenitic TWIP steels. International Journal of Materials Research, 102 (2011), p538-549

Ueji, R. et al.: Tensile properties and twinning behavior of high manganese austenitic steel with fine-grained structure. Scr.Mater., 59 (2008), p963-966

Curriculum Vitae

Personal information

Surname, given name	**Sevsek, Simon**
Address	Augustinergasse 2, 52062 Aachen, Germany
Nationality	German
Date of birth	September 1st, 1990
Place of birth	Kamp-Lintfort, Germany
Phone	0172 8990102
E-Mail	simon.sevsek@rwth-aachen.de

Professional experience

Since 11/2016	**IEHK - Institut für Eisenhüttenkunde / Steel Institute RWTH Aachen University, Aachen, Germany** Research assistant / doctorate student Topic: "On the Impact of Micro- and Nanostructural Characteristics on the Deformation Behavior and Mechanical Properties of High- and Medium-Manganese Steels"
Since 01/2019	**Core Team of management**, **Cluster of Excellence "Internet of Production"**, RWTH Aachen University, Aachen, Germany **Deputy Coordinator Cluster Research Domain "Materials"**
06/2017 – 12/2018	**Core Team of management, Cluster of Excellence "Integrative Production Technology for High-Wage Countries"**, RWTH Aachen University, Aachen, Germany
04/2016 - 10/2016	**IEHK - Institut für Eisenhüttenkunde / Steel Institute RWTH Aachen University, Aachen, Germany** Research student / master's thesis Topic: "Microstructure-based process optimization of the precipitation behaviour of vanadium in a cold-formable AFP-steel" (Grade: 1.0)
06/2014 – 08/2014	**ThyssenKrupp Steel Europe AG** Werk Westfalenhütte, Dortmund, Germany Internship: Innovation management
06/2013 – 02/2014	**IBF – Institut für bildsame Formgebung / Institute of Metal Forming, RWTH Aachen University, Aachen, Germany** Research student / bachelor's thesis Topic: "Process chain optimization for manufacturing of composite rings in ring rolling" (Grade: 1.3)

Education

10/2011 - 10/2016	**RWTH Aachen University, Aachen, Germany** **B.Sc. and M.Sc. Business Administration and Engineering** Specialization: Materials and Process Engineering
09/2001 - 07/2010	**Städtisches Gymnasium Kamp-Lintfort** (now: Georg-Forster-Gymnasium), Kamp-Lintfort, Germany Degree: **Abitur (Grade 1.0)**